TERA

NUREG/CR-0655
ORNL/NUREG/TM-297

Multirod Burst Test Program Progress Report for July–December 1978

R. H. Chapman

Prepared for the U.S. Nuclear Regulatory Commission
Office of Nuclear Regulatory Research
Under Interagency Agreements DOE 40-551-75 and 40-552-75

OAK RIDGE NATIONAL LABORATORY
OPERATED BY UNION CARBIDE CORPORATION · FOR THE DEPARTMENT OF ENERGY

Printed in the United States of America. Available from
National Technical Information Service
U.S. Department of Commerce
5285 Port Royal Road, Springfield, Virginia 22161

NUREG/CR-0655
ORNL/NUREG/TM-297
Dist. Category R3

Contract No. W-7405-eng-26

Engineering Technology Division

MULTIROD BURST TEST PROGRAM PROGRESS REPORT FOR JULY–DECEMBER 1978

R. H. Chapman

Manuscript Completed – May 8, 1979
Date Published – June 1979

Prepared for the
U.S. Nuclear Regulatory Commission
Office of Nuclear Regulatory Research
Washington, D.C. 20555
Under Interagency Agreements DOE 40-551-75 and 40-552-75

NRC FIN No. B0120

Prepared by the
OAK RIDGE NATIONAL LABORATORY
Oak Ridge, Tennessee 37830
operated by
UNION CARBIDE CORPORATION
for the
DEPARTMENT OF ENERGY

CONTENTS

FOREWORD

This report summarizes progress and preliminary results of the Multirod Burst Test (MRBT) Program [sponsored by the Division of Reactor Safety Research of the Nuclear Regulatory Commission (NRC)] for the period July–December 1978.

Work on this program was reported initially in Volume I of a four-volume series entitled *Quarterly Progress Report on Reactor Safety Programs Sponsored by the NRC Division of Reactor Safety Research*. Prior reports of MRBT activities in this series are:

Report No.	Pages	Period covered
ORNL/TM-4729	70–72	July–September 1974
ORNL/TM-4805	102–110	October–December 1974
ORNL/TM-4914	78–104	January–March 1975
ORNL/TM-5021	76–98	April–June 1975

Beginning with the period July–September 1975, work on this program is documented in reports titled *Multirod Burst Test Program Progress Report*. Prior reports in this series are:

Report No.	Period covered
ORNL/TM-5154	July–September 1975
ORNL/NUREG/TM-10	October–December 1975
ORNL/NUREG/TM-36	January–March 1976
ORNL/NUREG/TM-74	April–June 1976
ORNL/NUREG/TM-77	July–September 1976
ORNL/NUREG/TM-95	October–December 1976
ORNL/NUREG/TM-108	January–March 1977
ORNL/NUREG/TM-135	April–June 1977

In mid-1978 a duplicate report identification system was instituted whereby an NRC report number is also assigned to NRC-sponsored work. Previous progress reports issued in this category include:

NUREG Report No.	ORNL Report No.	Period covered
NUREG/CR-0103	ORNL/NUREG/TM-200	July–December 1977
NUREG/CR-0225	ORNL/NUREG/TM-217	January–March 1978
NUREG/CR-0398	ORNL/NUREG/TM-243	April–June 1978

Topical reports pertaining to research and development carried out by this program are:

1. R. H. Chapman (comp.), *Characterization of Zircaloy-4 Tubing Procured for Fuel Cladding Research Programs*, ORNL/NUREG/TM-29 (July 1976).

2. W. E. Baucum and R. E. Dial, *An Apparatus for Spot Welding Sheathed Thermocouples to the Inside of Small-Diameter Tubes at Precise Locations*, ORNL/NUREG/TM-33 (August 1976).

3. W. A. Simpson, Jr., et al., *Infrared Inspection and Characterization of Fuel-Pin Simulators*, ORNL/NUREG/TM-55 (November 1976).

4. R. H. Chapman et al., *Effect of Creep Time and Heating Rate on Deformation of Zircaloy-4 Tubes Tested in Steam with Internal Heaters*, NUREG/CR-0343 (ORNL/NUREG/TM-245) (October 1978).

The following limited-distribution quick-look reports have been issued by this program:

1. R. H. Chapman (comp.), *Quick-look Report on MRBT No. 1 4 × 4 Bundle Burst Test*, Internal Report ORNL/MRBT-2 (September 1977).

2. R. H. Chapman (comp.), *Quick-look Report on MRBT No. 2 4 × 4 Bundle Burst Test*, Internal Report ORNL/MRBT-3 (November 1977).

3. R. H. Chapman, *Quick-look Report on MRBT No. 3 4 × 4 Bundle Burst Test*, Internal Report ORNL/MRBT-4 (August 1978).

SUMMARY

The technology for fabricating electrically heated fuel simulators, based on the use of cold-pressed boron nitride (BN) preforms for isolating the heating element from the outer sheath, is under development in our laboratories. A number of prototype units were fabricated to develop design parameters and to establish fabricating procedures. Two of the prototypes were used in single-rod tests that demonstrated the acceptability of the simulators for this program. The tests also produced valid data points for inclusion in our single-rod data base.

After defining the design parameters and fabricating procedures, 92 acceptable fuel simulators were produced for use in future tests. The quality of the units is unusually good, and they were produced at a rate of 10 to 12 per week after the fabrication schedule was fully developed. Less than 10% of the total units produced were rejected during the production run.

Additional data analysis was performed on the B-1 test results, including characterization of the time-dependent bundle temperature distribution and heating rate. Also, the cross sections were examined to determine if the temperature difference between the bundle and shroud caused preferential wall thinning of the tubes in the outer ring of fuel pin simulators. This examination, being somewhat qualitative, did not show that there was a strong preference for localized deformation.

Posttest examination and analysis of the data were completed on the B-2 test. Deformation of the B-2 test array was essentially the same as that observed in the B-1 array. In fact, a comparison of all the test results revealed very little difference between the two tests. The one exception was that the larger temperature difference between the B-2 bundle and shroud caused preferential wall thinning of the tubes in the outer ring of fuel pin simulators. This appears to be a secondary effect, and the importance of this observation cannot be assessed at this time.

The third 4 × 4 bundle test (B-3) was conducted early in this reporting period after making repairs to the simulator seal glands that caused the aborting of an earlier test attempt. Initial pressure conditions (~11,600 kPa at 329°C) were selected to cause failure of the tubes

at ∿760°C. The heating rate of the bundle was ∿9.5°C/sec and that of the shroud ∿7.1°C/sec, although it was intended that both heating rates be the same. The test parameters were selected to cause bundle deformation under conditions believed by some to be more realistic pressurized-water reactor (PWR) loss-of-coolant accident (LOCA) parameters and to permit comparison of B-3 results with those obtained from two single-rod tests (SR-41 and SR-42) conducted earlier with a heating rate of 10°C/sec.

One of the B-3 simulator seal glands developed a significant leak prior to the test transient, and modifications were made to compensate for the leak by admitting helium (the pressurizing gas) to the simulator at a rate approximately equal to the leak rate. The helium flow rate was terminated immediately after the burst. As a result of this action, this particular simulator was tested under essentially constant pressure conditions; the remainder of the tubes were tested under conditions of constant gas mass. One simulator partially depressurized during the final stage of deformation and, as a result, its failure is attributed to creep.

All the tubes burst, with 15 of the failures occurring in a time period of 3.1 sec; the creep failure occurred 16.6 sec after power to the bundle was terminated. Burst conditions were in good agreement with expectations.

Deformation in B-3 was greater and more extensive than that observed in the B-1 and B-2 tests. This is probably due to a more uniform temperature distribution and to the lower heating rate (i.e., strain rate) in the B-3 test. The temperature difference between the bundle and the shroud was about 80°C when the bursts were occurring.

Deformation was such that flow testing the bundle in the larger of two available flow shrouds was precluded. A new shroud was fabricated, and flow tests were conducted on the reference and the B-3 bundles in it. These tests confirmed the visual observation that greater deformation occurred in B-3 than in B-1 and B-2.

The bundle has been cast in an epoxy matrix and is now being sectioned to permit determination of the strain.

Additional flow tests were conducted with the reference bundle with a single grid in shroud 1 to better define the friction factor correlation

and the grid pressure loss coefficient that should be used in COBRA analyses of the deformed bundle flow tests. The B-1 and B-2 flow tests were reanalyzed using these new parameters.

Due to experimental difficulties encountered in the B-1 and B-3 tests in maintaining the same heating rates for the shroud and the bundle, a decision was made to provide a separate power supply for heating the shroud. It will be controlled, via a temperature feedback control system, to maintain the shroud average temperature the same as the bundle average temperature. The power supply ordered for the single-rod test facility (it was sized with this application in mind) was delivered and is being mounted so that it can be used in both test facilities. The necessary programmers and controllers were designed and are being assembled for use with the portable power supply. A test model, consisting of the bundle shroud and four simulators, is being assembled to demonstrate the workability of this concept and to determine test parameters for use in the forthcoming B-4 test.

It was decided that the B-4 test should be conducted with fuel pin simulators containing the same fuel simulators (internal heaters) that were used previously in the B-3 and B-1 tests. The fuel simulators will be located in the same relative positions they occupied in the earlier tests. This eliminates one variable (heater characteristic) in comparing the test results. As a consequence of this decision, the fuel simulators were reconditioned, including new infrared characterization scans, and fabrication of the B-4 fuel pin simulators was initiated.

MULTIROD BURST TEST PROGRAM PROGRESS REPORT FOR JULY–DECEMBER 1978

R. H. Chapman

ABSTRACT

The technology for fabricating fuel simulators, based on the use of boron nitride (BN) preforms, was demonstrated by the production of 92 acceptable simulators for future test needs. Two single-rod tests were conducted, using prototype fuel simulators produced in this development effort, to demonstrate satisfactory performance. The results of the tests are reported.

Results are reported of further analyses performed to characterize the B-1 temperature distribution and to assess the importance of the effect of shroud temperature on bundle deformation. The results indicate a relatively minor effect on localized deformation.

Posttest examination and analysis of the B-2 test data were completed, and the results are reported and compared with B-1 results. The results are in very good agreement.

The B-3 test was performed, and quick-look results and some data analyses are reported. Deformation was greater and more extensive than that observed in the B-1 and B-2 tests, presumably due to more uniform temperature and the lower heating rate (strain rate) employed in the test. The bundle is being sectioned to obtain strain data.

Test equipment and components are being fabricated in preparation for the B-4 test.

1. INTRODUCTION

R. H. Chapman

The objectives of the Multirod Burst Test (MRBT) Program are (1) to delineate the deformation behavior of unirradiated Zircaloy cladding under conditions postulated for a loss-of-coolant accident (LOCA) and (2) to provide a data base which can be used to assess the magnitude and distribution of geometrical changes in the fuel rod cladding in a multirod array and the extent of flow channel restriction that might result. Data are being obtained from single-rod and multirod experiments that include possible effects of rod-to-rod interactions on ballooning and rupture

behavior; a tentative test matrix was given in a previous report.[1] Although the test matrix includes tests of large bundle arrays, these will be held in abeyance until a definite need, based on the results of the smaller test arrays, is established. Also, tests with boiling-water reactor (BWR) cladding are envisioned, but they will be deferred until completion of the pressurized-water reactor (PWR) cladding tests.

Approximately 53 single-rod burst tests have been conducted with a heating rate of ∿28°C/sec; experimental details and preliminary results of the tests have been reported routinely. (All published reports pertaining to this research program are listed in the Foreword of this report.) The data base covers a range of burst pressure from 770 to 19,150 kPa; the corresponding burst temperatures range from 1170 to 690°C. All the tests conducted prior to April 1977 were evaluated for validity, and the results were summarized in a previous report.[2] Readers making use of results obtained in this program should be aware of the fact that some of the earlier data points have been removed as a result of this evaluation.

Four steady-state, single-rod creep rupture tests were conducted at about 760°C to determine if large ballooning occurs over extended lengths of test specimens heated with internal fuel simulators. Test conditions were varied to cause failure in creep times of 49, 103, 162, and 250 sec. Two transient (∿28°C/sec) burst tests were conducted with the same internal fuel simulators for comparison. The initial conditions for these tests were adjusted to cause failure at approximately the same temperature as in the creep rupture tests; the results of these tests were reported.[3]

Subsequently, two transient burst tests, using each of the two fuel simulators, were conducted at nominal heating rates of 5 and 10°C/sec to bridge the span between the creep tests (∿0°C/sec) and the 28°C/sec transient burst tests. Initial pressure conditions for these tests were adjusted to cause failure at ∿760°C for comparison. The results of these low-heating-rate tests were reported.[4]

The creep rupture and the low-heating-rate tests were evaluated subsequently, and the results were reported in considerable detail in a recent topical report.[5]

Two transient (28°C/sec) burst tests were conducted to investigate the effect of steam flow rate on burst location. The steam flow rate in one test [Reynolds (Re) number ∿800] was typical of that normally employed in our single-rod tests; in the other, the flow (Re ∿180) was comparable to that employed in the B-1 and B-2 bundle tests. The results of these tests have been reported.[4]

Two 4 × 4 multirod tests, one (B-1) with and the other (B-2) without shroud heating, have been conducted with a bundle heating rate of ∿30°C/sec. Initial pressure conditions for these tests were selected to cause failure at ∿860°C. Another 4 × 4 array (B-3) was tested with a heated shroud during this reporting period, using a bundle heating rate of ∿10°C/sec; initial pressure conditions were selected to cause failure at ∿760°C to provide a basis for comparison with the low-heating-rate single-rod tests. A summary of results of the three bundle tests is given in Table 1.1 for quick comparison.

Posttest examination of B-1 and B-2 (including flow testing of the deformed bundles) is essentially complete and is under way on B-3.

Table 1.1. Comparison of B-1, B-2, and B-3 tests

	B-1	B-2	B-3
Bundle heating rate,[a] °C/sec	30.1	29.9	9.5
Shroud heating rate,[a] °C/sec	20.0	7.7[b]	7.1
Inlet steam temperature, °C	349	332	320
Inlet steam Reynolds number	250	290	263
Initial temperature, °C	356	334	329
Initial pressure, kPa	8680	8770	11,610
Maximum pressure, kPa	9100	9200	12,110
Burst pressure, kPa	7425	7560	9,425
Burst temperature, °C	865	857	764
Burst time, sec	17.0–17.6	17.8–18.3	44.5–47.6
Burst strain, %	32–59	34–58	N.A.[c]
Tube volume increase, %	27–55	28–52	N.A.[c]
$T_{Bundle} - T_{Shroud}$ at burst time, °C	137	355	80

[a]Average over the more or less linear portion of the temperature-time transient.

[b]Produced by heat lost from the bundle, since the shroud was not electrically heated in this test.

[c]Data not yet available.

Detailed results of the B-1 test and quick-look results of the B-2 test have been reported.[3,4] Additional data on B-1, detailed deformation data on B-2, and quick-look results on B-3 are included in this report.

2. PROGRAM PLANS AND ANALYSIS

2.1 Programmatic Activities

R. H. Chapman

Quick-look results of the B-3 test and additional B-1 and B-2 results were presented at the Nuclear Regulatory Commission (NRC) Quarterly Cladding Review Meeting and Experimenter's Workshop at Battelle Columbus Laboratories, Columbus, Ohio, on August 22-23.

An overview of the MRBT Program and pertinent results having implications for reactor safety evaluation were presented at the Atomic Safety and Licensing Board Panel Meeting in Oak Ridge on September 12.

A comprehensive presentation of currently available results of the B-1, B-2, and B-3 tests was made in the Multirod Bundle Test Workshop at the Sixth Water-Reactor Safety Research Information Meeting in Gaithersburg, Md., on November 6. Following the meeting, additional discussions of the Japanese and German cladding research programs were held in Oak Ridge with visitors from the respective research sites.

Major effort was devoted during this report period to B-3 pretest and posttest operations and examination and to further testing and evaluation of seal gland configurations for the lower end seal on bundle B-4 fuel pin simulators. Proof testing of the configuration selected for the B-4 simulators was concluded successfully, and fabrication of the simulators for the test assembly was initiated.

Two single-rod tests, SR-45 and SR-46, were performed during this reporting period. These tests were conducted primarily to demonstrate the acceptability of in-house fabricated fuel simulators for use in fuel pin simulators. Following this demonstration, 92 acceptable fuel simulators were produced for use in future tests. The quality of the units produced in-house (using BN preforms in place of compacted BN powder) is as good as or better than the best simulators obtained from commerical sources.

2.2 Single-Rod Tests

R. H. Chapman

The technology for fabricating fuel simulators, based on the use of cold-pressed BN preforms for electrically isolating the heating element from the outer sheath, is being developed in our laboratories. A number of prototype preproduction units have been successfully produced to define design parameters and to establish fabricating procedures. Two of the preproduction units were selected for single-rod tests to demonstrate the acceptability of the design for use in this test program. Since the tests also produced valid data points in our single-rod data base, the results of the tests are reported below.

SR-45 test results

Fuel pin simulator SR-45 was assembled according to established procedures, using prototype fuel simulator MR-5, to duplicate previous test assemblies. Since the test temperature was not in the eutectic-forming range, the fuel simulator was not coated with a protective layer of ZrO_2. Twelve bare-wire (0.25 mm OD), type K thermocouples were spot-welded to the outside diameter of the Zircaloy cladding to provide temperature measurements. Four thermocouples, equally spaced around the tube, were located at each of three axial locations selected on the basis of the pretest infrared characterization scan of the fuel simulator.

Test conditions for SR-45 were typical of those employed previously, (i.e., 28°C/sec heating rate and steam conditions such that the Reynolds number at the inlet was in the range of 600 to 800); Table 2.1 gives pertinent test conditions and results. The table also compares the SR-45 test results with those of SR-3, which was tested under similar conditions.

Quick-look data plots for the instrumented cross sections at the 40.0- and 53.3-cm elevations are given in Figs. 2.1 and 2.2, respectively. As noted in Fig. 2.3, the burst occurred at the 53.3-cm elevation. Circumferential gradients of 15–20°C existed at both elevations during the first 19.5 sec of the transient. The gradients decreased significantly (see Fig. 2.1) during the time of the transformation from α-Zircaloy to β-Zircaloy and then increased again. The burst temperature measurement

Table 2.1. Comparison of test conditions and preliminary results of SR-45 and SR-3

	SR-45	SR-3
Fuel simulator number	MR-5	2828027
Gas volume,[a] cm^3	51.0	46.1
Initial temperature, °C	334	346
Initial pressure, kPa	1840	1770
Maximum pressure, kPa	2010	1900
Burst pressure, kPa	1885	1720
Burst temperature, °C	1005	1011
Burst elongation, %	20	43
Time to burst, sec	25.9	22.4

[a]Measured at room temperature.

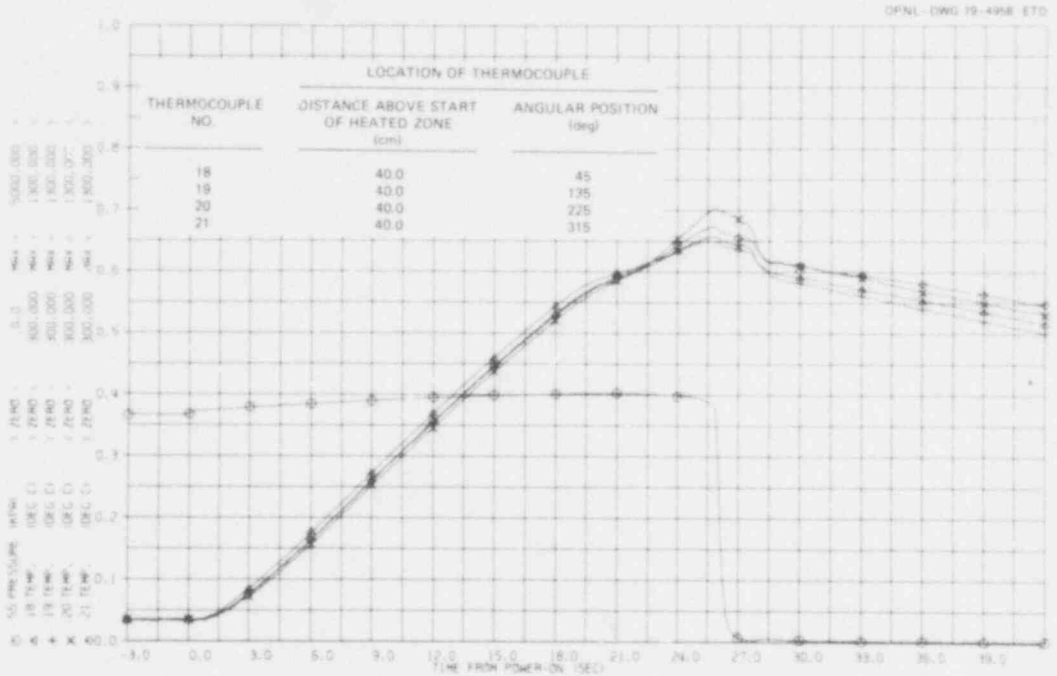

Fig. 2.1. Quick-look data plot of SR-45 showing temperatures measured at 40.0-cm elevation.

was obtained from TE-20, whose trace is plotted in Fig. 2.1. Actually, TE-24 was located almost on top of the burst, as shown in Fig. 2.4; but, as is evident in Fig. 2.2, it malfunctioned early in the transient and provided no useful information. It is interesting to note that TE-22, which was located diametrically opposite the burst, indicated the lowest temperature as would be expected at this cross section at the time of burst (see Fig. 2.2).

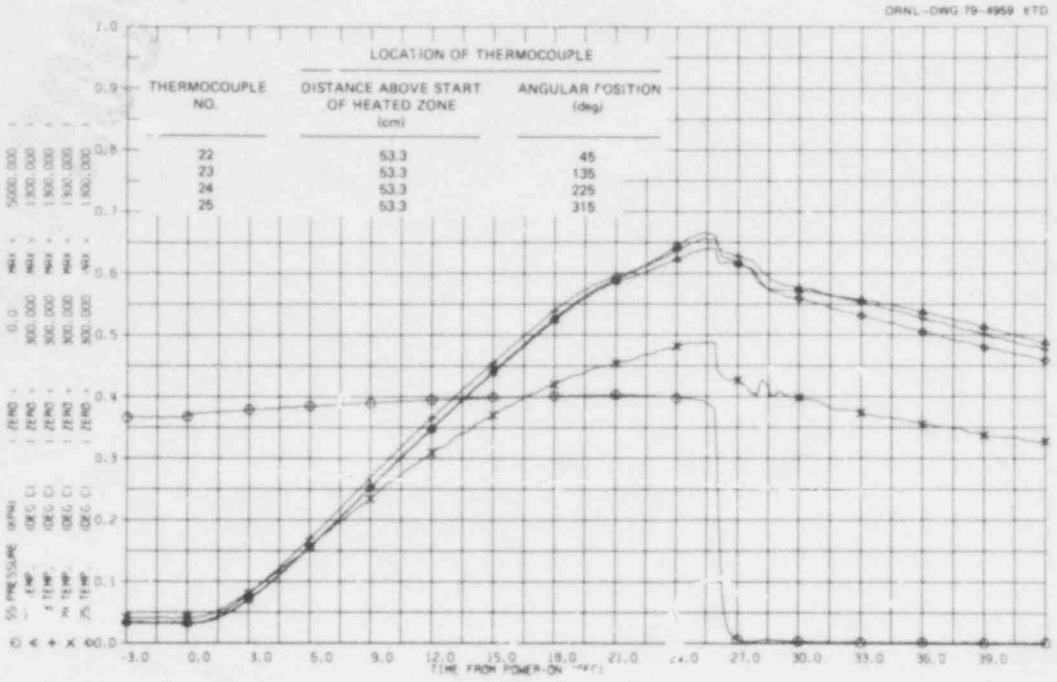

Fig. 2.2. Quick-look data plot of SR-45 showing temperatures measured at 53.3-cm elevation.

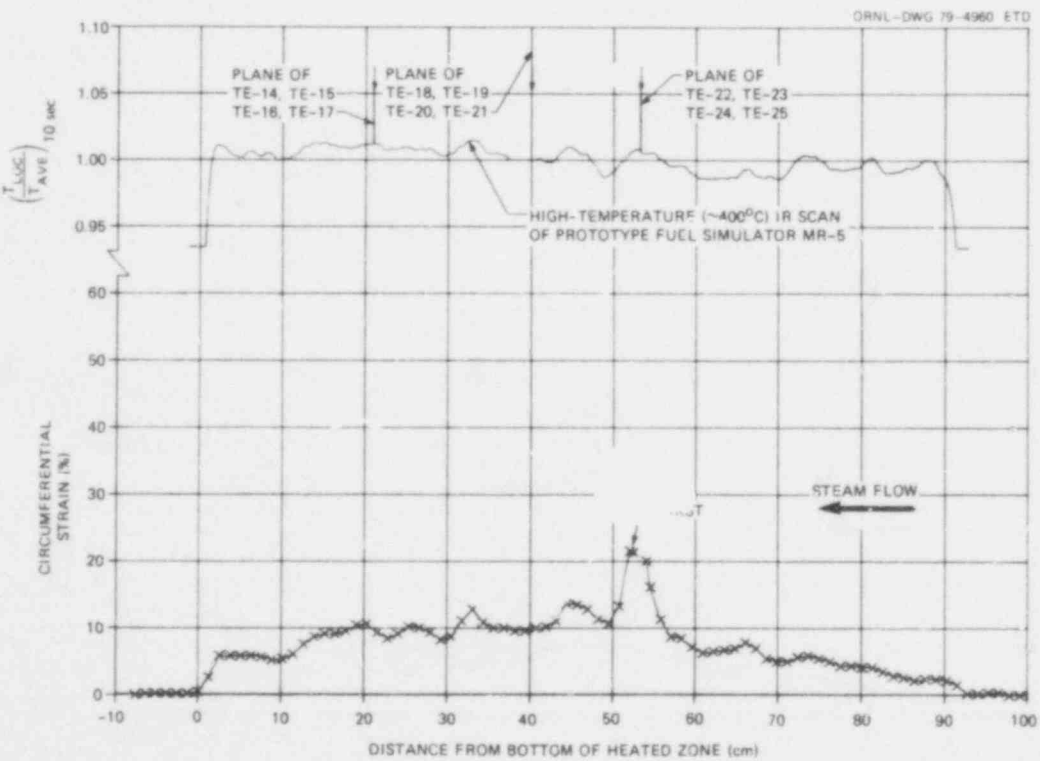

Fig. 2.3. Deformation profile of SR-45.

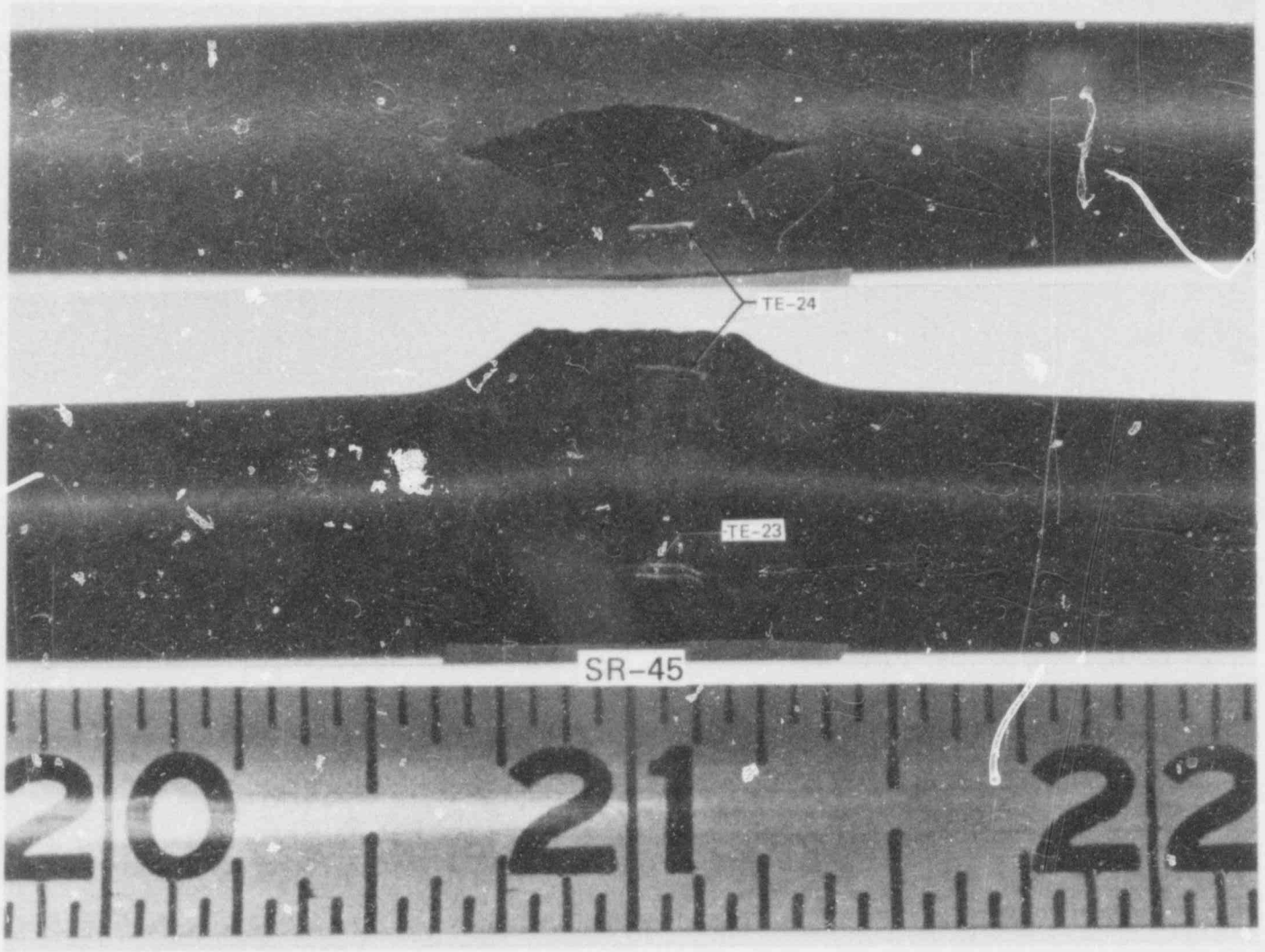

Fig. 2.4. Burst in SR-45.

The axial distribution of the circumferential elongation is plotted in Fig. 2.3; the pretest infrared characterization scan and the location of the thermocouples are also given in the figure for reference. The axial temperature profile of the fuel simulator (as judged from the scan) was very uniform compared to previously used simulators. The deformation profile is in good agreement with the characterization scan. The deformation was relatively small and very uniform over most of the heated length; the burst elongation was about half that observed in SR-3, the only other test conducted at approximately the same conditions (see Table 2.1). Since the deformation occurred while the Zircaloy was in the two-phase region (see Figs. 2.1 and 2.2), the difference in the deformation observed in the two tests is probably due to scatter rather than to differences in the two heaters.

Figure 2.4 shows the burst in the tube; the remains of thermocouples are evident in the photographs. The location of TE-24 was such that it should have given a very good measurement of the burst temperature, but, as seen in Fig. 2.2, it malfunctioned early in the test and did not provide useful data.

SR-46 test results

Fuel pin simulator SR-46 was assembled for testing at a higher temperature, using prototype fuel simulator L-001. The simulator was ungrooved, but a protective coating of ZrO_2 was applied to preclude formation of zirconium-based eutectics. This particular fuel simulator had been previously tested several times at high temperature in an argon atmosphere as a bare simulator (i.e., without the Zircaloy tubing being present) to evaluate the resistance characteristics.

Single-cell grids were included on the fuel pin simulator at the same relative positions as used in the bundle tests. These were included to give some indication of the high-temperature behavior of the tubing in the vicinity of the grids. Twelve bare-wire (0.25 mm OD), type S thermocouples were spot-welded to the outside diameter of the Zircaloy tube to provide temperature measurements at points of interest. Four thermocouples, equally spaced around the tube, were located at each of

three axial locations selected on the basis of the pretest infrared characterization scan of the fuel simulator.

Test conditions for SR-46 were typical of those employed previously; the heating rate was about 30°C/sec. The steam flow was somewhat higher (Re ∿1000 at the inlet) than normally used (Re 600 to 800), and this probably suppressed deformation in the upper portion of the heated zone, as will be discussed later. Table 2.2 gives pertinent test conditions and results; the table also compares SR-46 with SR-8, SR-13, SR-17, SR-20, and SR-21, all of which were tested under comparable conditions.

Quick-look data plots of the instrumented cross sections at the 23.5- and 85.1-cm elevations are given in Figs. 2.5 and 2.6, respectively. The axial distribution of the circumferential elongation is given in Fig. 2.7. The pretest infrared characterization scan of the fuel simulator and the axial locations of the instrumented cross sections and of the grids are also given in this figure for reference. The quality of the fuel simulator, as judged by the uniformity of the pretest infrared characterization scan, was very good, except close to the ends.

The slightly higher steam flow (Re ∿1000) suppressed the temperature and hence the deformation over the upper 30–35 cm of the heated zone. This is also evidenced by a comparison of the temperature plots in Figs. 2.5 and 2.6. The maximum measured temperature at the 85.1-cm elevation was 1038°C, while the maximum measured at the 23.5-cm elevation was 1076°C; the maximum at the 38.1-cm elevation was 1065°C. With a steam flow comparable to that employed in the bundle test (i.e., Re ∿250), the maximum temperature (and burst) would have been expected very near the upper end of the heated zone.

Temperature gradients at the upper instrumented cross section were very small throughout the transient; this observation is consistent with the small deformation in this region. On the other hand, significant gradients developed at the lower instrumented cross section during the deformation phase of the transient, reaching a maximum of about 67°C. It may also be noted in Fig. 2.5 that the temperatures attained maximum values about 1.3 sec before the burst. Although the burst occurred about 5 cm below the instrumented cross section (Fig. 2.7), we have assigned

Table 2.2. Comparison of test conditions and preliminary results of SR-46 with earlier tests conducted in a steam environment

	SR-46	SR-8	SR-13	SR-17	SR-20	SR-21
Fuel simulator number	L-001	2828010	2828016	2828010	2828031	2828005
Gas volume,[a] cm^3	50.9	49.3	47.3	44.9	33.4	36.7
Initial temperature, °C	334	336	325	344	332	340
Initial pressure, kPa	1240	1420	1310	1310	1290	1310
Maximum pressure, kPa	1360	1520	1430	1410	1410	1430
Burst pressure, kPa	1125	1230	1070	1060	1060	1120
Burst temperature, °C	1076	1020	1079	1049	1049	1023
Burst elongation, %	37	43	79	53	55	48
Time to burst, sec	27.10	25.15	24.65	25.25	25.10	24.50

[a]Measured at room temperature.

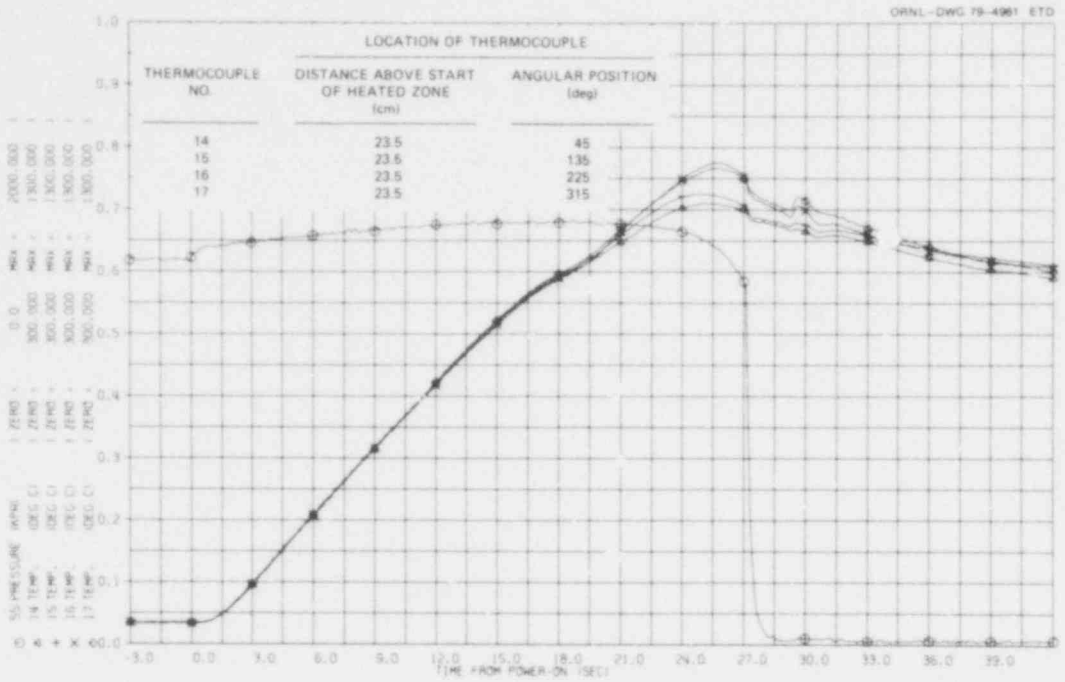

Fig. 2.5. Quick-look data plot of SR-46 showing temperatures measured at 23.5-cm elevation.

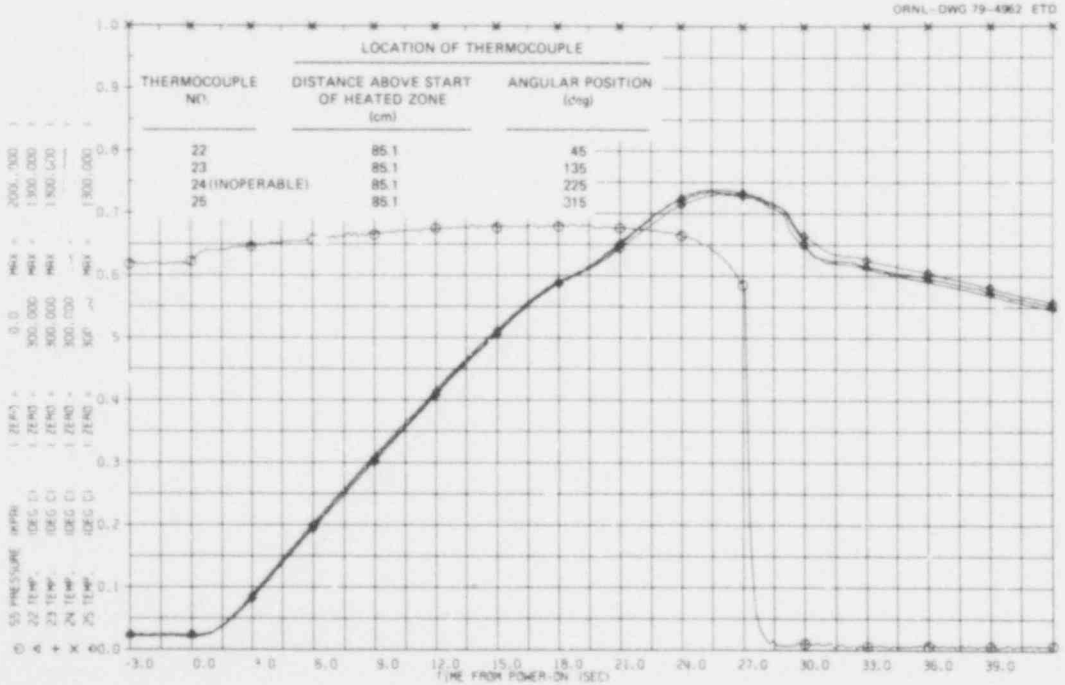

Fig. 2.6. Quick-look data plot of SR-46 showing temperatures measured at 85.1-cm elevation.

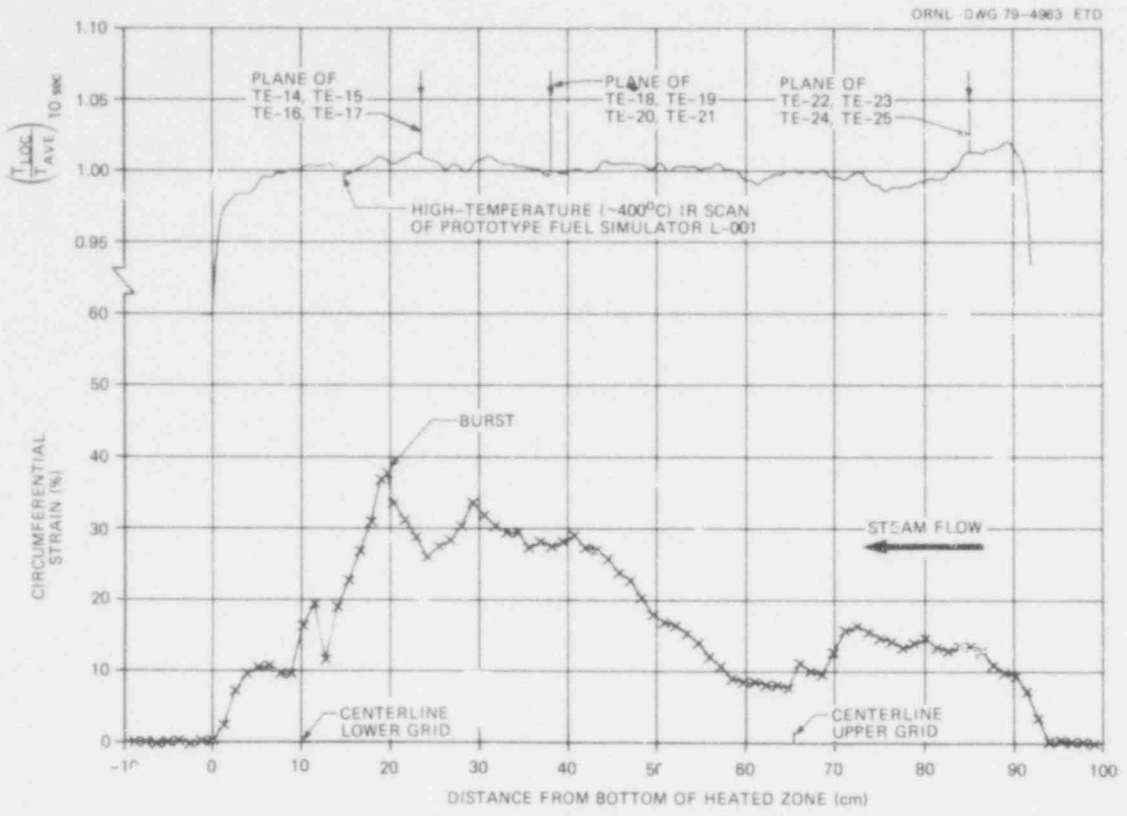

Fig. 2.7. Deformation profile of SR-46.

the value 1076°C as the burst temperature; this is consistent with our definition of burst temperature.

Deformation in SR-46, as noted in Table 2.2, was significantly less than that observed in the other tests conducted at comparable conditions. The reasons for the scatter in this temperature range have not been identified. The same observation was noted earlier in discussing the results of SR-45. Both SR-45 and SR-46 employed fuel simulators fabricated with BN preforms instead of compacted powder as the insulation material between the heating ribbon and the heater sheath, but we see no reason why this should influence the deformation as long as the temperature distribution is the same.

Figure 2.8 shows the tube in the vicinity of the burst; considerable cracking is evident in the oxide layer formed during the test.

This was the highest temperature test we have conducted with grids, and, as shown in Fig. 2.9, deformation was restrained by the grid. The

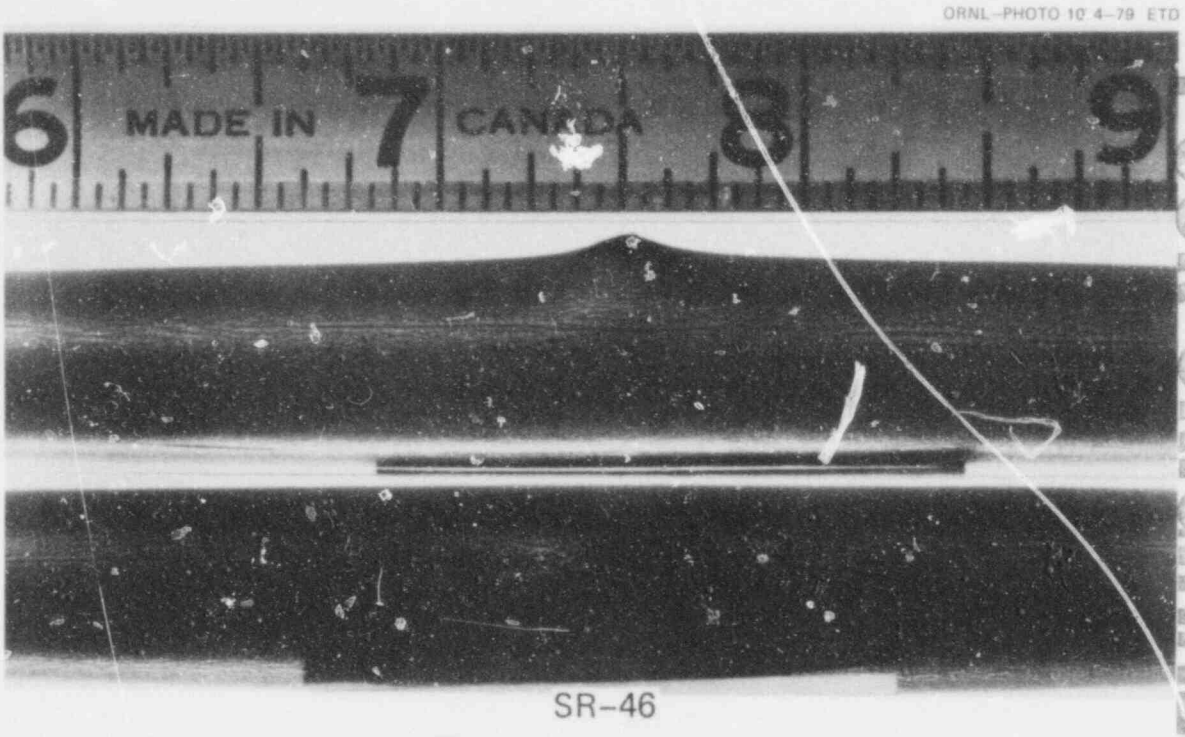

Fig. 2.8. Burst in SR-46.

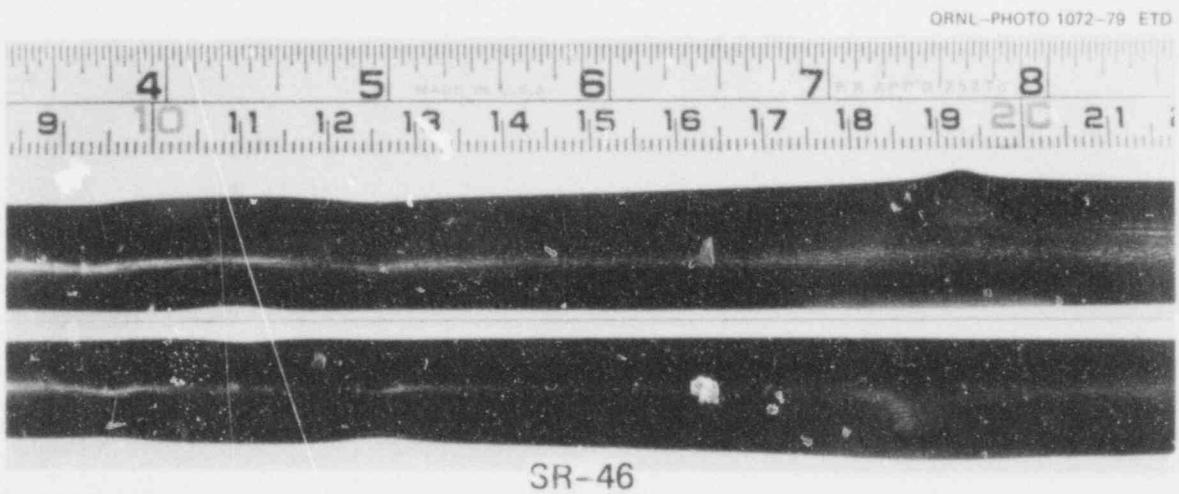

Fig. 2.9. Posttest view of SR-46 showing local deformation in vicinity of lower grid.

grid dimples, which center the tube within the grid, deformed the tube locally. The perturbations in the deformation profile (Fig. 2.7) in the vicinity of the grids are a consequence of the axial positions at which the measurements were taken.

2.3 Additional Bundle B-1 Results

R. H. Chapman D. O. Hobson*

The major results of posttest examination of B-1 were reported[3,4] earlier; a few additional results have become available and are included in this section.

Table 2.3 summarizes pertinent data for the individual tubes in the B-1 array. Some comments on the tabulated pressure decrease and volume increase values (see table footnotes for definitions) may be in order. It will be recalled that the gas volume distribution is not typical of a fuel rod and that the tests are conducted with a closed-volume system (i.e., with constant gas mass inventory). Of the total initial volume (at room temperature), about 13% is in the heated portion of the annulus between the fuel simulator and the inside diameter of the Zircaloy tube, 10% is in the unheated portion of the annulus, 33% is in the pressure transducer and connecting tube, and 44% is distributed in the end regions (mostly at the upper end) of the fuel pin simulator. At any given time during the test, all these volumes have different temperatures, ranging from room temperature to cladding temperature (the major volumes remain at or near room temperature) and one cannot calculate the fractional volume increase from the pressure decrease in a straightforward manner. Instead, we have calculated the volume increase from the deformation profiles (assuming circular cross sections) as reported earlier.[4]

Thermocouple locations in the B-1 test, shown in Fig. 2.10, were specified to provide general knowledge of the temperature uniformity in the bundle, primarily between the two grids positioned within the heated length. The data have been analyzed at selected times to characterize the test and to assess the importance of the effect of the heated shroud on the bundle temperature distribution and, hence, on the deformation.

---

*Metals and Ceramics Division.

Table 2.3. Characterization of B-1 tube failures

Rod No.	Initial gas volume[a] (cm^3)	Approximate burst condition			Fractional[b] pressure decrease	Fractional[c] volume increase	Volume increase[d] of tube over heated length (%)	Average strain[e] (%)
		Pressure (kPa)	Temperature (°C)	Strain (%)				
1	49.2	7750	852	36	1.12	1.50	28.9	14
2	51.5	7415	867	32	1.17	1.66	39.4	18
3[f]	49.7	3785[f]	937[f]	23[f]	1.72[f]	1.29[f]	16.6[f]	8[f]
4	49.8	7945	860	36	1.09	1.46	26.7	13
5	50.4	6930	872	43	1.26	1.93	55.0	24
6	50.3	7615	872	43	1.14	1.53	31.3	15
7	49.6	7255	869	36	1.30	1.75	43.6	20
8	50.0	7405	872	42	1.17	1.65	38.2	18
9	49.0	7100	870	44	1.23	1.86	49.3	22
10	50.7	7300	873	45	1.19	1.73	43.2	20
11	49.2	7270	847	49	1.19	1.77	44.5	20
12	50.5	7685	863	37	1.12	1.56	32.9	15
13	50.2	7525	878	59	1.16	1.70	40.8	19
14	50.1	7355	875	42	1.18	1.73	42.5	19
15	49.5	7325	865	42	1.19	1.75	43.5	20
16	50.2	7530	848	39	1.15	1.62	36.6	17

[a] Measured at room temperature; includes fuel pin simulator (FPS), pressure transducer, and connecting tube.

[b] Ratio of initial pressure to burst pressure.

[c] Ratio of final to initial gas volume; includes FPS, pressure transducer, and connecting tube.

[d] Obtained from deformation profiles assuming circular cross sections.

[e] Assumes volume increase is uniformly distributed over heated length.

[f] Tube developed severe leak prior to transient; deformation behavior is abnormal.

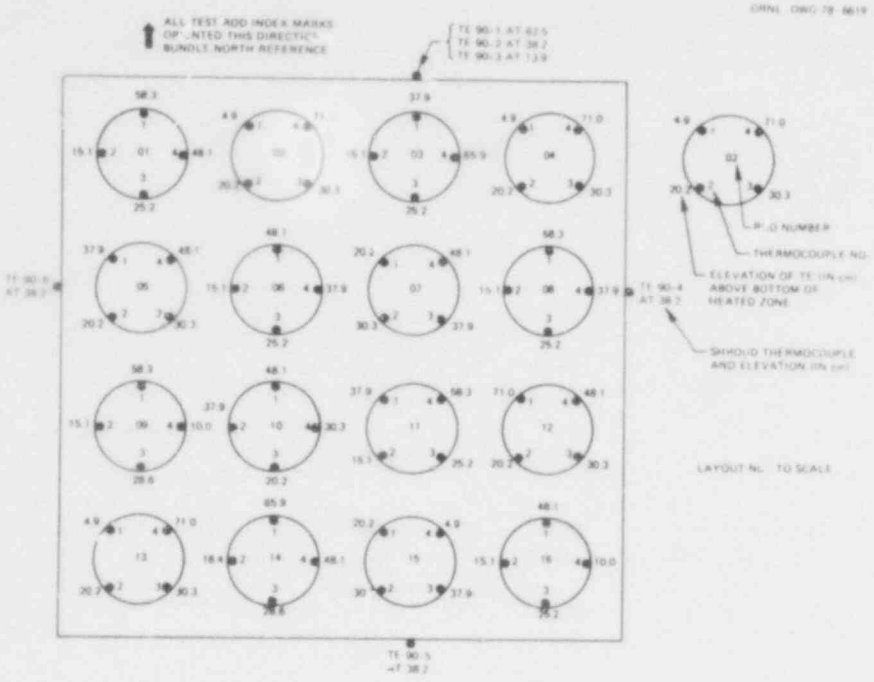

Fig. 2.10. As-built thermocouple locations in B-1 test.

The temperature measurements were analyzed to obtain average bundle (cladding) and shroud temperatures for the time period from power-on to the first tube burst. These data, presented graphically in Fig. 2.11, are useful in characterizing the test. The average temperature difference between the bundle and shroud is also plotted in the figure. This difference is indicative of the potential for shroud heating by bundle heat losses. However, the amount of shroud heating contributed by bundle heat losses cannot be calculated in a straightforward manner, since some of the bundle losses appear in the steam coolant flowing through the assembly and a portion of the shroud heating resulted from electrical heating. An additional complicating factor is the absence of information on shroud heat losses to the steam coolant and to the structure surrounding the shroud.

Bundle and shroud heating rates, shown in Fig. 2.12, were calculated from the averaged temperatures for the same time period. The curves in the figure have been "smoothed" through the data points obtained from a stepwise calculation that assumed constant heating for each 1-sec time increment. It is important to note that it is impossible to characterize constant electrical power-transient temperature tests, such as these (and

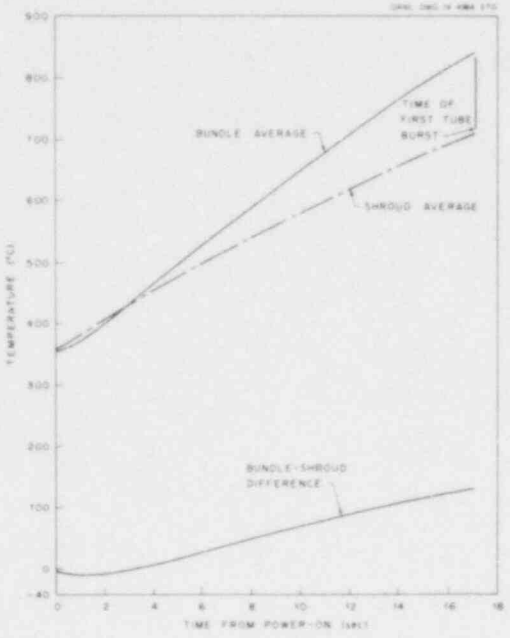

Fig. 2.11. Average temperatures in B-1 test.

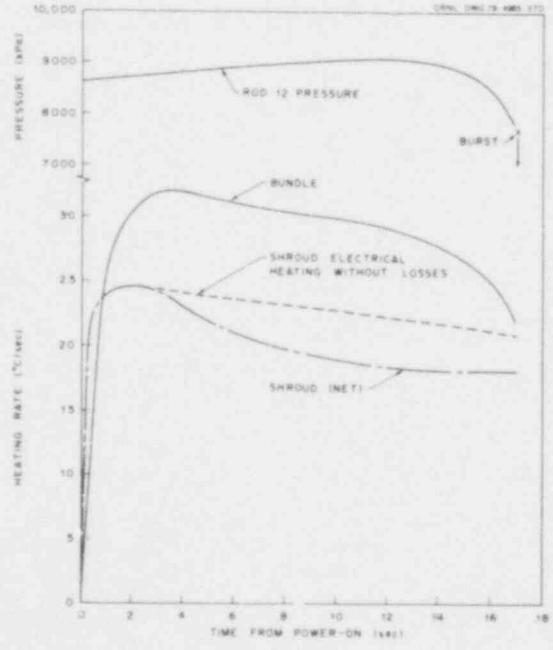

Fig. 2.12. Bundle and shroud heating rates in B-1 test.

those performed by many other investigators), with a unique value of the cladding heating rate, since heat losses, physical property changes with temperature (time), and deformation modify the instantaneous heating rate that would otherwise be obtained by the applied electrical power. It has been our practice to determine an average heating rate over the more or less linear portion of the temperature-time trace and to use this value to characterize the test.

The bundle heating rate reached a maximum of ∿32°C/sec in ∿3 sec and then decreased slowly over the next 10 sec or so [i.e., until deformation commenced as indicated by the pressure trace plotted in the figure for simulator 12 (the first to burst)], after which the heating rate decreased more rapidly due to increasing heat losses and cladding deformation. The latter effect increases the gas gap and effectively decouples the cladding heating rate from that of the internal fuel simulator. The average heating rate over the time interval of 3 to 15 sec was 30.1°C/sec; this is considered characteristic of the test.

The observed shroud heating rate maximized earlier (due to its electrical characteristics and smaller mass), decreased rather rapidly over a short time period, and then leveled off at a more or less constant value. The average rate over the 3- to 15-sec time period was 20.0°C/sec. The dashed line shows the expected shroud heating rate based on its physical properties and observed electrical power as a function of temperature (time). This theoretical curve was normalized to the observed value at 2 sec into the transient, at which time there was essentially no difference in shroud and bundle temperatures. The difference between expected and observed shroud heating rates at greater times is due to the shroud losses increasing with temperature (time). Heat added to the shroud from the bundle stabilized the shroud heating rate during the last 5 sec or so of the transient.

The measurements at a given elevation were averaged to obtain axial bundle-averaged temperature profiles at selected times, as shown in Fig. 2.13. The number of measurements averaged to obtain the plotted data point for each elevation is indicated in the figure. Also, the axial distribution of the tube bursts is indicated at the extreme right of the figure. (Burst temperatures and times are not represented in the plot.)

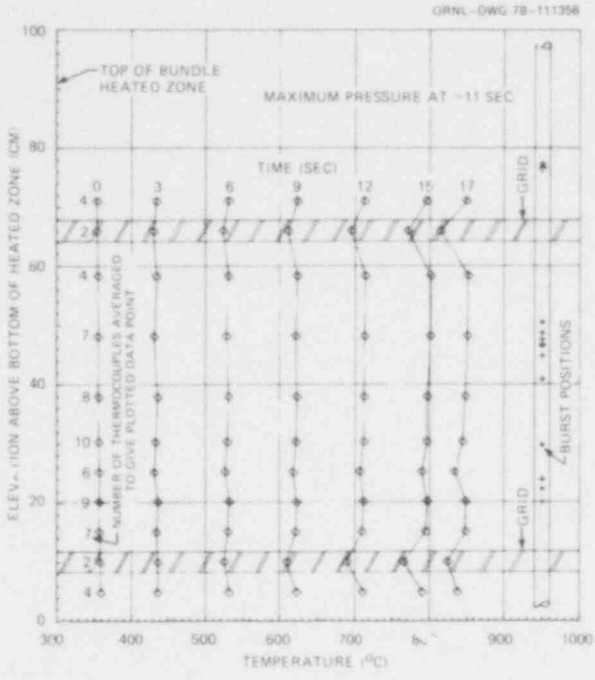

Fig. 2.13. Axial temperature distribution in B-1 test as a function of time.

The averaged data show that the bundle axial temperature profile was very uniform prior to the onset of deformation (i.e., until maximum pressure was attained). As might be expected, the temperature profile was perturbed during the deformation process; however, the overall average remained fairly uniform until the time of the first burst (i.e., until 17 sec).

Since the axial temperature distribution was reasonably uniform (based on averaged temperature measurements at the instrumented elevations), the data were reanalyzed to obtain radial temperature profiles. For this purpose, the thermocouples were considered to be located axially at a common elevation (i.e., the axial distribution was assumed to be perfectly uniform) and radially at one of five representative positions, as indicated in Fig. 2.14. The representative positions are the radii of the inside and outside tangent surfaces of the inner and outer ring of simulators, respectively, and the radius of the shroud. (Due to symmetry, the dimensionless radii, r_i/R, are the same on the diagonals and the axes of the array if the reference radius, R, is appropriately defined.) The measurements of the thermocouples at each of the representative radial locations were averaged to obtain a temperature characteristic

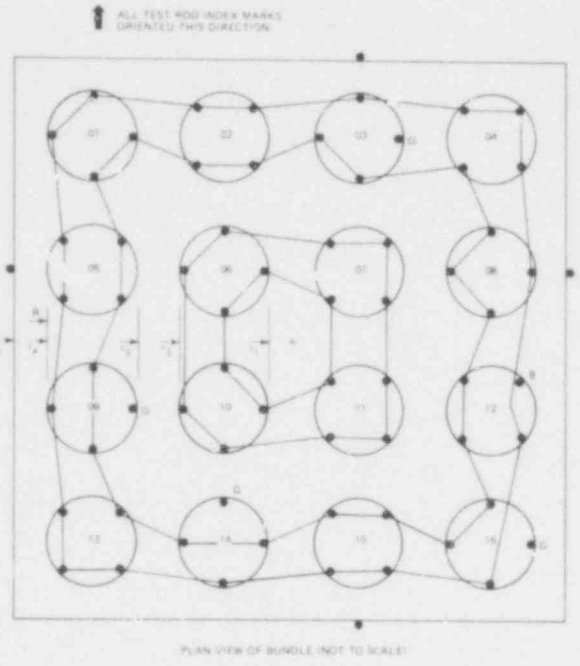

Fig. 2.14. Thermocouple assignments for calculation of radial temperature profile in B-1 test.

of that position. The profiles obtained in this manner are plotted in Fig. 2.15 and show that the bundle radial temperature distribution was very flat throughout the transient. There appears to be a small gradient across the inner ring of simulators, but not across the outer ring, even though a significant gradient existed across the coolant annulus between the bundle and the shroud.

Although the temperature transient and distributions presented in Figs. 2.11, 2.13, and 2.15 characterize the bundle as a whole, the individual simulators deviated significantly from these smoothed profiles. This would be expected, since the simulator temperature distributions are strongly influenced by the heat generation within the individual fuel simulators. The axial locations of the bursts (see Fig. 2.16) showed[3] better correlation with the pretest characterization scans than with the bundle axial temperature profile. The tube bursts are shown in the composite layout, Fig. 2.17, in which the tube-to-tube pitch is greatly exaggerated for clarity. The orientations reported earlier[3] have been reevaluated, taking into account wall thinning in adjacent sections, in

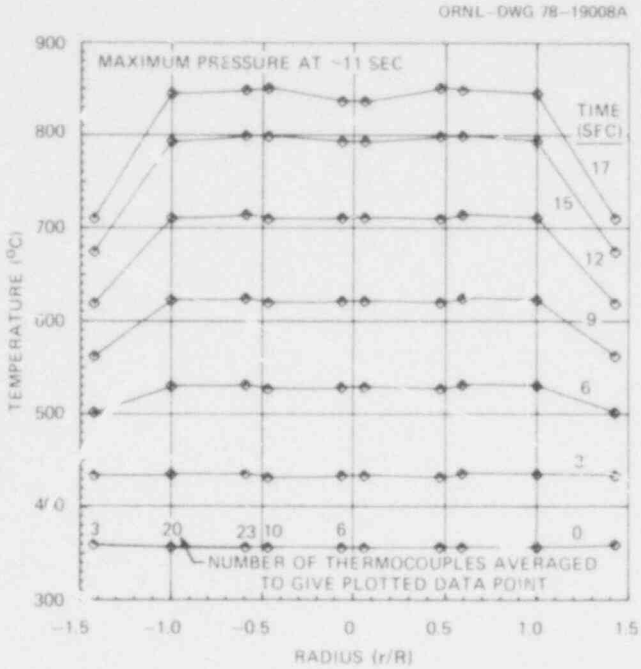

Fig. 2.15. Radial temperature distribution in B-1 test as a function of time.

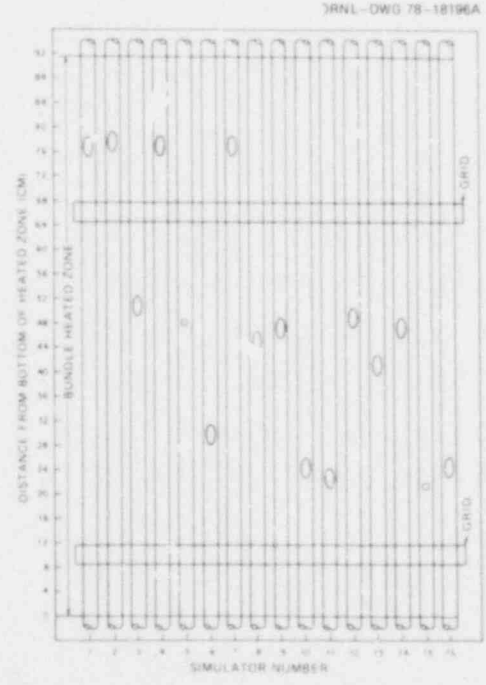

Fig. 2.16. Axial distribution of bursts in B-1 test.

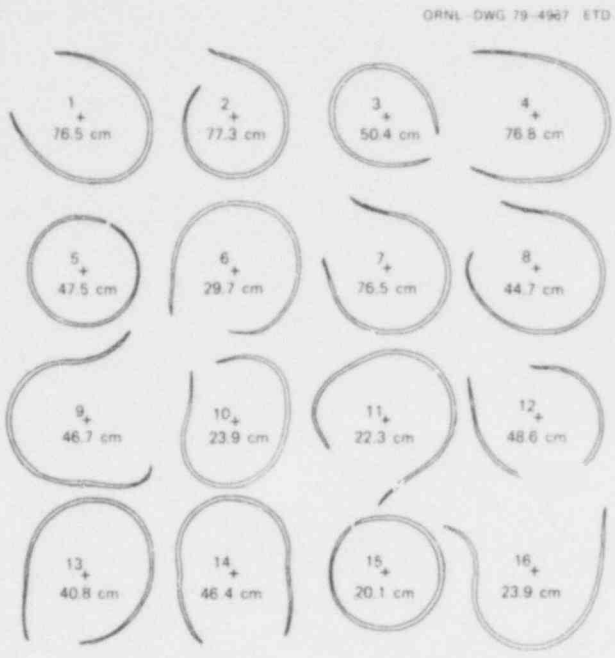

Fig. 2.17. Composite layout of tube bursts in B-1 test. Tube-to-tube pitch greatly exaggerated for clarity. Axial locations of bursts are noted.

an attempt to define the angle of the burst more precisely. The revised orientations, Table 2.4 and Fig. 2.18, differ only slightly from the earlier data.

Figures 2.17 and 2.18 show that the bursts in the inner ring of simulators tend to be directed generally toward the outer ring, while in the outer ring six bursts are generally directed inward, four are directed outward, and two are directed toward adjacent tubes in the outer ring. It should be noted that two of the outer tubes whose bursts were directed inward (i.e., tubes 5 and 15) experienced pinhole failures at or very near to thermocouple spot-welds; thus, the direction of their bursts was probably influenced by other mechanisms.

The smoothed radial temperature profiles, Fig. 2.15, and the burst orientation observations discussed above suggested that a more detailed examination of the circumferential variation in tube wall thinning in each of the bundle transverse sections might, indeed, show preferred directional characteristics. This was investigated by visually examining photographic enlargements (5X) of the cross sections of the B-1 test

Table 2.4. Summary of B-1 burst data

Rod No.	Burst characteristics		Approximate position	
	Temperature (°C)	Strain (%)	Elevation[a] (cm)	Angle[b] (deg)
1	852	36	76.5	310
2	867	32	77.3	330
3[c]	937[c]	23[c]	50.4	120
4	860	36	76.8	295
5	872	43	47.5	30
6	872	43	29.7	205
7	869	36	76.5	315
8	872	42	44.7	310
9	870	44	46.7	75
10	873	45	23.9	330
11	847	49	22.3	210
12	863	37	48.6	335
13	878	59	40.8	205
14	875	42	46.4	170
15	865	42	20.1	325
16	848	39	23.9	335

[a]Elevation above bottom of heated zone.

[b]Looking down on bundle and measured clockwise from bundle north.

[c]Tube developed severe leak prior to transient; deformation behavior is abnormal.

array to determine the angular position of the greatest wall thinning in each of the tubes in each of the sections. This examination was quite subjective, but it was sufficient to show a correlation between the angular positions of wall thinning (or tube bursts) and the temperature distribution.

In order to make the examination, the circumference of each tube was divided into eight sectors according to the angular view (36° and

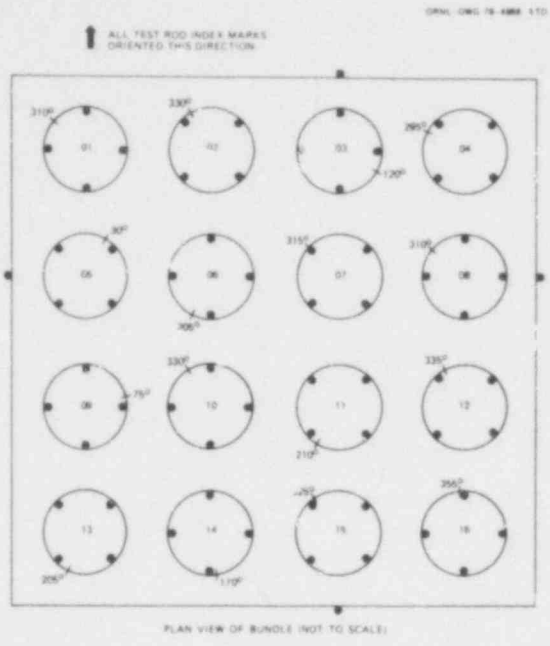

Fig. 2.18. Angular orientation of bursts in B-1 test.

54°) of neighboring tubes and to the symmetry of the tube position within the bundle. With this procedure, the plane of reference can be rotated and/or inverted such that only three reference positions need be considered. These are identified as type I for the corner rods (Fig. 2.19), type II for the side rods (Fig. 2.20), and type III for the interior rods (Fig. 2.21); note that the mirror-image symmetry of the type II rods results in two subtypes, identified by subscripts *a* and *b*.

With this nomenclature, the positions of maximum thinning or bursts were assigned to the proper sector for each tube in each of the transverse sections. These were then summed according to type and sector for the bundle as a whole. These data permitted calculation of the percentage of the total observations of wall thinning found in each of the sectors for each type rod. A total of 34, 105, and 57 observations were noted for type I, II, and III rods, respectively. The percentages of these totals occurring in each of the eight sectors are given in Fig. 2.22.

One would expect that the larger number of observations for the type II rods would result in a more uniform distribution of the observations with respect to the circumferential view sectors; Fig. 2.22 appears

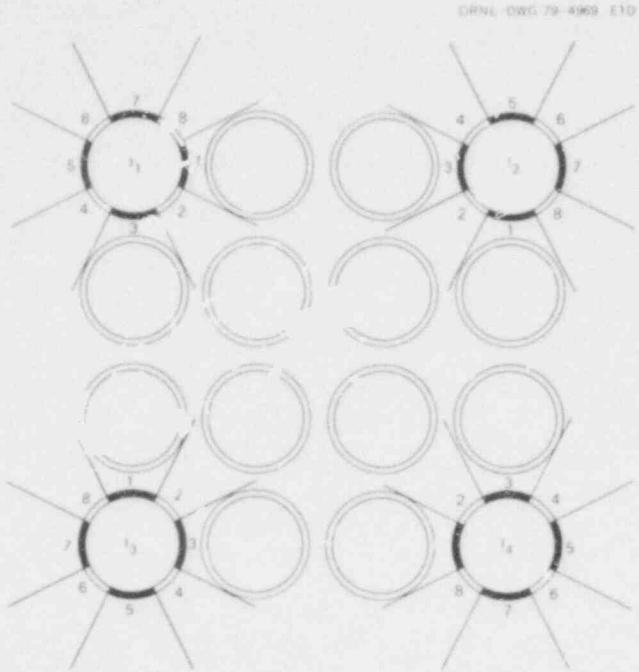

Fig. 2.19. View sectors and nomenclature for the corner rods of a 4 × 4 bundle.

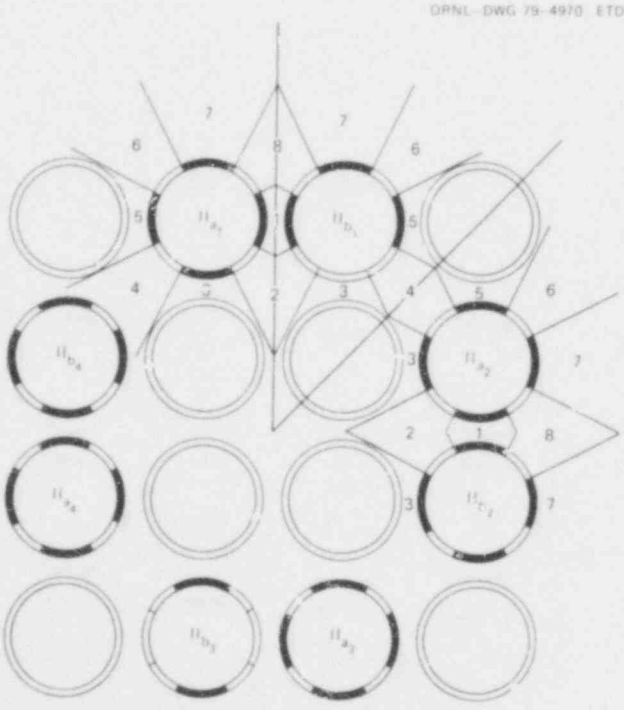

Fig. 2.20. View sectors and nomenclature for the side rods of a 4 × 4 bundle. Note the mirror symmetry of the nomenclature between rod types II_{a_1} and II_{b_1} and between rod types II_{b_2} and II_{a_2}. This symmetry is typical for all side rods.

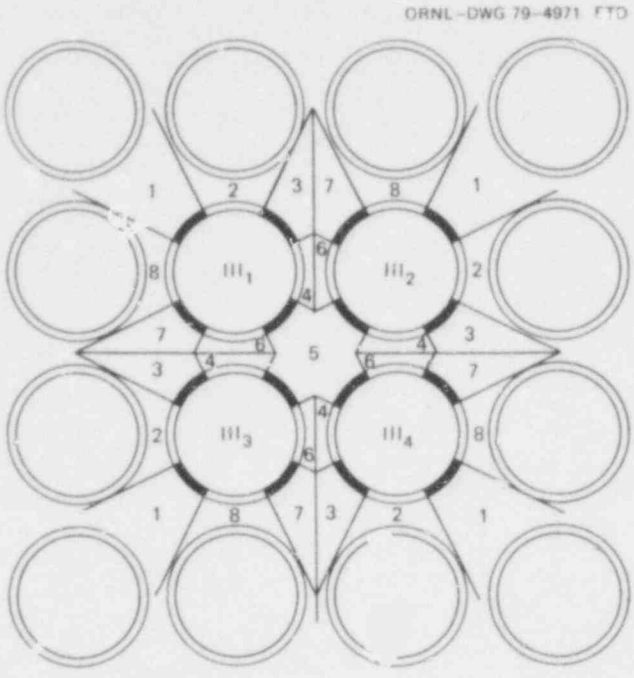

Fig. 2.21. View sectors and nomenclature for the interior rods of a 4 × 4 bundle.

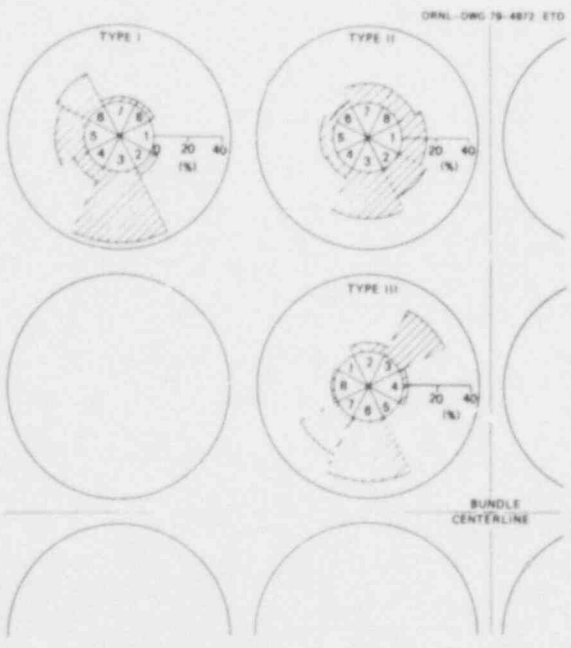

Fig. 2.22. Distribution of maximum wall thinning observations by view sector for the three rod types in B-1 test array.

to substantiate this expectation. Types I and III showed more irregular thinning and burst behavior according to this analysis. A comparison of Figs. 2.19 and 2.21 with Fig. 2.17 shows that the four type I rods burst in view sectors 3, 5, and 6 and the four type III rods burst in sectors 3, 6, and 7. The distributions given in Fig. 2.22 reflect this behavior, and one can infer that each rod thinned over a relatively large axial distance above and below the actual burst. A comparison of Fig. 2.20 with Fig. 2.17 for type II rods shows similar but less obvious trends.

According to Fig. 2.15, an average temperature difference of ~130–140°C existed between the outer rods and the heated shroud during the time of deformation. Neither Fig. 2.17 nor Fig. 2.22 shows any noticeable effect that can be attributed to this temperature difference. In addition, the uniformity of the radial temperature distribution (Fig. 2.15) within the bundle is consistent with the lack of a directional pattern in the burst behavior.

2.4. Additional Bundle B-2 Results

R. H. Chapman D. O. Hobson*

The primary objective of the B-2 test was to investigate the effect of a relatively cold boundary (i.e., a large temperature difference between the bundle and the shroud) on bundle deformation behavior (i.e., magnitude, distribution, burst orientation, etc.). The effect was to be evaluated by comparing the results from the B-1 test, in which the shroud was electrically heated (albeit at a lower rate than the B-1 bundle), with those from the B-2 test, in which the shroud was not electrically heated. Details of the test setup and operations were reported previously,[3] together with test results that could be obtained relatively soon after the test. These included temperature and pressure data, burst times and preliminary locations, and flow test results. A number of quick-look data plots and a selection of posttest photographs were also presented to give an idea of the test performance and the extent of deformation. Since those results were reported, the temperature data have

*Metals and Ceramics Division.

been analyzed, and the bundle has been destructively examined to obtain detailed deformation data; these topics are discussed below. A few of the previously reported results are also included to provide ready reference. A brief comparison between the B-1 and B-2 results will be presented in Section 2.5.

The fuel simulators (internal heaters) used in the B-2 test assemblies were the best available from those supplied by SEMCO after the B-1 simulators. In general, the quality of the B-2 fuel simulators (as judged by the uniformity of axial temperature distribution as determined from pretest infrared characterization) was not significantly higher than that of the simulators used in the B-1 test.

Each of the fuel pin simulators was instrumented with a fast-response, strain-gage-type pressure transducer and four Inconel-sheathed (0.71-mm-OD) type K thermocouples with ungrounded junctions. The thermocouples were spot-welded to the inside of the Zircaloy-4 tubes at axial and azimuthal positions (nominally the same as used in the B-1 test), as indicated in Fig. 2.23, selected to provide an overall indication of the temperature distribution. All the simulator thermocouples functioned properly during

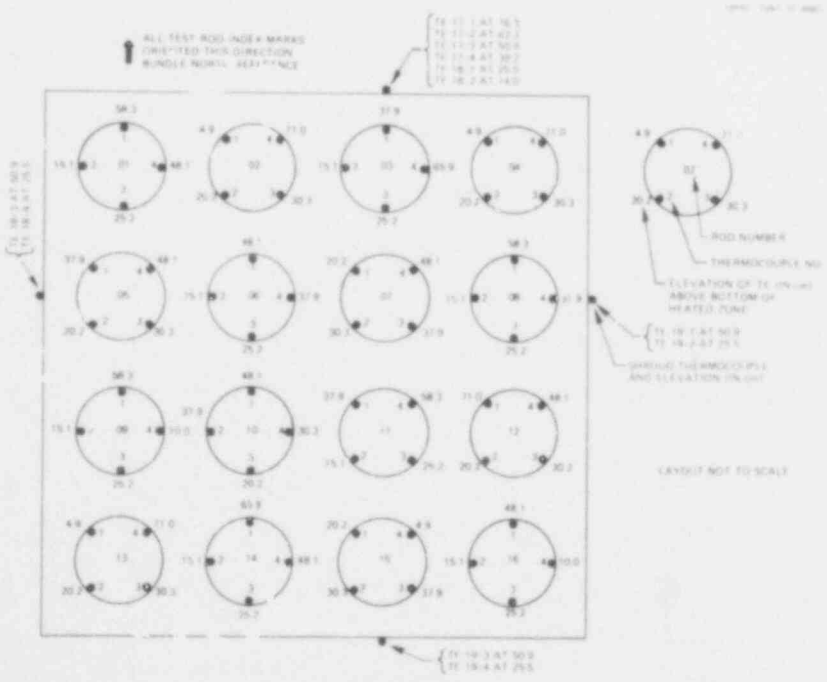

Fig. 2.23. As-built thermocouple locations in B-2 test.

the test. Twelve thermocouples (0.71 mm OD, stainless steel sheathed, type K, with ungrounded duckbill junctions) were spot-welded to the outside of the 0.25-mm-thick unheated shroud surrounding the rod array. One face of the shroud had six thermocouples to provide information on the axial temperature distribution, while two thermocouples were located on each of the other three faces. (See Fig. 2.23 for locations.)

Preparations for the test began with heatup of the test vessel and checkout of the instrumentation. Thermal equilibrium of the assembly was achieved in ∿6 hr; leak rates of the fuel pin simulators were acceptably low (less than 35 kPa pressure loss per minute). A short powered run (4-sec transient) was then conducted to ascertain that the computer-controlled data-acquisition system (CCDAS) and all the instrumentation were functioning properly and that the performance of the test assembly was as expected. An examination of the quick-look data from this short transient showed that the indicated performance was as expected, except that one fuel pin simulator (No. 9) had developed a moderate leak (∿200 kPa pressure loss per minute). Although this leak was not nearly as severe as that experienced by one of the simulators in the B-1 test, on-the-spot checks were insufficient to identify (and correct) the source. It was decided to proceed with the test as soon as thermal equilibrium was reestablished.

Following stabilization of the bundle temperature at ∿334°C after the short powered run, all the fuel pin simulators were pressurized simultaneously with helium to ∿8800 kPa and isolated from the pressure supply system. Superheated steam (inlet conditions of 332°C and 200 kPa) flowed downward through the bundle (flow rate, 5 kg/hr; Re = 290 based on inlet conditions and undeformed bundle dimensions) during the transient. The steam flow was increased to 30 kg/hr when power to the bundle was terminated to facilitate cooldown; the test vessel was vented to atmospheric pressure simultaneously with the increased steam flow.

Table 2.5 summarizes pertinent data from the test; they are included here for ready reference purposes, since they were reported and discussed in detail earlier.[3] The performance of the simulators was about the same with the exception of No. 9, which reflected the loss in pressure discussed earlier. Most of the simulators (15; the exception being No. 9) burst

Table 2.5. Summary of B-2 test results

Rod No.	Initial conditions					Approximate maximum pressure differential (kPa)	Approximate burst conditions					Burst temperature predicted from burst pressure[b] (°C)
	Differential pressure (kPa)	Temperature (°C)					Differential pressure (kPa)	Temperature[a] (°C)				Time (sec)	
		TE-1	TE-2	TE-3	TE-4			TE-1	TE-2	TE-3	TE-4		
1	8810	334	335	334	335	9240	7700	790	803	825	870	18.30	846
2	8805	335	335	336	339	9220	7685	818	841	846	844	18.00	847
3	8795	333	334	332	336	9245	7560	852	853	845	826	18.30	849
4	8775	336	336	335	337	9205	7585	861	872	807	854	18.30	848
5	8775	333	334	336	336	9205	7770	854	866	835	852	17.85	845
6	8785	335	335	334	335	9220	6925	8[illegible]	827	843	834	17.95	858
7	8740	334	333	333	333	9160	7360	824	861	838	850	17.85	852
8	8750	335	334	333	334	9200	7565	856	840	813	792	17.80	849
9[c]	7715[c]	335	334	332	335	7715[c]	6110[c]	928	846	864	871	20.05[c]	872
10	8730	334	334	332	334	9175	9345	827	862	827	856	18.10	852
11	8735	333	334	332	333	9165	7670	832	819	832	853	17.80	847
12	8760	336	334	334	333	9200	7545	851	832	829	827	18.15	849
13	8755	338	333	334	332	8175	7820	856	805	883	867	18.15	845
14	875[illegible]	333	334	334	335	9140	7230	828	8[illegible]9	832	855	18.30	854
15	8790	336	334	334	337	9205	7945	824	807	799	836	18.05	843
16	8790	333	334	333	334	9220	7700	848	839	795	814	18.15	846

[a]Underlined value is burst temperature based on premise that maximum measured value is minimum possible burst temperature.

[b]Based on burst temperature–burst pressure correlation from single-rod burst tests (external bare-wire thermocouples).

[c]Rod 9 developed a moderate leak prior to the test and its behavior is abnormal.

within a 0.5-sec interval, the same as observed in the B-1 test. The burst sequence did not indicate a propagation effect.

Selected quick-look data plots (e.g., temperature vs time and pressure vs time) were presented earlier[3] to show the behavior of these parameters in individual simulators. The temperature data have been analyzed at selected times to characterize the test and to assess the importance of the effect of the unheated shroud on the bundle-averaged temperature distribution.

The temperature measurements were analyzed to obtain average bundle (cladding) and shroud temperatures for the time period from power-on to the first tube burst. These data, presented graphically in Fig. 2.24, are useful in characterizing the test. The average temperature difference between the bundle and shroud is also plotted in the figure. This difference is indicative of the potential for shroud heating by bundle losses. It is interesting to note that the difference leveled off at the end of the transient, indicating that the instantaneous shroud heating rate was approximately equal to that of the bundle.

Bundle and shroud heating rates, shown in Fig. 2.25, were calculated from the averaged temperatures for the same time period, using a stepwise

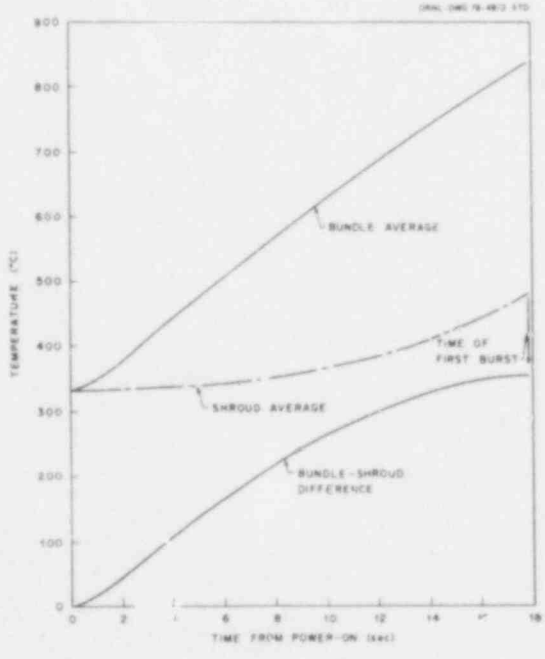

Fig. 2.24. Average temperatures in B-2 tests.

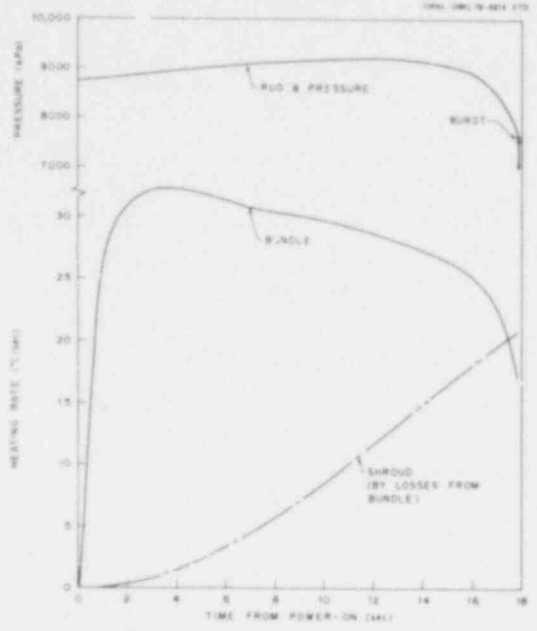

Fig. 2.25. Bundle and shroud heating rates in B-2 test.

procedure as discussed for the B-1 bundle in the previous section. The pressure trace for the first tube to burst (No. 8) is also shown in the figure for reference. The bundle heating rate snows the same behavior as shown by the B-1 bundle discussed earlier. The average heating rate over the time interval of 3 to 15 sec was 29.9°C/sec; this is considered characteristic of the test.

Even though the B-2 shroud was not electrically heated, heat losses from the bundle produced a significant heating rate in the shroud. In fact, as mentioned earlier, the shroud heating rate was approximately the same as that of the bundle at the end of the transient. The average shroud heating rate over the time period of 3 to 15 sec was 7.7°C/sec.

The temperature measurements at a given elevation (see Fig. 2.23) were averaged to obtain axial bundle-averaged temperature profiles at the selected times, as shown in Fig. 2.26. The number of measurements averaged to obtain the plotted data point for each elevation is indicated in the figure. Also, the axial distribution of the tube bursts is indicated at the extreme right of the figure. (Burst temperatures and times are not represented in the plot.) The averaged data show that the bundle

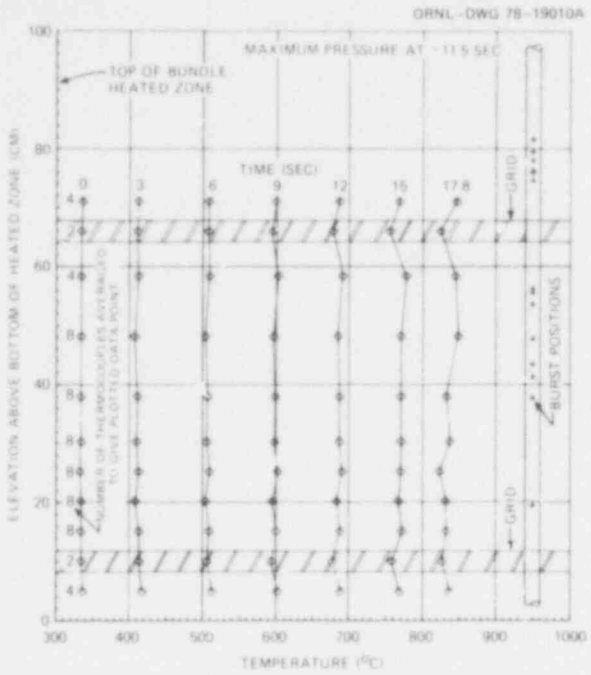

Fig. 2.26. Axial temperature distribution in B-2 test as a function of time.

axial temperature profile was very uniform prior to the onset of deformation (i.e., until maximum pressure was attained). As might be expected, the temperature profile was perturbed during the deformation process; however, the overall average remained fairly uniform until the time of the first burst (i.e., until 17.8 sec).

The data were reanalyzed to obtain radial temperature profiles. For this purpose, the thermocouples were considered to be located axially at a common elevation (i.e., the axial distribution was assumed to be perfectly uniform) and radially at one of five representative positions, as indicated in Fig. 2.27. The representative positions are the radii of the inside and outside tangent surfaces of the inner and outer ring of simulators, respectively, and the radius of the shroud. (Due to symmetry, the dimensionless radii, r_i/R, are the same on the diagonals and the axes of the array if the reference radius, R, is appropriately defined.) The measurements of the thermocouples at each of the representative radial locations were averaged to obtain a temperature characteristic of that position. The profiles obtained in this manner are plotted in Fig. 2.28

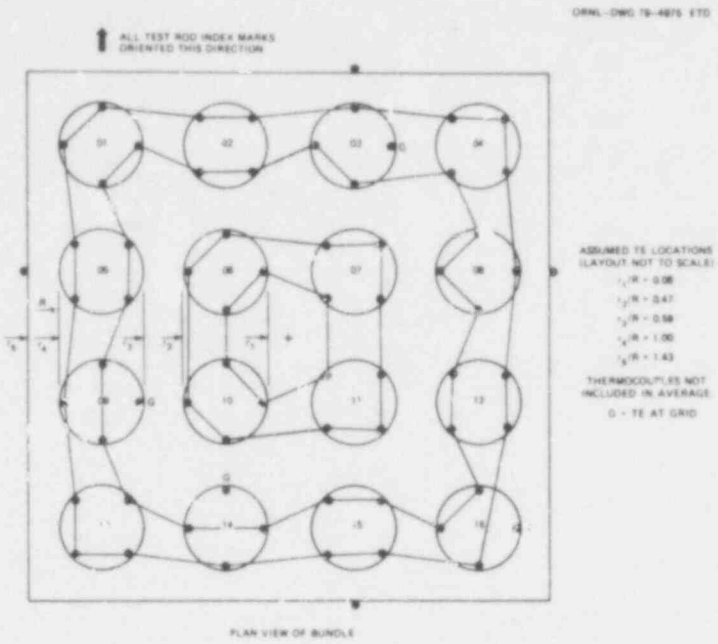

Fig. 2.27. Thermocouple assignments for calculation of radial temperature profile in B-2 test.

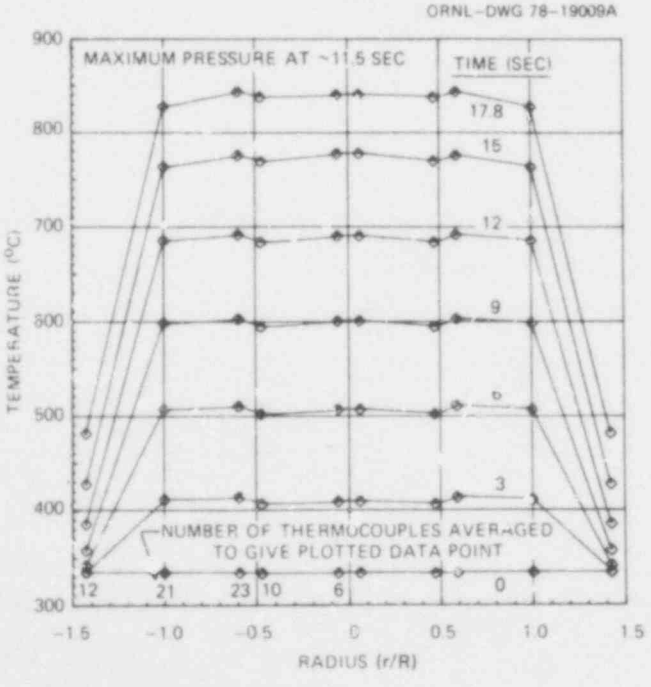

Fig. 2.28. Radial temperature distribution in B-2 test as a function of time.

and show that the bundle radial temperature distribution was reasonably flat throughout the transient. There is a small gradient evident across the outer ring of simulators, but not across the inner ring, even though a very large gradient existed across the coolant annulus between the bundle and the shroud.

Although the temperature transient and distributions presented in Figs. 2.24, 2.26, and 2.28 characterize the bundle as a whole, the individual simulators deviated significantly from these smoothed profiles. This would be expected, since the simulator temperature distributions are strongly influenced by the heat generation within the individual fuel simulators. The axial locations of the bursts (see deformation profiles below) showed better correlation with the pretest characterization scans than with the bundle axial temperature profiles. There is strong evidence that deformation (as indicated by localized wall thinning in the individual tubes) and burst orientations can be correlated with the radial temperature profile, as will be discussed later.

Following flow characterization tests on the bundle (reported earlier[3] and discussed in Section 2.7 of this report), the bundle was cast in an epoxy matrix and sectioned at selected positions using a rubber-bonded silicon carbide cutting wheel; a total of 53 sections were made. The sections were photographed to facilitate the strain measurements (the as-cut surface finish was sufficient to produce adequate quality photographs without polishing). A number of the sections are shown in Figs. 2.29 through 2.48 to give an indication of the deformation behavior and to show interesting features. The photographs show a top view of the bundle with the No. 1 simulator in the upper left corner (i.e., the views conform to the layout and tube identification given in Fig. 2.23).

With the exception of Fig. 2.29, all the figures have white arrow points in the upper left corner. The distance along the edge of the epoxy matrix between the arrow points is proportional to the elevation of the section and can be used to calculate the height (above the bottom of the heated zone) at which the actual cut was made.

Figure 2.29, taken 6.9 cm below the bottom of the heated zone, is representative of the undeformed bundle. All the tubes had moderate strain peaks (a minimum of 8.3% on No. 16 and a maximum of 18.8% on

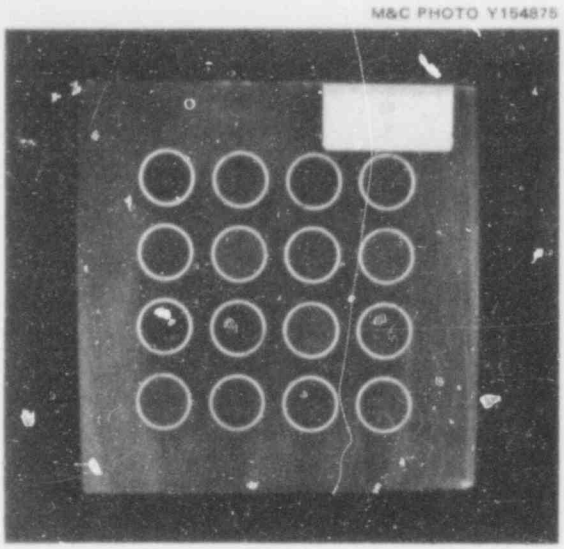

Fig. 2.29. Section of undeformed region of B-2 at −6.9-cm elevation.

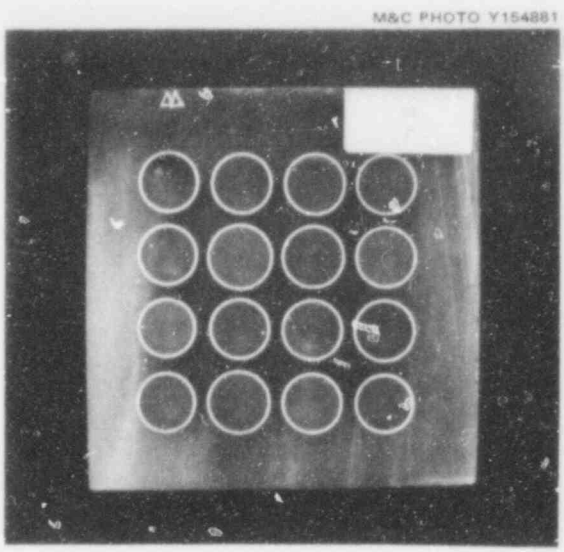

Fig. 2.30. Section through B-2 at 3.4-cm elevation.

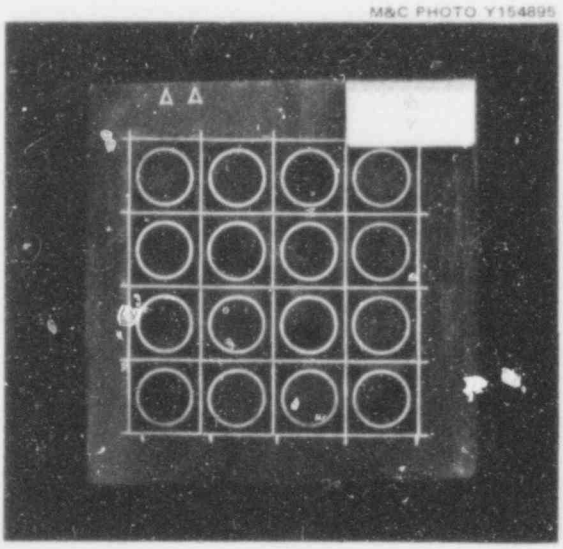

Fig. 2.31. Section through lower grid of B-2 at 11.5-cm elevation.

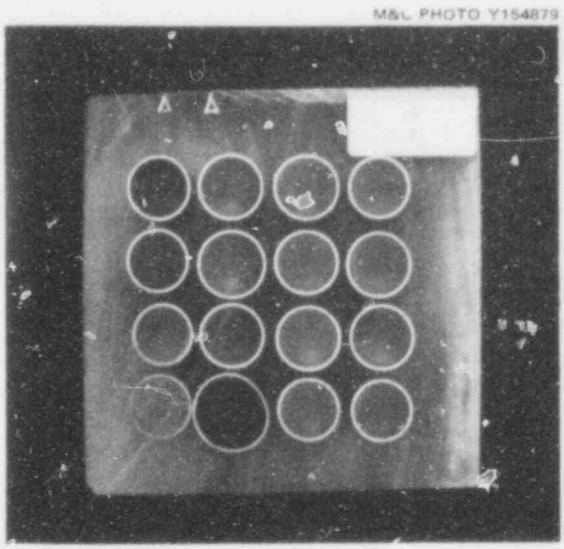

Fig. 2.32. Section through B-2 at 18.1-cm elevation.

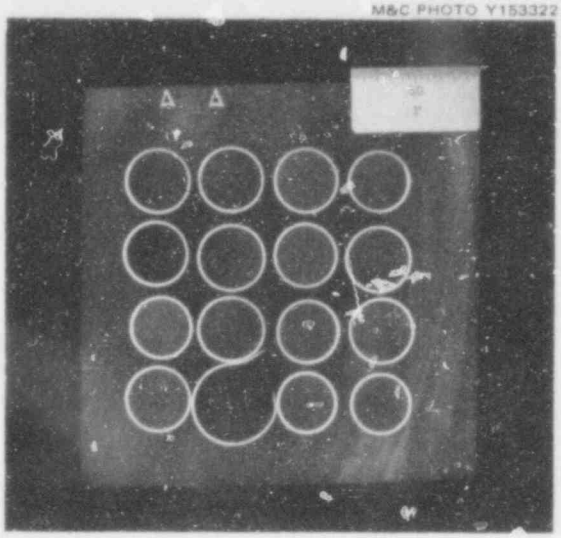

Fig. 2.33. Section through B-2 at 19.5-cm elevation.

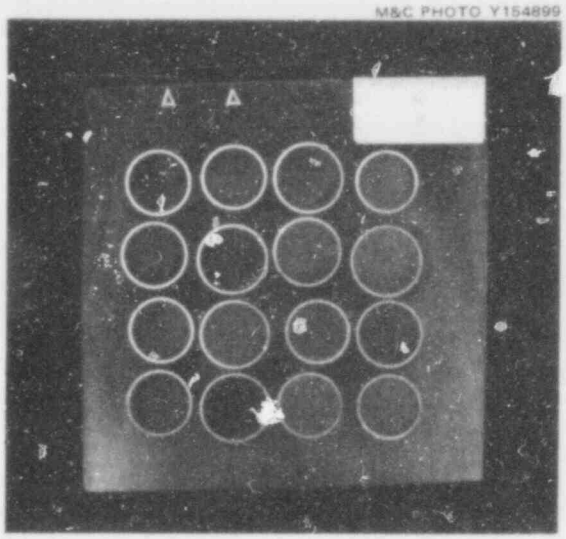

Fig. 2.34. Section through B-2 at 25.0-cm elevation.

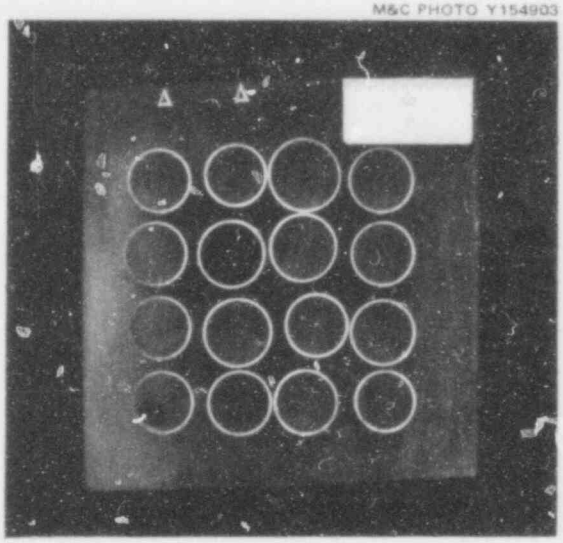

Fig. 2.35. Section through B-2 at 30.0-cm elevation.

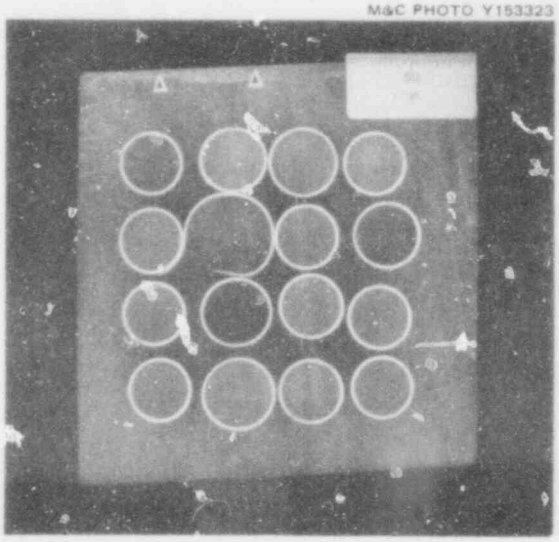

Fig. 2.36. Section through B-2 at 37.7-cm elevation.

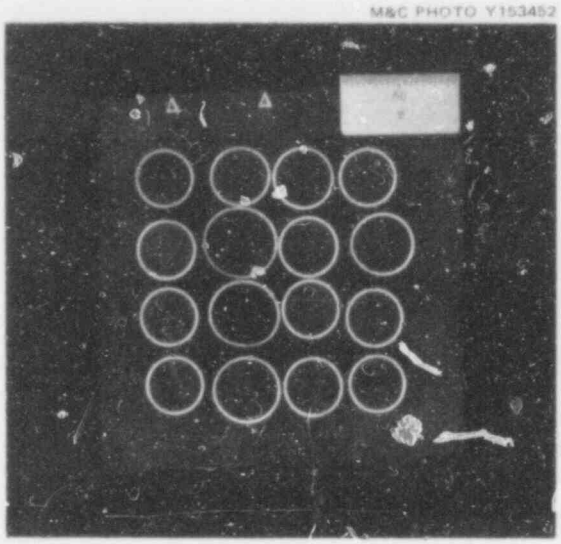

Fig. 2.37. Section through B-2 at 39.5-cm elevation.

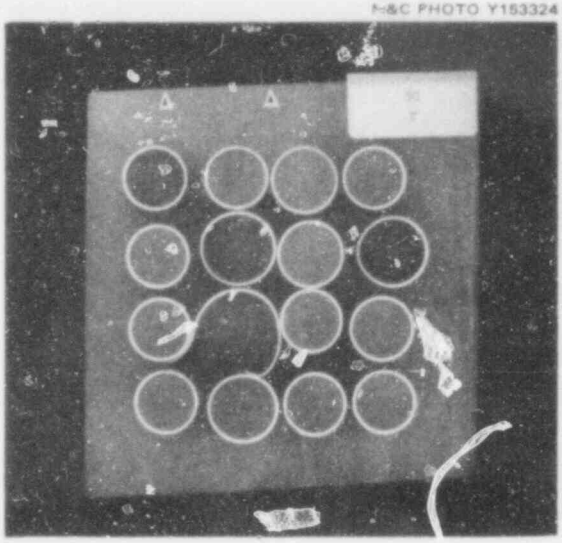

Fig. 2.38. Section through B-2 at 41.2-cm elevation.

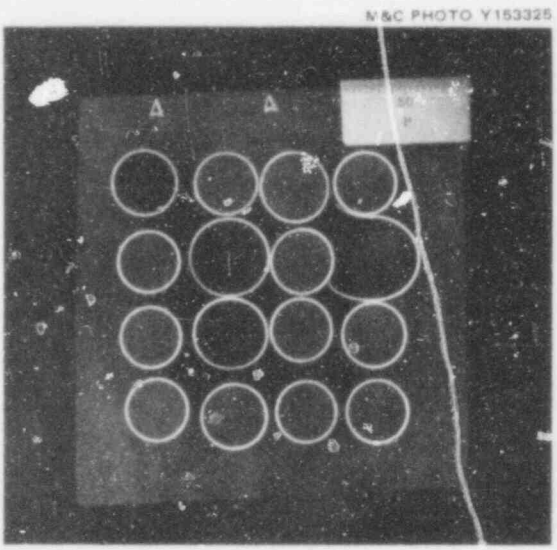

Fig. 2.39. Section through B-2 at 43.3-cm elevation.

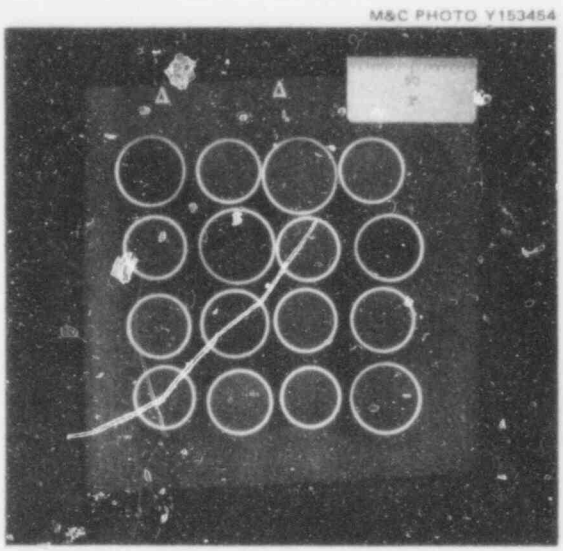

Fig. 2.40. Section through B-2 at 46.2-cm elevation.

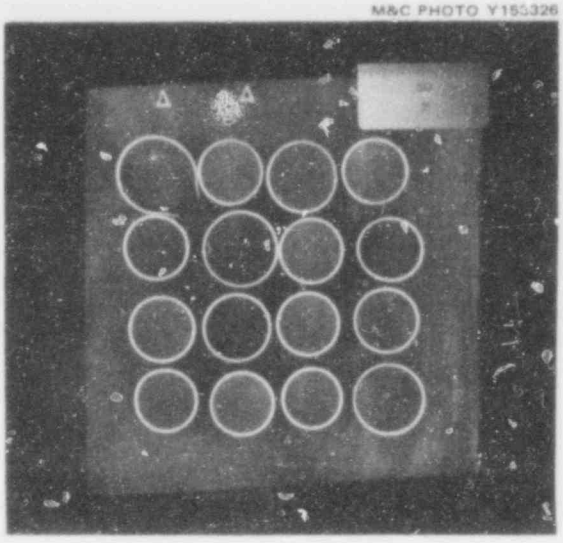

Fig. 2.41. Section through B-2 at 47.7-cm elevation.

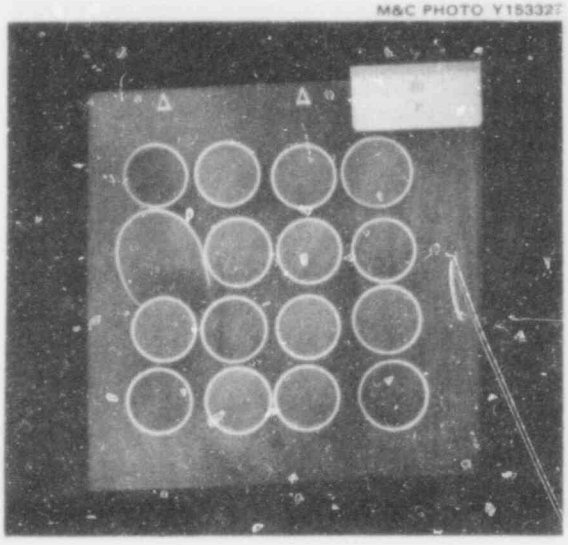

Fig. 2.42. Section through B-2 at 53.5-cm elevation.

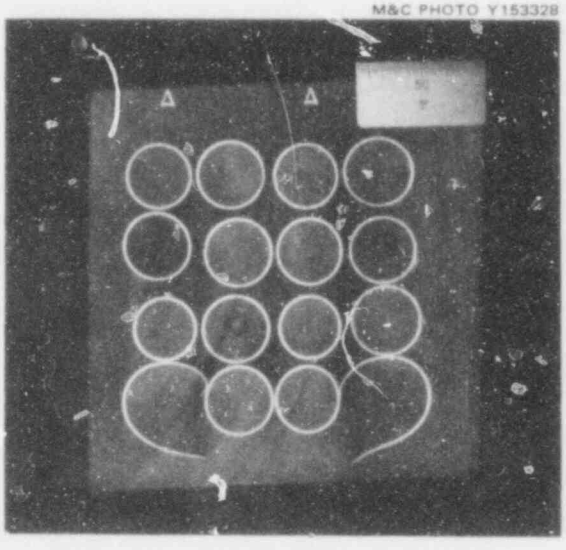

Fig. 2.43. Section through B-2 at 56.2-cm elevation.

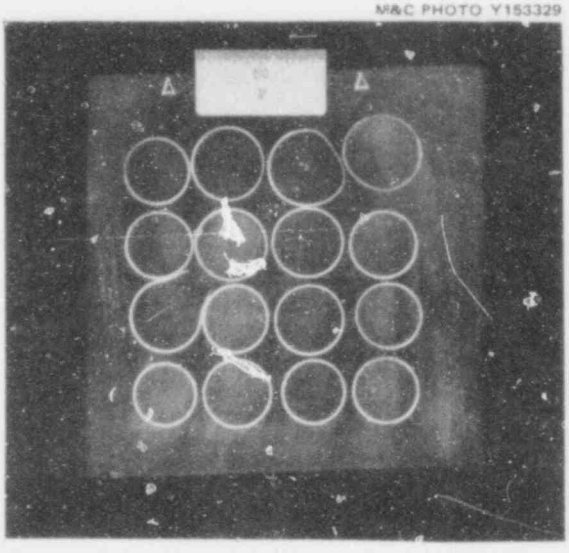

Fig. 2.44. Section through B-2 at 74.6-cm elevation.

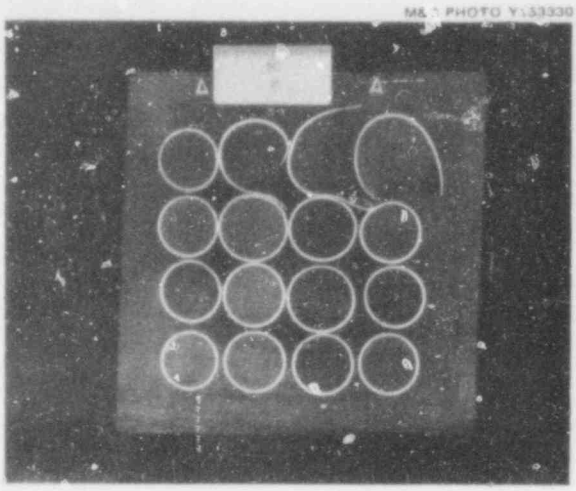

Fig. 2.45. Section through B-2 at 76.2-cm elevation.

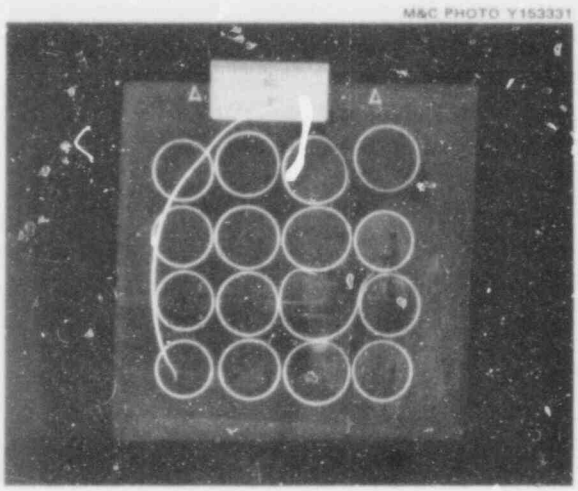

Fig. 2.46. Section through B-2 at 78.0-cm elevation.

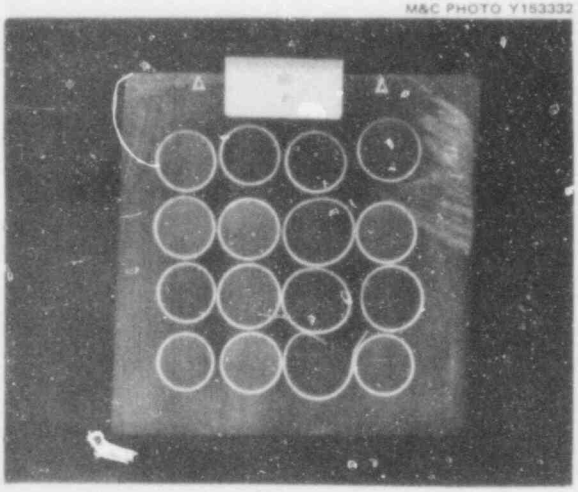

Fig. 2.47. Section through B-2 at 79.5-cm elevation.

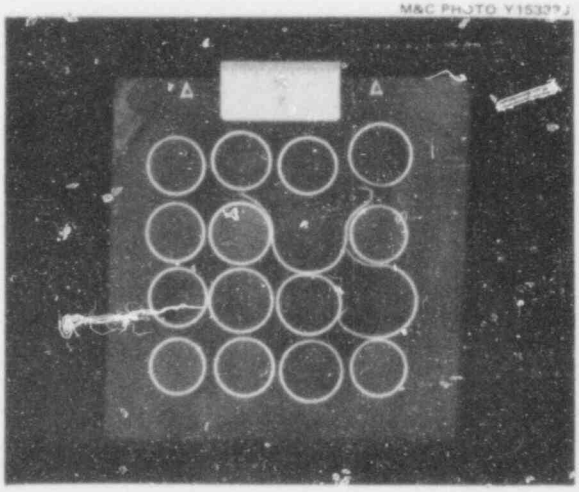

Fig. 2.48. Section through B-2 at 81.6-cm elevation.

No. 6) about halfway between the start of the heated zone and the lower grid; Fig. 2.30 shows a section in this region. A section through the lower grid (at elevation 11.5 cm) is shown in Fig. 2.31; the restraining influence of the grid (due to lateral grid forces and/or local cooling of the tube by the grid) is clearly evident by the range of strains (2.9 to 5.6%) observed in this section. Figure 2.32 shows localized wall thinning and distortion just below the burst in the No. 14 simulator, which is shown in Fig. 2.33.

Figures 2.34 and 2.35 show sections representative of those in a broad minimum in the coolant channel flow area restriction that will be discussed later. The maximum burst strain (57.8%) occurred in the No. 6 simulator and is shown in Fig. 2.36. Localized wall thinning toward the interior of the bundle is evident on several of the simulators, particularly the corner ones, in this and the remainder of the sections. There is little evidence on the four interior rods of wall thinning toward the center of the bundle. Bursts in the outer ring of simulators tend to be directed toward adjacent rods or the bundle interior. These observations are consistent with the bundle radial temperature profile shown in Fig. 2.28.

Strain measurements were obtained from enlarged (~5X) photographs of the sections, using the methodology reported[3] for the B-1 test. Table 2.6 tabulates the strains determined thus for each tube in each section. The maximum observed strain was 57.8%; this occurred at the burst in the No. 6 simulator (Fig. 2.36). The minimum burst strain, 29.2%, was experienced by the No. 9 simulator (Fig. 2.44), which underwent partial depressurization (see Table 2.5) due to a leak during the test. The cross section with the maximum total deformation (sum of all tubes) is shown in Fig. 2.45.

The strain data were used to plot axial profiles of the individual tubes; these are presented in Figs. 2.49 through 2.64. The pretest infrared characterization scan of the fuel simulator (internal heater) and the axial positions of the thermocouples are also shown for reference purposes.

Table 2.6. Strain in B-2 tubes in percent

Elevation (cm)	Tube No.															
	1	2	3	4	5	6	7	8	9	10	11	12	13	14	15	16
0.0	-0.2	-0.2	-0.3	0.3	0.0	-0.4	-0.1	0.3	-0.8	-0.6	-0.4	0.1	-0.9	-0.5	-0.1	0.0
1.8	4.4	5.7	6.0	5.8	4.1	7.1	7.4	6.9	4.6	5.1	5.1	7.2	4.1	6.3	4.8	4.8
3.4	10.5	11.3	12.3	10.6	10.5	18.8	14.1	11.6	8.2	10.6	10.9	13.0	8.9	15.0	9.6	7.7
5.0	10.4	11.5	11.0	11.5	9.9	17.1	12.8	11.1	8.5	10.7	11.0	11.2	9.3	13.2	10.4	8.3
6.5	8.5	9.7	8.0	7.8	7.6	13.5	10.4	7.5	7.0	9.0	9.0	8.5	7.4	9.8	7.5	6.6
8.8	4.6	4.9	3.9	4.1	3.9	5.0	4.4	4.2	3.1	3.1	3.9	3.9	3.5	3.7	3.1	3.1
11.5	3.7	3.9	3.9	4.4	3.7	5.6	4.3	4.5	3.4	3.7	4.8	4.6	3.5	4.2	2.9	4.3
13.3	8.6	7.7	6.2	7.9	6.7	14.7	12.1	9.8	9.3	9.4	13.2	10.5	8.2	10.3	5.1	6.5
15.1	13.3	11.4	11.5	9.5	8.5	20.9	15.1	13.2	10.7	12.4	16.8	15.6	11.6	17.3	6.8	7.1
16.8	15.3	16.3	14.6	11.6	11.7	22.9	15.7	16.2	10.9	16.2	18.3	17.5	14.4	28.4	11.2	10.5
18.1	15.8	18.2	17.6	13.0	14.3	23.2	15.6	18.7	11.0	16.5	16.9	17.9	15.7	37.8	12.3	11.7
19.5	19.2	19.5	19.7	13.7	18.7	22.4	17.9	21.1	14.7	21.5	16.6	20.7	20.9	41.8	12.6	12.9
21.4	19.8	17.5	19.9	10.8	18.0	21.6	17.9	22.8	13.8	22.6	15.2	24.7	19.5	32.4	11.1	11.8
23.2	19.5	16.1	21.4	9.7	18.3	24.7	18.4	27.0	14.9	23.3	15.1	21.8	18.5	25.8	13.1	13.3
25.0	16.2	13.8	24.4	11.0	17.4	23.4	21.0	27.4	15.4	21.0	13.5	18.5	16.0	22.3	15.5	14.7
26.5	15.4	11.5	25.9	13.5	14.6	19.8	23.4	20.7	14.5	21.1	13.5	18.7	14.9	15.7	17.3	11.8
28.5	16.5	12.7	29.8	16.7	15.1	21.0	24.5	17.4	14.8	23.8	14.3	19.5	14.8	15.5	18.4	10.7
30.0	14.7	12.4	32.5	18.6	14.9	21.5	23.3	16.1	13.2	23.3	15.1	18.8	12.4	15.8	17.5	11.7
32.0	12.6	15.3	28.0	19.8	14.7	20.8	21.8	16.2	13.3	21.0	14.4	20.2	12.8	17.3	13.7	13.5
34.0	11.6	15.4	22.0	17.7	14.8	23.8	19.4	15.1	13.8	18.6	14.8	20.7	16.1	17.7	12.7	13.2
35.5	12.[illegible]	18.0	21.6	14.0	15.3	44.3	17.4	16.1	13.5	20.1	16.7	18.[illegible]	16.5	22.7	13.9	11.7
37.7	13.5	18.7	14.0	13.5	17.9	57.8	15.7	20.7	15.0	25.0	16.2	15.5	14.6	20.1	16.2	12.7
39.5	12.2	15.0	20.1	13.8	15.6	35.6	18.4	23.4	13.5	32.6	14.4	14.2	12.3	28.9	16.0	13.3
41.2	18.8	15.7	23.7	[illegible]3.6	16.4	35.3	23.1	29.6	16.2	42.8	16.9	18.9	17.5	26.8	17.3	16.9
43.3	22.2	15.8	25.5	17.0	15.6	44.3	19.7	37.6	14.2	33.0	16.8	21.0	17.1	21.3	15.3	18.3
44.7	23.4	15.0	31.7	18.3	14.9	40.7	17.3	33.0	14.4	27.3	16.0	18.4	15.9	18.9	12.9	21.6
46.2	27.8	17.0	38.4	[illegible]5.7	16.0	36.4	17.2	23.3	17.0	23.2	16.1	18.1	14.7	17.9	11.8	29.0
47.7	34.5	18.9	30.8	19.8	19.0	37.3	20.1	18.2	21.1	24.5	17.7	18.8	16.0	18.3	13.5	30.8
49.7	28.9	19.6	21.5	18.9	20.7	34.9	20.6	17.4	19.0	22.2	19.9	20.4	14.3	19.2	16.5	22.2
51.6	21.0	20.0	16.0	23.4	27.1	28.9	17.3	18.4	17.7	20.5	18.5	22.1	14.5	20.8	17.4	19.6
53.5	18.1	19.7	19.3	29.4	35.0	25.9	20.1	17.5	19.5	21.8	18.3	25.7	22.0	23.5	20.6	28.2
54.9	19.1	21.9	19.2	27.2	29.0	28.0	22.6	17.6	18.1	22.6	17.6	27.1	24.9	24.2	20.5	37.1
56.2	20.8	25.3	21.3	27.2	25.2	25.6	23.6	22.2	17.6	24.8	17.7	28.1	41.4	27.7	23.2	41.7
57.6	17.1	22.3	21.4	28.1	21.5	21.3	19.3	24.1	14.7	21.6	13.6	23.4	34.6	25.2	20.4	32.4
59.8	13.4	14.7	18.7	23.7	15.0	17.7	16.9	16.8	12.9	17.3	10.9	17.4	16.1	18.2	14.1	17.0
61.8	11.0	10.3	12.4	12.7	10.5	13.6	14.8	11.8	11.2	13.6	10.5	14.0	13.1	12.1	10.5	10.8
63.8	5.1	5.3	4.9	6.1	5.1	5.5	5.7	6.0	3.7	5.4	5.3	5.8	6.4	5.7	5.0	6.4
66.5	4.8	4.9	5.2	6.5	4.7	5.8	6.3	5.9	4.1	5.1	5.5	5.2	5.5	5.0	4.0	5.1
68.4	10.2	10.8	13.0	10.6	11.0	17.7	18.1	11.6	12.4	13.7	15.0	11.0	10.9	10.8	8.2	9.3
70.1	14.6	18.3	19.7	15.9	16.0	27.0	23.1	16.7	17.0	17.8	20.7	16.8	9.7	19.1	12.6	12.6
71.6	15.0	22.2	21.3	21.5	20.6	27.0	21.8	17.8	19.4	18.1	20.2	17.6	9.7	25.8	12.7	14.3
73.1	16.1	25.1	24.8	30.5	22.0	25.6	23.1	19.3	23.0	18.7	20.9	17.7	10.8	26.7	13.5	17.6
74.6	21.7	33.0	37.4	37.8	23.3	30.6	27.7	22.1	29.2	22.2	26.4	19.7	16.5	24.8	17.0	20.1
76.2	23.2	38.5	40.3	42.0	22.0	35.4	31.9	22.3	23.9	25.3	34.4	23.2	17.3	22.7	22.2	22.5
78.0	24.3	29.0	33.6	33.2	23.6	28.8	34.2	21.9	20.2	27.6	39.8	26.3	17.3	23.1	31.4	23.1
79.5	22.9	20.7	22.4	27.1	23.9	22.5	39.7	21.6	19.6	28.0	35.2	29.4	16.7	22.2	35.1	22.0
81.6	17.3	17.9	16.8	26.5	19.0	23.8	55.6	16.3	19.1	28.3	25.9	39.7	14.3	18.7	25.2	16.2
83.8	11.4	15.9	15.6	18.9	14.1	24.0	32.7	12.8	16.1	21.1	20.1	21.8	10.6	16.1	14.4	11.6
86.0	8.0	13.8	12.7	12.9	15.4	14.8	20.7	11.5	13.9	23.0	14.6	11.8	7.5	14.3	9.8	10.8
88.1	6.5	8.1	6.3	7.5	10.3	9.2	12.2	8.4	7.8	12.1	7.8	7.1	5.2	9.7	6.8	8.4
89.5	1.2	1.6	1.7	3.0	1.9	1.9	2.4	1.2	1.5	3.5	0.7	3.3	-0.1	2.4	0.3	1.1
91.5	0.4	0.4	0.8	1.2	1.1	0.1	1.0	-0.1	0.5	1.7	0.5	0.9	0.1	1.5	0.4	0.5

In general, the strain increases sharply at each end of the heated length, reflecting the strength associated with the sharp axial temperature gradients in these regions. The upper ends reflect the short thermal entrance region required to heat the incoming steam (~332°C) to near the tube surface temperature. The Reynolds number of the steam, based on inlet conditions and original tube dimensions, was 290; this is compared to a range of 600 to 800 used in our single rod tests. The higher steam flow in the single-rod tests produced a longer thermal entrance region and suppressed deformation and bursts in the upper 20 cm of the heated zone of those tests. On the other hand, the short thermal entrance zone

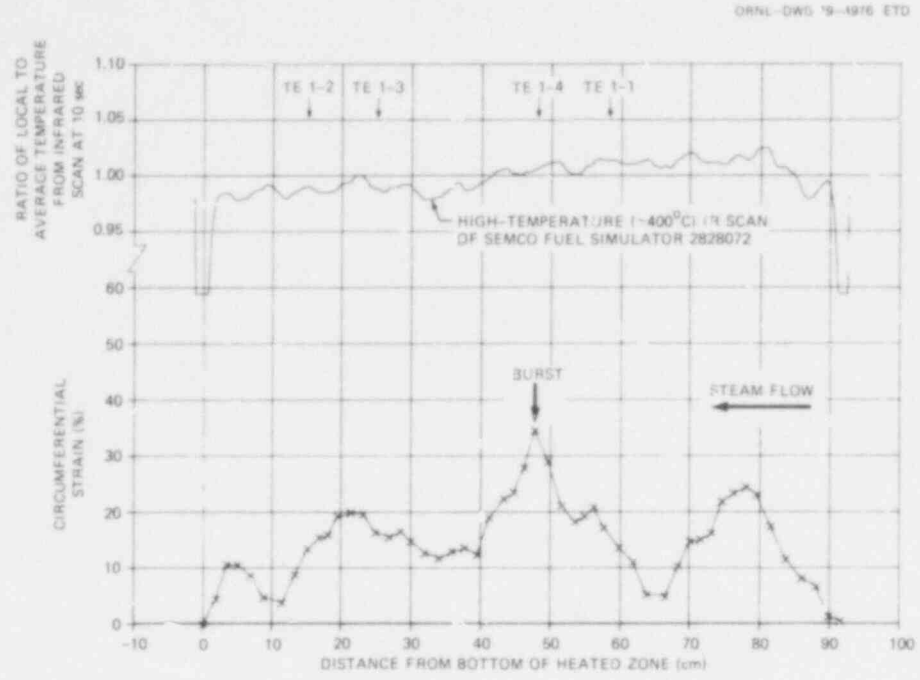

Fig. 2.49. Deformation profile of tube 1 in B-2 test.

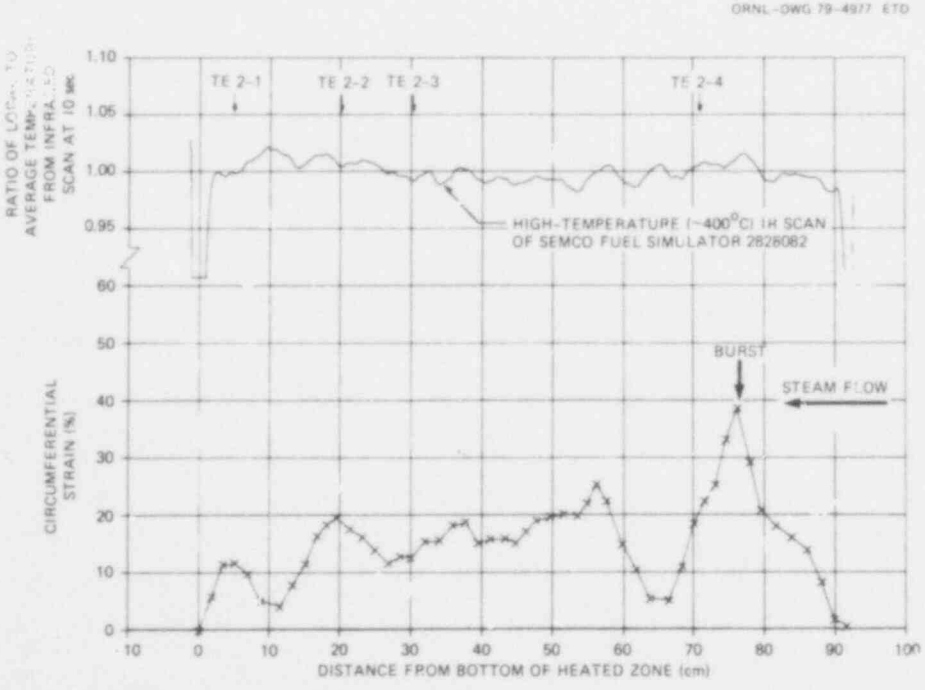

Fig. 2.50. Deformation profile of tube 2 in B-2 test.

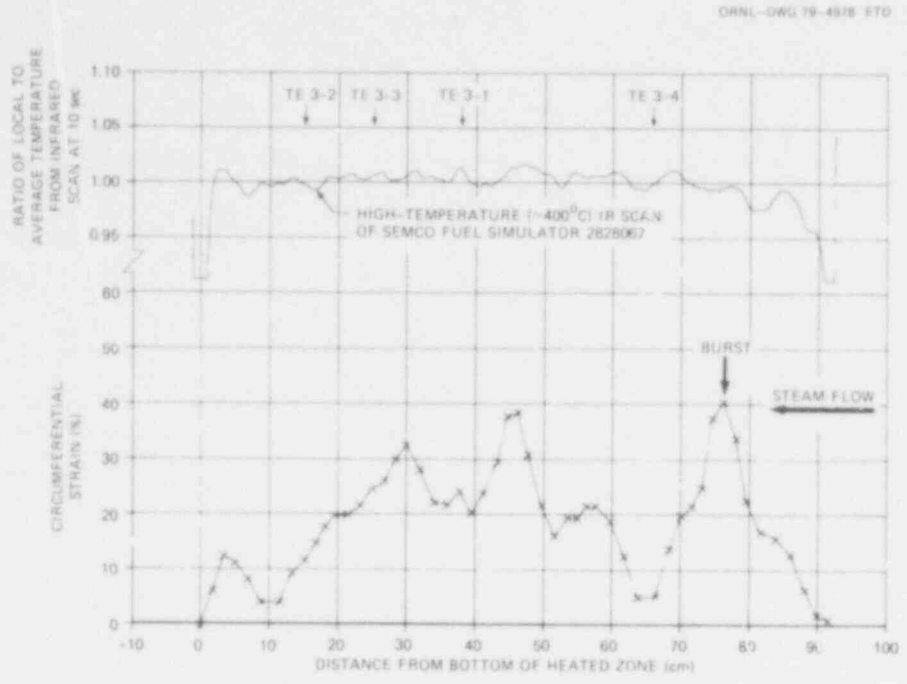

Fig. 2.51. Deformation profile of tube 3 in B-2 test.

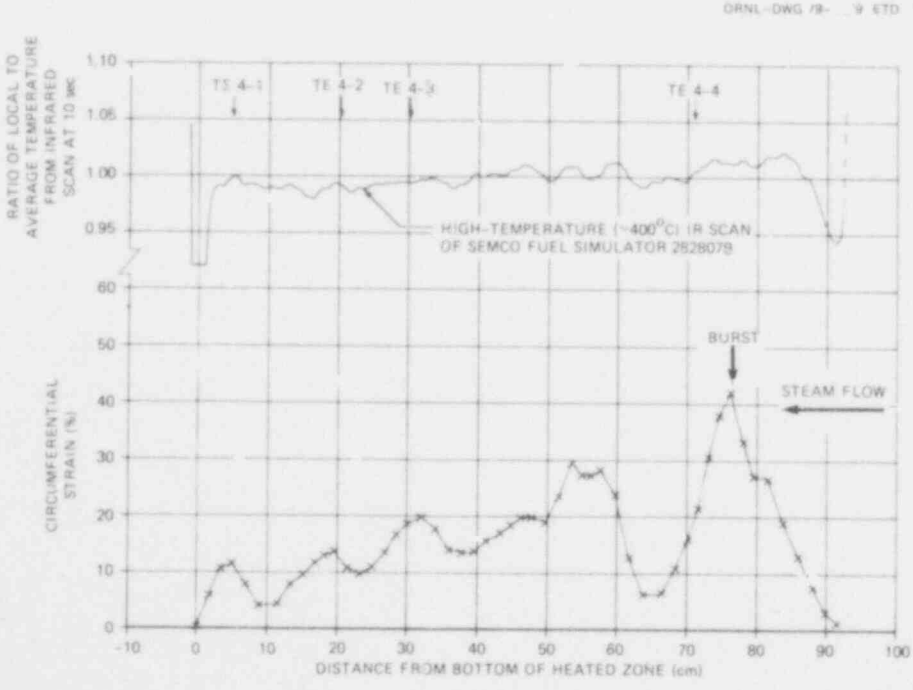

Fig. 2.52. Deformation profile of tube 4 in B-2 test.

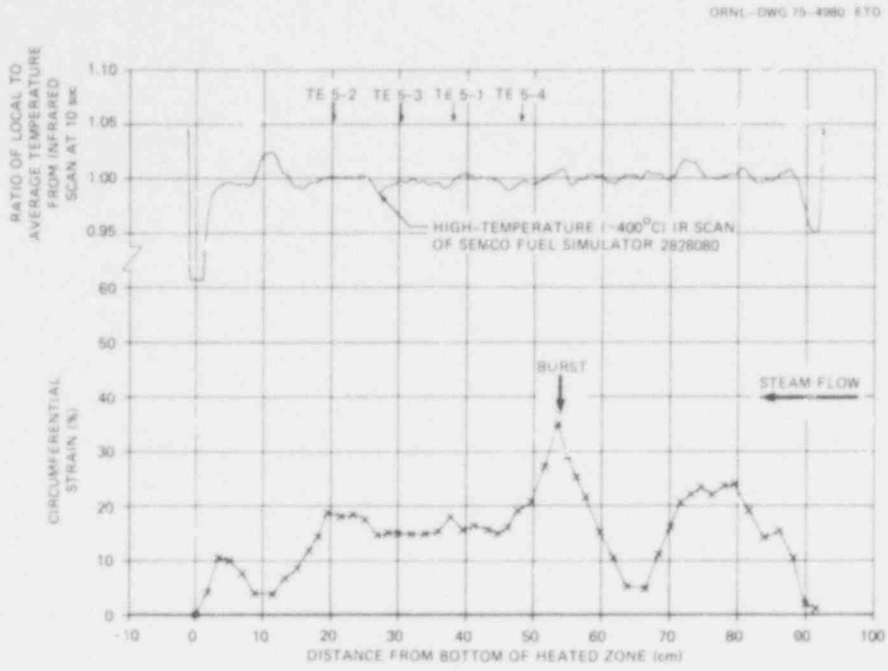

Fig. 2.53. Deformation profile of tube 5 in B-2 test.

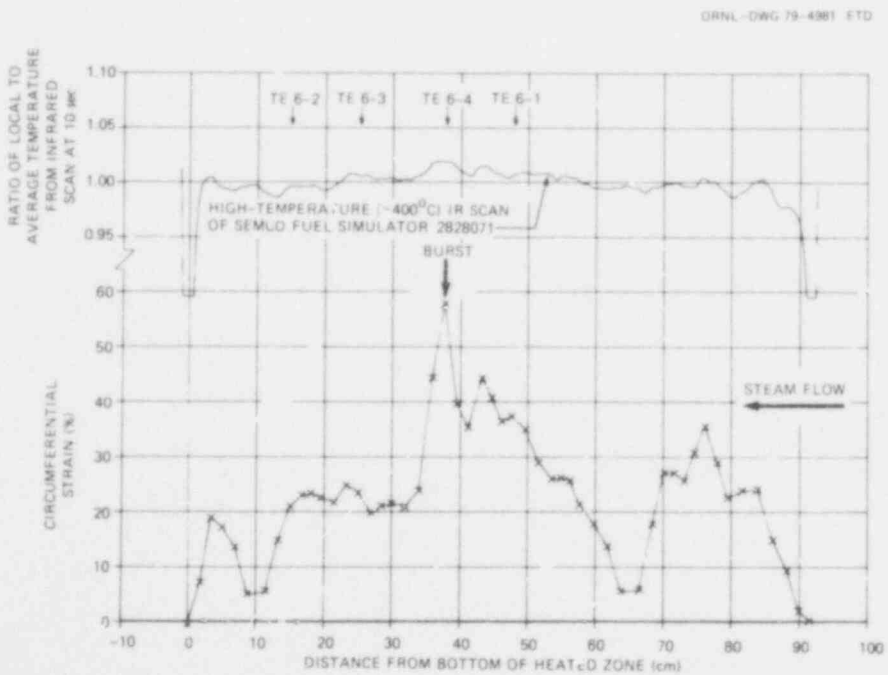

Fig. 2.54. Deformation profile of tube 6 in B-2 test.

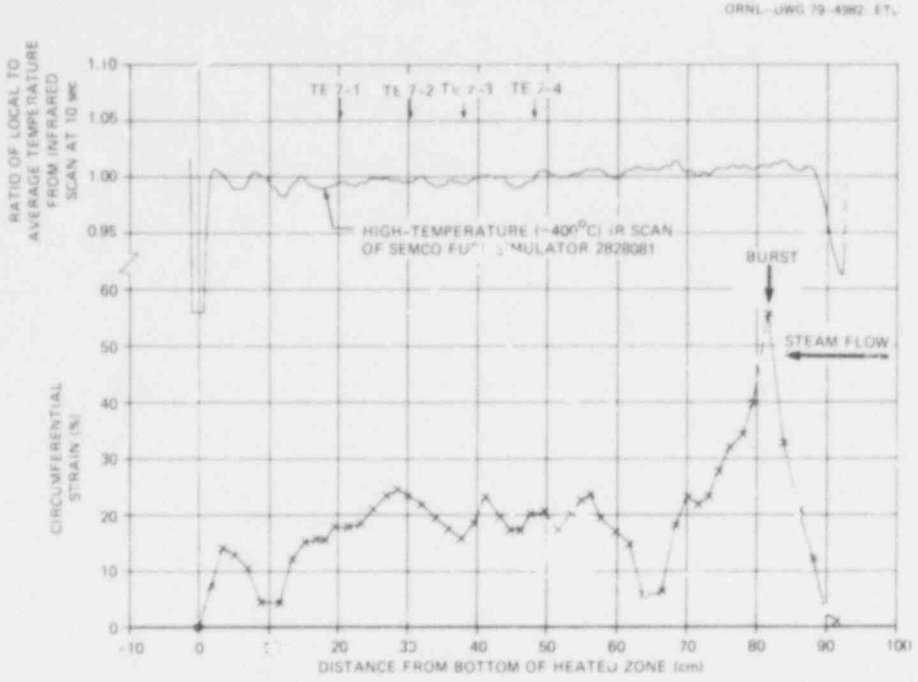

Fig. 2.55. Deformation profile of tube 7 in B-2 test.

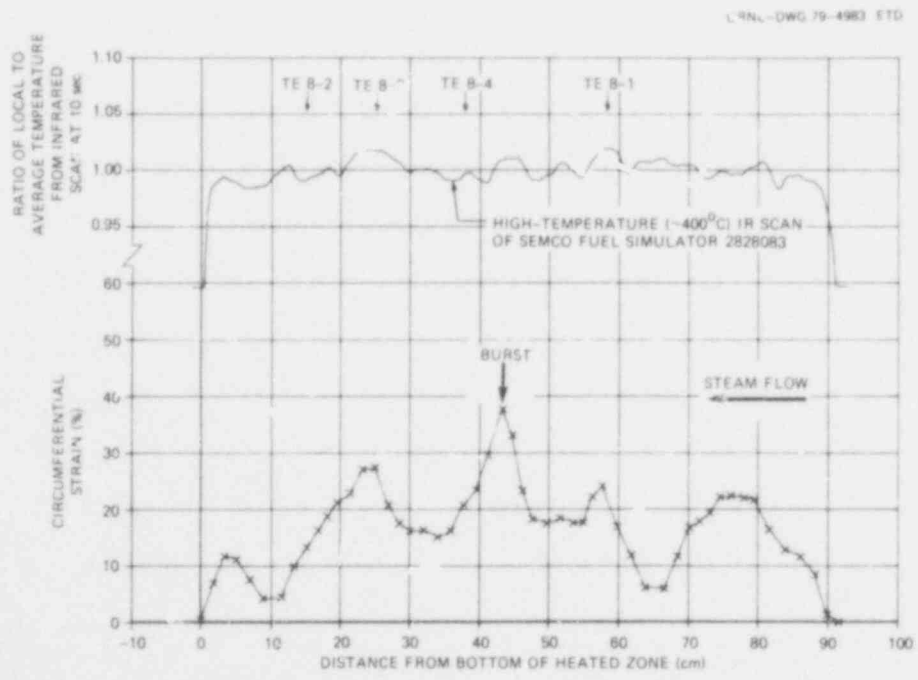

Fig. 2.56. Deformation profile of tube 8 in B-2 test.

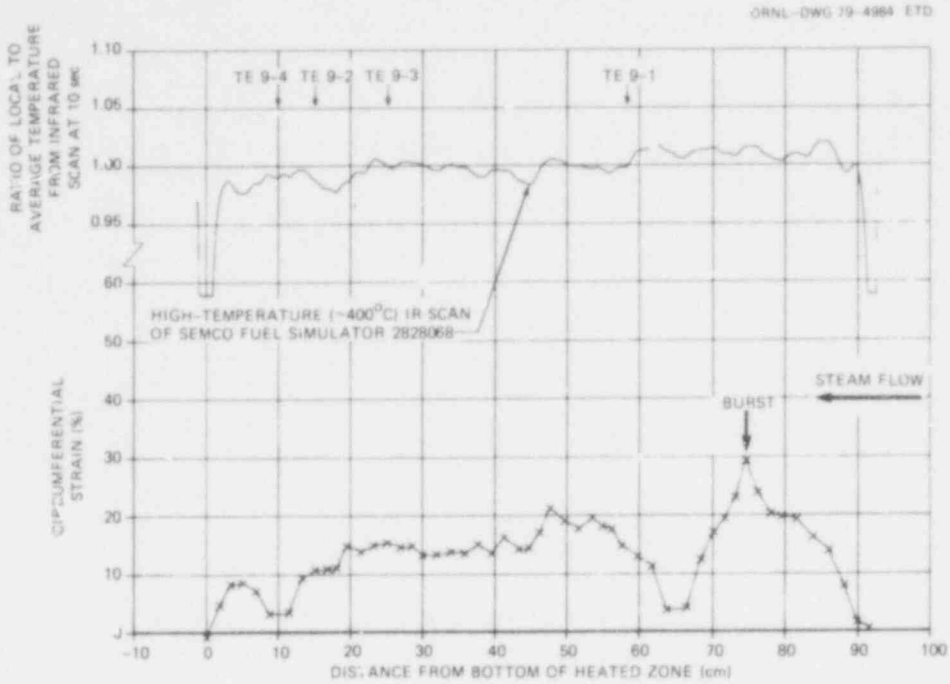

Fig. 2.57. Deformation profile of tube 9 in B-2 test.

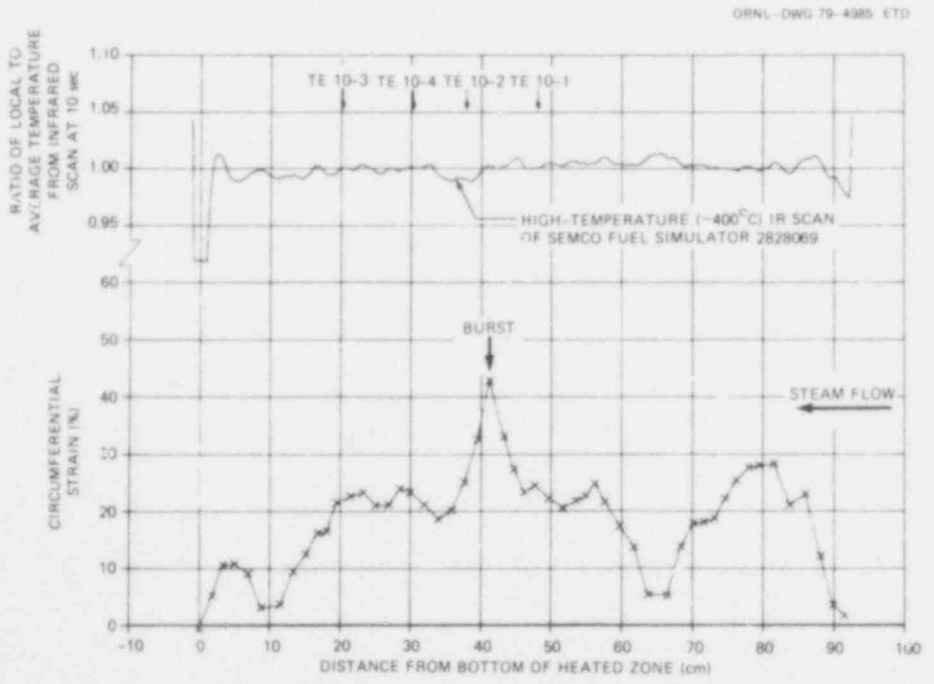

Fig. 2.58. Deformation profile of tube 10 in B-2 test.

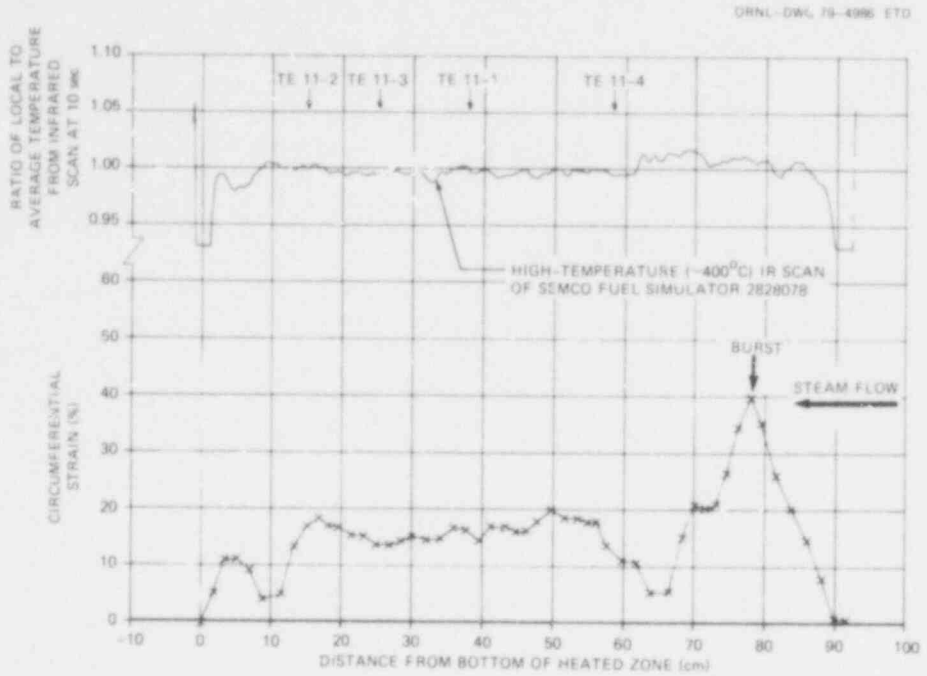

Fig. 2.59. Deformation profile of tube 11 in B-2 test.

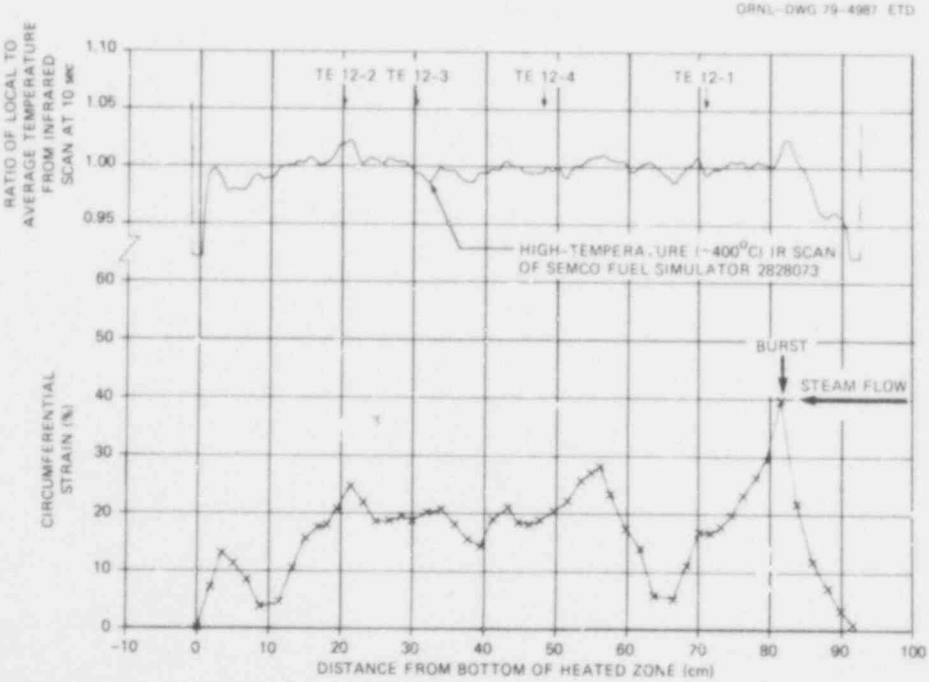

Fig. 2.60. Deformation profile of tube 12 in B-2 test.

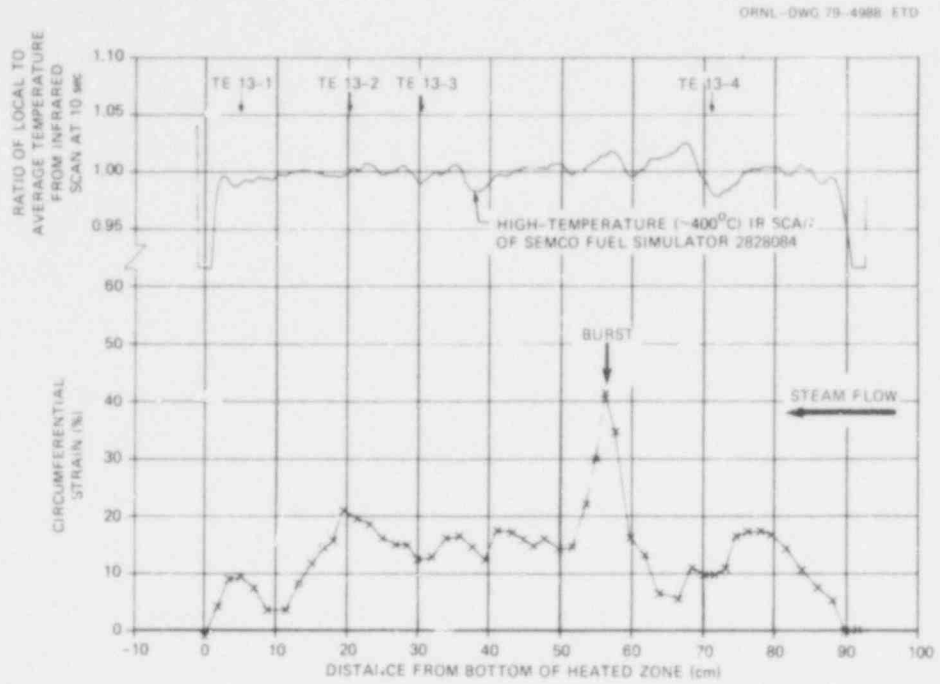

Fig. 2.61. Deformation profile of tube 13 in B-2 test.

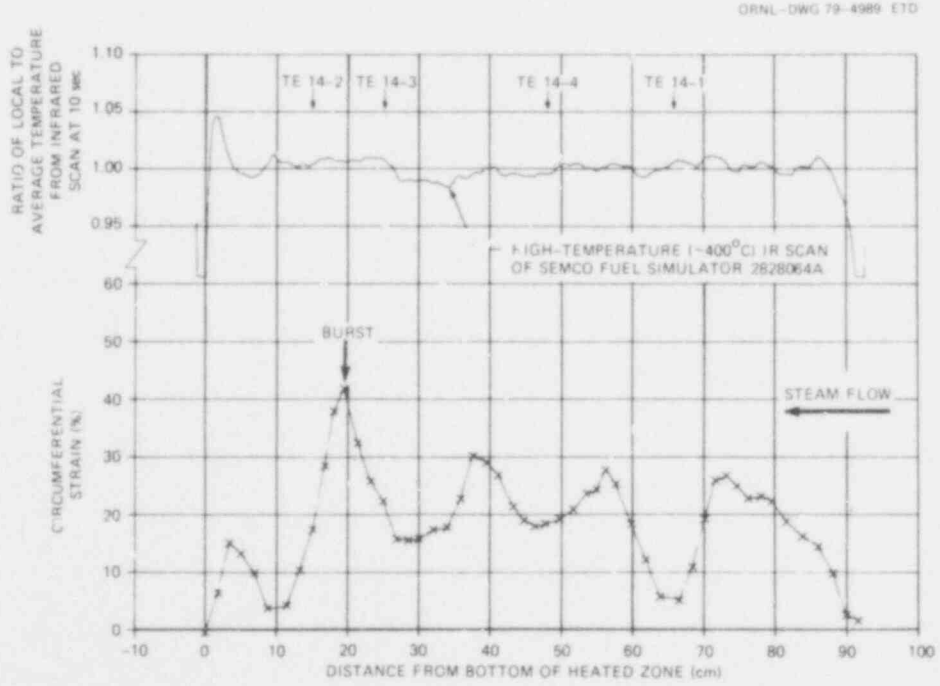

Fig. 2.62. Deformation profile of tube 14 in B-2 test.

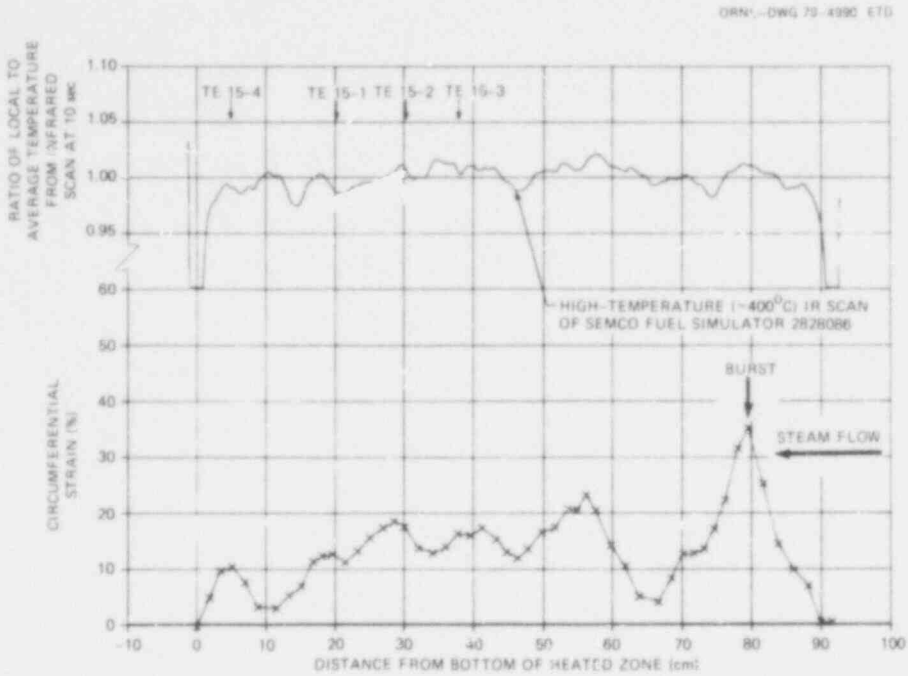

Fig. 2.63. Deformation profile of tube 15 in B-2 test.

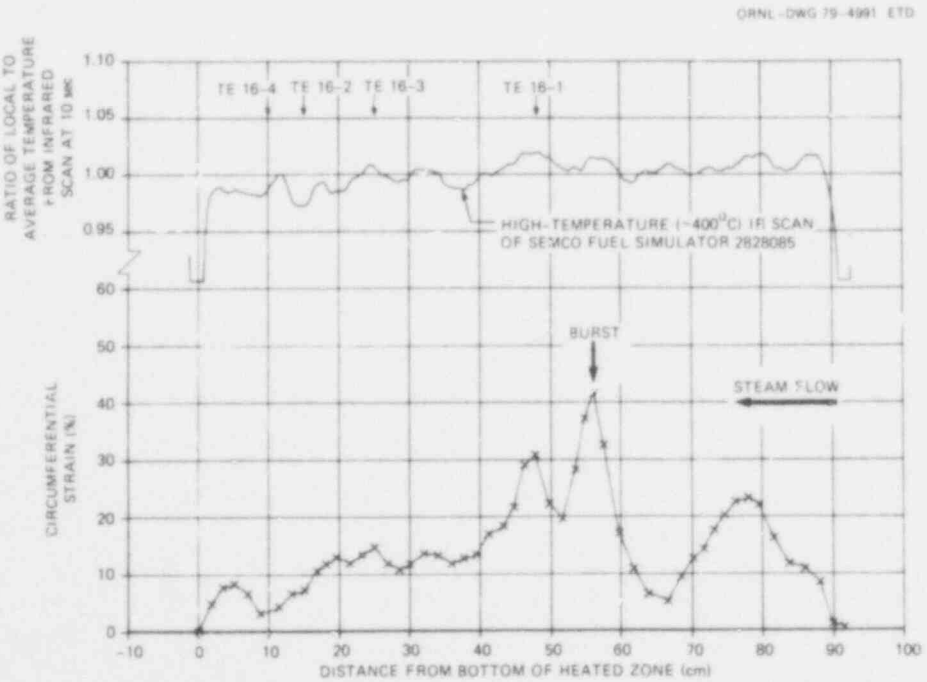

Fig. 2.64. Deformation profile of tube 16 in B-2 test.

in the B-1 and B-2 tests caused higher temperatures in this region, resulting in deformation and bursts. This was demonstrated[4] by single-rod tests performed later with the fuel simulator (internal heater) from the No. 4 rod in the B-2 test.

All the profiles show about 5% strain in the grid positions (i.e., centered at the 10- and 66-cm elevations), reflecting grid restraint on the tubes and/or higher cladding strength at the lower temperature (see Fig. 2.26) in these regions. It should be noted that these effects influence the strain significantly for about 5 cm on either side of the grid. The strain profiles show good correlation with the pretest characterization scans. Considering the facts that (1) the grids had a strong restraining effect, (2) circumferential temperature gradients are known to exist in the fuel simulators, and (3) the characterization scans are for a single angular orientation, there is generally good agreement between the scans and the burst positions. Figure 2.51 for tube 3 would appear to be a notable exception; however, the scan for an adjacent quadrant clearly shows a peak at the burst position.

Excessive ballooning over an extended length is of concern in LOCA analyses. For the tubes and spacing (10.92 mm OD on a 14.43-mm-square pitch; 1.32 pitch-to-diameter ratio) used in our tests, adjacent tubes will touch with 32% uniform expansion. Figure 2.65 plots those portions of each tube over which the strain exceeds 32%; maximum deformation in tube 9, which leaked prior to the transient, was less than this value, as indicated in Fig. 2.57. In tube 6, greater than 32% expansion occurred over a length equal to about 15 tube (original) diameters; all the rest were relatively short (i.e., less than 7 tube diameters in length).

The volume increase over the heated length is perhaps a more meaningful characterization of the deformation with respect to coolant flow restriction. This parameter is related to (about a factor of 2 greater than) the average deformation and was obtained by integrating the individual deformation profiles, assuming circular cross sections. Table 2.7 summarizes the data and gives other characterizations for comparison with the B-1 test (see Table 2.3). The B-2 strain data are compared to the B-1 and single-rod test data in Section 2.5.

Table 2.7. Characterization of B-2 tube failures

Rod No.	Initial gas volume[a] (cm^3)	Approximate burst condition			Fractional[b] pressure decrease	Fractional[c] volume increase	Volume increase[d] of tube over heated length (%)	Average strain[e] (%)
		Pressure (kPa)	Temperature (°C)	Strain (%)				
1	48.5	7700	870	35	1.14	1.56	31.8	[illegible]
2	49.7	7685	846	39	1.15	1.57	33.2	15
3	48.8	7560	853	40	1.16	[illegible]	42.0	19
4	49.4	7585	872	42	1.16	1.62	35.8	17
5	49.5	7770	866	35	1.13	1.56	32.6	15
6	48.9	6925	857	58	1.27	1.91	51.8	23
7	51.0	7360	861	56	1.19	1.69	41.2	19
8	49.5	7565	856	38	1.16	1.62	36.0	17
9[f]	48.9	6110[f]	928[f]	29[f]	1.25[f]	1.50[f]	28.7[f]	13[f]
10	49.8	7345	862	43	1.19	1.70	40.9	19
11	48.8	7670	853	40	1.14	1.59	33.4	15
12	50.1	7545	851	40	1.16	1.63	36.9	17
13	48.6	7820	867	41	1.12	1.52	29.4	14
14	49.1	7230	858	42	1.21	1.71	40.9	19
15	49.6	7945	836	35	1.11	1.49	28.5	13
16	48.5	7700	848	42	1.14	1.56	31.7	15

[a] Measured at room temperature; includes fuel pin simulator (FPS), pressure transducer, and connecting tube.

[b] Ratio of initial pressure to burst pressure.

[c] Ratio of final to initial gas volume; includes FPS, pressure transducer, and connecting tube.

[d] Obtained from deformation profiles assuming circular cross sections.

[e] Assumes volume increase is uniformly distributed over heated length.

[f] Tube developed moderate leak prior to transient; deformation behavior is abnormal.

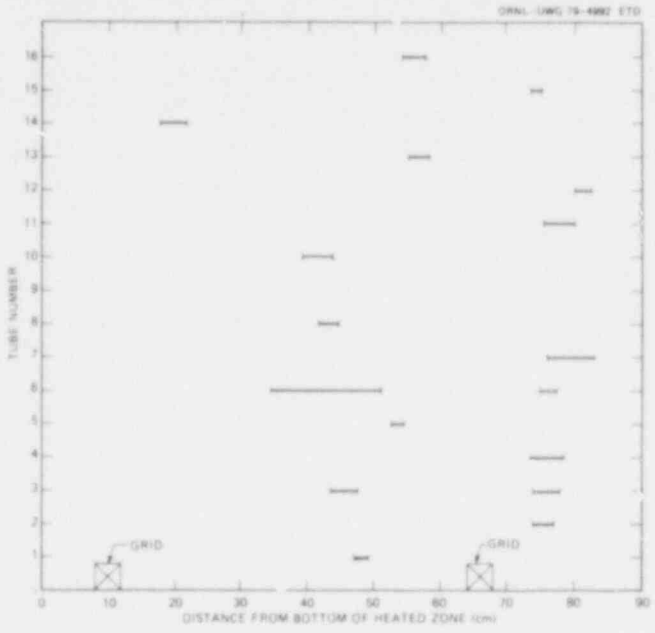

Fig. 2.65. Portions of tubes with greater than 32% strain in B-2 test.

The locations of the individual tube bursts are tabulated in Table 2.8; axial and angular distributions are depicted graphically in Figs. 2.66 and 2.67, respectively. A composite layout of the bursts, in which the tube-to-tube pitch is greatly exaggerated for clarity, is shown in Fig. 2.68. The angular orientations were difficult to determine from the burst cross sections; however, a study of the positions of maximum wall thinning in adjacent cross sections provided additional information to aid in defining the orientations. Thus, the data given in Table 2.8 are our best estimates of the burst locations. The orientation of the bursts in the outer ring of tubes appeared to be influenced by the relatively cold shroud, as discussed below.

Figures 2.67 and 2.68 show that the burst orientations of the inner ring of tubes were generally directed outward, while those in the outer ring of tubes were generally directed inward or toward adjacent tubes; none of the bursts were directed toward the shroud. This suggests that the relatively cold shroud had an effect on localizing wall thinning toward the interior of the bundle. Enlarged (~5X) photographs of the B-2 cross sections were examined in the same manner as the B-1 cross

Table 2.8. Summary of B-2 burst data

Rod No.	Burst characteristics		Approximate position		Fig. No. in which burst appears
	Temperature (°C)	Strain (%)	Elevation[a] (cm)	Angle[b] (deg)	
1	870	35	47.7	135	2.41
2	840	39	76.2	115	2.45
3	853	40	76.2	85	2.45
4	872	42	76.2	180	2.45
5	866	35	53.5	165	2.42
6	857	58	37.7	220	2.36
7	861	56	81.6	350	2.48
8	856	38	43.3	280	2.39
9[c]	928[c]	29[c]	74.6	45	2.44
10	862	43	41.2	190	2.38
11	853	40	78.0	20	2.46
12	851	40	81.6	295	2.48
13	867	41	56.2	100	2.43
14	858	42	19.5	65	2.33
15	836	35	79.5	15	2.47
16	848	42	56.2	255	2.43

[a]Elevation above bottom of heated zone.

[b]Looking down on bundle and measured clockwise from bundle north.

[c]Tube developed moderate leak prior to transient; deformation behavior was abnormal.

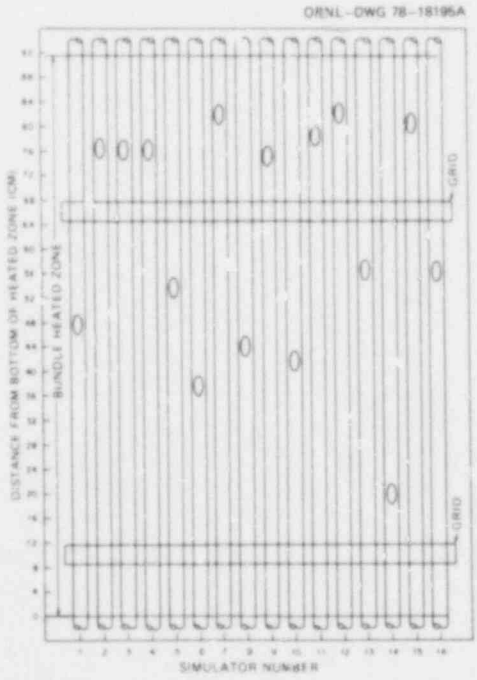

Fig. 2.66. Axial distribution of bursts in B-2 test.

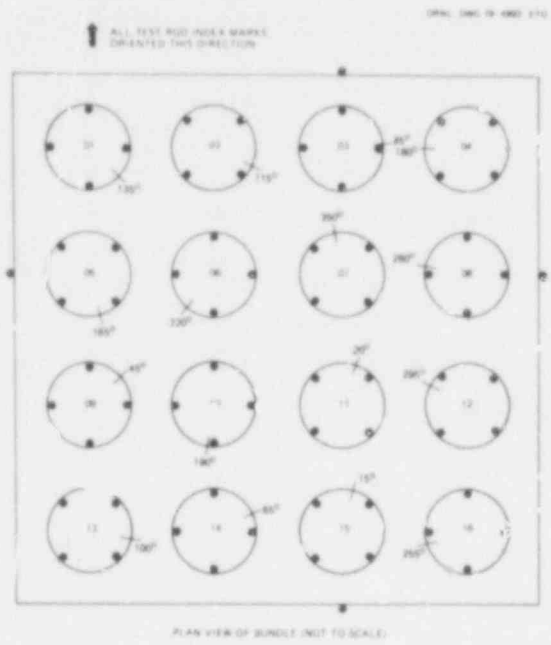

Fig. 2.67. Angular distribution of bursts in B-2 test.

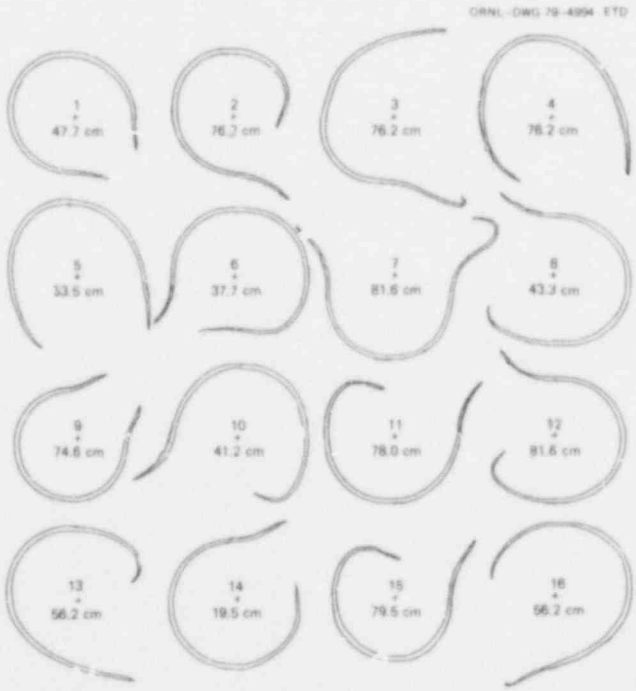

Fig. 2.68. Composite layout of burst orientations in B-2 test. Tube-to-tube pitch greatly exaggerated for clarity. Axial locations of burst are noted.

sections discussed in Section 2.3. The positions of maximum wall thinning were identified and correlated according to the view sectors and nomenclature of Figs. 2.19 through 2.21. The observations totaled 51, 121, and 43 for rod types I, II, and III, respectively. Figure 2.69 shows the percentage of these totals occurring in each of the eight sectors. As was the case with the B-1 array, the distribution of the thinned areas agreed with the burst directions (compare Figs. 2.67, 2.68, and 2.69), indicating an axial extension of the thinning at the same circumferential positions as the bursts.

The unheated shroud in the B-2 test apparently caused the positions of thinning and bursts to be biased, as evidenced by Fig. 2.69, which shows an almost complete lack of thinning (or bursts) in those view sectors of rod types I and II that face the shroud. For example, 60% of rod type I surface area faces the shroud, yet only 10% of the wall thinning observations were contained in these sectors. For rod type II, 35% of the surface area faces the shroud, but only 6% of the wall thinning observations were contained in these sectors.

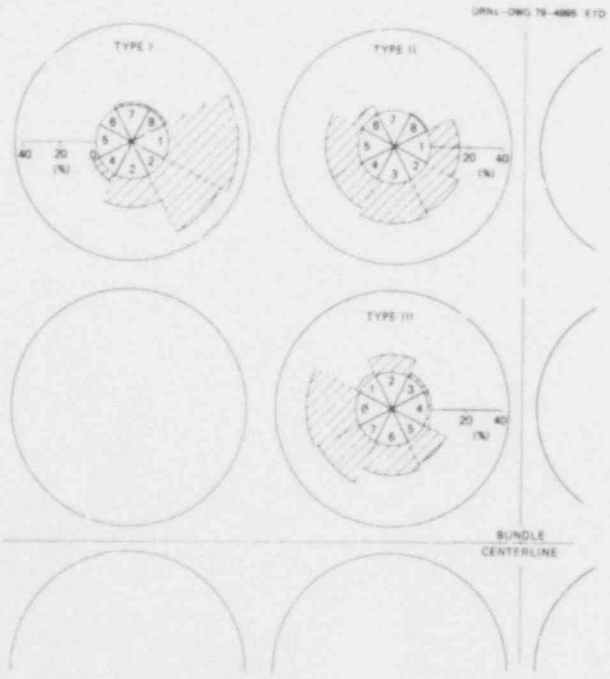

Fig. 2.69. Distribution of maximum wall thinning observations by view sector for the three rod types in B-2 test array.

As evident from the above discussion and the deformation profiles for the individual tubes (Figs. 2.49 through 2.64), significant deformation was observed at a number of points. However, the total expansion for all the tubes at any cross section is much more important, since it determines the restriction in the coolant channel flow area.

One method for calculating the restriction in the coolant channel flow area is to consider unit cells centered about the open space between fuel rods; an alternative method considers unit cells centered about the fuel rods. Obviously, both methods give the same result for infinite arrays, but for small test arrays, different results will be obtained. We calculated the percentage of coolant channel flow area restriction with the rod-centered unit cell method, using the equation

$$B = 100 \times \frac{\sum_{n=1}^{n=16} (A_{d,n} - A_o)}{16\ (p^2 - A_o)} .$$

where

B = percentage of restriction in coolant channel flow area,

$A_{d,n}$ = outside area of deformed tube (mm^2),

A_o = outside area of original tube (mm^2),

p = tube-to-tube pitch in square array (mm).

With this definition, B is zero for no deformation and 100 if all the tubes deform into a square whose sides are of length p (completely filling the open area). For the case of uniform ballooning such that the tubes just come into contact (i.e., 32% strain for the dimensions appropriate to this test), B is 61%.

In summing the deformed tube areas in the above equation for those sections that contain bursts, one must decide how to treat the burst tube flare-out. We used two definitions that appear to be reasonable upper and lower limits of the coolant channel flow area restriction. The first definition, which we believe is representative of the upper limit, consists of drawing straight lines between the ends of the tube flare-outs to establish a burst tube area, as illustrated in Fig. 2.70. Special consideration was given to those flare-outs that enclosed adjacent tubes to

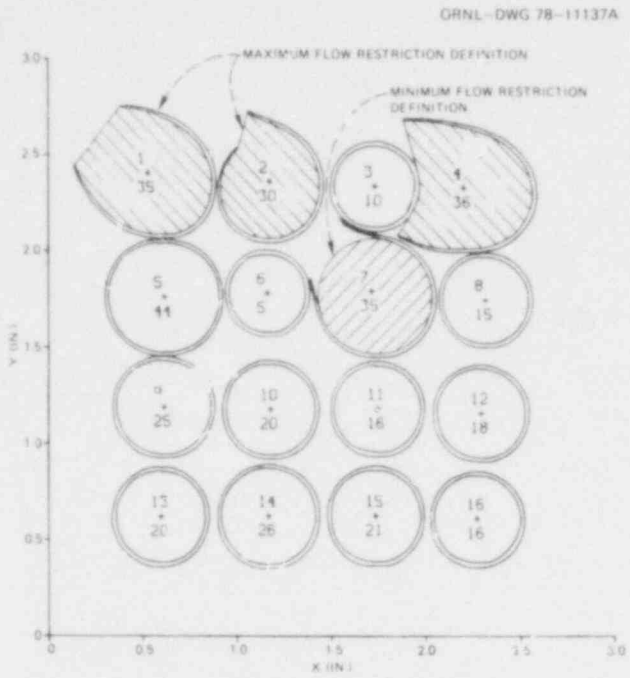

Fig. 2.70. An example of a computer simulation of a bundle cross section showing the definitions for maximum and minimum flow restrictions for burst tubes.

exclude overlapping areas, as noted by tube 4 in the figure. The second definition, which we believe is representative of the lower limit, considered the burst tube cross section as a circle with a perimeter equal to that of the tube. The latter definition is considered a reasonable approximation of the tube just before burst.

The deformed tube areas were obtained by the data analysis techniques reported[3] for the B-1 test. Table 2.9 gives the deformed tube areas, $A_{d,n}$, for each tube at each section based on the first definition for the burst tube area, and Table 2.10 gives similar information based on the second definition. The last column (on the right side) gives the summation of the individual $A_{d,n}$. The summed areas were used in the above equation to calculate the coolant channel flow area restriction at each section; the results are given in Table 2.11 and plotted in Fig. 2.71 as a function of heated length. The flow channel restriction differs only in the sections where tube bursts occurred. The cross-sectional area occupied by the grids ($\sim$47 mm^2) was not included in the calculation;

Table 2.9. Upper limit of B-2 deformed tube areas (mm^2)

Elevation (cm)	Tube No.																
	1	2	3	4	5	6	7	8	9	10	11	12	13	14	15	16	TOTAL
0.0	93	93	93	94	93	92	93	94	92	92	92	93	91	92	92	93	1490
1.8	102	104	105	104	101	107	107	106	102	103	103	107	101	105	102	102	1670
3.4	114	115	117	114	114	132	121	116	109	114	115	119	111	123	112	108	1862
5.0	114	116	115	116	113	128	119	115	110	114	115	115	111	119	114	109	1850
6.9	110	112	109	108	108	120	114	108	107	111	111	110	107	112	108	106	1767
8.8	102	103	101	101	100	103	101	101	99	99	101	100	100	100	99	99	1616
11.5	100	101	101	102	100	104	101	102	100	100	102	102	100	101	99	101	1622
13.3	110	108	111	108	106	123	117	112	111	112	119	114	109	113	103	106	1791
15.1	120	116	116	112	110	136	124	119	114	118	127	125	116	128	106	107	1902
16.8	124	126	122	116	116	141	125	126	115	126	131	129	122	154	115	114	2009
18.1	125	130	129	119	122	142	125	131	115	127	126	130	125	177	118	116	2065
19.5	133	133	134	121	131	140	130	137	123	138	127	136	136	233	118	119	2195
21.4	134	129	134	114	130	138	130	141	121	140	124	145	133	164	115	117	2115
23.2	133	126	138	112	131	145	131	151	123	142	123	139	131	148	119	120	2118
25.0	126	121	144	115	129	142	137	152	1[illegible]	137	120	131	126	140	124	123	2096
26.9	124	116	148	120	122	134	142	136	122	137	120	132	123	125	128	117	2054
28.5	127	118	157	127	123	137	145	129	123	143	122	133	123	124	131	114	2083
30.0	123	118	164	131	123	133	142	126	120	142	124	132	118	125	129	116	2076
32.0	118	124	153	134	3	136	138	126	120	137	122	125	119	128	121	120	2060
34.0	116	124	139	129	3	143	133	123	121	121	123	136	126	129	119	119	2042
35.9	115	130	138	121	4	194	129	126	120	134	127	130	127	140	121	116	2105
37.7	120	131	143	120	0	248	125	136	123	146	126	124	122	158	126	118	2205
39.5	117	123	135	121	5	182	131	142	120	164	122	122	118	155	125	120	2128
41.2	132	125	143	125	6	171	141	157	126	256	127	132	129	150	128	127	2302
43.3	139	125	156	128	125	194	133	259	122	165	127	137	128	137	124	131	2338
44.7	142	123	177	131	123	185	128	165	122	151	126	131	125	132	119	138	2225
46.2	152	128	179	134	126	174	128	147	128	142	126	130	123	130	117	155	2218
47.7	204	132	160	134	132	176	135	130	137	145	129	132	125	131	120	160	2288
49.7	155	133	138	132	136	170	136	129	132	135	134	135	122	133	127	139	2196
51.6	136	134	126	142	151	155	128	131	129	136	131	139	122	136	129	133	2166
53.5	130	134	133	156	261	148	134	129	133	138	130	147	139	142	136	153	2352
54.9	132	139	133	151	155	148	140	129	130	140	129	151	158	144	135	175	2296
56.2	136	146	137	151	146	147	143	139	129	145	129	157	253	152	142	271	2527
57.6	128	140	138	153	138	137	133	144	123	138	120	142	169	146	135	164	2254
59.8	120	123	131	143	123	129	127	127	119	128	115	129	126	130	121	128	2027
61.8	115	113	118	118	114	120	123	117	115	120	114	121	119	117	114	114	1881
63.8	103	103	103	105	103	104	104	105	100	103	103	104	105	104	103	105	1665
66.5	102	102	103	106	102	104	105	104	101	103	104	103	104	103	101	103	1658
68.4	113	115	120	114	115	129	130	116	118	121	123	115	115	114	109	111	1886
70.1	123	130	134	125	126	151	1[illegible]	127	128	125	136	127	112	132	118	118	2065
71.6	123	139	137	138	136	151	138	129	133	130	135	127	112	148	119	122	2124
73.1	126	146	145	159	139	147	141	133	141	131	136	129	114	150	120	129	2195
74.6	138	165	174	177	142	159	152	139	184	139	149	134	127	145	128	135	2394
76.2	142	203	264	288	139	171	162	139	143	146	168	141	128	140	139	140	2663
78.0	144	155	166	166	143	155	168	139	135	152	228	149	128	141	161	141	2478
79.5	141	136	140	151	143	140	182	138	134	153	170	156	127	139	189	139	2384
81.6	128	130	127	149	132	143	295	126	132	154	148	228	122	131	146	126	2425
83.8	116	125	125	132	121	143	164	119	126	137	135	138	114	12[illegible]	122	116	2066
86.0	109	121	118	119	124	123	136	116	121	141	122	117	108	122	112	114	1930
88.1	106	109	105	108	113	111	117	109	108	117	108	107	10[illegible]	112	106	109	1758
89.9	95	96	96	99	97	97	98	95	96	100	94	99	93	98	94	95	1550
91.5	94	94	95	95	95	93	95	93	94	96	94	95	93	96	94	94	1518

Table 2.10. Lower limit of B-2 deformed tube area (mm^2)

Elevation (cm)	Tube No.																
	1	2	3	4	5	6	7	8	9	10	11	12	13	14	15	16	TOTAL
0.0	93	93	93	94	93	92	93	94	92	92	92	93	91	92	92	93	1490
1.8	102	104	105	104	101	107	107	106	102	103	103	107	101	105	102	102	1670
3.4	114	115	117	114	114	132	121	116	109	114	115	119	111	123	112	108	1862
5.0	114	116	115	116	113	128	119	115	110	114	115	115	111	119	114	109	1850
6.9	110	112	109	108	108	120	114	108	107	111	111	110	107	112	108	106	1767
8.8	102	103	101	101	100	103	101	101	99	99	101	100	100	100	99	99	1616
11.5	103	101	101	102	100	104	101	102	100	100	102	102	100	101	99	101	1622
13.3	110	108	111	108	106	123	117	112	111	112	119	114	109	113	103	106	1791
15.1	120	116	116	112	110	136	124	119	114	118	127	125	116	128	106	107	1902
16.8	124	126	122	116	116	141	125	126	115	126	131	129	122	154	115	114	2009
18.1	125	130	129	119	122	142	125	131	115	127	128	130	125	177	118	116	2065
19.5	133	133	134	121	131	140	130	137	123	138	127	136	136	188	118	119	2150
21.4	134	129	134	114	130	138	130	141	121	140	124	145	133	164	115	117	2115
23.2	133	126	138	112	131	145	131	151	123	142	123	139	131	148	119	120	2118
25.0	126	121	144	115	129	142	137	152	124	137	120	131	126	140	124	123	2096
26.9	124	116	148	120	122	134	142	136	122	137	120	132	123	125	128	117	2054
28.5	127	118	157	127	123	137	145	129	123	143	122	133	123	124	131	114	2083
30.0	123	118	164	131	123	138	142	126	120	142	124	132	118	125	129	116	2076
32.0	118	124	153	134	123	136	138	126	120	137	122	135	119	128	121	120	2060
34.0	116	124	139	129	123	143	133	123	121	131	123	136	126	129	119	119	2042
35.9	119	130	138	121	124	194	129	126	120	134	127	130	127	140	121	116	2105
37.7	120	131	143	120	130	233	125	136	123	146	126	124	122	158	126	118	2190
39.5	117	123	135	121	125	182	131	142	120	164	122	122	118	155	125	120	2128
41.2	132	125	143	125	126	171	141	157	126	191	127	132	129	150	128	127	2237
43.3	139	125	156	128	125	194	133	177	122	165	127	137	128	137	124	131	2256
44.7	142	123	177	131	123	185	128	165	122	151	126	131	125	132	119	138	2225
46.2	152	128	179	134	126	174	128	142	128	142	126	130	123	130	117	155	2218
47.7	169	132	160	134	132	176	135	130	137	145	129	132	125	131	120	160	2253
49.7	155	133	138	132	136	170	136	129	132	135	134	135	122	133	127	139	2196
51.6	136	134	126	142	151	155	128	131	129	136	131	139	122	136	129	133	2166
53.5	130	134	133	156	170	148	134	129	133	138	130	147	139	142	136	153	2261
54.9	132	139	133	151	155	148	140	129	130	140	129	151	158	144	135	175	2296
56.2	136	146	137	151	146	147	143	139	129	145	129	153	187	152	142	188	2378
57.6	128	140	138	153	138	137	133	144	123	138	120	142	169	146	135	164	2254
59.8	120	123	131	143	123	129	127	127	119	128	115	129	127	130	121	128	2027
61.8	115	113	118	118	114	120	123	117	115	120	114	121	119	117	114	114	1881
63.8	103	103	103	105	103	104	104	105	100	103	103	104	105	104	103	105	1665
66.5	102	102	103	106	102	104	105	104	101	103	104	103	104	103	101	103	1658
68.4	113	115	120	114	115	129	130	116	118	121	123	115	115	114	109	111	1886
70.1	123	130	134	125	126	151	141	127	128	125	136	127	112	132	118	118	2065
71.6	125	139	137	138	136	151	138	129	133	130	135	127	112	148	119	122	2124
73.1	125	146	145	159	139	147	141	133	141	131	136	129	114	150	120	129	2195
74.6	138	165	174	177	142	159	152	139	156	139	149	134	127	145	128	135	2366
76.2	142	179	184	188	139	171	162	139	143	146	168	141	128	140	139	140	2459
78.0	144	155	166	166	143	155	168	139	135	152	183	149	128	141	161	141	2432
79.5	141	136	140	151	143	140	182	138	134	153	170	156	127	139	170	139	2366
81.6	128	130	127	149	132	143	226	126	132	154	148	182	122	131	146	126	2311
83.8	116	125	125	132	121	143	164	119	126	137	135	138	114	126	122	116	2066
86.0	109	121	118	119	124	123	136	116	121	141	122	117	103	122	112	114	1930
88.1	106	109	105	108	113	111	117	109	108	117	108	107	103	112	106	109	1758
89.9	95	96	96	99	97	97	98	95	96	100	94	99	93	98	94	95	1550
91.5	94	94	95	95	95	93	95	93	94	96	94	95	93	96	94	94	1518

Table 2.11. B-2 coolant channel restriction

Elevation (cm)	Upper limit (%)	Lower limit (%)
0.0	-0.5	-0.5
1.8	9.4	9.4
3.4	19.9	19.9
5.0	19.2	19.2
6.9	14.7	14.7
8.8	6.4	6.4
11.5	6.7	6.7
13.3	16.0	16.0
15.1	22.0	22.0
16.8	27.9	27.9
18.1	30.9	30.9
19.5	38.0	35.6
21.4	33.6	33.6
23.2	33.8	33.8
25.0	32.7	32.7
26.9	30.3	30.3
28.5	31.9	31.9
30.0	31.5	31.5
32.0	30.7	30.7
34.0	29.7	29.7
35.9	33.1	33.1
37.7	38.6	37.7
39.5	34.4	34.4
41.2	43.9	40.3
43.3	45.8	41.3
44.7	39.7	39.7
46.2	39.3	39.3
47.7	43.1	41.2
49.7	38.1	38.1
51.6	36.5	36.5
53.5	46.6	41.7
54.9	43.6	43.6
56.2	56.2	48.0
57.6	41.2	41.2
59.8	28.9	28.9
61.8	20.9	20.9
63.8	9.1	9.1
66.5	8.7	8.7
68.4	21.2	21.2
70.1	31.0	31.0
71.6	34.2	34.2
73.1	38.0	36.0
74.6	48.9	47.4
76.2	63.6	52.5
78.0	53.5	51.0
79.5	48.4	47.4
81.6	50.6	44.4
83.8	31.0	31.0
86.0	23.6	23.6
88.1	14.2	14.2
89.9	2.8	2.8
91.5	1.1	1.1

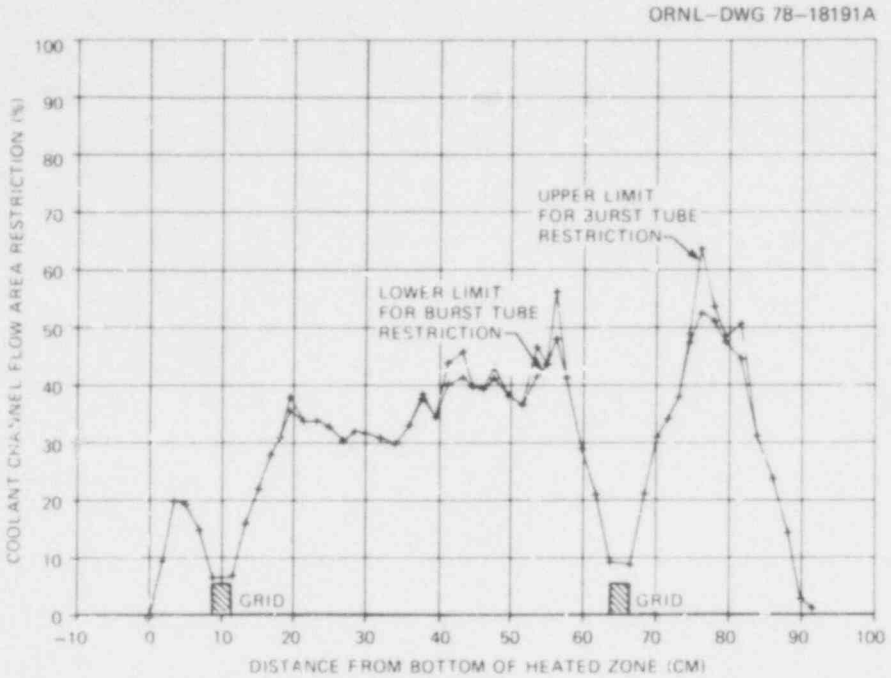

Fig. 2.71. Coolant channel flow area restriction in B-2 based on a rod-centered unit cell and estimated upper and lower limits of burst tube flow restriction.

including this area would slightly increase the restriction at the grid locations (centered about elevations 10 and 66 cm). The maximum restriction (at elevation 76.2 cm) was 64 or 53%, depending on which method for handling the tube flare-out was used.

2.5 Comparison of B-1 and B-2 Results

D. O. Hobson* R. H. Chapman

The first two bundle tests were quite similar in many respects, and the results were, indeed, comparable on the bases of the major parameters by which bundle behavior is measured. Table 2.12 compares the conditions and results for B-1 and B-2.

The main difference between the two tests was that the shroud was electrically heated in B-1 and not in B-2. This resulted in the temperature differences shown in the last line of the table, but caused no

*Metals and Ceramics Division.

Table 2.12. Comparison of B-1 and B-2 tests

	B-1	B-2
Bundle heating rate,[a] °C/sec	30.1	29.9
Shroud heating rate,[a] °C/sec	20.0	7.7[b]
Inlet steam temperature, °C	349	332
Inlet steam Reynolds number	250	290
Initial temperature, °C	356	334
Initial pressure, kPa	8680	8770
Maximum pressure, kPa	9100	9200
Burst pressure, kPa	7425	7560
Burst temperature, °C	865	857
Burst time, sec	17.0–17.6	17.8–18.3
Burst strain, %	32–59	34–58
Tube volume increase, %	27–55	28–52
$T_{Bundle} - T_{Shroud}$ at burst time, °C	134	355

[a]Average rate between 3 and 15 sec after power-on. See Sections 2.3 and 2.4 for discussion and additional details.

[b]Produced by heat lost from the bundle, since the shroud was not electrically heated in this test.

apparent differences in the test results — at least not in those shown in the table. It became apparent from further analysis of the tests, however, that there were differences. For discussion purposes, an arbitrary distinction has been made between "macro-effects" (i.e., those that characterize the gross behavior) and "micro-effects" (i.e., those which do not appear to influence the gross behavior), and these terms will be used throughout this comparison. The macro-effects, comprising the major test results (see Table 2.13), did not differ significantly in the two tests, but the micro-effects, which are considered secondary results, did differ in the two tests. Both "micro" and "secondary" imply that these results are less important than the "macro" or "primary" results.

Table 2.13. Characterization of B-1 and B-2 test results

Macro-effects	Micro-effects
Burst temperature	Burst direction
Burst pressure	Wall thinning direction
Burst strain	Correlation of thinning and burst directions
Tube volume increase	
Flow restriction	

While this may be true, we do not at present know what importance to assign to burst direction and deformation distribution results.

The burst temperature vs burst pressure results were almost identical for B-1 and B-2 and agreed well with the single-rod correlation, as shown in Fig. 2.72. The majority of bursts were clustered together on the 28°C/sec curve developed from the single-rod results. The two outlying points are from rods that leaked during testing.

The range of burst strains measured in the B-1 and B-2 tests was also in good agreement. Figure 2.73 illustrates the strain results and compares them with single-rod results from tests with an unheated shroud. There is considerable scatter in the bundle test results, and in both cases the strains were greater than those observed in single-rod tests.

The volume increases (related to average strain) of the heated lengths of the tubes in tests B-1 and B-2 were approximately the same, as shown in Fig. 2.74, and were greater than the corresponding single-rod data for the same heating rate.

The final macro-effect to be compared is the coolant channel flow area restriction for the two tests. This parameter represents the total bundle deformation, as discussed in Section 2.4. Comparisons for the minimum and maximum flow restriction definitions are shown in Figs. 2.75 and 2.76, respectively. Although the curves in each figure differ in detail, the average flow restrictions were quite close. This statement

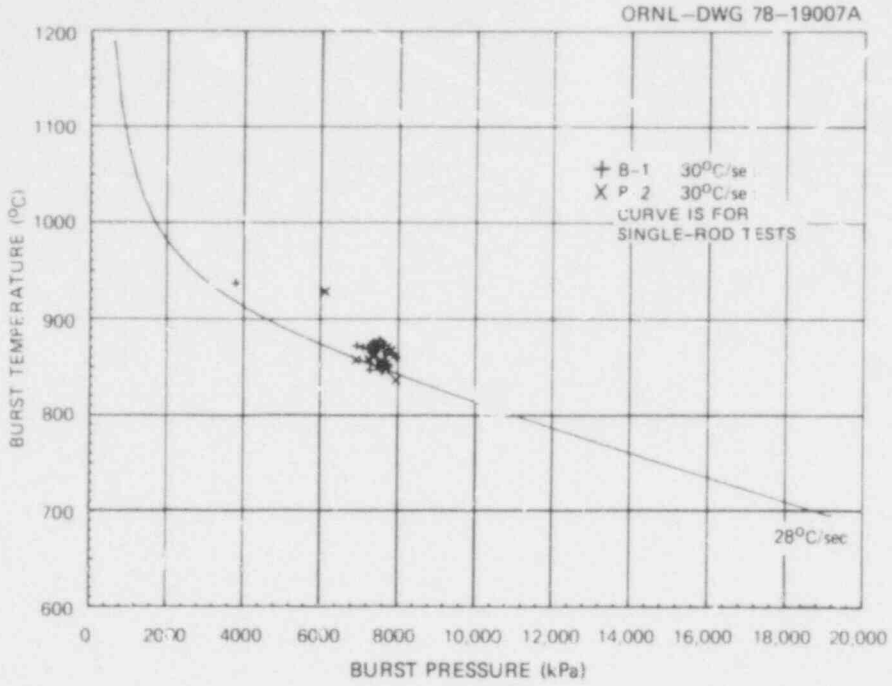

Fig. 2.72. Comparison of burst temperature and pressure results for B-1 and B-2 tests.

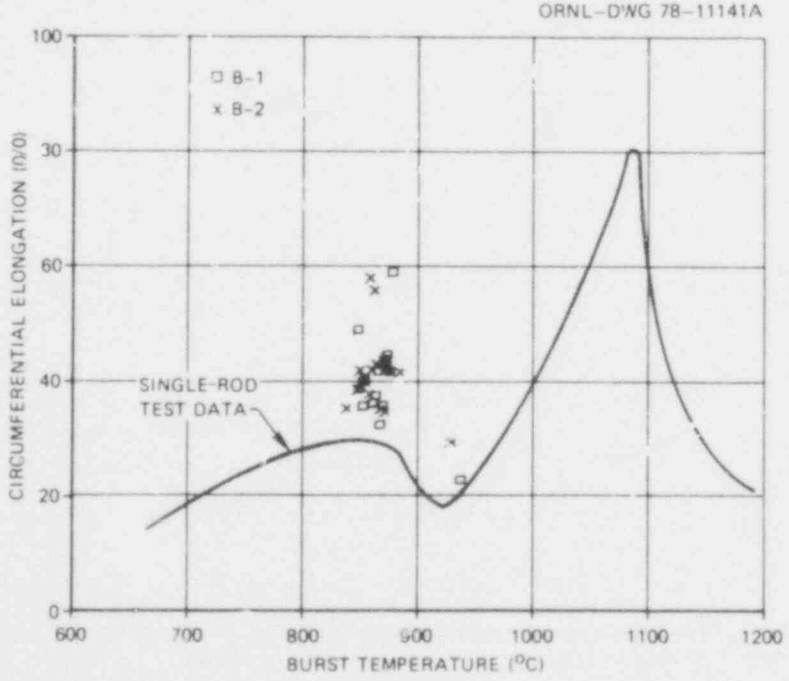

Fig. 2.73. Comparison of burst strain results for B-1 and B-2 tests.

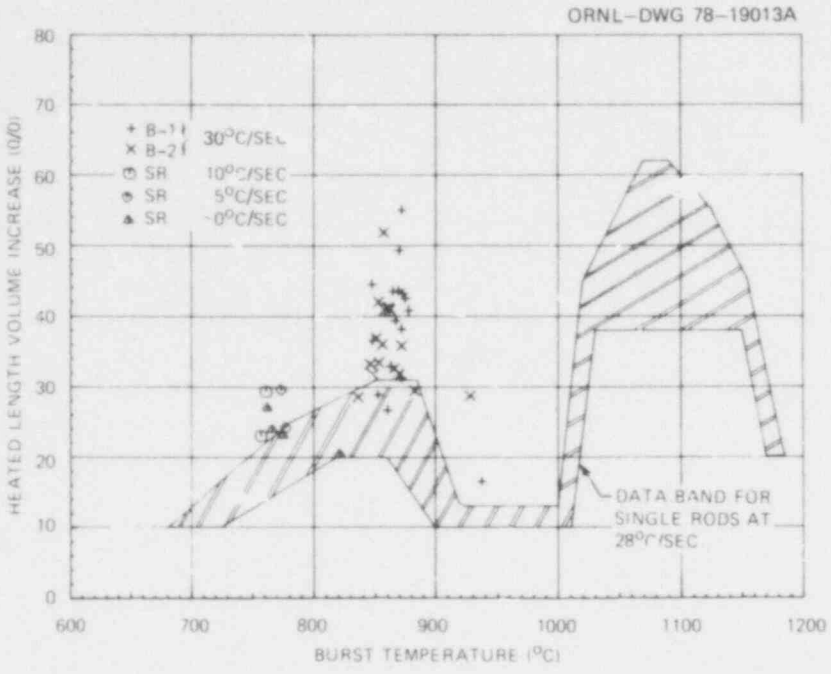

Fig. 2.74. Comparison of tube volume increase (proportional to average strain) in B-1 and B-2 tests.

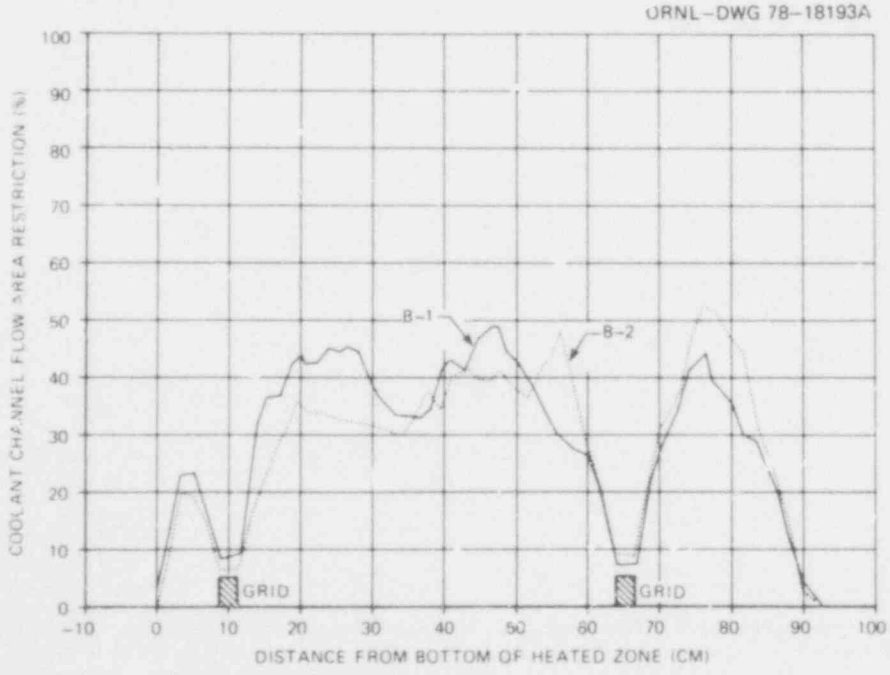

Fig. 2.75. Comparison of B-1 and B-2 coolant channel flow area restriction based on minimum flow restriction definition.

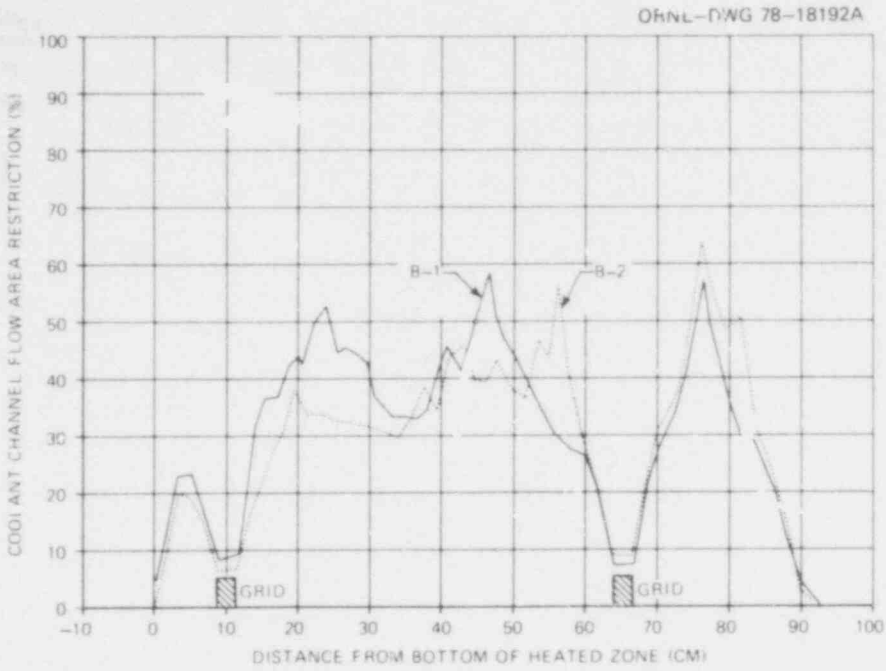

Fig. 2.76. Comparison of B-1 and B-2 coolant channel flow area restriction based on maximum flow restriction definition.

is based, in part, on the individual rod volume increases shown in Fig. 2.74, which averaged 38.3% in B-1 and 35.9% in B-2.

The preceding results are important in the interpretation of multirod bundle burst behavior. Indeed, as far as these results are concerned, it could be argued that the effect of the heated shroud in the B-1 test was unimportant. However, the micro-effects showed a strong effect of shroud temperature, an effect that could influence rod-to-rod interaction.

It was shown earlier (see Figs. 2.22 and 2.69) that the orientations of maximum tube wall thinning and tube bursts were influenced by the shroud temperature. Tubes in B-2 preferentially thinned and burst away from the shroud; this was less pronounced in the B-1 test, in which the shroud temperature was much closer to the bundle temperature. The inference that the unheated shroud cooled the outer rods in B-2 is reinforced by consideration of the difference in average shroud and bundle temperatures and heating rates as a function of time for the two tests.

Figure 2.77 compares the averaged temperatures (see Sections 2.3 and 2.4 for discussion) for the period from power-on until the time of

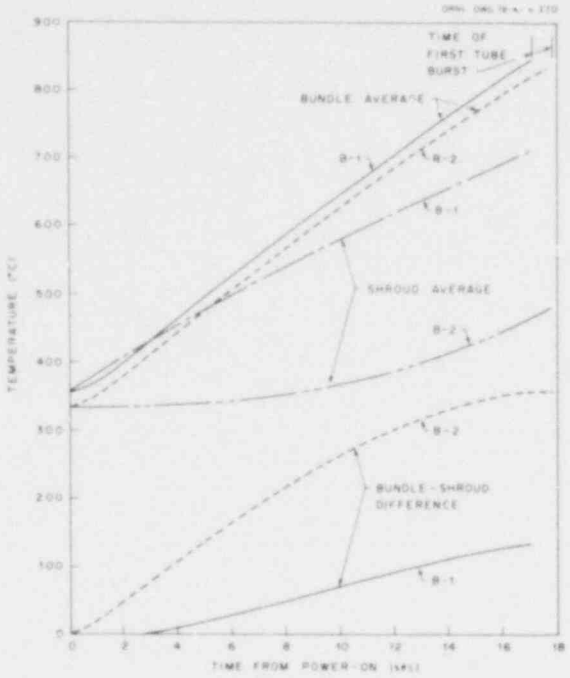

Fig. 2.77. Comparison of average temperatures in B-1 and B-2 tests.

the first tube burst in each of the tests. The temperature difference between each bundle and its shroud is also plotted in the figure. At the time of the first tube burst, this difference was ∿134°C in the B-1 test and ∿355°C in the B-2 test. It is interesting to note that the B-2 difference flattened out 1 to 2 sec before the first tube burst, indicating that the shroud heating rate (due to heat transfer from the bundle) was approximately the same as that of the bundle. The B-1 difference did not reflect this behavior nearly so much.

Figure 2.78 compares the bundle and shroud heating rates. The heating rate reached a maximum of ∿32°C/sec in both bundles in ∿3 sec, after which it slowly decreased due to heat losses. As discussed earlier, the rapid decrease at the end of the transient is due partly to bundle deformation. The average heating rate over the interval of 3 to 15 sec (the more or less linear portion of the temperature vs time curves) was 30.1 and 29.9°C/sec for the B-1 and B-2 bundles, respectively. Since the test parameters (other than shroud heating) were essentially the same, the bundle heating rate curves show that bundle heat losses were approximately the same during the first 12 or 13 sec, after which the B-2 losses exceeded the B-1 losses.

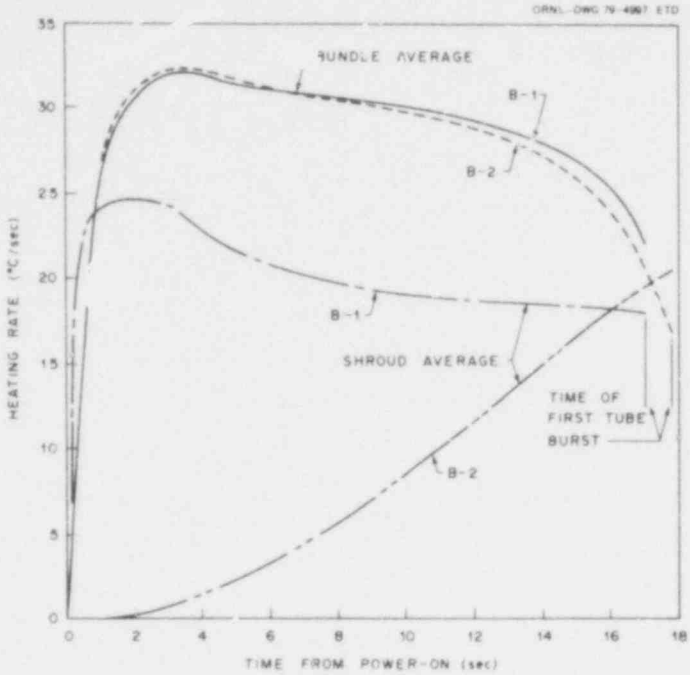

Fig. 2.78. Comparison of average heating rates in B-1 and B-2 tests.

For example, at 16 sec the B-2 average heating rate was ∿1.5°C/sec less than the B-1 rate; an approximate calculation showed that this difference represents ∿8 kW of power, which would have been more than enough to heat the B-2 shroud at its observed 18°C/sec rate in 16 sec. Thus, the higher B-2 losses during the final stages of the test cooled the outer surfaces of the B-2 bundle, relative to the interior, and caused deformation to be directed preferentially inward in this bundle, in agreement with results obtained from the bundle cross sections.

In summary, it has been shown that the differences in test conditions for B-1 and B-2 did not strongly influence the macro-effects of the two tests. The major dependent variables, such as burst pressure, temperature, times, and strain, were relatively unaffected. The micro-effects, such as the orientation of bursts and wall thinning, were quite dependent upon the bundle-to-shroud temperature differences. It is increasingly obvious that small temperature fluctuations in cladding temperature — due both to fuel simulator variations and to bundle-to-shroud differences — have measurable effects on certain test results. The importance of these particular results has not yet been established.

2.6 4 × 4 Bundle Test B-3

R. H. Chapman

Introduction

The third 4 × 4 bundle burst test (identified as B-3) was successfully performed on July 13, 1978. The average heating rate of the bundle and shroud was about 9.5°C/sec and 7.1°C/sec, respectively, although it was intended that both heating rates be the same. Initial pressure conditions (~11,600 kPa) were adjusted to cause failure at approximately 760°C; the initial temperature condition was 329°C. Test conditions were chosen to cause bundle deformation at conditions believed by some to be more realistic PWR LOCA parameters. Also, these conditions would permit direct comparison of B-3 results with those[4,5] obtained from single-rod tests SR-41 and SR-42 conducted (with unheated shrouds) earlier with a heating rate of 10°C/sec. Following the test, a quick-look report,[6] summarizing preliminary observations and findings, was issued (with limited distribution). The quick-look results have been subjected to further evaluation, and the findings to date are reported below.

On April 11 an attempt to perform the burst test was aborted during the final phase of pretest preparations at high temperature due to severe leaks in 15 of the 16 fuel pin simulators. The test vessel was allowed to cool and the lower flange was removed; several of the lower seals were checked for leaks (using the soap bubble method) and found to be leaking at the gasket between the Zircaloy adapter and the stainless steel portion of the Ceramaseal gland. The bundle was subsequently removed from the test vessel and returned to the shop for further examination and repair.

The joint design in the aborted test was the same as that used successfully in early seal development tests and in the B-1 and B-2 tests[3] (one simulator developed a severe leak in the B-1 test, and one developed a moderate leak in the B-2 test). Although we are unable at this time to explain fully why 15 of the 16 simulators in the B-3 assembly developed gross leaks, extensive testing performed subsequently showed that multiple (two to six) thermal cycles would generally cause leaks to develop.

A number of possible solutions, both short-term for repair of the B-3 array and long-term for future test arrays, were investigated[7] in

the single-rod test facility. Using a modification of the original design (see discussion in Section 3.2), the B-3 assembly was repaired and installed in the test vessel again in preparation for the test.

Figure 2.79 shows a simplified drawing of the B-3 test assembly. The shroud and shroud insulation (see Section A-A in the figure) were the same as those used in the B-2 test. Shroud heating tests performed on this shroud after the B-2 test indicated[3] that this design concept would be adequate for meeting the test objectives.

Figure 2.80 gives pertinent details of a typical fuel pin simulator. The fuel simulators (internal heaters) used in B-3 were recovered from the B-1 test assembly and refurbished (including new infrared characterization scans) for this test; they were located in the same relative position (both lattice position and internal thermocouple groove orientation) in both tests. This permits comparison of the distribution of the deformation in the two tests with respect to fuel simulator characteristics. It will be recalled that the quality of these fuel simulators, as determined by pretest infrared characterization scans, was not as good as desired, but they were the best available at the time the B-1 simulators were assembled. Also, the highest quality simulators were positioned in the inner ring of the array, and the lowest quality ones were used in the corner positions.

Each fuel pin simulator was instrumented with a fast-response, strain-gage-type pressure transducer and four Inconel-sheathed (0.71-mm-OD), type K thermocouples with ungrounded junctions. The thermocouples were spot-welded to the inside of the Zircaloy-4 tubes (10.9 mm OD × 0.635 mm wall thickness) at the positions shown in Fig. 2.81. The figure also gives thermocouple identifications for use in subsequent figures (the nomenclature TE 10-4 identifies the No. 4 thermocouple in the No. 10 simulator). The orientation of the thermocouples in B-3 was the same as in the B-1 test; however, the axial locations (shown in Fig. 2.82) were changed to reflect information gained in the earlier test. In particular, the thermocouples were distributed more uniformly (axially) in the B-3 test, and a few were located in regions where bursts occurred in the B-1 test. Thermal search and response checks of all the simulator thermocouples during assembly indicated TE 9-3 was detached from the

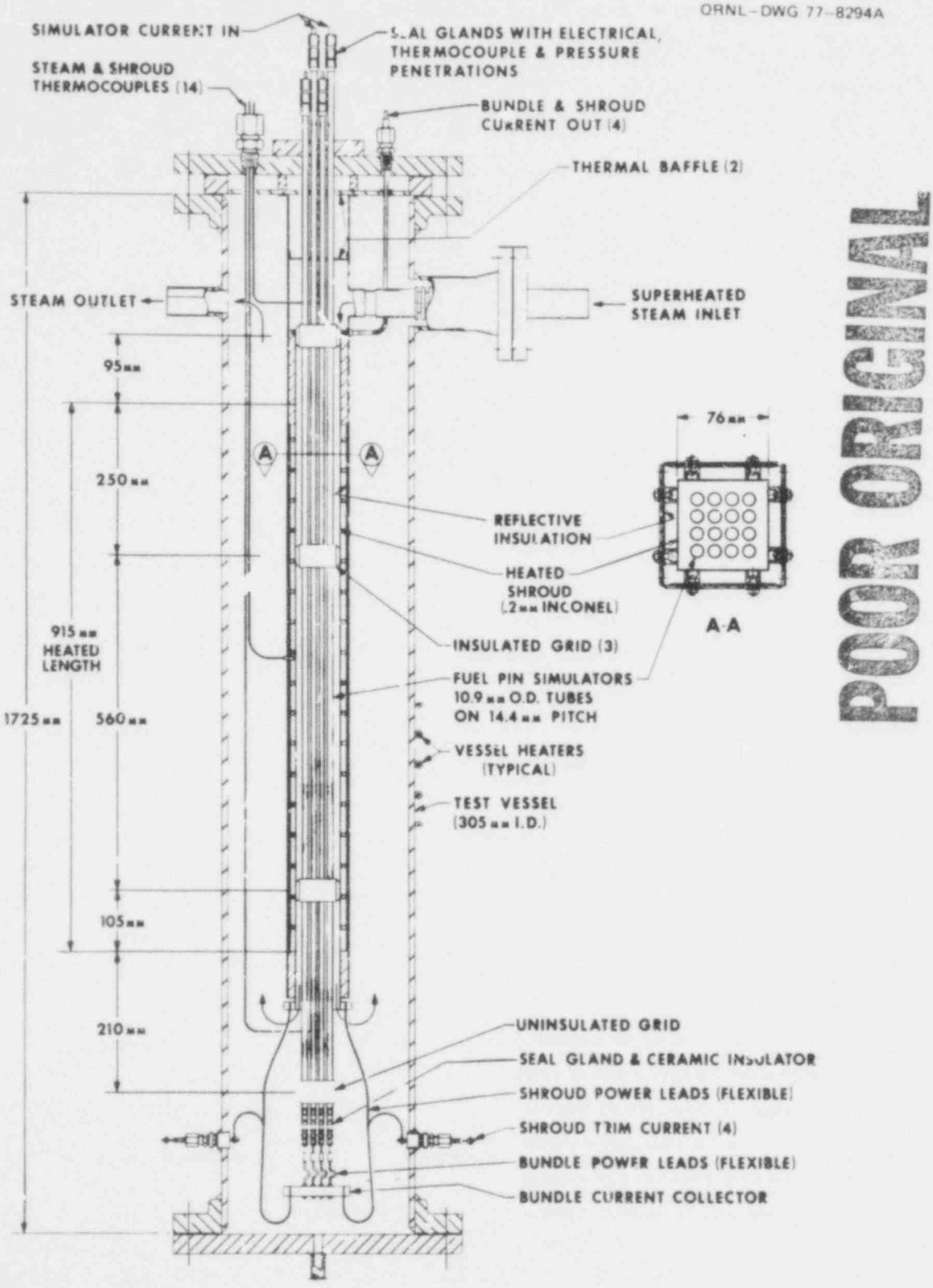

Fig. 2.79. Bundle B-3 test assembly.

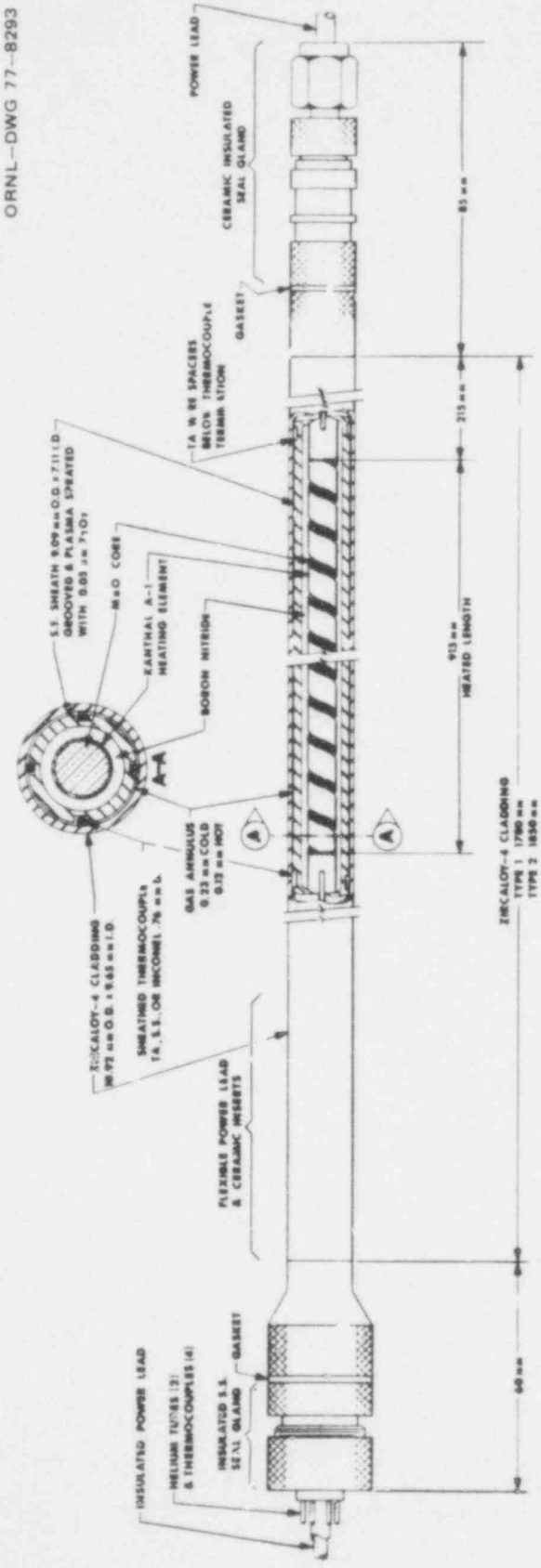

Fig. 2.80. MRBT fuel pin simulator.

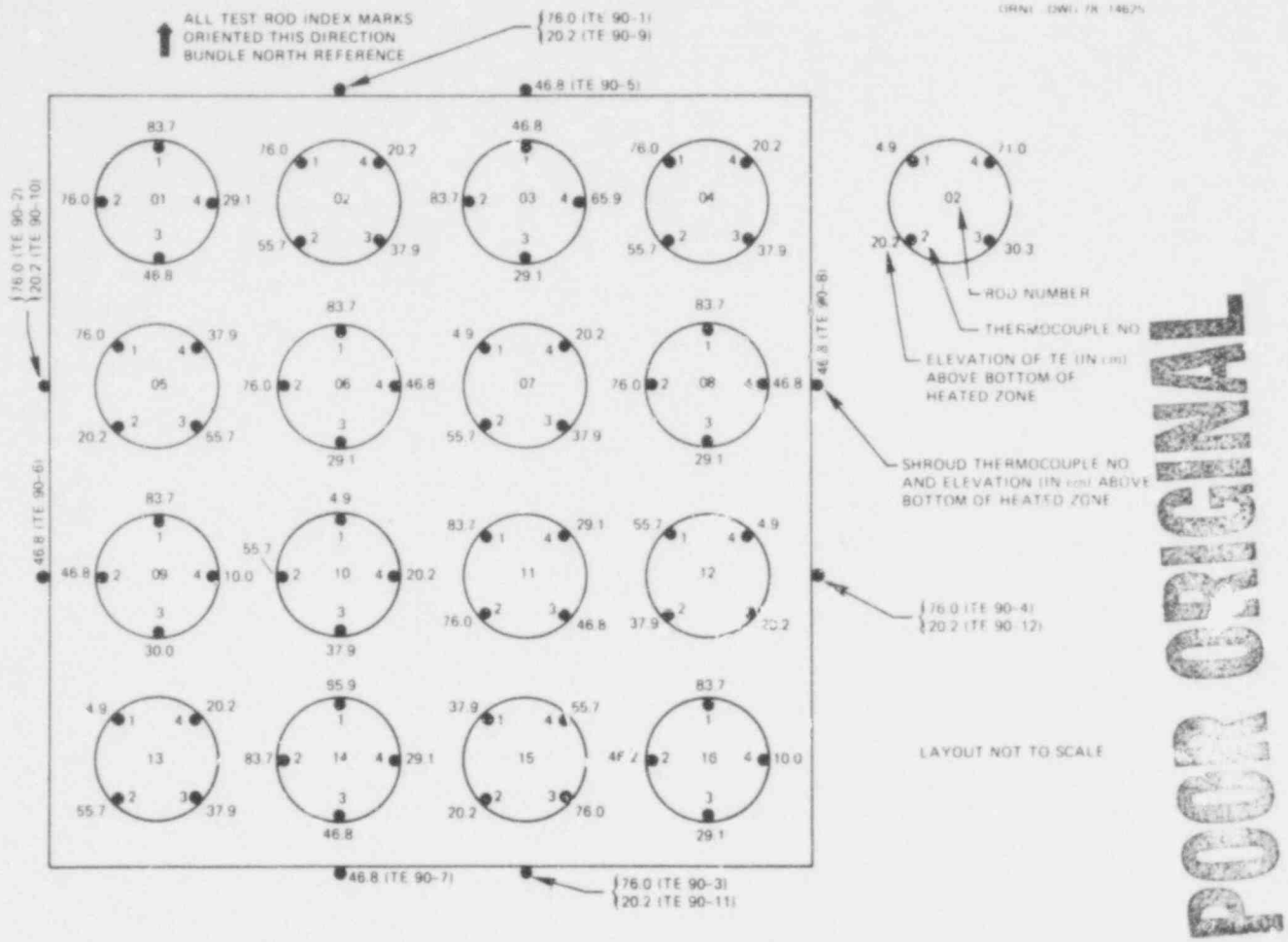

Fig. 2.81. Simulator and shroud thermocouple identifications and as-built locations in B-3 test assembly.

Zircaloy tube, and its reading is suspected of being in error. Also, the response of TE 12-4 was sluggish during both heatup and cooldown of the bundle. Other than these two, whose measurements have been ignored in this preliminary evaluation, all the thermocouples functioned properly during the test.

Twelve 0.25-mm-diam, bare-wire, type S thermocouples were spot-welded directly on the outside surface of the thin (0.25-mm-thick Inconel), electrically heated shroud surrounding the rod array. Three thermocouples were attached to each side at positions shown in Fig. 2.81 in an attempt to obtain information on both the axial and circumferential temperature distributions. Shroud thermocouple identifications are also given in the figure for use in subsequent temperature plots. The performance of

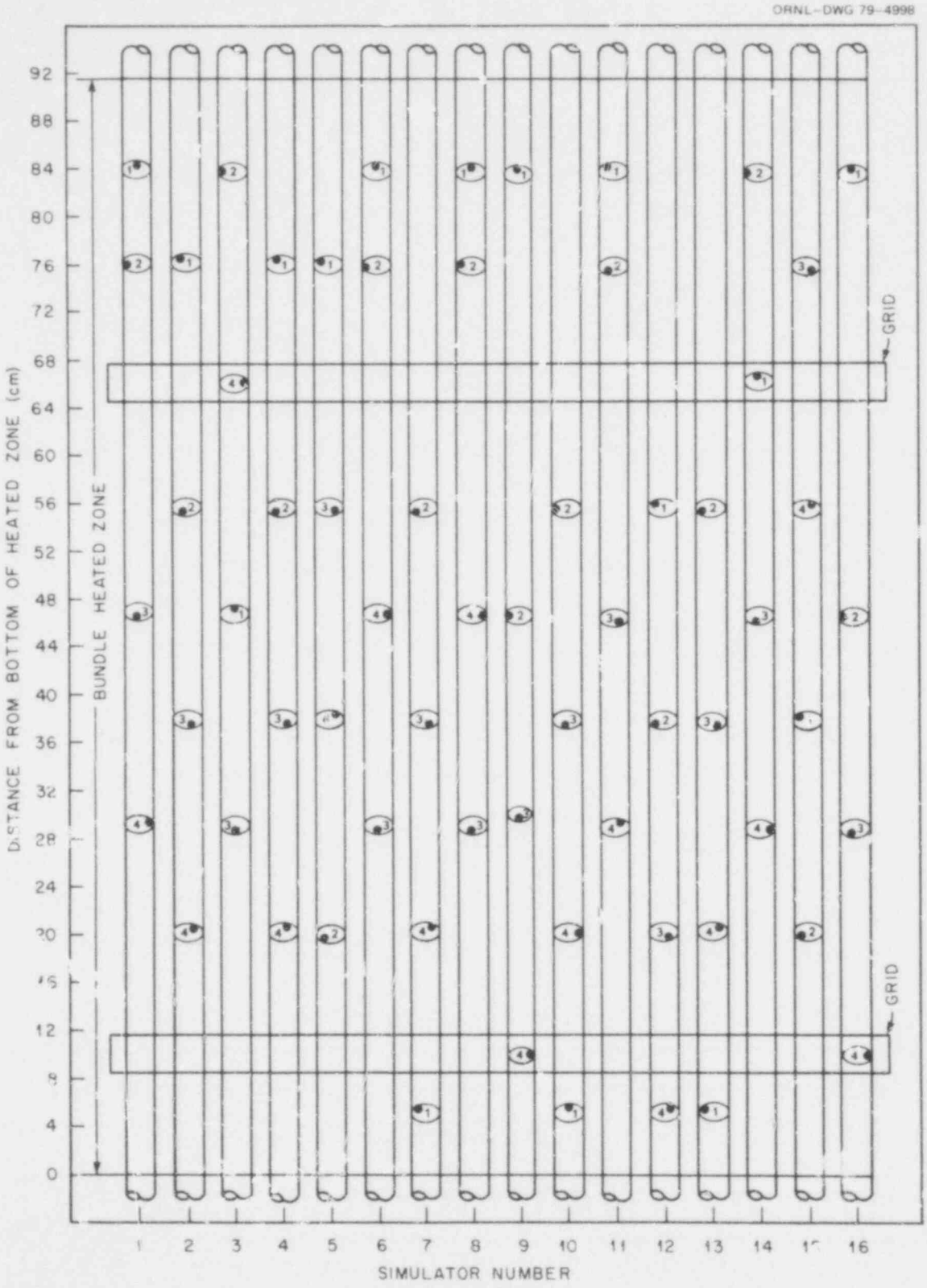

Fig. 2.82. As-built thermocouple locations in bundle B-3.

these thermocouples was not as good as expected. Only two gave wholly reliable information, four gave useful information, and six provided no useful information; the cause of the poor performance was in the external wiring circuits, as discussed in Section 5.2.

The steam thermocouples were relocated from the positions they occupied in the B-1 and B-2 tests to improve the steam temperature measurements. The thermocouples, identical to those used in the fuel pin simulators (0.71-mm-diam, Inconel-sheathed, type K, insulated junction), were positioned inside the tube matrix (see Fig. 2.79) to obtain these measurements. The inlet steam thermocouple (TE 310) was located at the midpoint of the matrix directly in front of the steam inlet. The outlet steam thermocouple (TE 305) entered the matrix at the bottom and extended upward (in the center coolant flow channel) to a point about 5 cm below the bottom of the bundle heated zone (i.e., just inside the heated shroud). These measurements provide some data for those interested in performing thermal analyses of the test; however, the outlet thermocouple data may be difficult to interpret, since it may not represent the true mixed-mean steam temperature.

Millivolt signals from the pressure transducers, thermocouples, and instruments for measuring electrical power were recorded on magnetic tape by a computer-controlled data-acquisition system (CCDAS) for subsequent analysis.

Termination of the powered portion of the test could be initiated by any of four actions: (1) CCDAS action resulting from a signal that 14 of the 16 simulators had burst, (2) CCDAS action following a signal indicating that 10 simulator thermocouples had exceeded the upper temperature limit (55°C above the anticipated burst temperature) on each of three successive data scans, (3) a timer that limited the transient to a predetermined time period, and (4) operator override. It was decided to program the power termination (action 1) to the bundle after 14 bursts (with the expectation that all 16 tubes would burst) to minimize the temperature overshoot at the end of the test. Also, the criterion for initiating action 2 (i.e., the high-temperature limit) was established reasonably close to the expected burst temperature (100°C was used for

the B-1 and B-2 tests) for the same reason. The test was terminated by action 1, and all 16 tubes burst as expected.

Heatup of the test assembly was initiated early in the afternoon of July 12; the temperature was near 200°C at the end of the work shift. Power adjustments were made to the vessel heaters to maintain the temperature near this value overnight to avoid temperature cycling of the repaired simulator seals. Early on July 13, power to the vessel heaters was increased, and superheated steam was admitted to the vessel in the approach to the initial test temperature. Throughout this phase of operation, periodic leak checks indicated that the seals were performing very well (i.e., less than 15 kPa pressure loss per minute at 7600 kPa and 330°C).

After thermal equilibration (335°C) of the test assembly was attained (∿6.5 hr), the simulators were pressurized to ∿7700 kPa, and a short powered run (∿9.5-sec transient) was conducted to ascertain that the data-acquisition system and all the instrumentation were functioning properly and that the performance of the test components was as expected. An examination and evaluation of the quick-look data from this short transient (the temperature of the simulators increased to ∿430°C) indicated slight adjustments were needed to achieve the desired heating rate. In particular, the bundle heating rate was adjusted downward and the shroud heating rate was adjusted upward in an attempt to achieve the desired heating rate of 10°C/sec for each. The data also showed that only 2 of the 12 shroud thermocouples were functioning properly. (The shroud thermocouples are attached directly to the current-carrying shroud and are susceptible to common-mode voltage problems.) Attempts to identify and correct the erratic behavior of the malfunctioning shroud thermocouples were unsuccessful, and it was decided to proceed with the burst test as soon as thermal equilibrium was reestablished.

During the high-temperature hold time (∿6 hr) between the power-bump test and burst test, the repaired seal in simulator 7 deteriorated. By the time thermal equilibrium was reestablished, the leak had increased to about 1850 kPa pressure loss per minute at 11,750 kPa, while the remaining simulators had not changed from the earlier values (i.e., ∿15 kPa pressure loss per minute).

Since simulator 7 is one of the interior ones, it was desirable that its deformation be representative, requiring that its pressure be comparable to the others during the transient. This was accomplished by admitting helium to the simulator at a rate approximately equal to the leak rate; all the other simulators were tested in the usual manner (i.e., with the isolation valves to the supply header closed to provide a closed-volume system on each). As a result of this action, as will be discussed below, simulator 7 was tested under essentially constant pressure conditions. As soon as simulator 7 burst, an operator closed the isolation valve on the supply header to stop the flow of helium into the vessel.

During the powered portion of the transient, superheated steam flowed downward through the test assembly at the same rate as used in the B-1 test — ∿4.5 kg/hr. Inlet steam conditions of 320°C and 300 kPa (absolute) resulted in a Reynolds number of 263. These inlet conditions remained essentially constant until disrupted by helium escaping from the bursting tubes.

Following stabilization of the bundle temperature at 329°C, all the fuel pin simulators except No. 7 were pressurized simultaneously to ∿11,600 kPa and individually isolated from the supply header. The header was vented, and the leak rate of each of the 15 simulators was checked over a 2-min period, with the pressure loss being ∿10 kPa/min. The No. 7 simulator was then pressurized to 11,700 kPa and the manifold supply valve throttled to essentially maintain this pressure level (i.e., the inflow of helium was approximately equal to the seal leakage). With these initial conditions established, the test transient was initiated.

When power to the bundle was terminated, the steam flow was increased to an estimated minimum of 54.5 kg/hr (about twice that used in the B-1 and B-2 tests) to effect rapid cooldown of the bundle.

Bundle performance

Table 2.14 gives a summary of quick-look results of the test; these data are preliminary and are subject to change as further evaluation is performed. Initial pressure conditions were selected to cause bursts at a temperature of ∿760°C; the pressure selection was based on data from single-rod tests SR-41 and SR-42, which were conducted[4,5] under similar

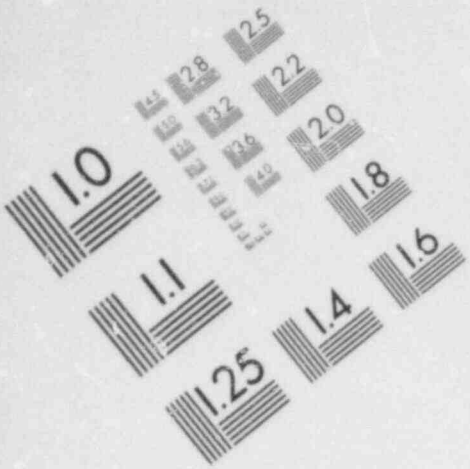

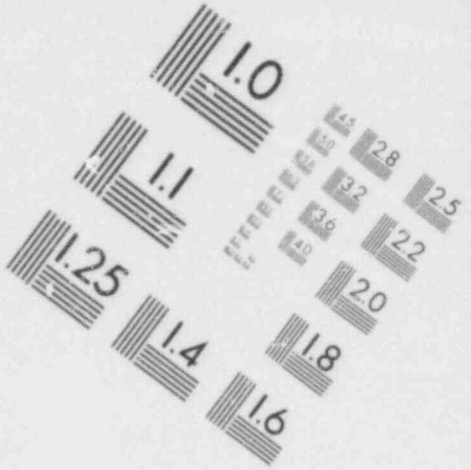

IMAGE EVALUATION
TEST TARGET (MT-3)

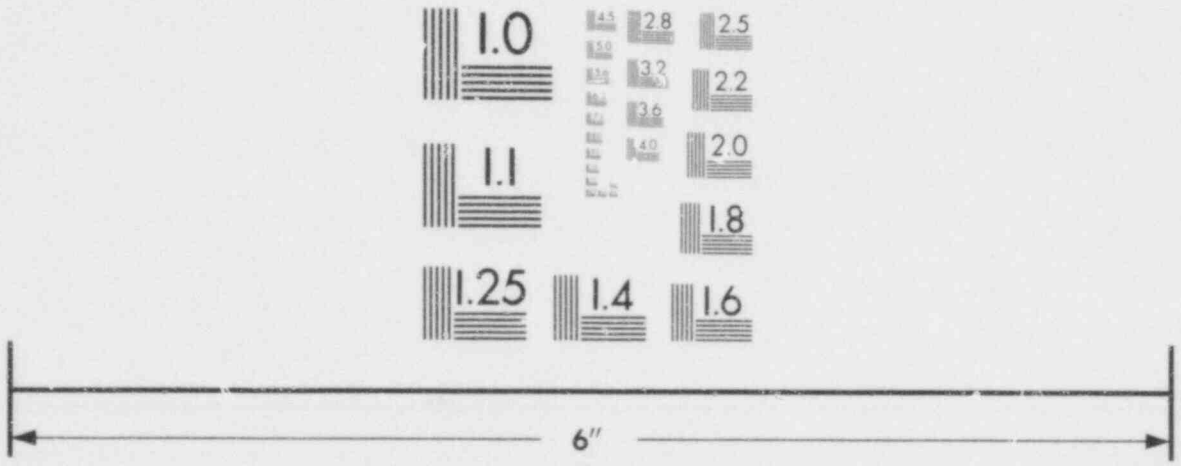

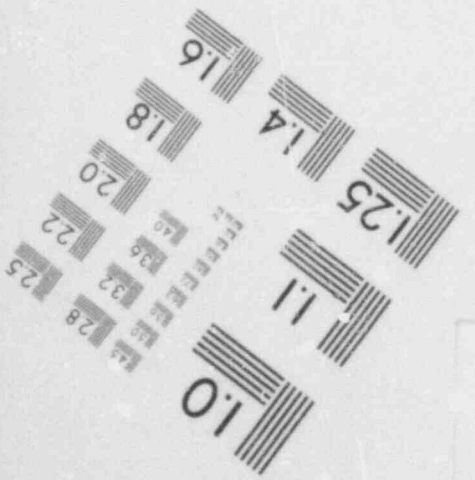

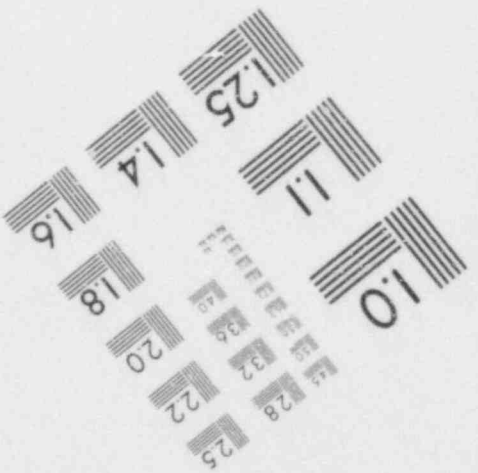

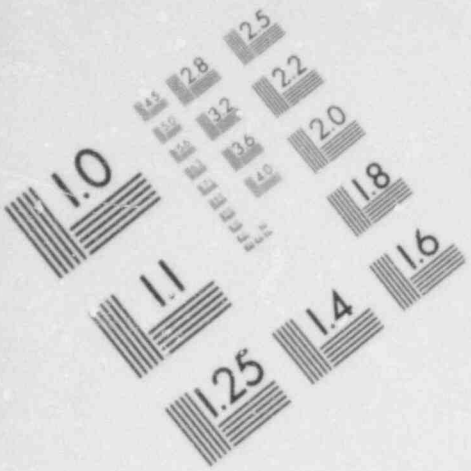

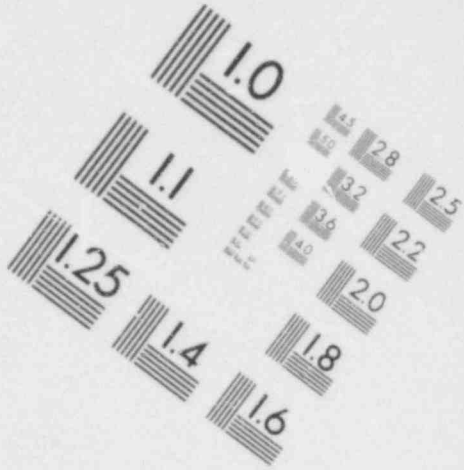

IMAGE EVALUATION TEST TARGET (MT-3)

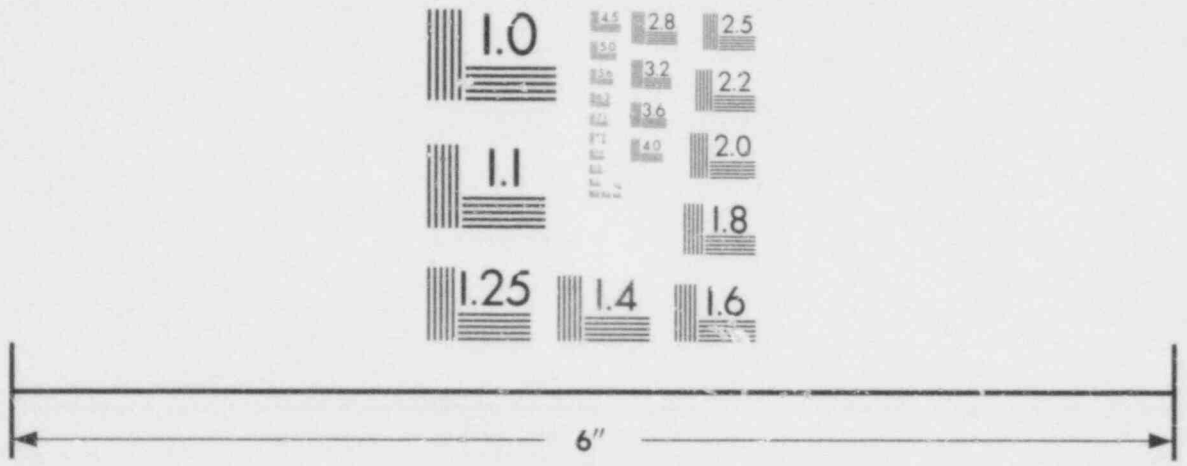

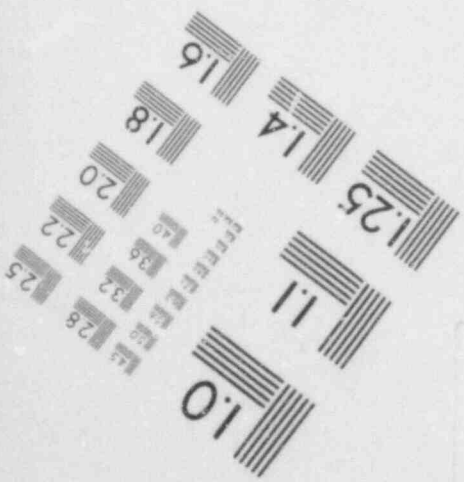

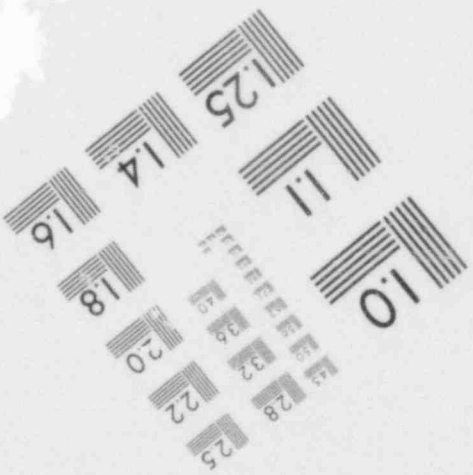

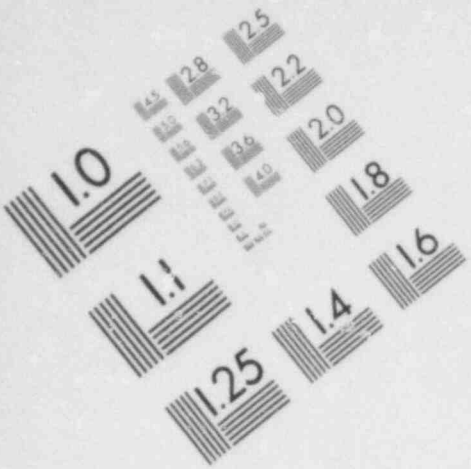

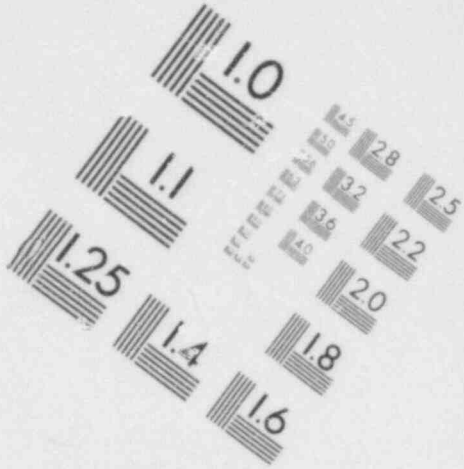

IMAGE EVALUATION TEST TARGET (MT-3)

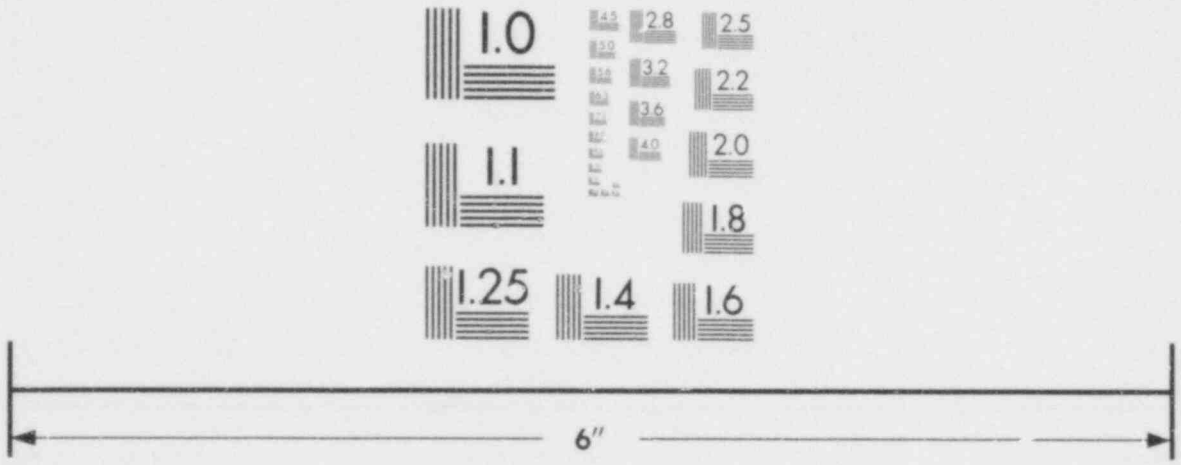

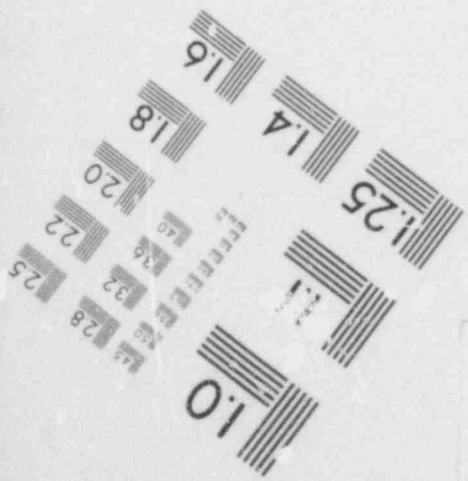

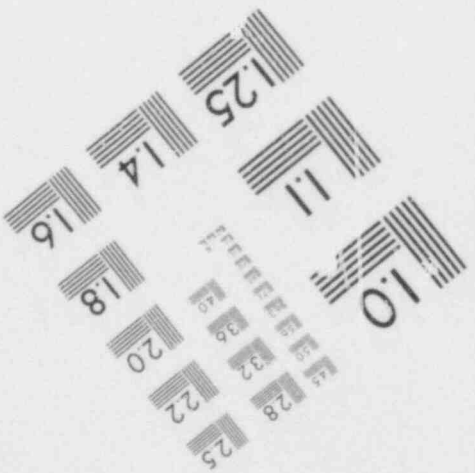

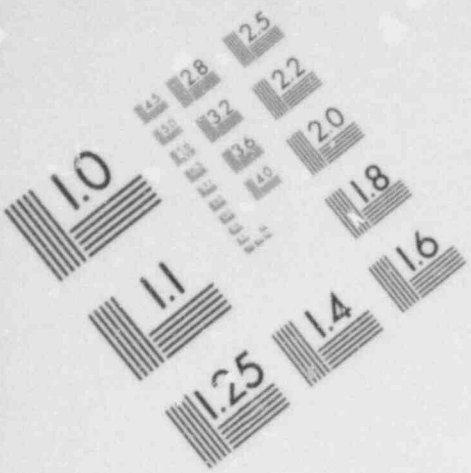

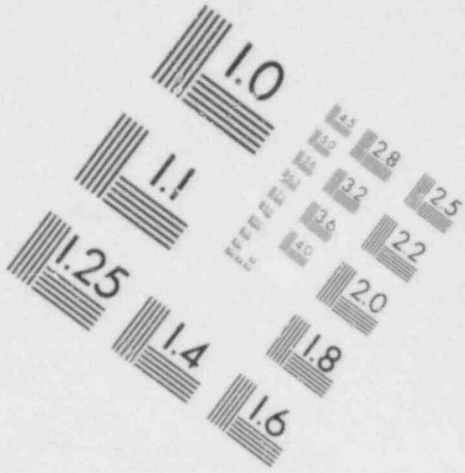

IMAGE EVALUATION TEST TARGET (MT-3)

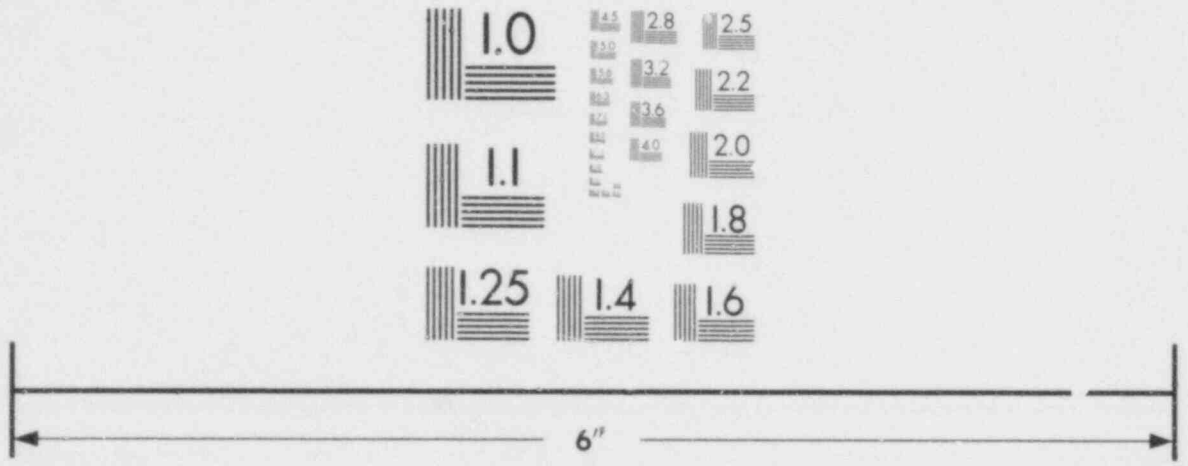

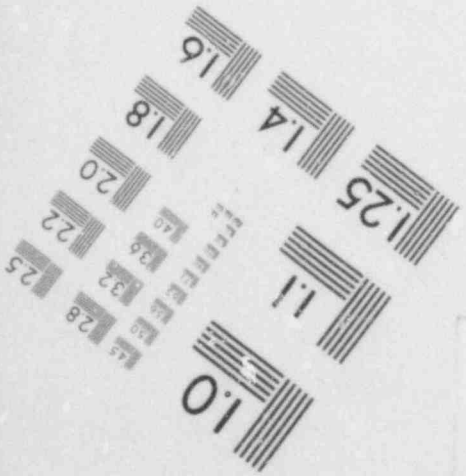

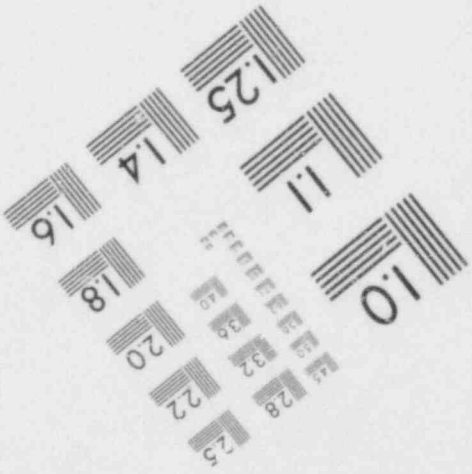

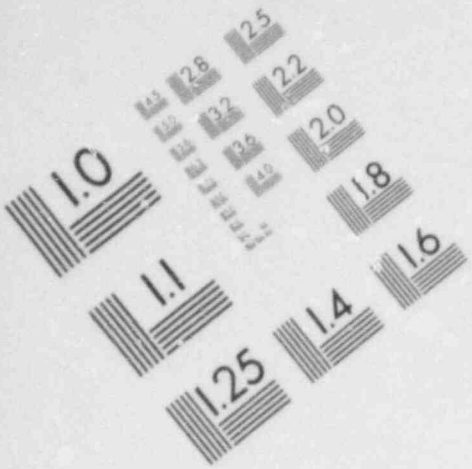

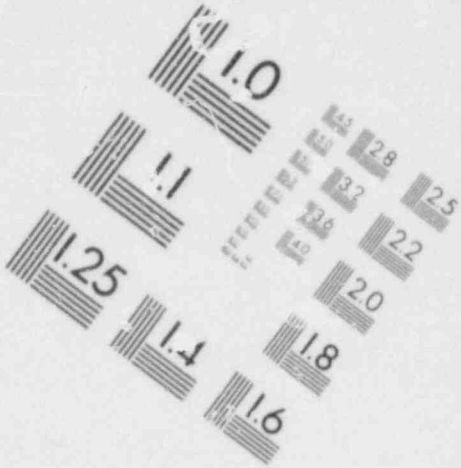

IMAGE EVALUATION
TEST TARGET (MT-3)

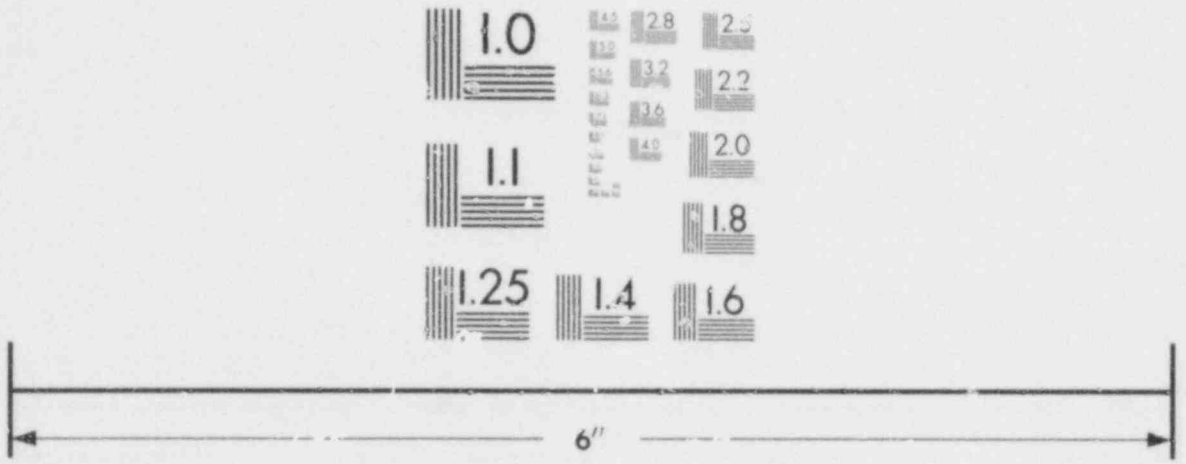

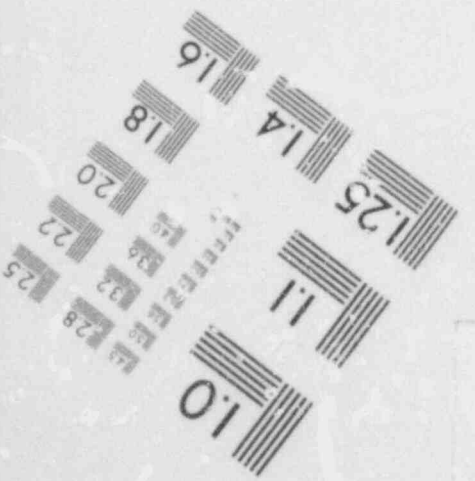

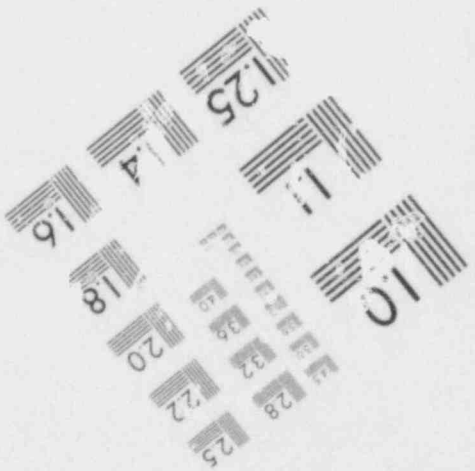

Table 2.14. Preliminary summary of B-3 test results

Rod No.	Initial conditions: Differential pressure (kPa)	Initial conditions: Temperature (°C) TE-1	TE-2	TE-3	TE-4	Approximate maximum pressure differential (kPa)	Approximate burst conditions: Differential pressure (kPa)	Temperature[a] (°C) TE-1	TE-2	TE-3	TE-4	Time (sec)	Pretest predicted burst conditions[b]: Pressure (kPa)	Temperature (°C)	Time (sec)	Burst temperature predicted from burst pressure[c] (°C)
1	11585	325	326	329	330	12060	9605	755	737	751	771	46.89	9500	761	47.1	819
2	11600	328	330	330	330	12065	8825	748	779	762	741	46.89	9500	761	47.1	830
3[d]	11620	331	326	330	329	12135	5115[d]	674[d]	605[d]	763[d]	682[d]	63.84[d]	9500	761	47.1	889
4	11630	328	330	330	330	12130	9090	761	765	767	736	47.64	9500	761	47.1	826
5	11565	327	330	329	330	12055	9480	752	763	764	760	46.29	9500	761	47.1	821
6	11580	326	329	331	330	12055	9155	757	770	767	769	46.19	9500	761	47.1	825
7	11725[e]	332	325	330	330	11755[e]	11355[e]	724	742	754	738	44.79[e]	9500	761	47.1	795
8	11655	326	328	330	329	12180	9105	748	755	756	746	46.19	9500	761	47.1	826
9	11535	324	330	330	331	12035	9105	754	750	785[f]	731	45.74	9500	761	47.1	826
10	11575	332	330	330	330	12075	9390	739	774	761	768	45.79	9500	761	47.1	822
11	11610	327	329	331	330	12130	9625	750	739	749	775	45.14	9500	761	47.1	819
12	11685	330	330	330	321[g]	12190	9755	757	761	745	700[g]	45.59	9500	761	47.1	817
13	11570	331	329	329	330	12075	10245	737	763	755	748	44.64	9500	761	47.1	810
14	11610	326	324	329	329	12105	9690	714	728	756	769	45.59	9500	761	47.1	818
15	11650	329	329	328	329	12170	9205	753	749	751	750	46.49	9500	761	47.1	825
16	11680	325	330	329	330	12190	9705	740	747	743	731	45.79	9500	761	47.1	817

[a] Underlined value is burst temperature based on premise that maximum measured value is minimum possible burst temperature.

[b] Prediction based on results of single-rod test SR-42, using external, bare-wire thermocouple measurement for determining burst temperature.

[c] Based on correlation from single-rod burst tests (at 28°C/sec heating rate), using burst pressures from Column 8 as input.

[d] Rod 3 may have developed a leak at ~11200 kPa (see text for discussion); burst occurred 16.65 sec after power was terminated.

[e] Rod 7 developed a leak prior to test; this rod was tested essentially at constant pressure due to attempt to compensate for leak.

[f] TE 9-3 was known to be detached from Zircaloy prior to test, causing a high reading; TE 9-1 reading was selected as burst temperature.

[g] TE 12-4 had very slow response on both heatup and cooldown transients, and its readings should be ignored.

heating rate conditions. As indicated in the table, the initial temperature was 329°C, and the temperature distribution in the bundle was very uniform (see Figs. 2.81 and 2.82 for thermocouple locations). The average temperature indicated by the 12 shroud thermocouples was 335°C. Steam inlet temperature was 320°C and the outlet temperature was 335°C. The latter value indicates slight heating of the small steam flow (4.5 kg/hr) as it flowed downward through the test assembly.

The time sequence of the bursts is given in Table 2.15; resolution of time is to the nearest 0.05 sec. Power was on for 47.19 sec; the first simulator (No. 13) burst after 44.64 sec of heating, and the 13th and 14th bursts, which gave the signal to terminate power to the bundle,

Table 2.15. Distribution of bursts with time in B-3 test

Time[a] (sec)	No. of bursts	Simulator No.
44.64	1	13
44.79	1	7
45.14	1	11
45.59	2	12, 14
45.74	1	9
45.79	2	10, 16
46.19	2	6, 8
46.29	1	5
46.49	1	15
46.89	2	1, 2
47.64	1	4
63.84	1	3[b]

[a]Power was terminated at 47.19 sec.

[b]As a result of partial depressurization, simulator 3 failed 16.65 sec after power was terminated.

occurred 2.35 sec later. The 15th and 16th bursts occurred 0.45 and 16.65 sec, respectively, after power was terminated. The 16th tube to burst (No. 3) partially depressurized 43.44 sec after the start of the transient (see discussion below) and caused the burst to be delayed significantly.

The net gas volume of the simulators (measured at room temperature) ranged between 49.0 and 51.5 cm^3, and all simulators (see Table 2.14) attained approximately the same maximum pressure (No. 7 was lower due to the inflow of gas to compensate for the leak). The maximum pressure was reached in ~31 sec (±1.3 sec) in all the simulators except No. 7 in which it was reached at 21.5 sec. The table also shows that the burst pressures, temperatures, and times of the normal tubes were in good agreement with expectations, based on the results of SR-42; this is shown better perhaps by the data plot in Fig. 2.83. A linear least squares fit to the data (excluding the No. 3 simulator) is shown in the figure for comparison to the correlation we obtained (based on external thermocouple measurements) from single-rod tests heated at 28°C/sec. The bursts occurred at a temperature about 55°C lower than would be expected if the heating rate had

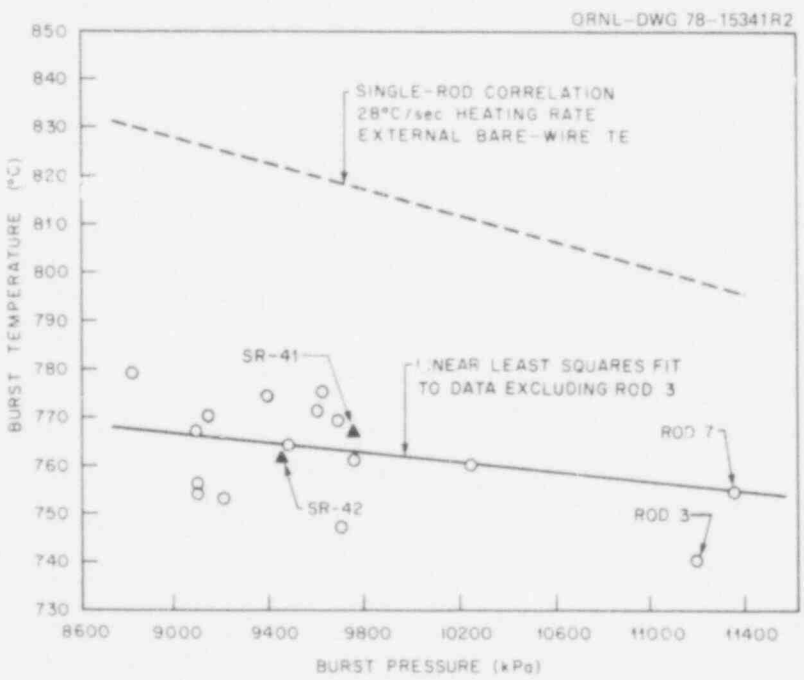

Fig. 2.83. Comparison of B-3 burst temperature–burst pressure data.

been 28°C/sec and the temperatures had been determined by external bare-wire thermocouples. Although the range of data is insufficient to establish a relationship between the two heating rates (strain rate is perhaps the proper correlating parameter), the two curves would be expected to converge with decreasing burst pressure rather than diverge as observed. The data point shown in the figure for the No. 3 simulator will be discussed later.

A number of quick-look data plots are given in Figs. 2.84 to 2.87 to give an indication of the general behavior of the test. An arrow is located on the abscissa in the figures to mark the time power was terminated.

Figure 2.84 depicts the pressure and temperature behavior of simulator 13, the first one to burst. As indicated in Fig. 2.81, this is a corner position of the test array. A similar data plot is given in Fig. 2.85 for one of the interior simulators (No. 10).

As discussed earlier, the lower seal of simulator 7 developed a significant leak prior to the test, and modifications to the test procedure were made to compensate for the leak by admitting helium to the simulator at a rate approximately equal to the leakage rate. As a result, this simulator was tested under essentially constant pressure conditions, as indicated by the data plot shown in Fig. 2.86. The unusual shape of the pressure decay curve following the burst at 44.79 sec was caused by the continued inflow of helium to compensate for the seal leak and the subsequent closing of the supply valve at 47.49 sec (see Section 5.2 for further discussion).

Simulator 3 exhibited unusual behavior, as shown by the data plot in Fig. 2.87. As evident from the pressure trace, the tube burst 16.65 sec after power was terminated. The burst occurred at an elevation about midway between TE 3-3 and TE 3-1 (see Fig. 2.82 for thermocouple locations), presumably the result of creep. As indicated by the temperature trace of TE 3-3, the temperature at this elevation remained above 750°C for ~20 sec after power termination. Burst conditions for the simulator, 763°C and 5115 kPa, compare reasonably well with the isothermal creep rupture results[3,5] from single-rod test SR-34 (i.e., 766°C, 5820 kPa, and 49 sec isothermal hold time).

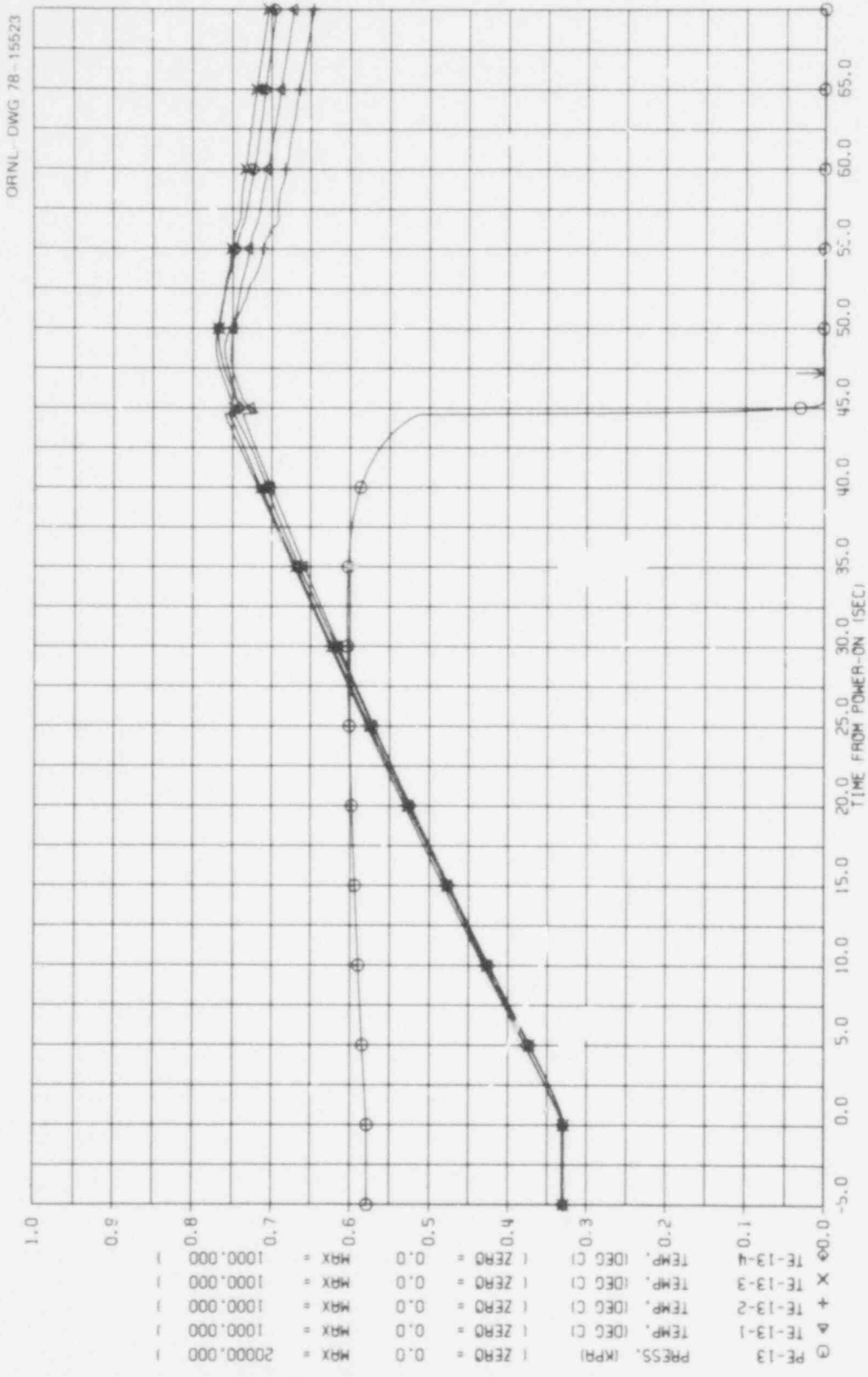

Fig. 2.84. Quick-look data of the first simulator to burst (No. 13).

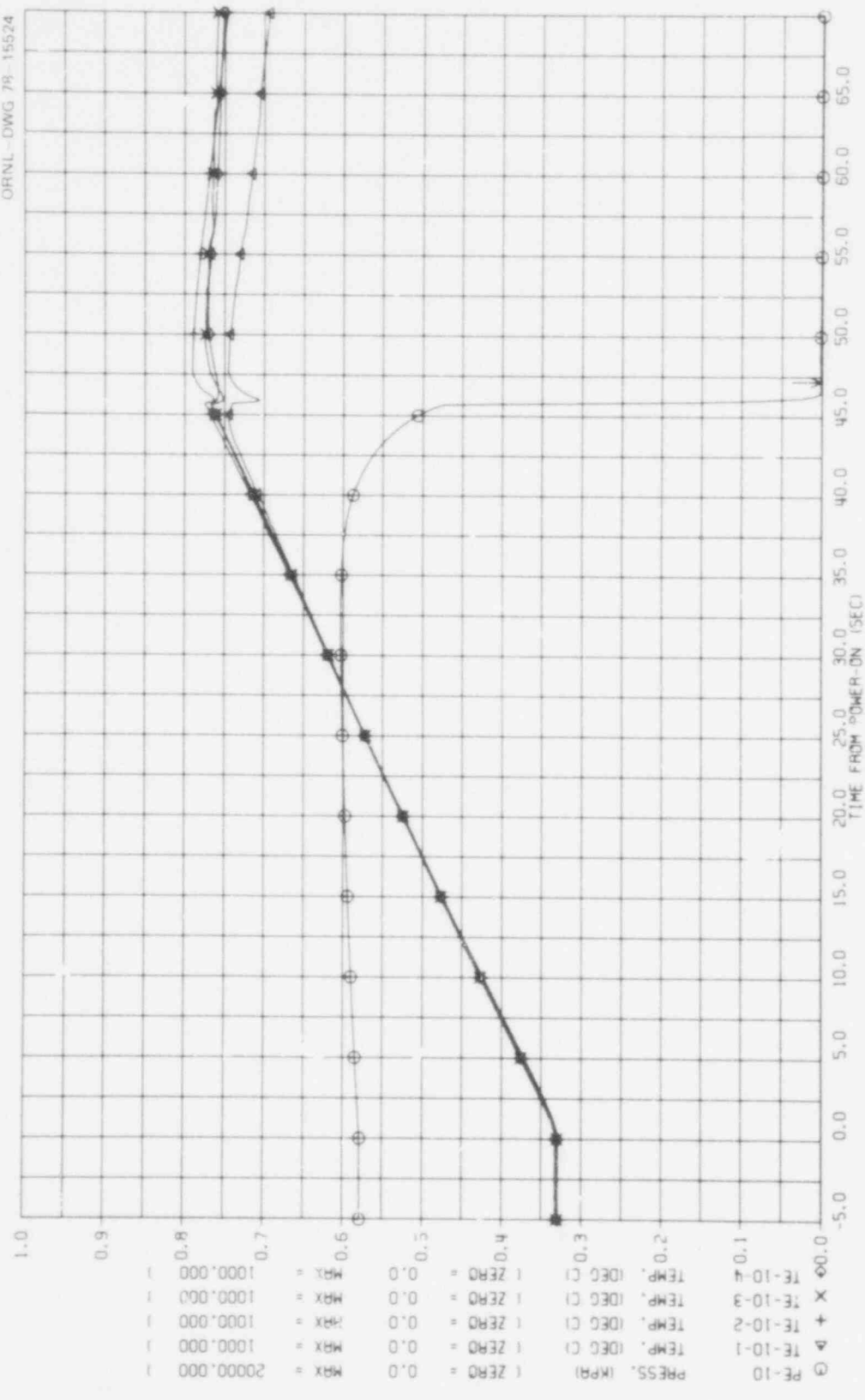

Fig. 2.25. Quick-look data of an interior simulator (No. 10).

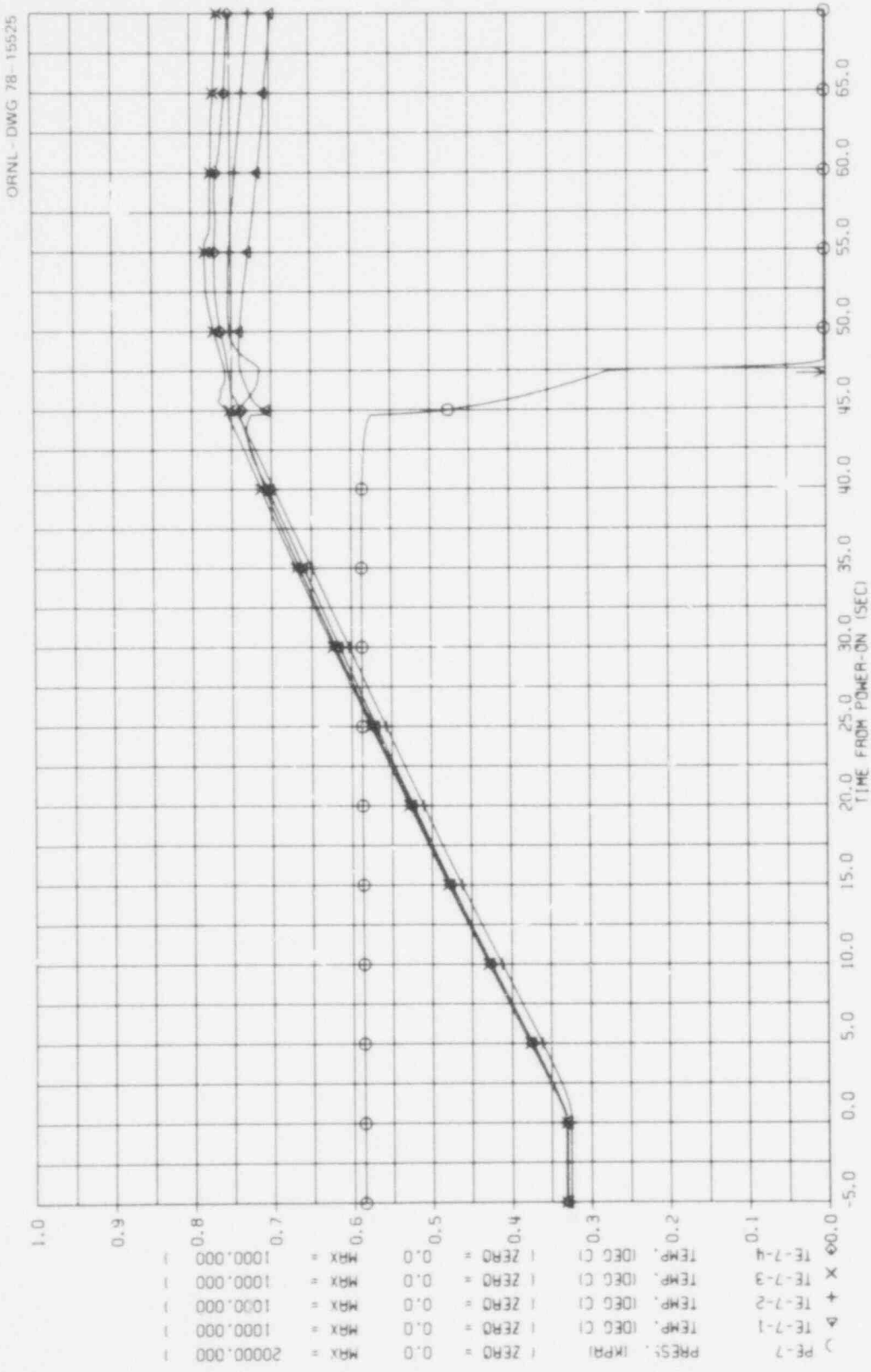

Fig. 2.86. Quick-look data showing that test on simulator 7 was essentially at constant pressure.

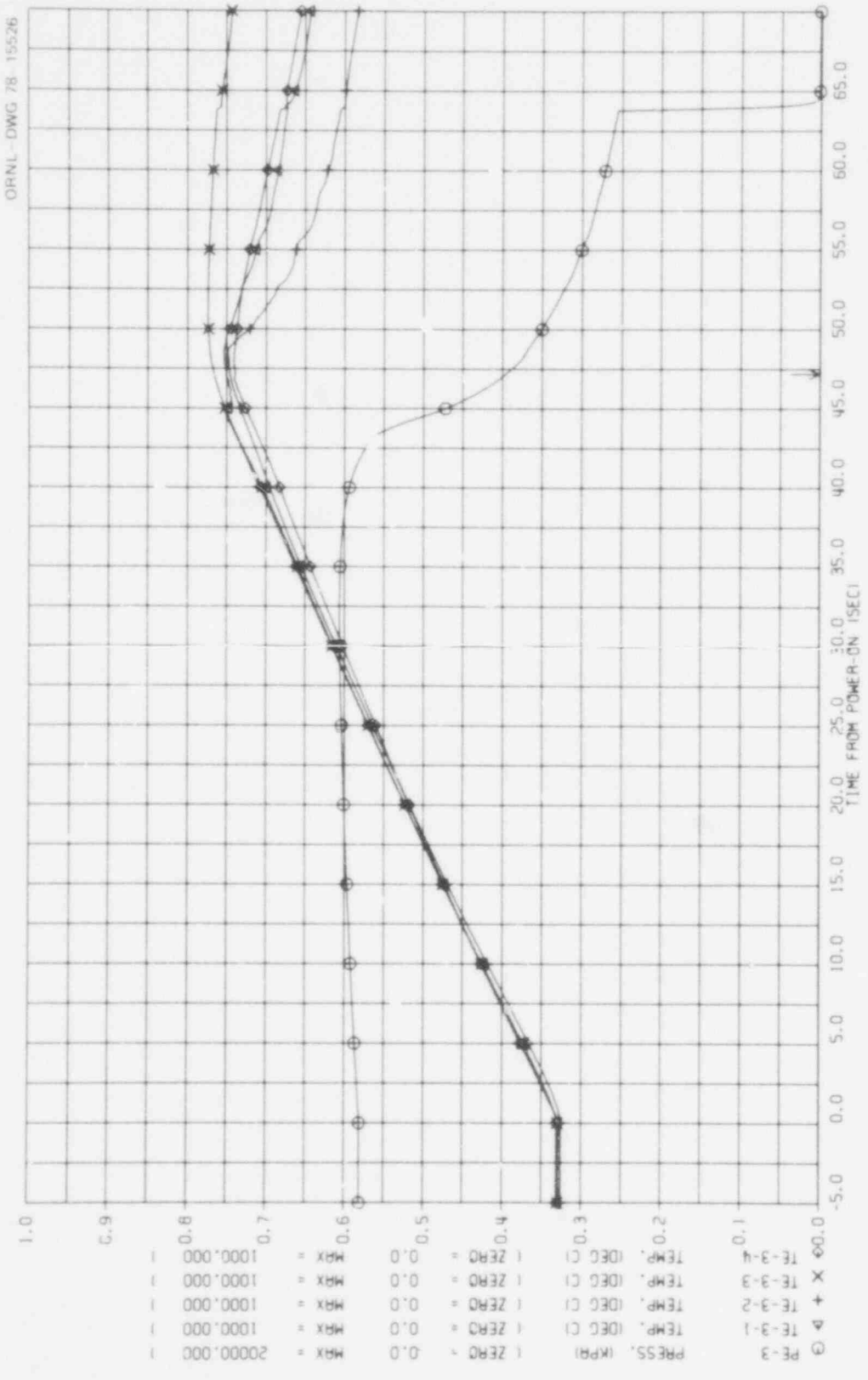

Fig. 2.87. Quick-look data of simulator 3 showing normal behavior for 43.44 sec at which time a small leak caused partial depressurization and subsequent creep rupture of the tube at 63.84 sec.

If the pressure trace of Fig. 2.87 is compared with that of Fig. 2.85, it can be seen that the behavior of simulator 3 was normal for the first 43.44 sec of the transient. However, at this time the depressurization rate increased suddenly as if a minute burst had occurred, and there was a significant loss of pressure before power was terminated and posttest steam cooling of the bundle commenced. The pressure and maximum (measured) temperature in the simulator at this time, 11,200 kPa and 740°C, respectively, are plotted in Fig. 2.83 as a questionable data point (i.e., as if it were a burst), and it is in reasonable agreement with the data points for the other simulators.

The reason for this unusual behavior is unknown at this time. However, possible explanations include (1) sudden development of a leak at the lower seal or at the upper seal where we have not experienced leaks, or (2) a minute pinhole in the tube. Little evidence exists for any of these possibilities. The simulator seals did not show indications of leaking or deterioration prior to the transient, as evidenced by the pressure loss 3 min before the test being only 5 kPa/min at 11,700 kPa and 330°C, which is about the same as measured several times during the pretest checkouts. Data from detailed tabulations indicate the rate of depressurization was $\sim 1.7 \times 10^4$ kPa/min (at 11,200 kPa) just before (i.e., at 43.44 sec) the sudden loss of pressure, 6.2×10^4 kPa/min (at 10,100 kPa) just after (at 44.44 sec) the sudden loss, and 5.1×10^3 kPa/min (at 5100 kPa) just before (at 63.44 sec) the burst occurred. Posttest pressure checks (see Section 5.2) of the lower end seal at both room and operating temperature failed to reveal indications of deterioration of the seal; checks could not be performed on the upper seal, since it was disassembled to permit removal of the internal fuel simulator. Boroscope and dye penetrant inspection and helium leak checking of the tube also failed to reveal evidence of a minute pinhole. However, these examinations do not prove conclusively that such a failure did not occur, since it may have been too small to detect by the techniques we used or the tube may have subsequently failed catastrophically at the site of the suspected pinhole. Unless evidence in support of the minute-pinhole hypothesis is found in posttest examination of the cross section of the

burst, the cause of the abnormal behavior of simulator 3 will not be determined.

Figure 2.88 shows the pressure traces of the first (No. 13), the second (No. 7), the fifteenth (No. 4), and the last (No. 3) simulator to burst on an expanded time scale, covering the period from 30 sec (about 1 sec prior to the time of maximum pressure) to 75 sec. This plot shows the range of burst times and the types of pressure traces observed in the test. Also, it shows the benavior of simulator 3 as being normal (almost identical to No. 4) until 43.44 sec, at which time it underwent partial depressurization as discussed above.

Only 2 of the 12 shroud thermocouples gave completely reliable information; the others exhibited electrical interference (discussed in Section 5.2) during the time the shroud was subjected to a voltage potential. Figure 2.89 compares the temperature traces of the two reliable shroud thermocouples (TE 90-4 and TE 90-5) at elevations 76.0 and 46.8 cm, respectively, with the traces for two of the simulator thermocouples (TE 2-2 and TE 3-1) at the same respective elevations (see Fig. 2.81 for locations relative to the shroud thermocouples). As evident from Fig. 2.89, the shroud heating rate decreased significantly during the transient and was ∿2.5°C/sec lower than that of the bundle during the latter portion of test. As a result, the shroud temperature was ∿80°C lower than the bundle temperature at the time the bursts occurred. The figure also shows ∿13°C difference in the two shroud temperatures, with the higher elevation (TE 90-4) being cooler, as expected from the shroud heating tests performed[3] earlier this year. Although adjustments to match the bundle and shroud heating rates were made after the pretest transient (see Section 5.2), the data were of insufficient duration to accurately reflect (and compensate for) the effect of shroud electrical characteristics and heat losses to the steam. Calibration data obtained earlier this year in the shroud heating tests did not extend to the lower heating rate used in the B-3 test, and extrapolation of the data was necessary but apparently unreliable.

Figure 2.90 shows the radial temperature distribution along the NW-SE diagonal (see Fig. 2.31) of the bundle at an elevation of 46.8 cm (i.e., at the same elevation as shroud thermocouple TE 90-5, which is shown for

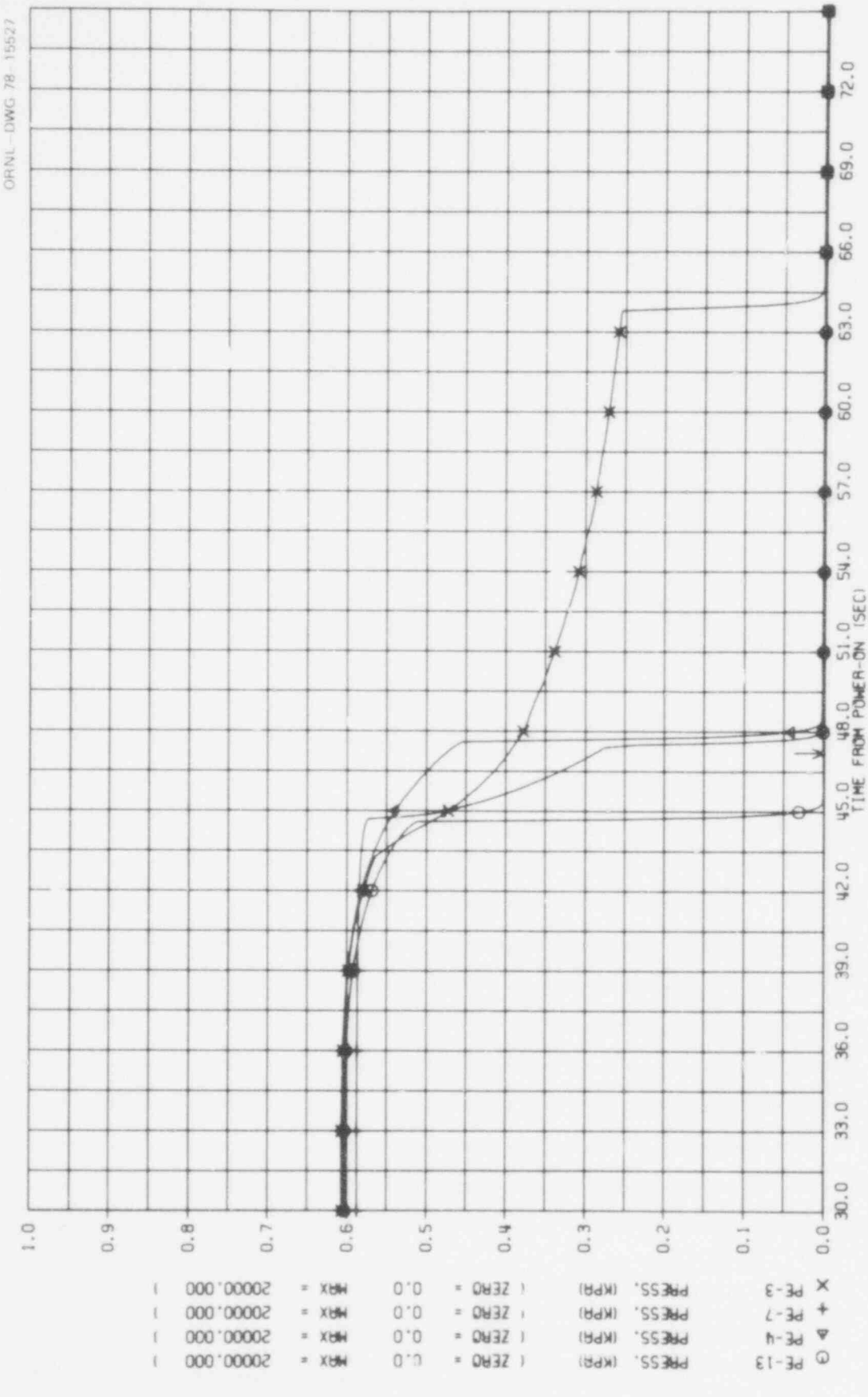

Fig. 2.88. Comparison of pressure traces during deformation of normal simulators (Nos. 13 and 4, respectively, the first and fifteenth tubes to burst) and the two abnormal simulators (Nos. 3 and 7).

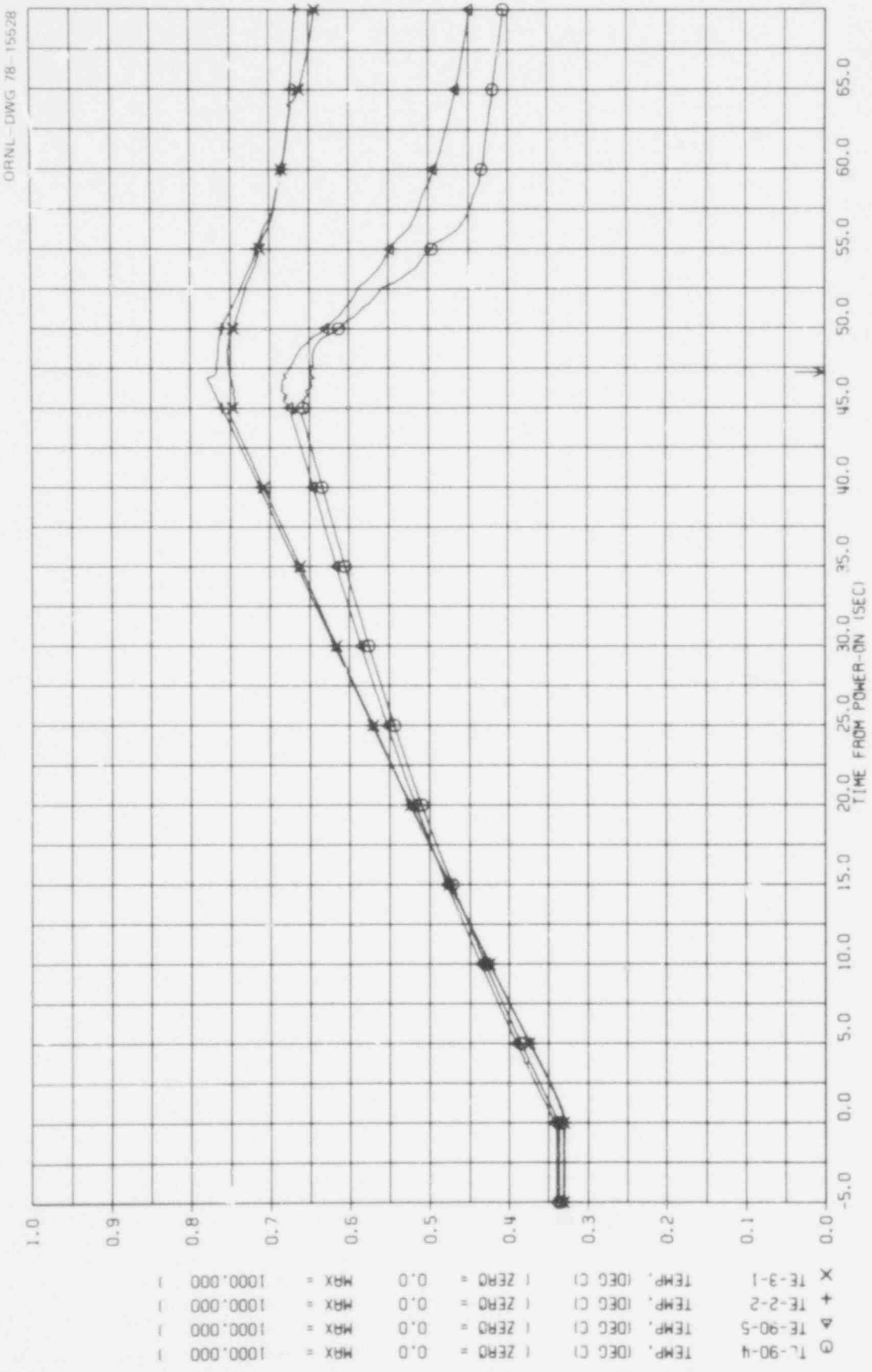

Fig. 2.89. Comparison of shroud and bundle temperatures at elevations of 46.8 and 76.0 cm.

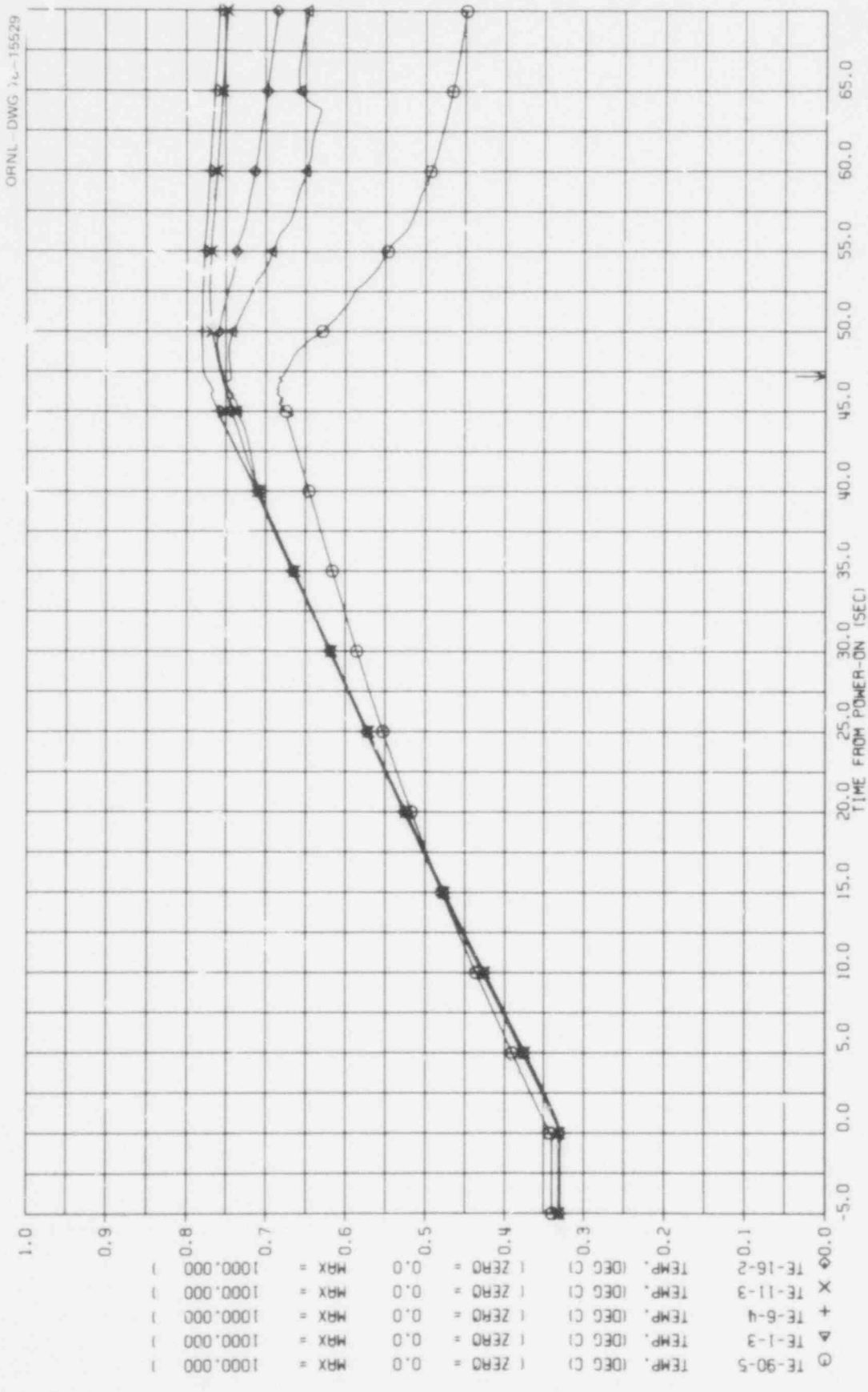

Fig. 2.90. Radial temperature profile of bundle at elevation 46.8 cm.

comparison). Temperature uniformity across the bundle is particularly good at this elevation.

As mentioned earlier, the steam inlet (TE 310) and outlet (TE 305) thermocouples were relocated in the B-3 test from the positions they occupied in the B-1 and B-2 tests in the hope that more useful information would be obtained. Both thermocouples were positioned in the center coolant channel, as described earlier (see Fig. 2.79).

Figure 2.91 shows the temperatures measured by these thermocouples over an interval of ∿5 min starting with power-on; the arrow on the abscissa indicates the time that power to the bundle was terminated and the posttest cooling steam valve was opened. During the heating transient, steam (4.5 kg/hr) entered the bundle (see Fig. 2.79 for steam flow path) at ∿320°C and 300 kPa (absolute), giving a Reynolds number of 263 at the top of the heated zone. These conditions remained essentially constant until the tubes began bursting and the posttest cooling steam valve opened. The temperature measured by the outlet thermocouple (TE 305) did not increase nearly so much during the heating transient as might have been expected. Although the reason for this is not understood at this time, it is suspected that either the flow was too low for effective mixing to take place or the lower end of the unheated portion of the bundle cooled the steam before it reached the thermocouple (TE 305 was located ∿5 cm below the bottom of the bundle heated zone). We know[4] from single-rod tests SR-39 and SR-40 that steep radial temperature gradients exist in the steam adjacent to the simulators and that very little mixing occurs; this probably explains the reason TE 305 did not follow the bundle temperature. The precipitous decrease in steam inlet temperature (to near saturation conditions) immediately after power was terminated was caused by moisture entering the bundle (from the stagnant steam upstream of the bypass valve); this phase lasted for 15–20 sec, after which the temperature recovered. The steam outlet temperature increased significantly (due to better mixing) as the flow rate increased with the valve opening. The flow inside the tube matrix during cooldown was estimated (from the steam temperatures and the energy input to the bundle) to be ∿54.5 kg/hr. This is assumed to be the effective flow for cooling the bundle and does not

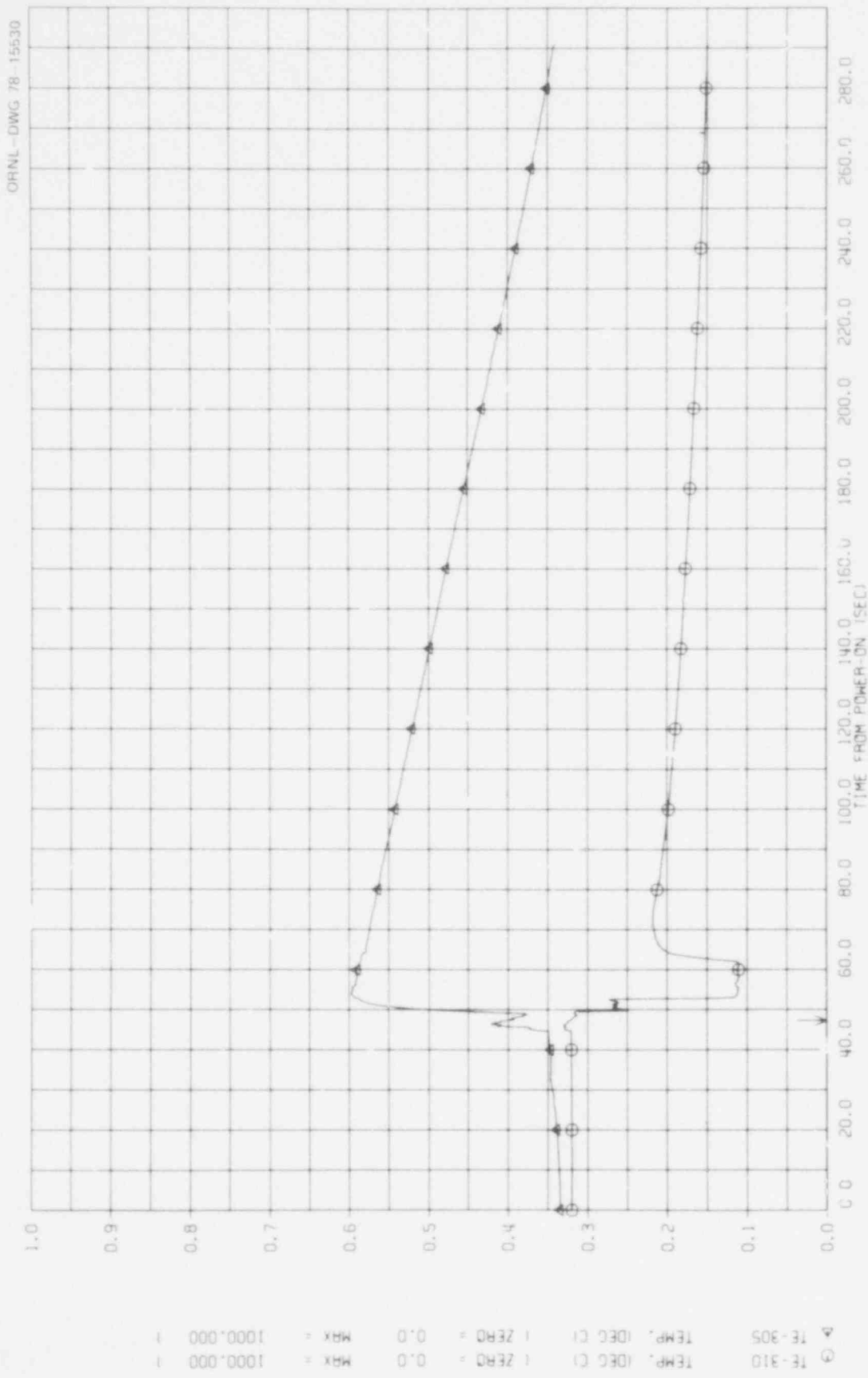

Fig. 2.91. Comparison of bundle steam inlet and outlet temperatures.

take into account the flow in the annulus between the bundle and the shroud, which contributes very little to bundle cooling.

The steam inlet and outlet temperature fluctuations during the time of the bursts are shown somewhat better in the expanded-time-scale plot of Fig. 2.92, in which the pressure traces of simulators 13 and 4 (the first and fifteenth ones to burst) and that of the vessel (PE 301) are plotted together with the steam inlet (TE 310) and outlet (TE 305) temperatures. The vessel pressure increase during the time of the bursts was caused by the release of high-temperature helium from the simulators. Since the vessel pressure was controlled by a valve in the steamline downstream of the vessel, the pressure could not be vented quickly. Also, the pressure inside the bundle shroud was slightly higher than that in the vessel, causing considerable deformation of the shroud (as will be discussed in the next section) and flow reversal of the steam (and high-temperature helium), as indicated by the fluctuations in both the steam temperature measurements. Relatively cold helium flowed into the vessel through the burst in simulator 7 for ~2.7 sec (see earlier discussion) to further complicate the complex dynamics. After 3–4 sec, the vessel pressure decreased rapidly to essentially atmospheric as the large steam valves upstream and downstream of the vessel opened to permit the posttest cooling steam to flow through the bundle with negligible pressure loss.

There appears to be evidence that a significant fraction of the posttest cooling steam flowed through the annulus between the bundle and the shroud, causing preferential cooling of the outer ring of simulators over that of the inner ring. This is shown by a comparison of the axial temperature profile (see Fig. 2.81 for thermocouple locations) of a corner simulator (No. 1; Fig. 2.93) to that of an interior simulator (No. 6; Fig. 2.94) during the cooldown phase. Also, the shroud was cooled much faster than the bundle, as shown in Figs. 2.95 and 2.96; this is partly due to less stored energy in the shroud and partly to the higher steam mass flow in the annulus between the bundle and the shroud.

All the previous temperature-time plots have depicted individual thermocouple measurements to show local temperature behavior. In order to characterize the bundle as a whole, all the measurements were analyzed to obtain average bundle (cladding) and shroud temperatures for the period

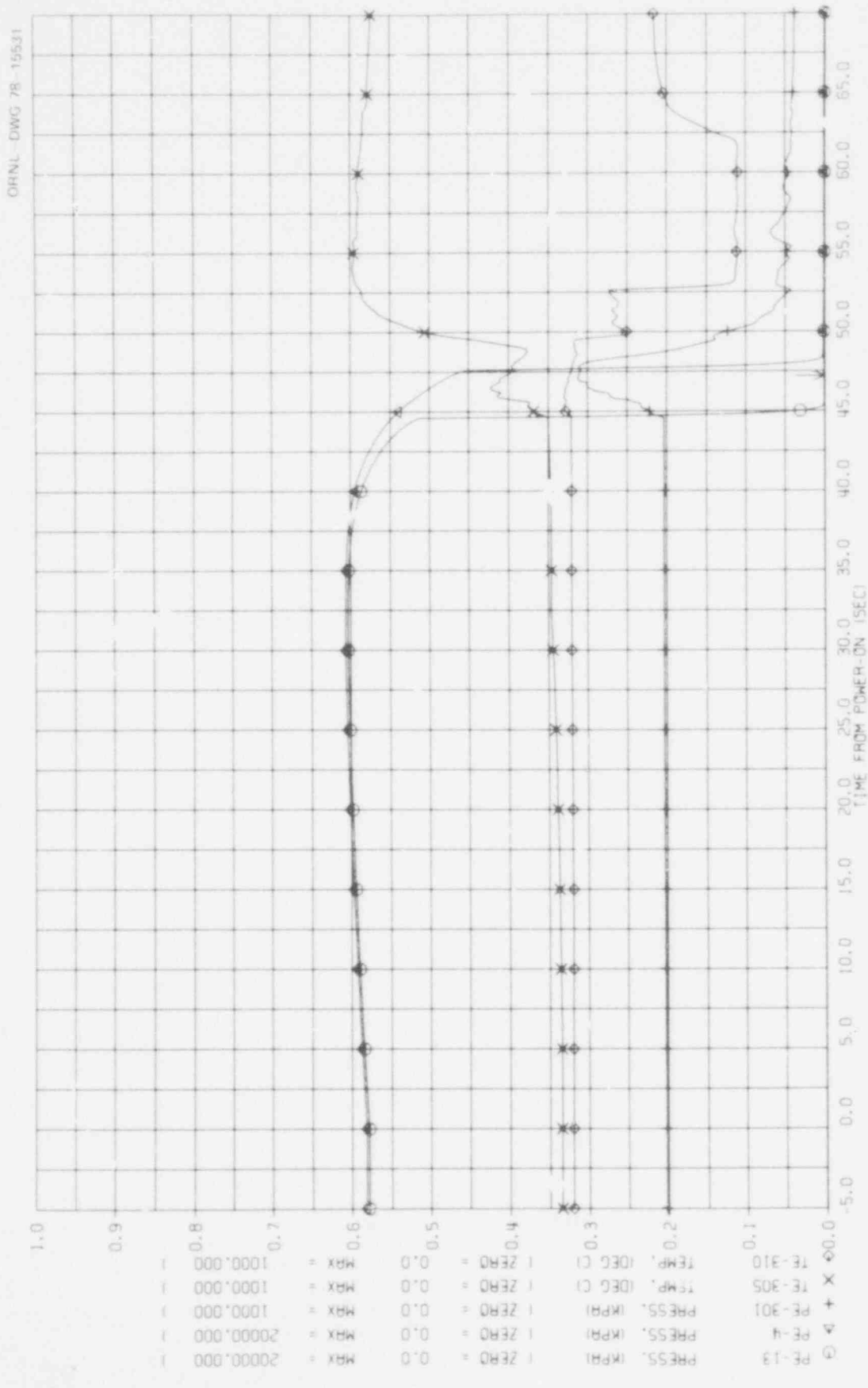

Fig. 2.92. Quick-look data showing correlation of vessel pressure rise with tube bursts and fluctuations in steam temperatures, indicating reverse flow in bundle during the time of bursts.

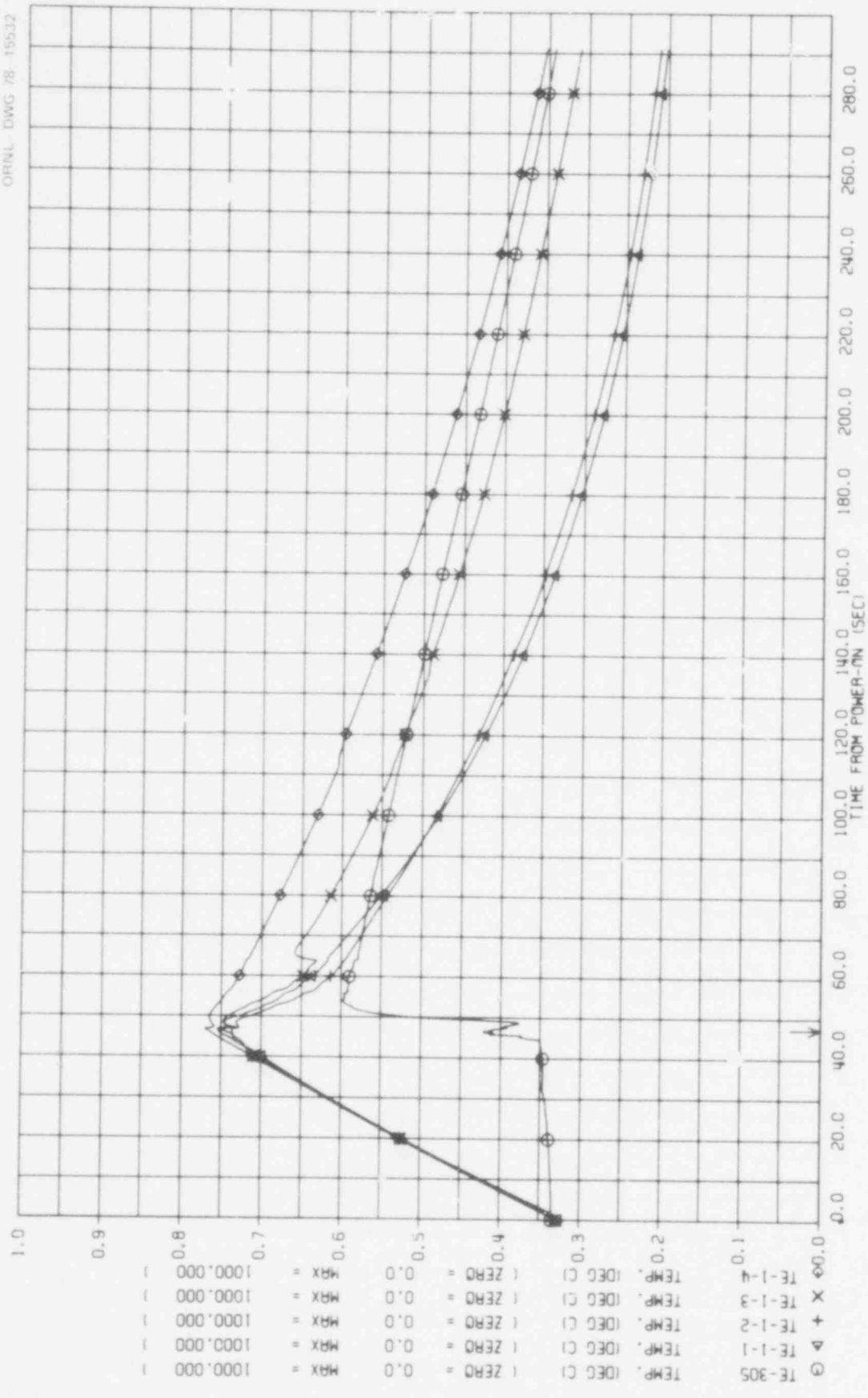

Fig. 2.93. Axial temperature profile of a corner simulator (No. 1) during posttest cooldown.

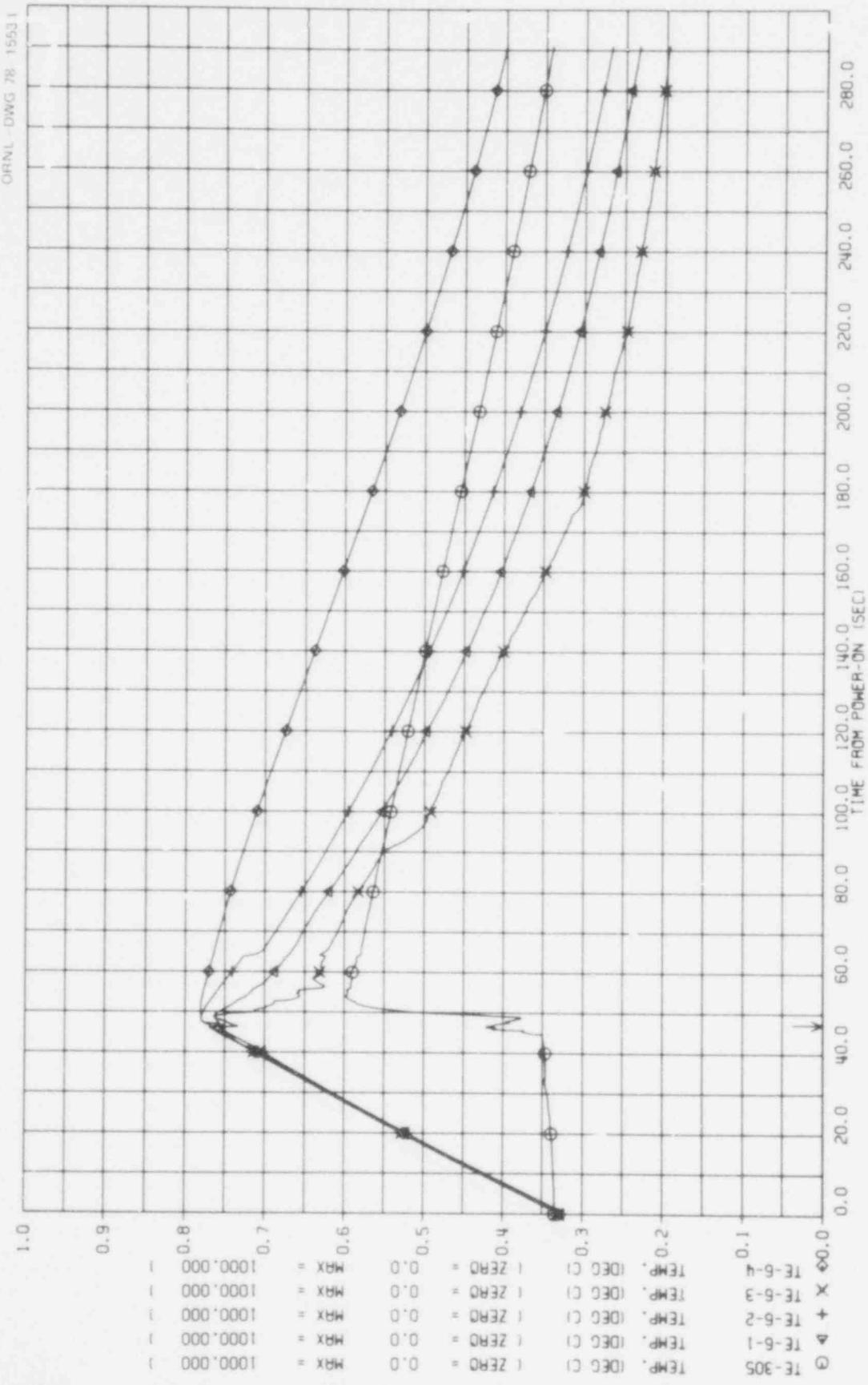

Fig. 2.94. Axial temperature profile of an interior simulator (No. 6) during posttest cooldown.

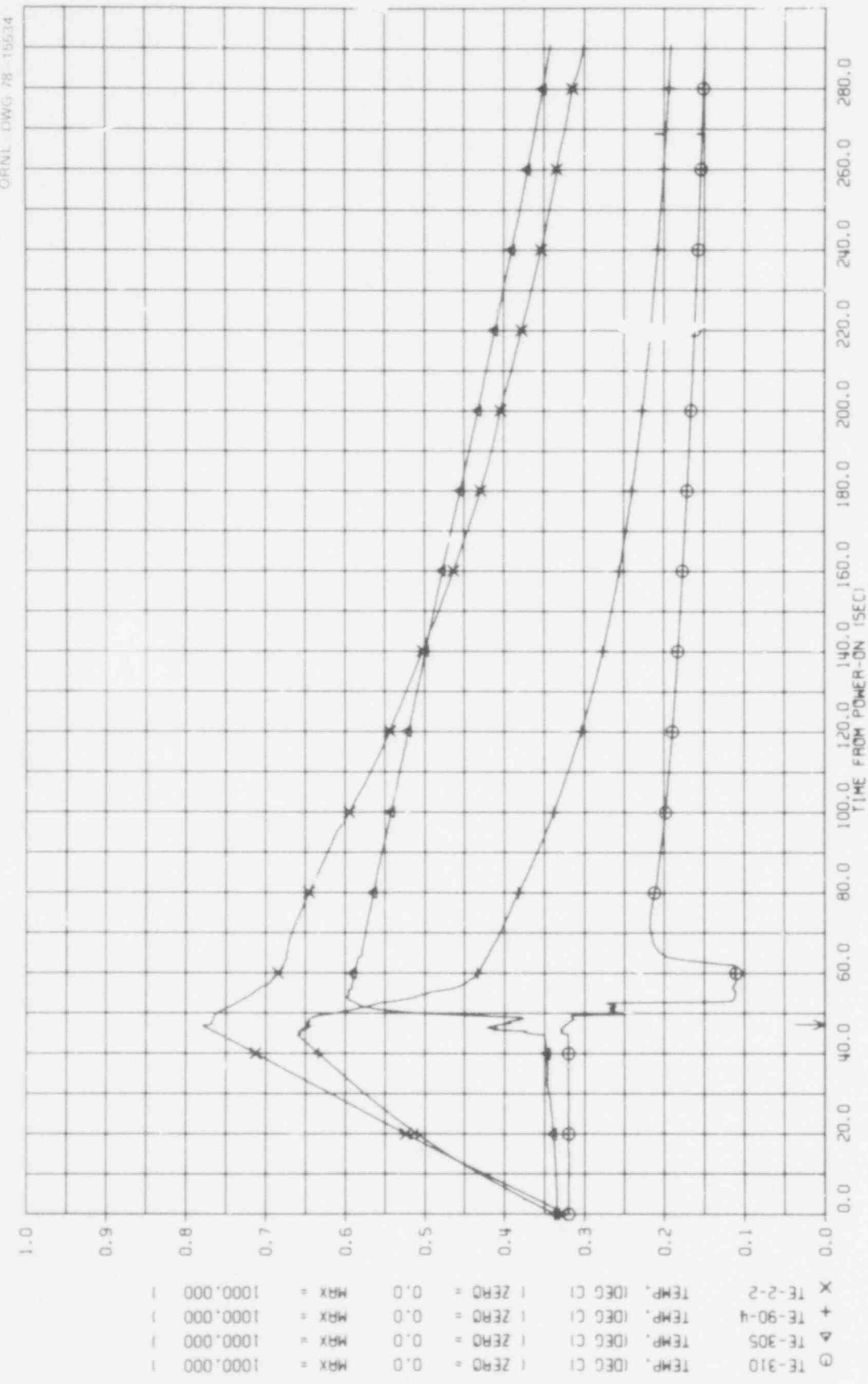

Fig. 2.95. Comparison of shroud and bundle temperatures at 76.0-cm elevation during posttest cooldown.

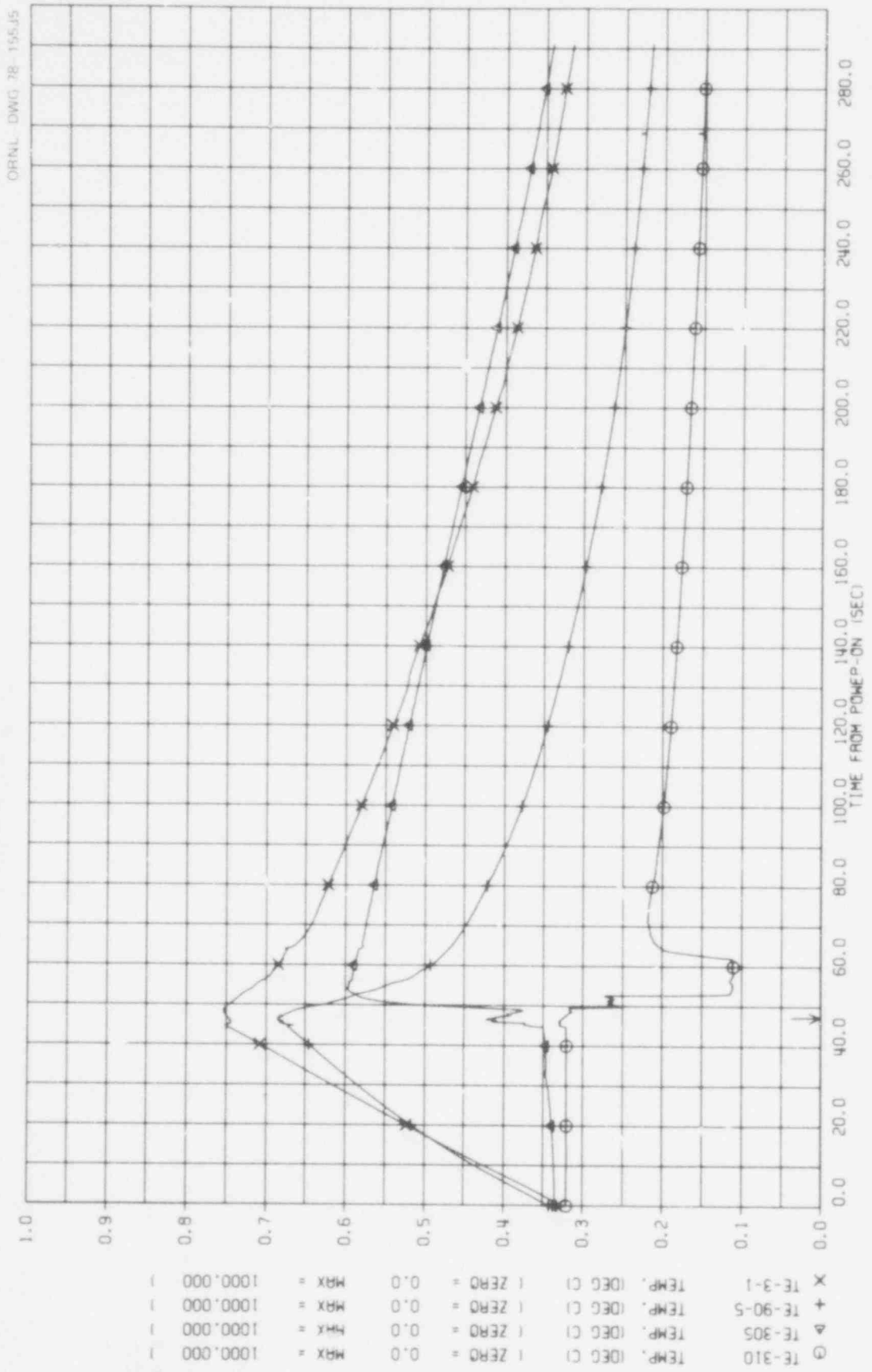

Fig. 2.96. Comparison of shroud and bundle temperatures at 46.8-cm elevation during posttest cooldown.

from power-on to the first tube burst; these data are shown graphically in Fig. 2.97. The average temperature difference between the bundle and shroud is also plotted in the figure. This difference is indicative of the potential for shroud heating by bundle heat losses. However, for the reasons cited in the discussion of the B-1 test in Section 2.3, the estimation of the contribution to the shroud heating by heat losses from the bundle is not straightforward.

Bundle and shroud heating rates, shown in Fig. 2.98, were calculated from the averaged temperatures for the same time period, using the same stepwise procedure employed for the B-1 test. The pressure trace for the first tube to burst (No. 13) is also shown for reference. The behavior of the bundle heating rate was much the same as observed in the B-1 and B-2 tests (i.e., reaching a maximum very soon after power was applied, then decreasing rather slowly until deformation commenced, and then decreasing more rapidly). The average heating rate over the time period of 9.5 to 36.5 sec was 9.5°C/sec, which is considered characteristic of the test.

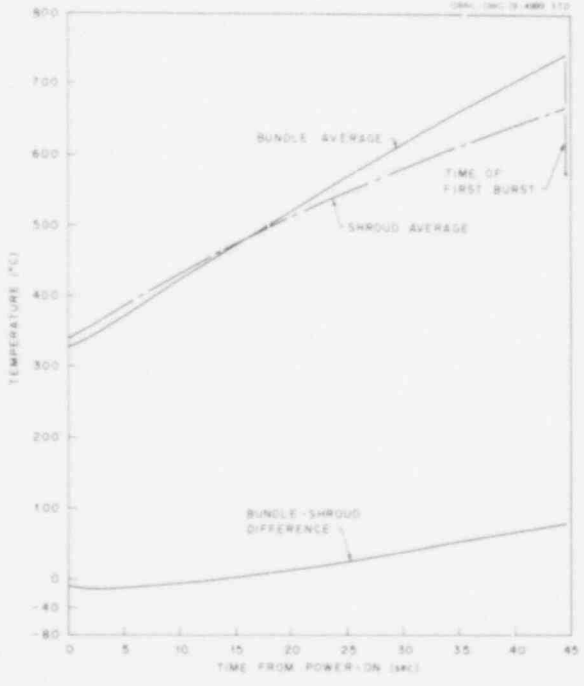

Fig. 2.97. Average temperatures in B-3 test.

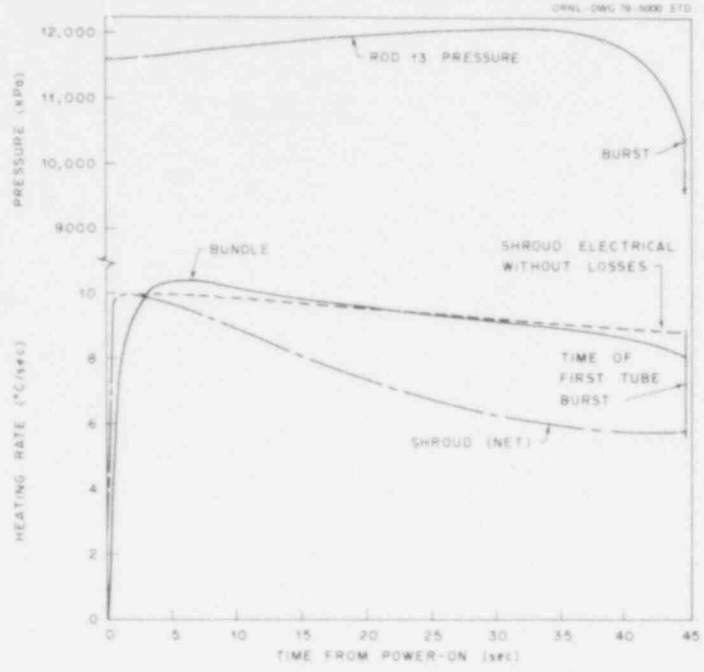

Fig. 2.98. Bundle and shroud heating rates in B-3 test.

The behavior of the observed shroud heating rate was also similar to that in the B-1 test. The expected shroud heating rate (based on physical properties, the applied electrical power, and heat losses at 1.5 sec) is shown by the dashed line. It is interesting to note that this curve is in very good agreement with the observed curve for the bundle. Also, it is evident that bundle heat losses contributed to shroud heating near the end of the transient. The average shroud heating rate over the time period of 9.5 to 36.5 sec was 7.1°C/sec.

Thermocouple locations in the B-3 test assembly, shown in Figs. 2.81 and 2.82, were selected to provide general knowledge of the temperature distribution within the bundle and to obtain more data in the region near the upper end of the heated zone. It may be recalled that in the B-1 bundle, which used the same fuel simulators in the same relative positions as the B-3 bundle, four tube bursts occurred in this region. Since very few thermocouples were located in this region of the B-1 test, there was some question about the general temperature level, and this was investigated in the B-3 test.

The temperature distribution in the B-3 assembly has been analyzed at selected times in an attempt to assess the importance of the effect of the heated shroud on the bundle temperature distribution and, hence, on the deformation. (Detailed B-3 deformation data have not yet been obtained to complete the assessment.) The B-3 temperature measurements at given elevations were averaged to obtain axial bundle-averaged temperature profiles at selected times, as shown in Fig. 2.99. The number of measurements averaged to obtain the plotted data point for each elevation is indicated in the figure. Also, the axial distribution of the tube bursts is noted at the extreme right of the figure. (Burst temperatures and times are not represented in the plot.) The averaged data show that the axial temperature profile was fairly uniform prior to the onset of deformation (i.e., until maximum pressure was attained). The profile actually became more uniform during deformation. The plots show that the region near the upper end of the heated zone was not hotter than the remainder of the bundle; this is in agreement with posttest investigation and evaluation of B-1 test results[2] that concluded that the B-1

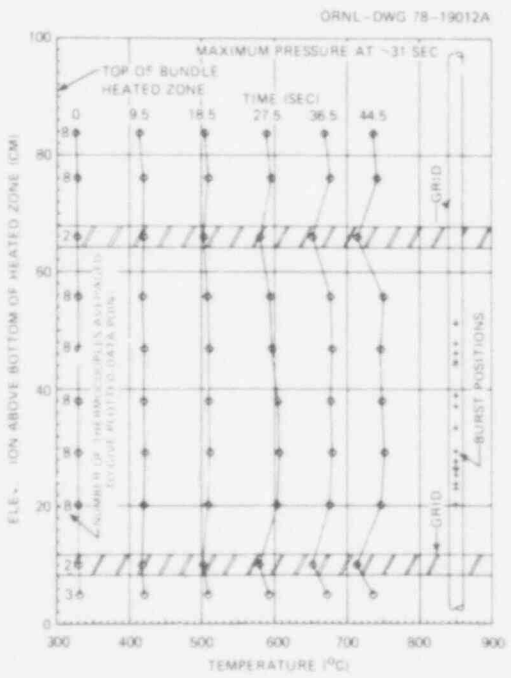

Fig. 2.99. Axial temperature distribution in B-3 test as a function of time.

bursts were not caused by overheating in this region. Also, in agreement with the B-1 and B-2 test results, the bundle was cooled by the grids.

The data have also been analyzed to obtain radial temperature profiles. For this purpose, the thermocouples were considered to be located axially at a common elevation (i.e., the axial distribution was assumed to be perfectly uniform) and radially at one of five representative positions, as indicated in Fig. 2.100. The representative positions are the radii of the inside and outside tangent surfaces of the inner and outer ring of simulators, respectively, and the radius of the shroud. (Due to symmetry, the dimensionless radii, r_i/R, are the same on the diagonals and the axes of the array if the reference radius, R, is appropriately defined.) The temperature measurements at each of the representative radial locations were averaged to obtain a temperature characteristic of that position. The profiles obtained in this manner are plotted in Fig. 2.101 and show that the bundle radial temperature distribution was very flat throughout the transient, even though a significant gradient existed across the coolant annulus between the bundle and the shroud.

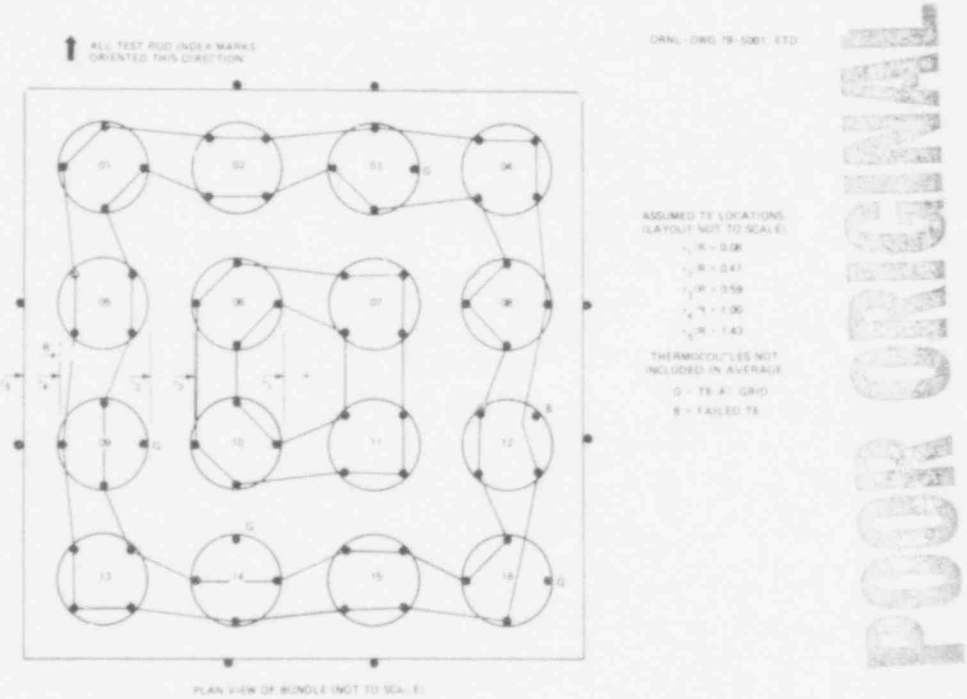

Fig. 2.100. Thermocouple assignments for calculation of radial temperature profile in B-3 test.

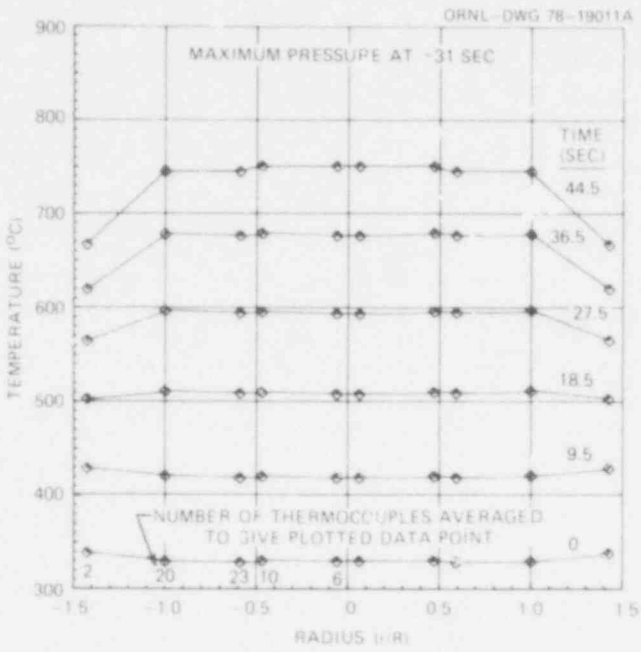

Fig. 2.101. Radial temperature distribution in B-3 test as a function of time.

Although the temperature distributions presented in Figs. 2.97, 2.99, and 2.101 characterize the bundle as a whole, the individual simulators deviated significantly from these smoothed profiles. This would be expected, since the simulator temperature distributions would be strongly influenced by the heat generation within the individual fuel simulators. Hence, the burst locations for the individual simulators are expected to show better correlation with the pretest characterization scans than with the bundle axial temperature profile.

Bundle deformation

The bundle assembly was removed from the vessel after the test and partially disassembled to facilitate posttest photography and measurement of pertinent dimensions. A selection of photographs and observations are included herein to give the reader an indication of the deformation and distortion caused by the test. It is emphasized that these data are very preliminary and qualitative; quantitative data cannot be obtained until the bundle is sectioned transversely (now in progress) and detailed strain measurements are made.

Figure 2.102 shows the north and east faces of bundle P-3; similar views of the south and west faces are shown in Fig. 2.103. As evident in the figures, there is considerable distortion and localized deformation of the tubes, and both appear more extensive than that observed in the B-1 and B-2 tests. Also, the regions of relatively large deformation appear more extensive in this test. There is evidence that the tubes

ORNL PHOTO 3882-78

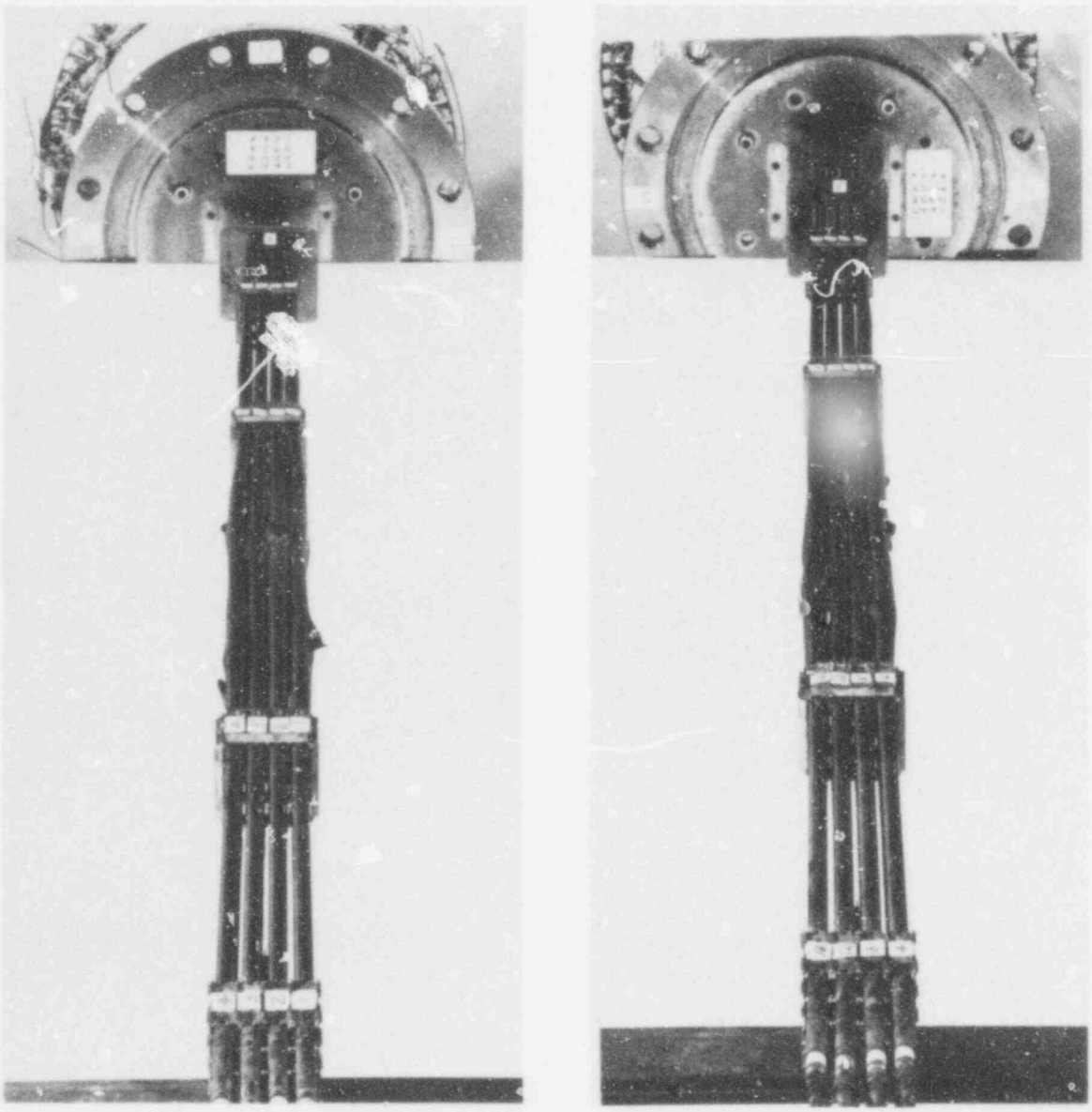

Fig. 2.102. Posttest view showing deformation and distortion on north (left) and east (right) faces of B-3 bundle.

ORNL PHOTO 3883-78

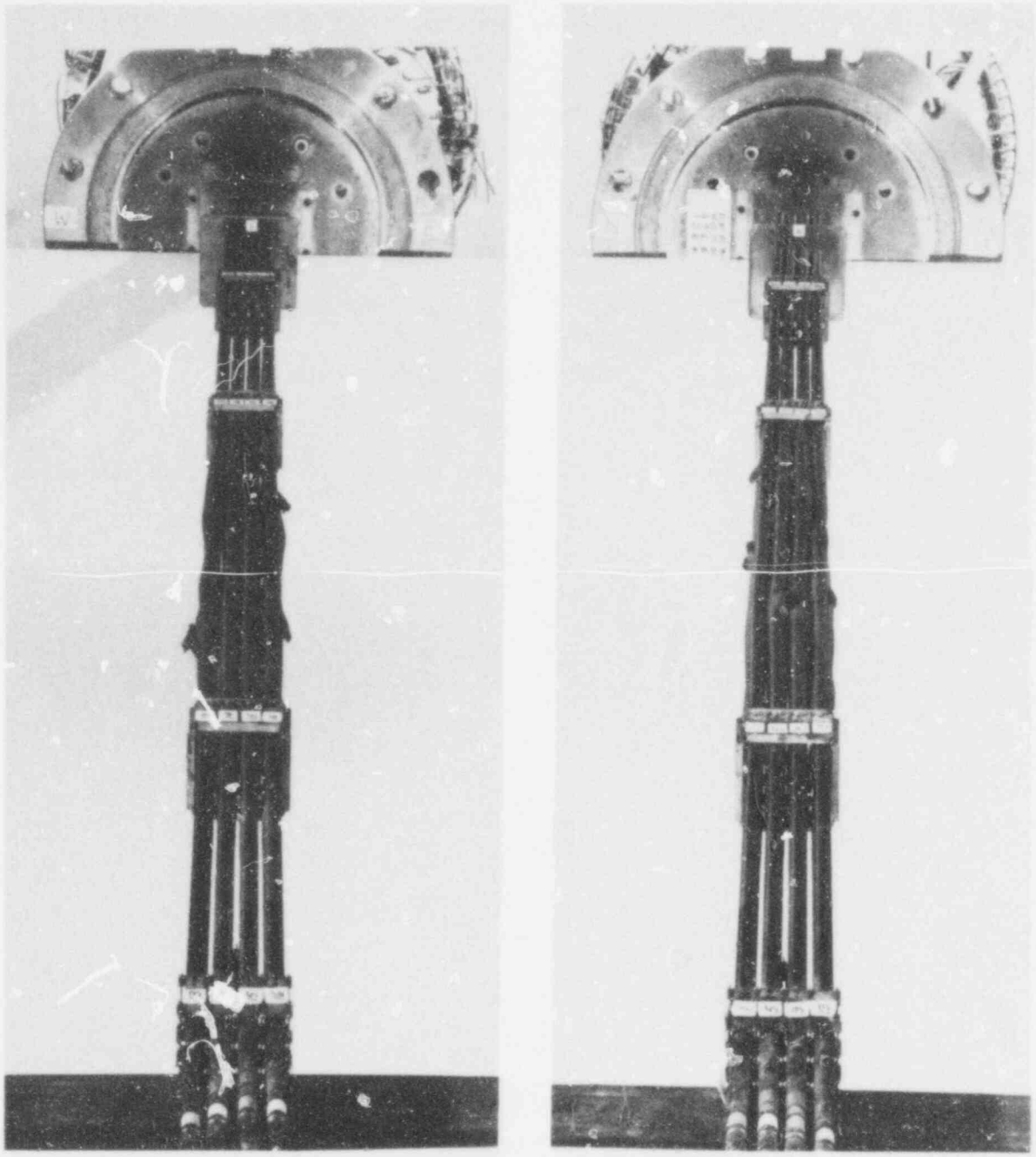

Fig. 2.103. Posttest view showing deformation and distortion on south (left) and west (right) faces of B3 bundle.

accommodated each other to a certain extent (i.e., the deformed regions are somewhat staggered and nested together).

All the bursts occurred between the two interior (to the heated zone) grids; deformation in this region is shown in Figs. 2.104 and 2.105 for the four faces of the bundle. The corresponding faces of the

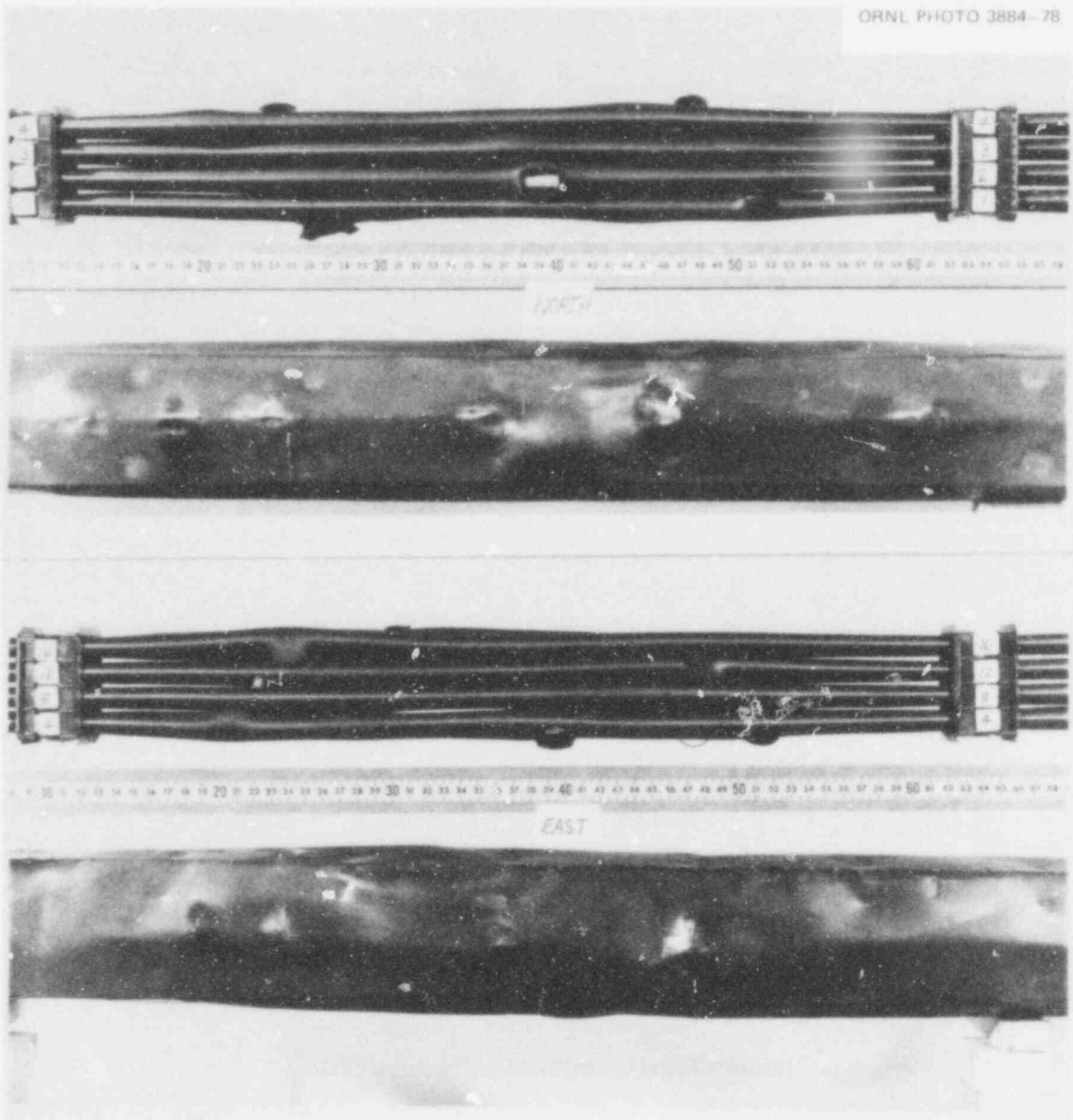

Fig. 2.104. Deformation and distortion of B-3 bundle and shroud between interior grids as viewed from north (top) and east (bottom) faces.

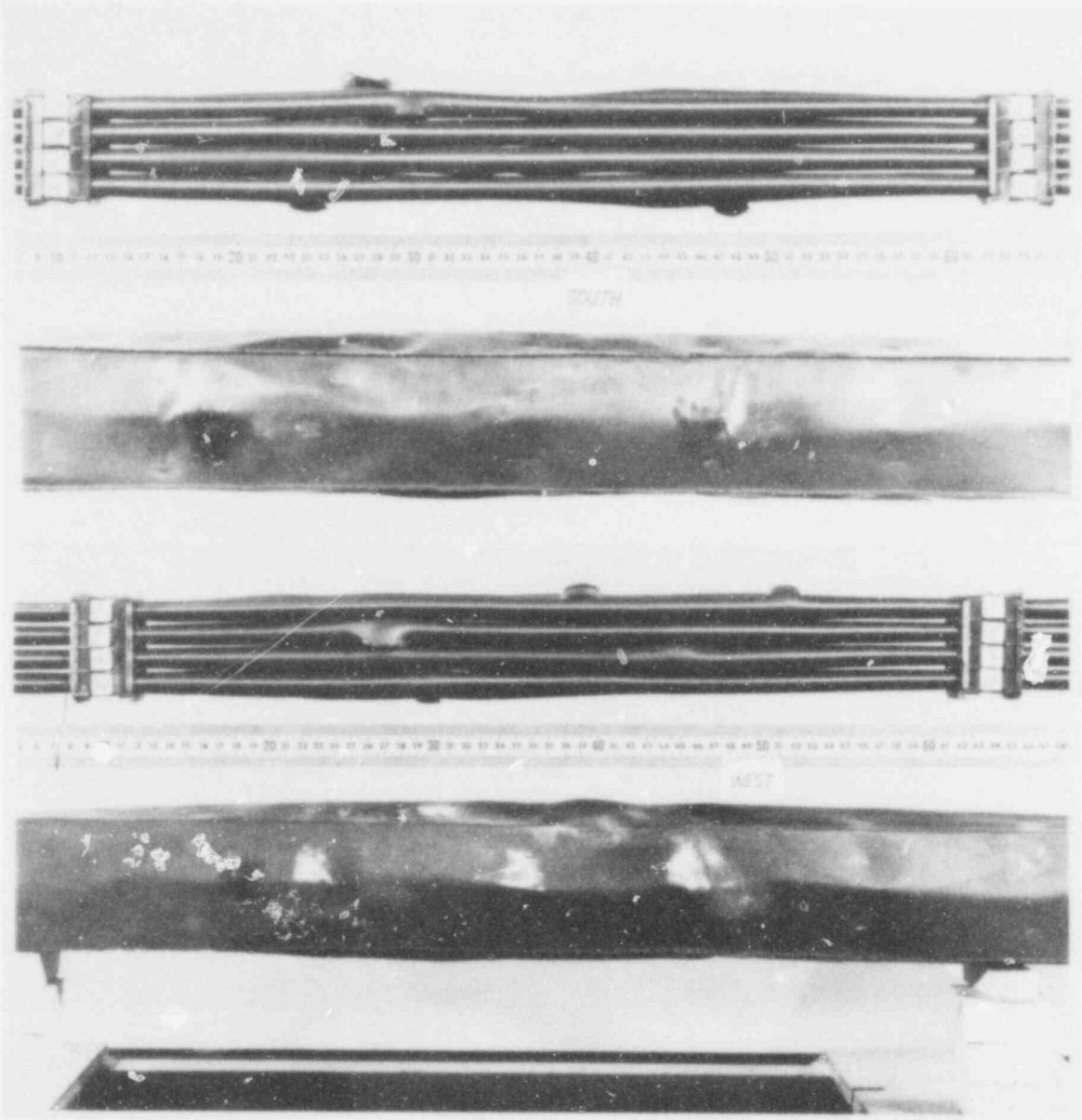

Fig. 2.105. Deformation and distortion of B-3 bundle and shroud between interior grids as viewed from south (top) and west (bottom) faces.

shroud are also shown to indicate the deformation caused by the slight increase in vessel pressure during the time of the bursts. The scale in the photographs gives the distance (in centimeters) from the bottom of the bundle heated zone. Most of the burst regions are clearly evident

in the photographs. Even though the burst zones show significant deformation, there appears to be space for coolant cross flow.

Figure 2.106 gives the axial locations of the B-3 bursts, and Fig. 2.107 gives the approximate orientation. The axial position and length of the bursts were determined by viewing the burst opening from the inside of the tube with a boroscope and are considered reasonably accurate. The angular orientations were also determined in this manner, but with considerable less accuracy.

Since the same fuel simulators (internal heaters) were used in the same relative positions in both the B-1 and B-3 test assemblies, some similarity in deformation would be expected, even though the heating rates were quite different (i.e., ~30°C/sec for B-1 and ~9.5°C/sec for B-3). This is evident in Fig. 2.108, which shows the east face of each of the bundles. Figure 2.109 shows the north face of the B-3 bundle in the region above the upper grid where four tubes (Nos. 1, 2, 4, and 7) burst in the B-1 test. Although there is a fair amount of deformation in this region (i.e., the thermal entrance zone), the temperature was slightly cooler (see Fig. 2.99) relative to the region between the two grids, and the bursts were shifted downward to the hotter zone.

Also, except for the above mentioned B-1 tubes and Nos. 5 and 15, which had pinhole bursts at or very near thermocouple welds, correlation of the burst locations in the two tests might be expected; this comparison is made in Table 2.16. Excluding the six exceptions for the reasons cited above, the axial locations of seven bursts (one of which is questionable) agree well and three do not, while only one angular orientation agrees well (with two being questionable). The lack of angular orientation agreement may reflect a difference in radial temperature uniformity in the two tests.

The burst in the No. 7 simulator was unusual, aside from the fact that the simulator was tested at essentially constant pressure conditions, as discussed previously. Figure 2.110 shows the north face of the bundle in the region of the burst, which is directly beneath simulator 3 in the photograph. The small rectangle encloses a portion of TE 7-4, which was blown out of the tube by the escaping gas. One lip of the No. 7 burst extends under the No. 4 simulator and contains a small crack, as shown

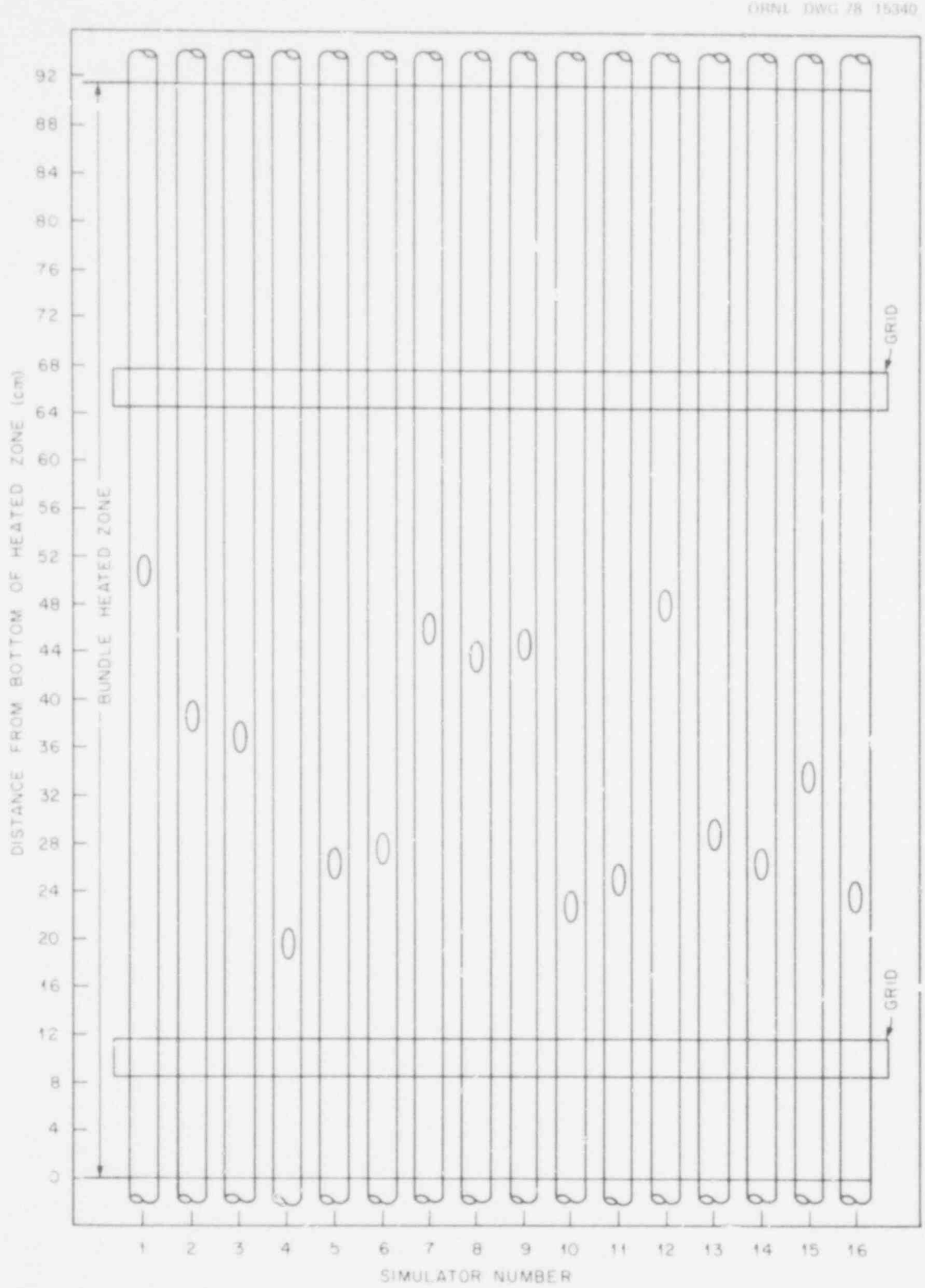

Fig. 2.106. Axial location of bursts in B-3.

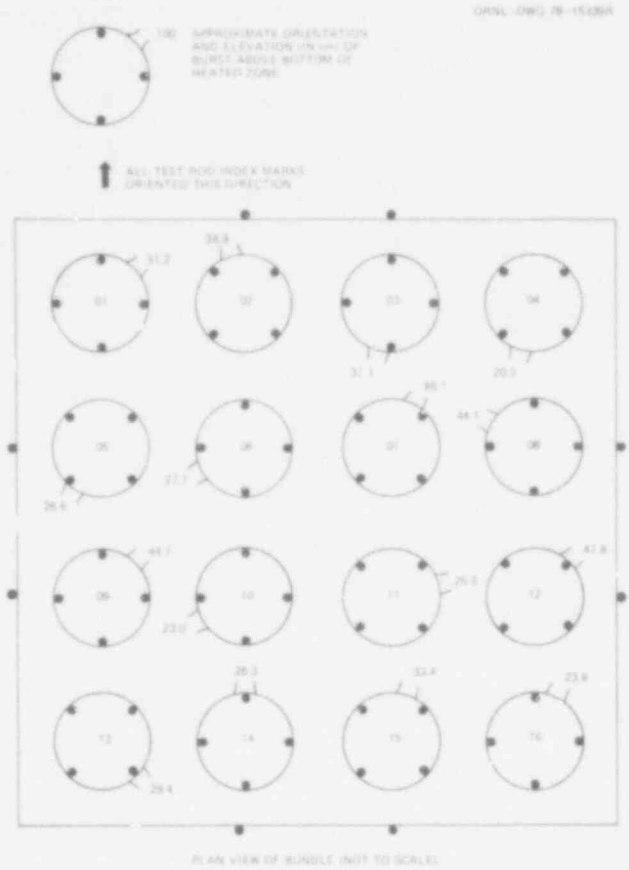

Fig. 2.107. Approximate orientation of bursts in B-3.

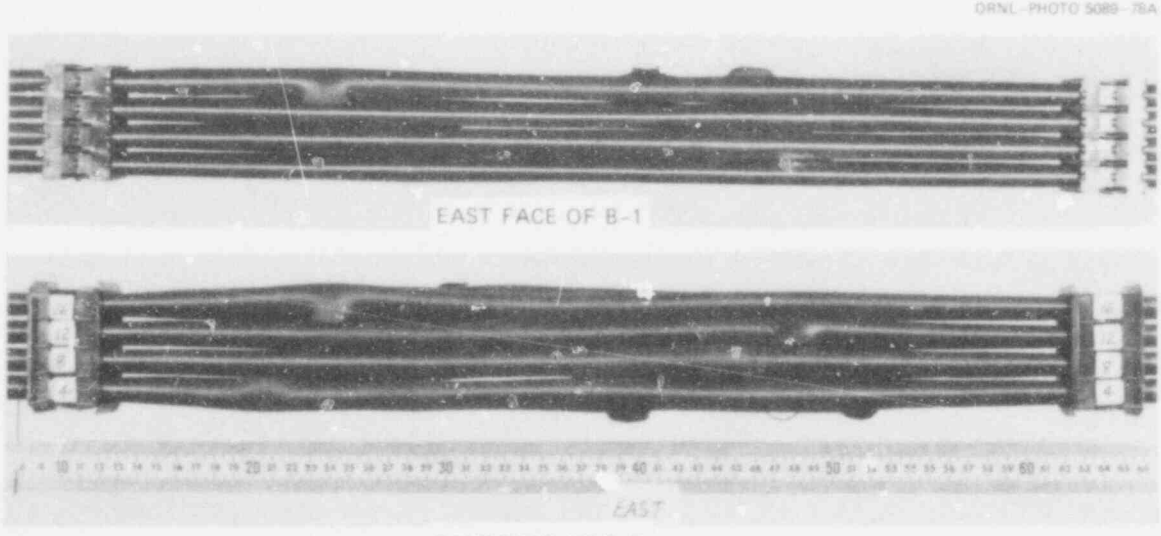

Fig. 2.108. Comparison of deformation in B-1 and B-3 as viewed from east face of bundles.

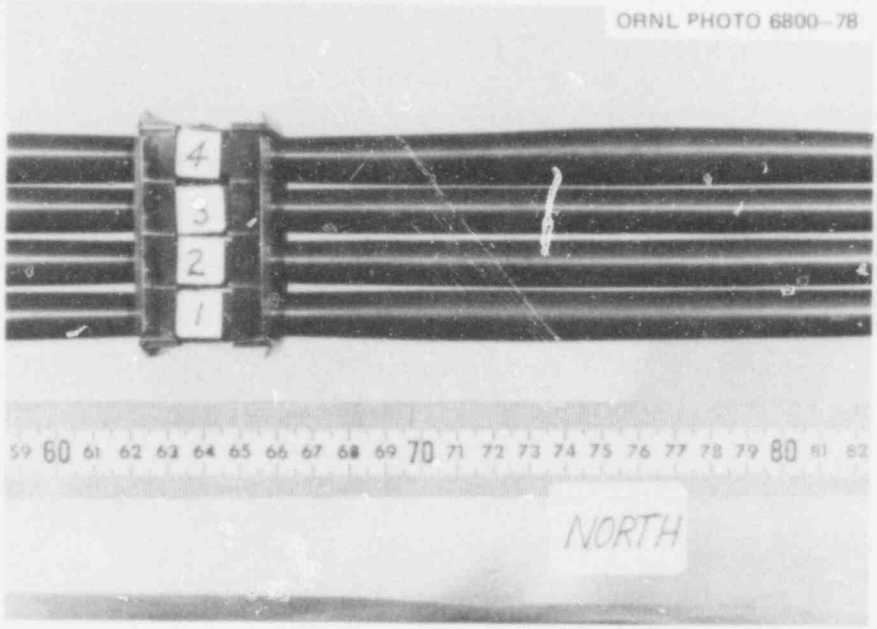

Fig. 2.109. View of north face of B-3 showing deformation in region where four tubes (Nos. 1, 2, 4, and 7) burst in B-1.

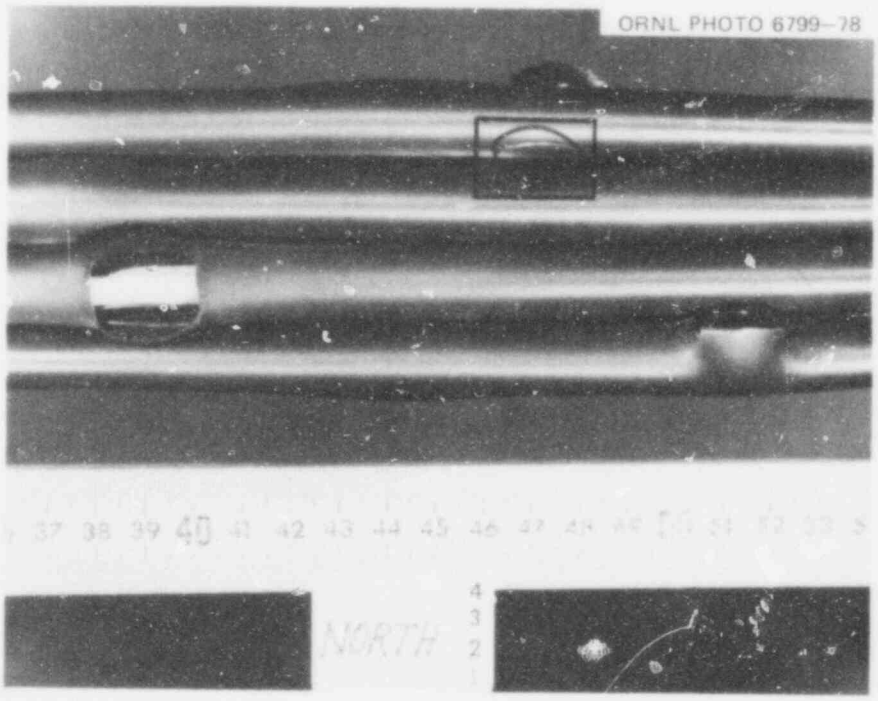

Fig. 2.110. View of north face of B-3 in region of the burst in simulator 7. Although the burst (directly below simulator 3) is not evident, a portion of TE 7-4 may be seen (in small rectangle) protruding from the burst opening.

Table 2.16. Preliminary comparison of burst locations in B-3 and B-1 tests

Simulator No.	B-3 burst location		B-1 burst location		Agreement	
	Axial[a] (cm)	Angle[b] (deg)	Axial[a] (cm)	Angle[b] (deg)	Axial	Angle
1	51.2	45	76.5	310	No[c]	No[c]
2	38.9	350	77.3	330	No[c]	No[c]
3	37.1	190	50.4	120	No	No
4	20.3	190	76.8	295	No[c]	No[c]
5	26.6	220	47.5	30	No[d]	No[d]
6	27.7	240	29.7	205	Yes	?
7	46.1	35	76.5	315	No[c]	No[c]
8	44.1	300	44.7	310	Yes	Yes
9	44.7	45	46.7	75	Yes	?
10	23.0	240	23.9	330	Yes	No
11	25.3	80	22.3	210	?	No
12	47.8	45	48.6	335	Yes	No
13	29.4	135	40.8	205	No	No
14	26.3	0	46.4	170	No	No
15	33.4	20	20.1	325	No[d]	No[d]
16	23.8	20	23.9	355	Yes	?

[a]Elevation above bottom of heated zone.

[b]Measured clockwise looking down on top of bundle.

[c]Bursts occurred above upper grid in B-1; combined effect of heating rate and steam flow redistributed these bursts in B-3.

[d]Pinhole failure at or near thermocouple weld in B-1.

in Figs. 2.111 and 2.112. These photographs, which are enlarged views of the region enclosed by the small rectangle marked on Fig. 2.110, were taken looking down into the bundle at the No. 7 simulator. The lip of the large burst extends beneath the No. 4 simulator approximately as indicated by the dotted line; the small crack is clearly evident in the lip of the large burst. The crack is ~3 mm long and is located axially

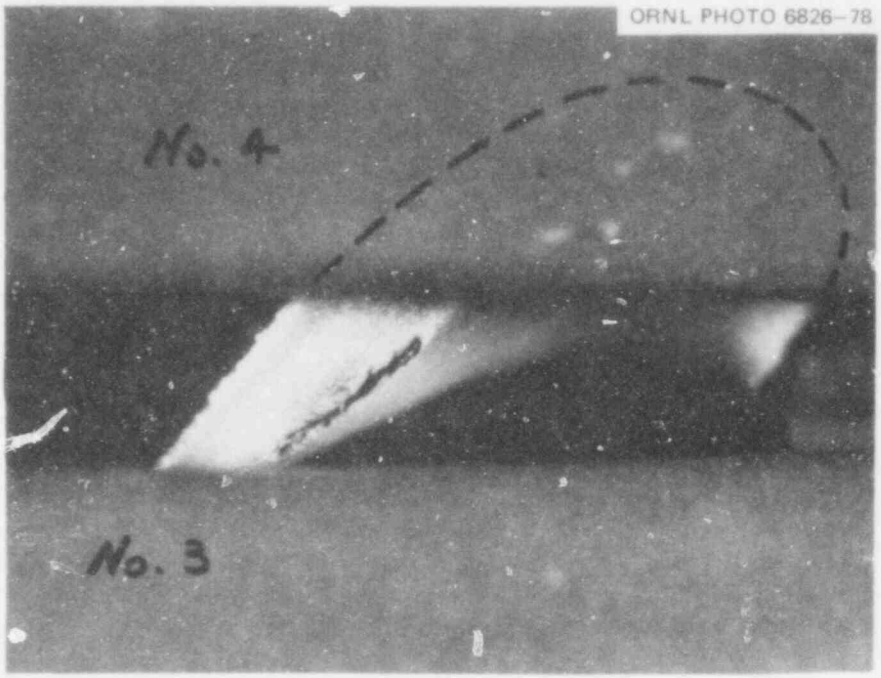

Fig. 2.111. Enlarged view of region enclosed in small rectangle in Fig. 2.110 showing small crack in lip of simulator 7 burst. Dotted line shows approximate edge of lip beneath simulator 4.

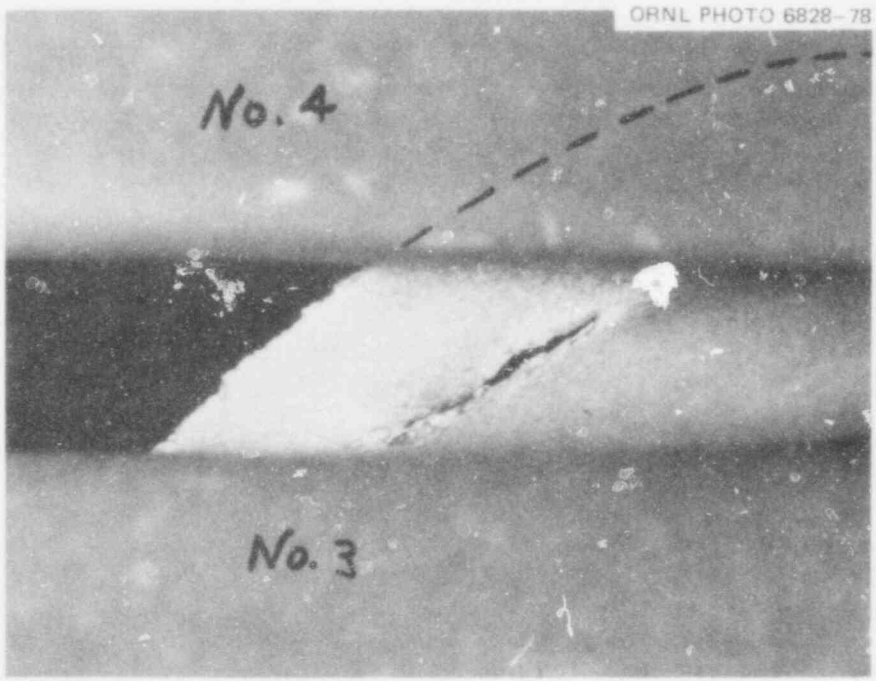

Fig. 2.112. Small crack in the lip of simulator 7 as viewed from a different angle.

about the center and 2 to 3 mm around from the primary burst opening. The cause and timing of the small crack are not known at this time. Metallurgical examination of the failure will be performed in an attempt to explain the small crack.

Axial shrinkage of the tubes in the B-3 assembly was significantly greater and showed more variation than was observed in the B-1 assembly, as indicated in Table 2.17. The reason for this is unknown, but it may be the result of a more uniform temperature distribution and greater circumferential deformation in the B-3 test assembly.

Table 2.17. Comparison of axial shrinkage in B-3 and B-1 tests

Simulator No.	B-3 heated length change[a]		B-1 heated length change[a]	
	mm	%	mm	%
1	21.4	2.3	7.9	0.9
2	26.2	2.9	8.7	1.0
3	19.1	2.1	4.8	0.5[b]
4	24.6	2.7	6.4	0.7
5	22.2	2.4	11.9	1.3
6	22.2	2.4	8.7	1.0
7	21.4	2.3	16.7	1.8
8	22.2	2.4	16.7	1.8
9	21.0	2.3	10.3	1.1
10	20.2	2.2	9.5	1.0
11	17.1	1.9	8.7	1.0
12	18.3	2.0	7.1	0.8
13	12.7	1.4	16.7	1.8
14	17.9	2.0	9.5	1.0
15	24.6	2.7	9.5	1.0
16	15.9	1.7	8.7	1.0

[a]B-3 test temperature ~760°C; B-1 test temperature ~870°C.

[b]Elongation rather than shrinkage, since burst temperature was ~937°C.

...formation of the thin (0.25 mm) Inconel shroud was also greater in the B-3 than in the B-1 test. This is probably due primarily to the higher simulator pressure in B-3 (∿11,600 kPa vs ∿8700 kPa in B-1), although the shroud temperature was approximately the same (∿680°C in B-3 and ∿700°C in B-1) in both tests. Figure 2.113, a photograph taken looking down into the B-3 shroud, clearly shows the deformation and a tendency for the square cross section to assume a circular shape. The deformation apparently was caused by a slight pressure increase in the shroud relative to the vessel increase at the time of the bursts. Since the shroud was not supported by insulation (as it was in the B-1 test), it was free to deform.

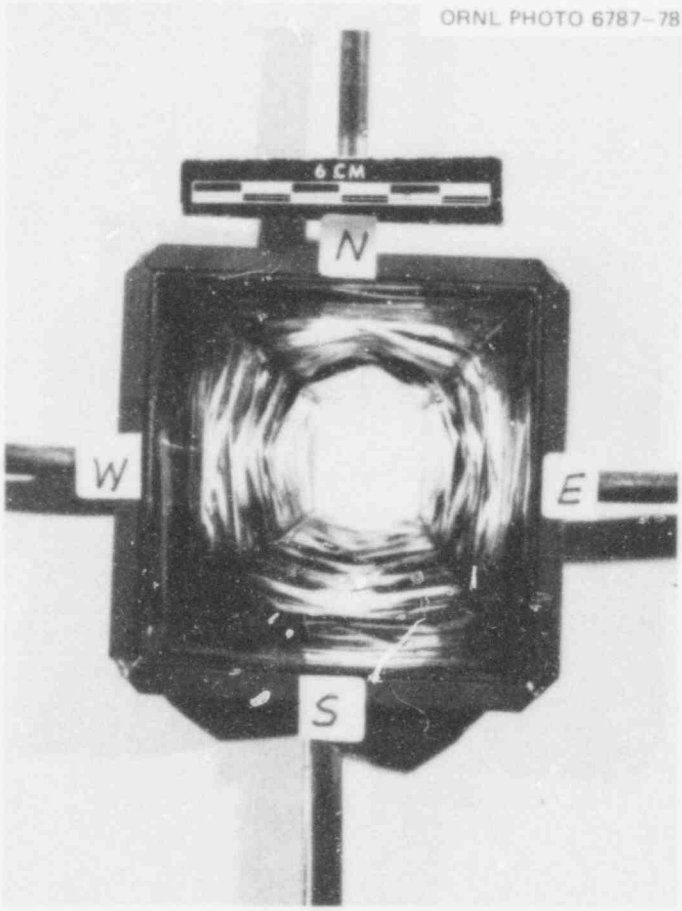

Fig. 2.113. End view of B-3 shroud showing deformation and tendency to become round.

Deformation and distortion were such that flow testing of the bundle in the two available flow shrouds was precluded, and a larger shroud was fabricated for the flow tests. Preliminary results of these tests and similar flow studies on the reference bundle in the new shroud (to facilitate correlation of these data with those of the other flow shrouds) are reported in Section 2.8.

After the flow tests were completed, the bundle was cast in an epoxy matrix and is now being sectioned to determine the strain in each tube as a function of axial position.

2.7 Analysis of B-1 and B-2 Flow Tests

J. F. Mincey

Additional flow tests were conducted with the 4 × 4 reference bundle in shroud 1 to clarify uncertainties regarding the proper friction factor correlation and the grid spacer pressure loss coefficient to be used in predicting pressure losses of the deformed bundles with COBRA-IV.[8] The results from these tests were then used as COBRA-IV input to recalculate pressure loss profiles for B-1 and B-2 in shroud 1. After comparing the calculated pressure loss profiles with those obtained by experiment, the new friction factor correlation and the spacer loss coefficient were found to be more applicable to MRBT experimental data than those previously reported.[4] In addition, estimates of the error limits on these new values were obtained that reflect the precision with which the determining experimental parameters are known.

Two additional series of flow tests were conducted with the reference bundle in shroud 1 (see Fig. 2.114), using only one grid spacer in the instrumented portion of the shroud. In the first series of tests, this single grid spacer was located about 19.25 cm below the point which corresponds to the bottom of the B-1 heated zone. The primary objective of this test series was to examine the change in slope, as a function of flow rate, of the pressure loss vs bundle position curves downstream of the grid spacer. As noted in Fig. 2.115, a friction factor correlation of $0.235\ Re^{-0.2}$ in combination with a grid spacer loss coefficient of 0.60 produced COBRA-IV calculations in agreement with the experimental

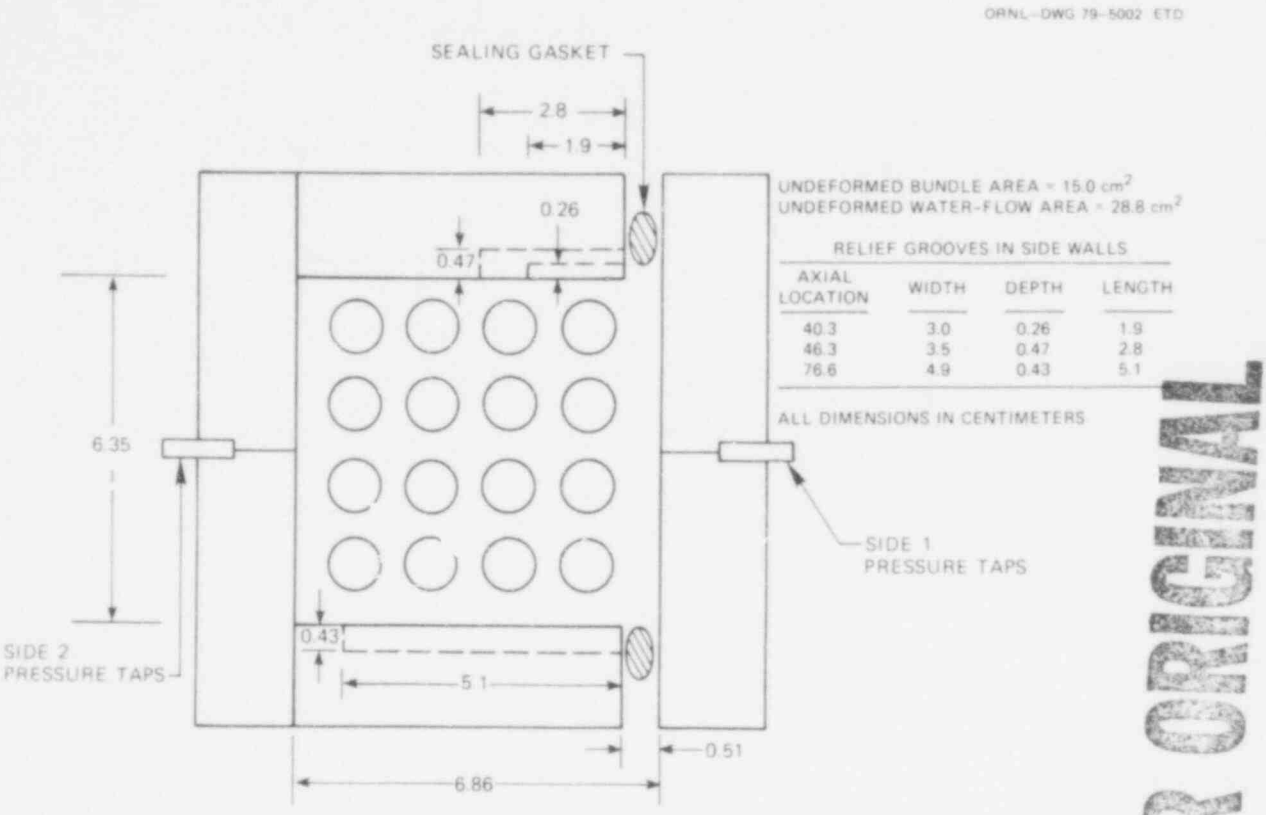

Fig. 2.114. Dimensions of shroud 1.

pressure loss profiles. A discrepancy of about 4% (not observed in the second series of tests) was found to exist between the volumetric flow rate measurements of the turbine meter and the magnetic flow meter. The turbine meter flow rate measurements indicated consistently higher values and were discarded in favor of the magnetic flow meter values, which are believed to be more correct. Analyses performed with the turbine meter values as input to COBRA-IV required a friction factor of $0.220\ Re^{-0.2}$ and a spacer loss coefficient of 0.55 to produce good agreement with the experimental pressure loss profiles consistent with the approximate dependence of pressure loss on the square of the flow rate. The figure shows a region of disturbance persisting about 30 cm (about 21 hydraulic diameters) downstream of the grid spacer. The disturbance, barely evident in Fig. 2.115a, becomes prominent at a Reynolds number of $\sim 10^5$. Also, at ~65 cm, the linear dependence of the pressure loss profile on the bundle length is seen to deteriorate. As previously reported,[3] relief grooves

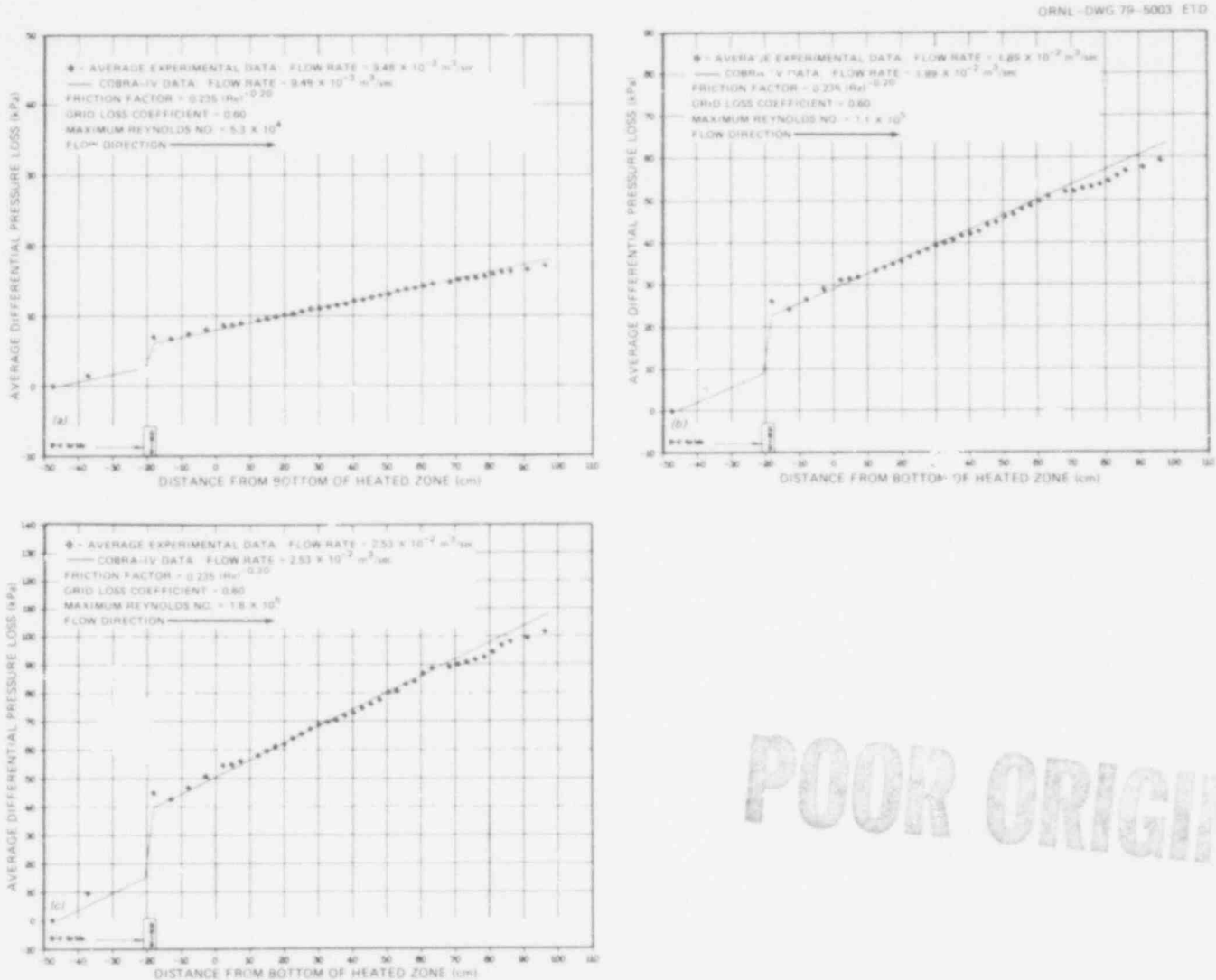

Fig. 2.115. Comparison of predicted and measured pressure loss profiles of reference bundle in shroud 1 with grid located 19.25 cm below zero reference point. (a) Re = 5.3×10^4; (b) Re = 1.1×10^5; and (c) Re = 1.6×10^5.

were cut in the sidewalls of shroud 1 at 40.3, 46.3, and 76.6 cm (see Fig. 2.114) to accommodate local deformation of the B-1 bundle. Since only slight indications exist in the figure to suggest the presence of the two lower grooves, the deterioration noted above 65 cm is thought to be primarily a shroud exit effect rather than being caused by the groove at 76.6 cm.

In the second series of tests, the grid spacer was located ∿18.35 cm above the point corresponding to the bottom of the B-1 heated zone. As shown in Fig. 2.116, the friction factor correlation which gave good agreement in the first test series again produced COBRA-IV calculations which nicely duplicated the slopes of the curves for a range of flow rates. However, the spacer loss coefficient appears to be somewhat low even though the same spacer and relative orientation on the bundle were used for both test series. Also, the lack of a pronounced disturbance downstream of the grid spacer in the second test series indicates some difficulty in closely reproducing grid-spacer-induced effects. Finally, the linearity of the pressure loss profiles for the second series of tests deteriorates at about the same position and for the same reasons mentioned with regard to the first test series.

Using friction factor correlations and spacer loss coefficients in the neighborhood of those values discussed above, COBRA-IV calculations were made for the reference bundle (with a complete grid set), B-1, and B-2 in shroud 1. The calculated pressure loss profiles for the reference bundle are compared with experimental data in Fig. 2.117 as a function of flow rate. The friction factor correlation used in this comparison ($0.220\ Re^{-0.2}$), while producing a slightly steeper slope than the experimental data indicated in Fig. 2.117c, fairly well represents the data for the other flow rates. The primary discrepancy in the comparisons appears to arise as a result of the spacer loss coefficient being too large. Figure 2.118 gives the results of a second computational analysis of the experimental data utilizing the friction factor correlation and spacer loss coefficient value determined from the single-grid test series; the agreement in Fig. 2.118 between calculation and experiment is poor relative to that exhibited in Figs. 2.115 and 2.116. Hence, the reference bundle experimental data for the two single-grid series

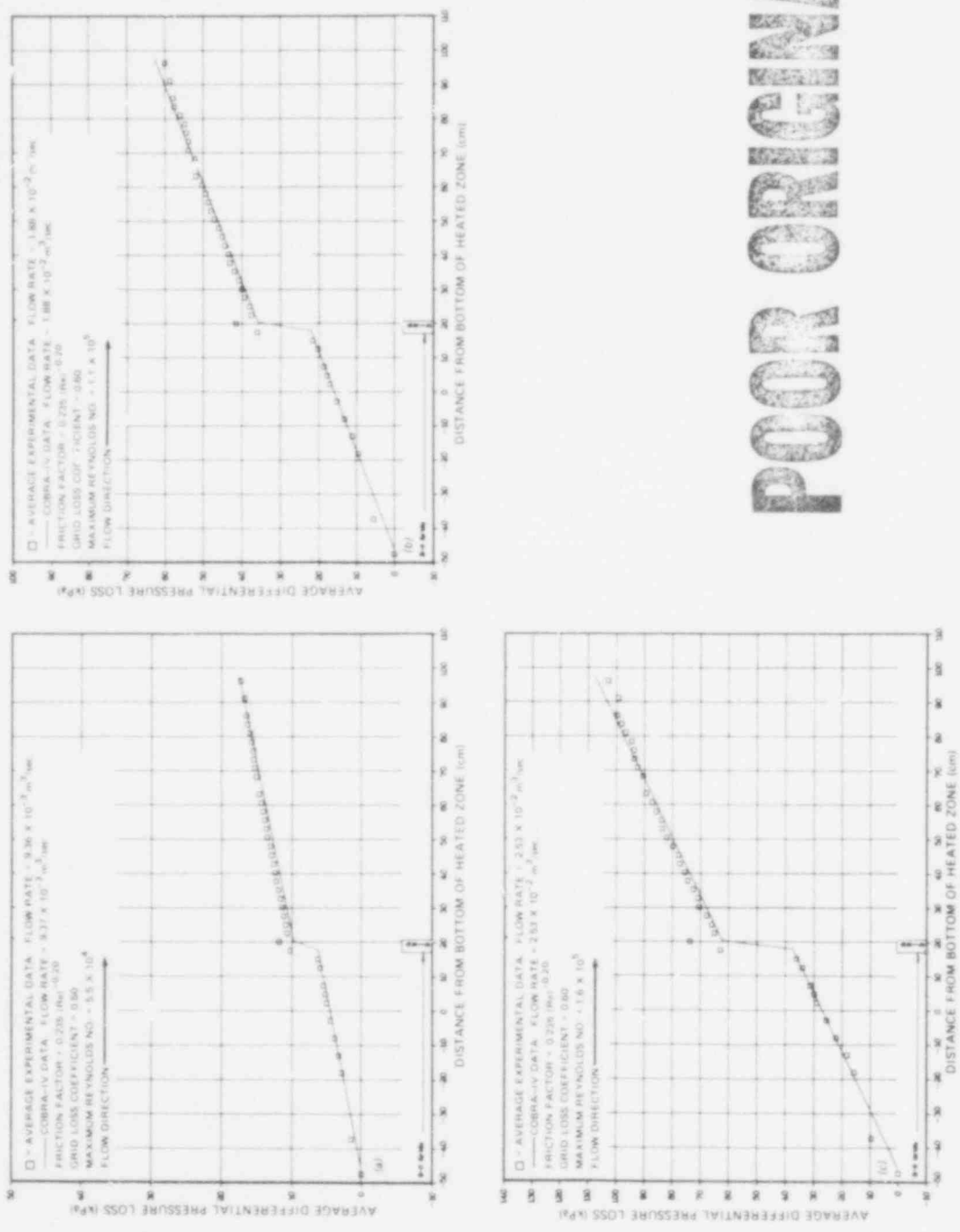

Fig. 2.116. Comparison of predicted and measured pressure loss profiles of reference bundle in shroud 1 with grid located 18.85 cm above zero reference point. (a) Re = 5.5×10^4; (b) Re = 1.1×10^5; and (c) Re = 1.6×10^5.

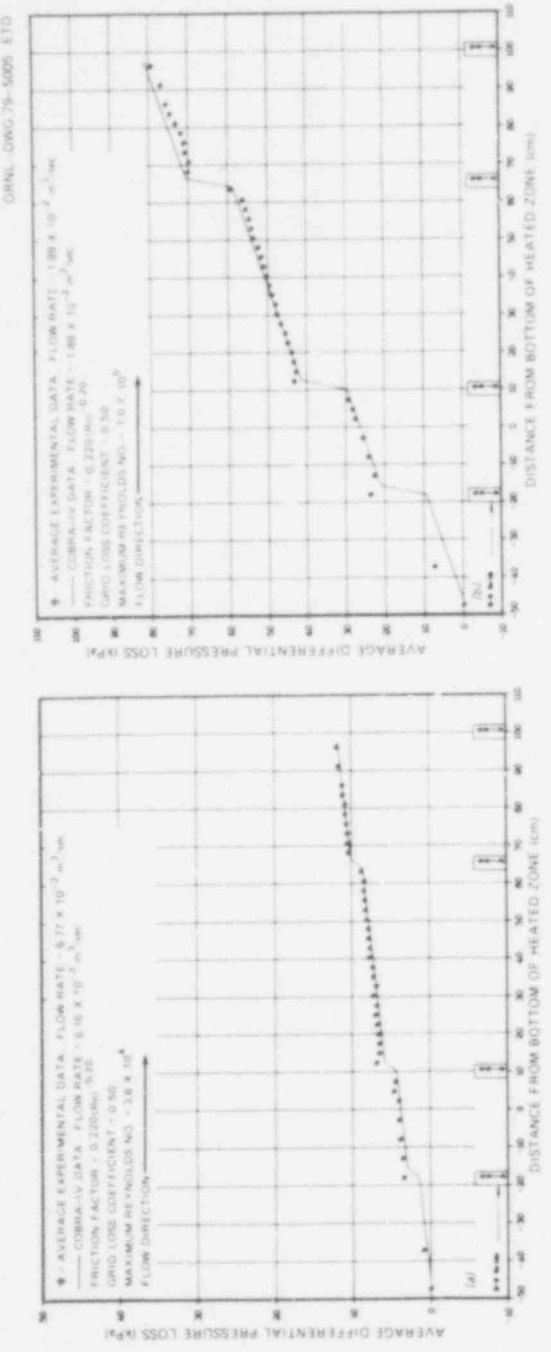

Fig. 2.117. Comparison of predicted and measured pressure loss profiles of reference bundle with four grids in shroud 1. (a) Re = 3.6×10^4; (b) Re = 1.0×10^5; and (c) Re = 1.3×10^5.

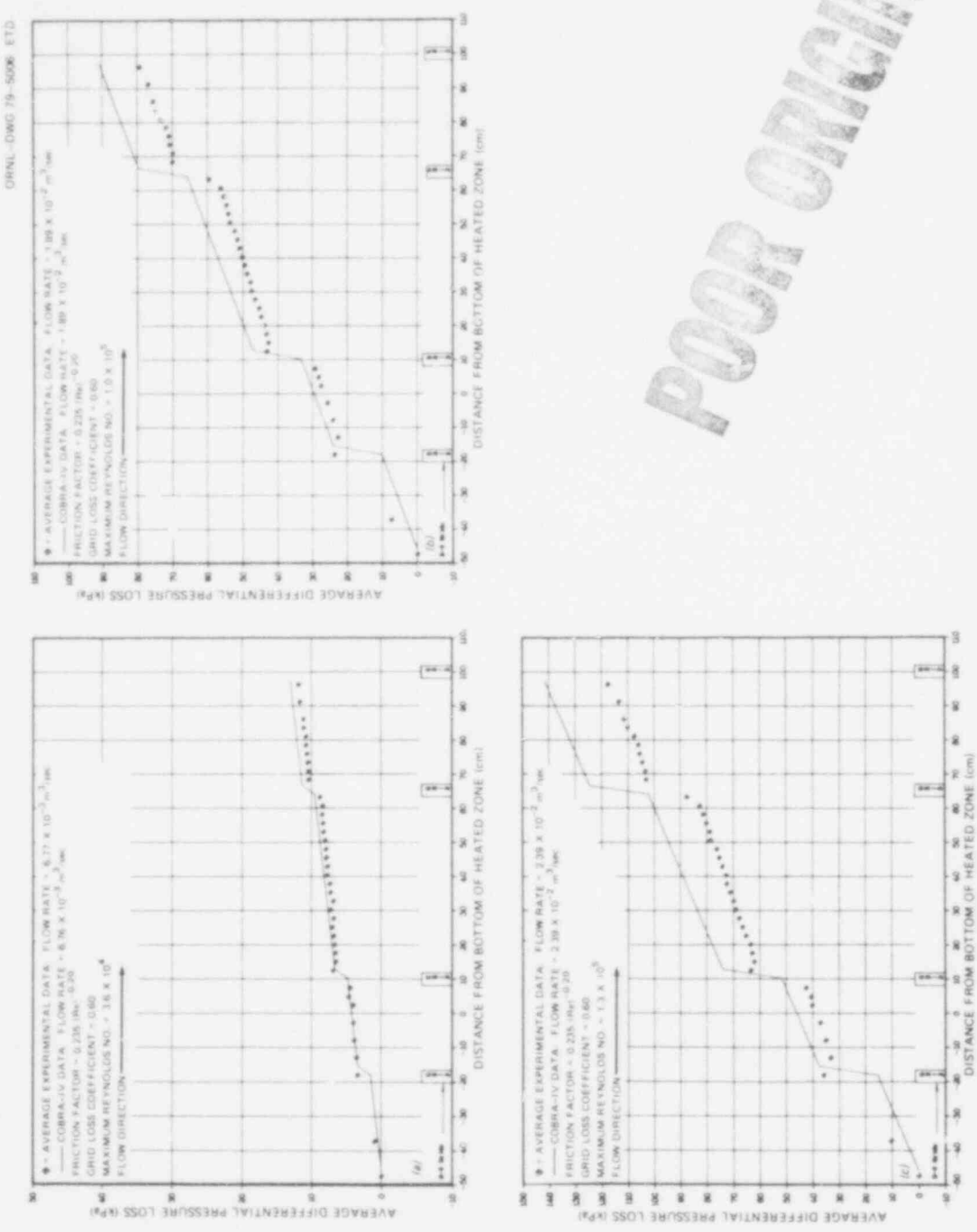

Fig. 2.118. Comparison of predicted and measured pressure loss profiles of reference bundle with four grids in shroud 1 using the friction factor correlation and grid loss coefficient determined from the single-grid test series. (a) Re = 3.6×10^4; (b) Re = 1.0×10^5; and (c) Re = 1.3×10^5.

of tests and that for the complete grid set suggests that the observed 4% precision placed on the flow rate measurements limits the determined friction factor to $0.228 \pm 0.010\ Re^{-0.2}$ and that this and other factors limit the determination of the spacer loss coefficient to 0.55 ± 0.08.

Using approximately the lower and upper limit values for these two quantities, calculational analyses reported earlier[3,4] were repeated using the maximum and minimum flow area definitions (see Section 2.4 for definition) of the B-1 and B-2 tube deformation data. The lower and upper estimates of the friction factor and spacer loss coefficient gave, respectively, the results shown in Figs. 2.119 and 2.120 for B-1 using the minimum flow restriction definition. The best calculational fit to the experimental data appears in Figs. 2.119b, 2.119c, and 2.120a. Results of a comparable analysis of the B-1 data using the maximum restriction definition are presented in Figs. 2.121 and 2.122. Again, the best fit is given by the upper-limit set in Fig. 2.122a and by the lower-limit set in Figs. 2.121b and 2.121c for the larger flow rates. Also, using the maximum flow area restriction definition in the analysis appears to overestimate the actual pressure loss profile, whereas the minimum flow area restriction definition seems to be a good approximation of B-1 experimental flow test results.

Figures 2.123 and 2.124 present the results of similar analyses of the B-2 data using the lower- and upper-limit sets and the minimum flow area restriction definition. Although both analyses underestimated the effect of the large flow area restriction above the 65-cm elevation, the best fit to the experimental data is again given by the upper-limit set for the smaller flow rates and the lower-limit set for the higher flow rates (i.e., Figs. 2.124a and 2.124b and Figs. 2.123b and 2.123c). Results of similar analyses of the B-2 data, using the maximum flow area restriction definition, are given in Figs. 2.125 and 2.126. Although the large flow restriction above 65 cm is underestimated, the best fit to the experimental pressure loss data appears to be Fig. 2.126. Both minimum and maximum flow restriction definitions underestimated the B-2 experimental data, with the maximum definition giving the best agreement.

In summary, additional flow tests of the reference bundle with a single grid in shroud 1 were conducted to better define the friction

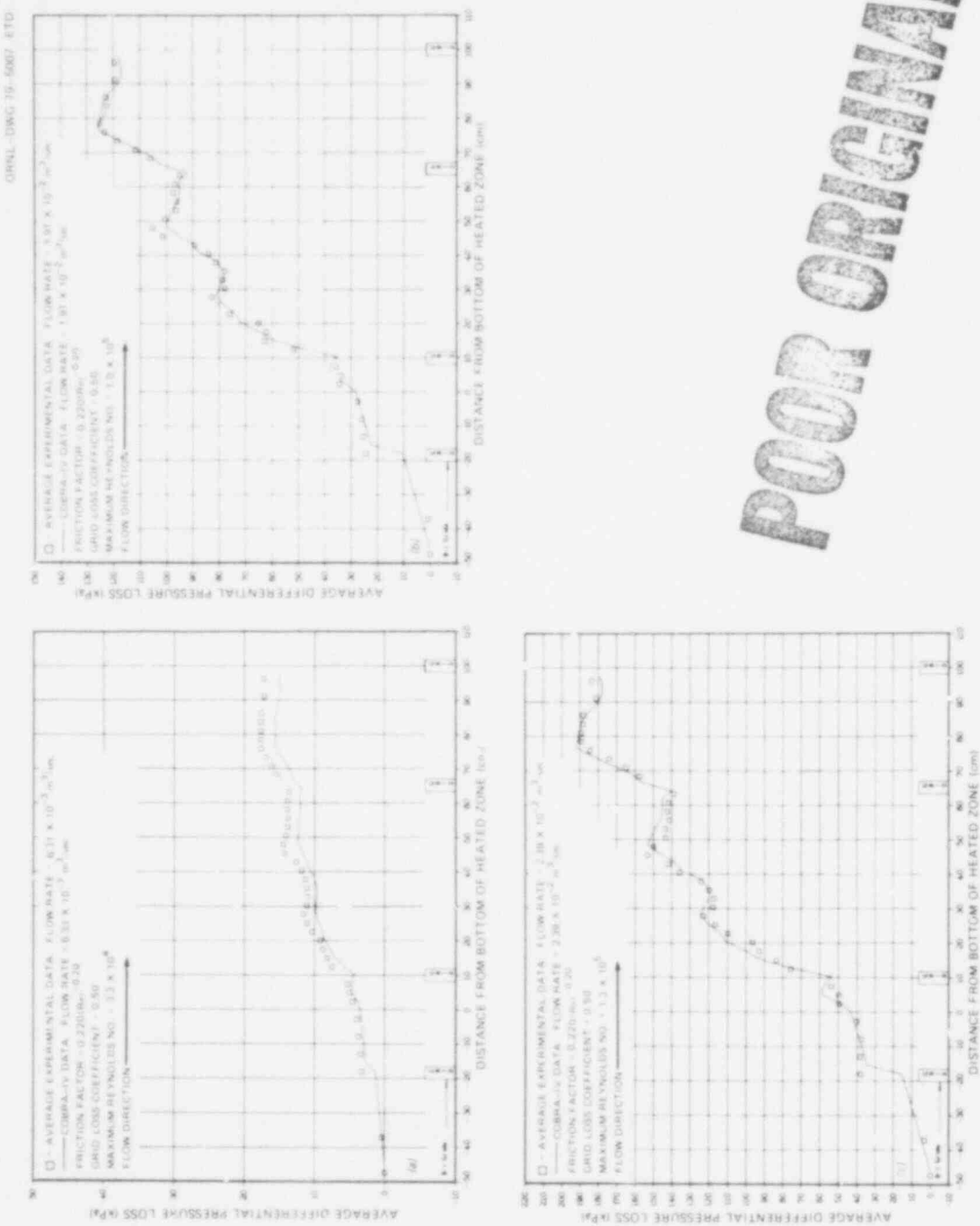

Fig. 2.119. Comparison of predicted and measured pressure loss profiles of B-1 in shroud 1 using lower-limit estimates for friction factor correlation and grid loss coefficient and minimum flow area restriction definition. (a) Re = 3.3×10^4; (b) Re = 1.0×10^5; and (c) Re = 1.3×10^5.

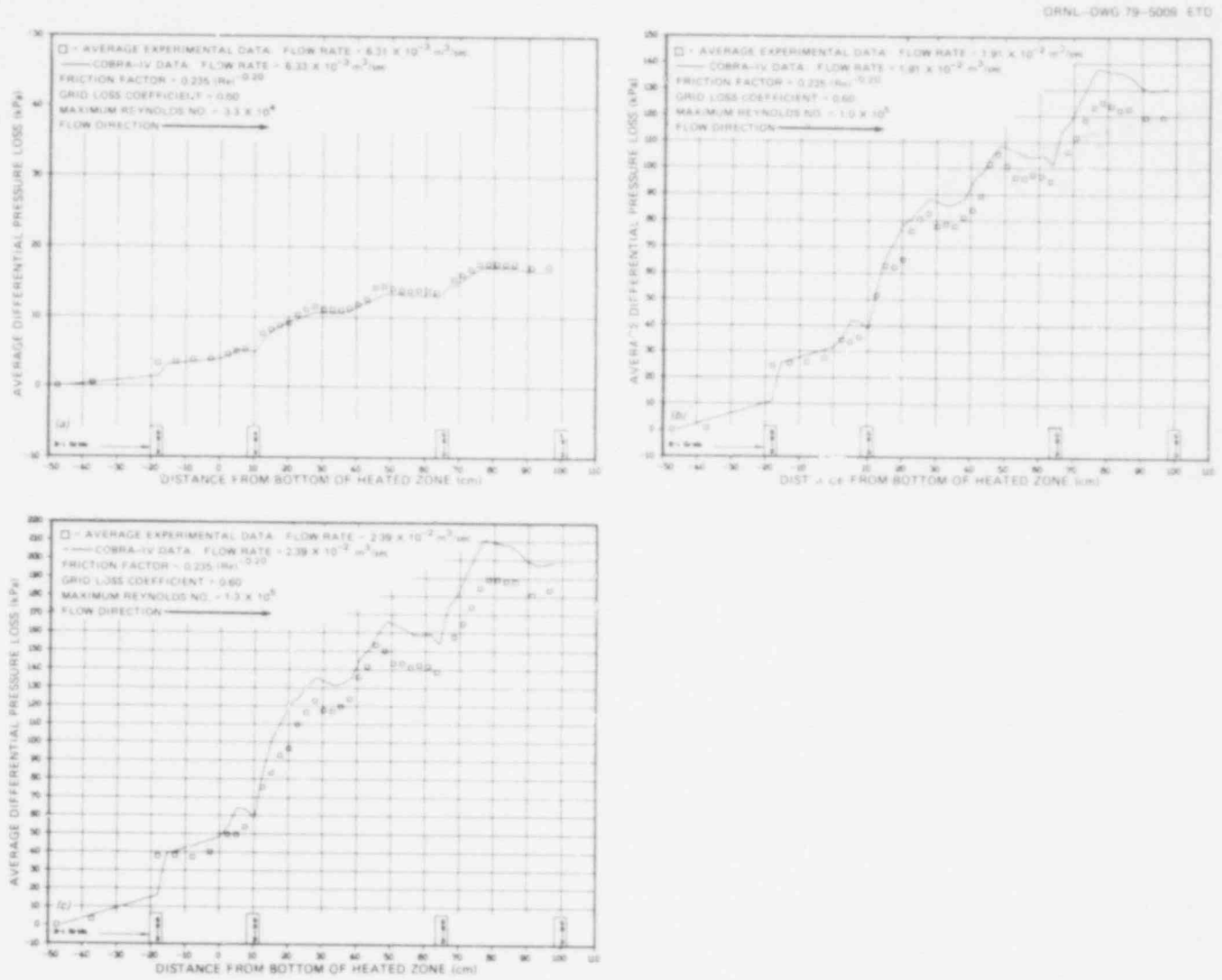

Fig. 2.120. Comparison of predicted and measured pressure loss profiles of B-1 in shroud 1 using upper-limit estimates for friction factor correlation and grid loss coefficient and minimum flow area restriction definition. (a) Re = 3.3×10^4; (b) Re = 1.0×10^5; and (c) Re = 1.3×10^5.

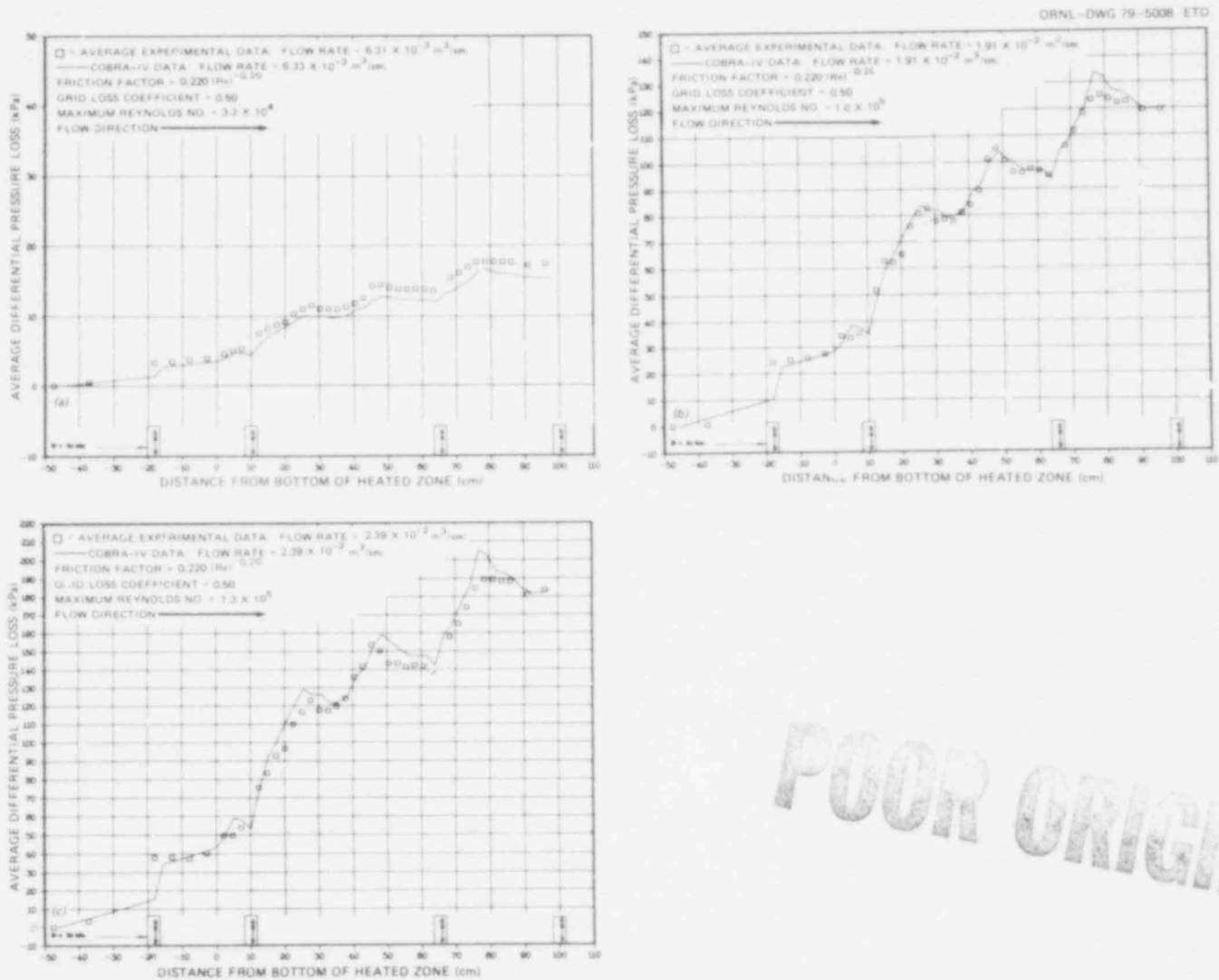

Fig. 2.121. Comparison of predicted and measured pressure loss profiles of B-1 in shroud 1 using lower-limit estimates for friction factor correlation and grid loss coefficient and maximum flow area restriction definition. (a) Re = 3.3×10^4; (b) Re = 1.0×10^5; and (c) Re = 1.3×10^5.

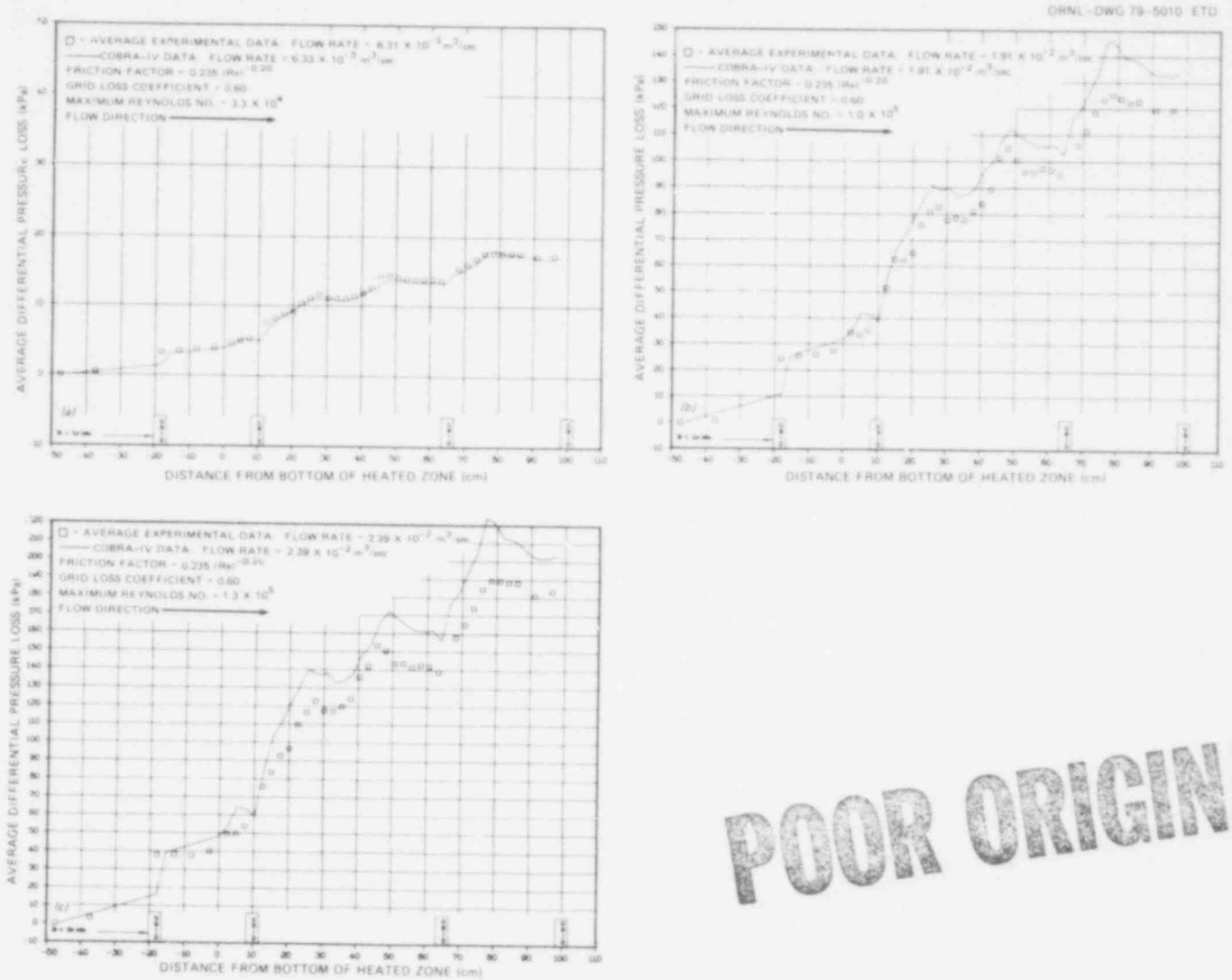

Fig. 2.122. Comparison of predicted and measured pressure loss profiles of B-1 in shroud 1 using upper-limit estimates for friction factor correlation and grid loss coefficient and maximum flow area restriction definition. (a) Re = 3.3×10^4; (b) Re = 1.0×10^5; and (c) Re = 1.3×10^5.

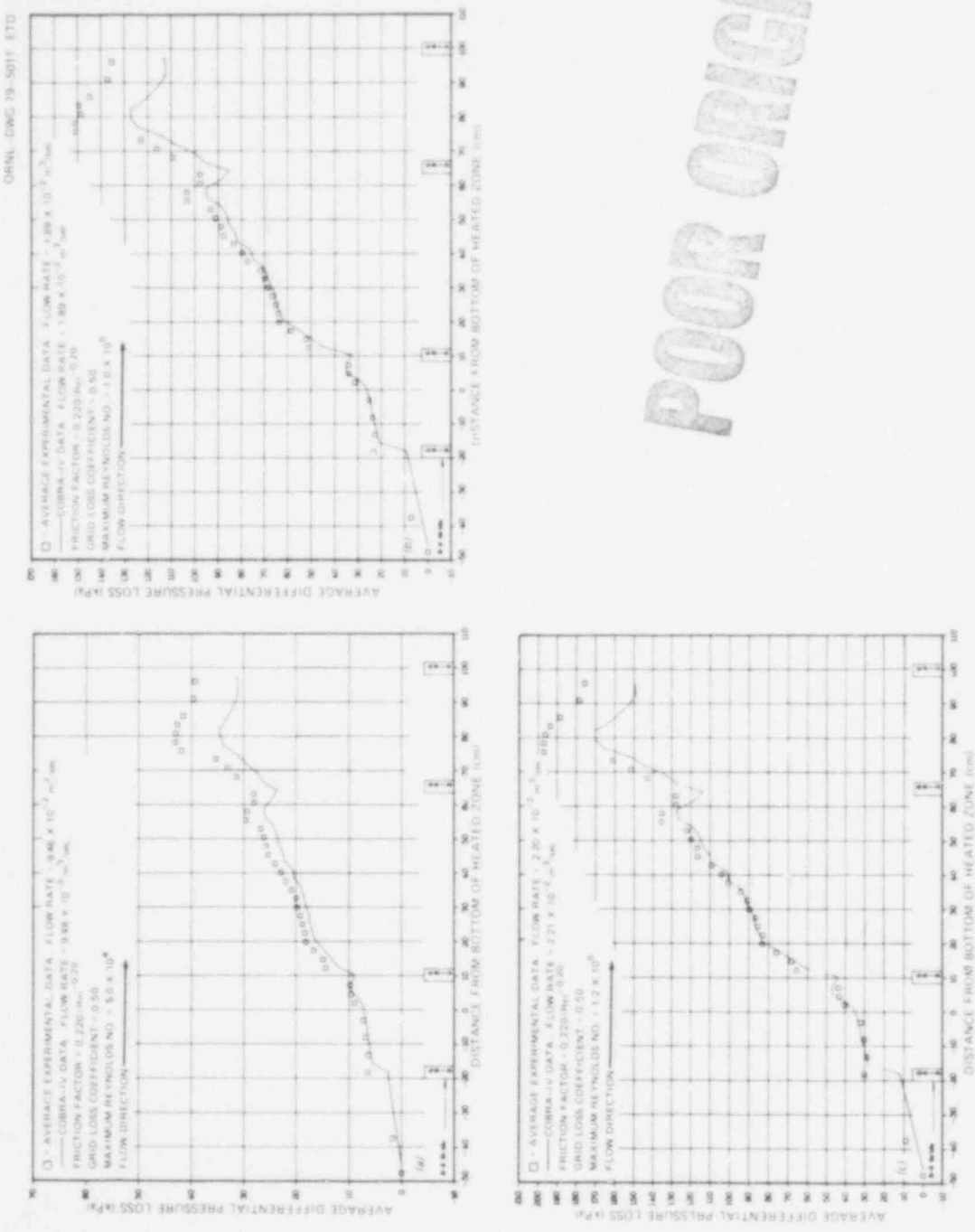

Fig. 2.123. Comparison of predicted and measured pressure loss profiles of B-2 in shroud 1 using lower-limit estimates for friction factor correlation and grid loss coefficient and minimum flow area restriction definition. (a) Re = 5.0×10^4; (b) Re = 1.0×10^5; and (c) Re = 1.2×10^5.

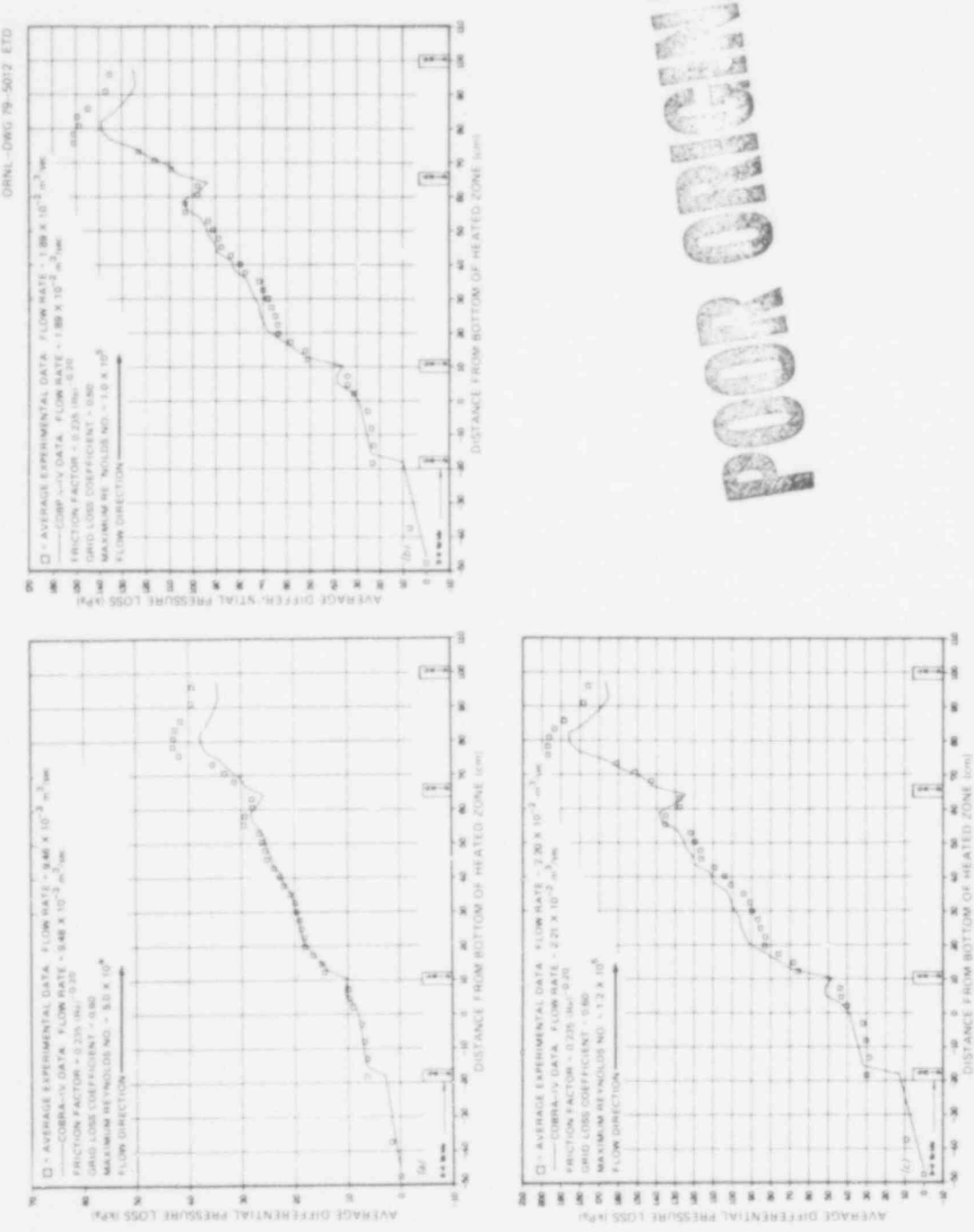

Fig. 2.124. Comparison of predicted and measured pressure loss profiles of B-2 in shroud 1 using upper-limit estimates for friction factor correlation and grid loss coefficient and minimum flow area restriction definition. (a) Re = 5.0×10^4; (b) Re = 1.0×10^5; and (c) Re = 1.2×10^5.

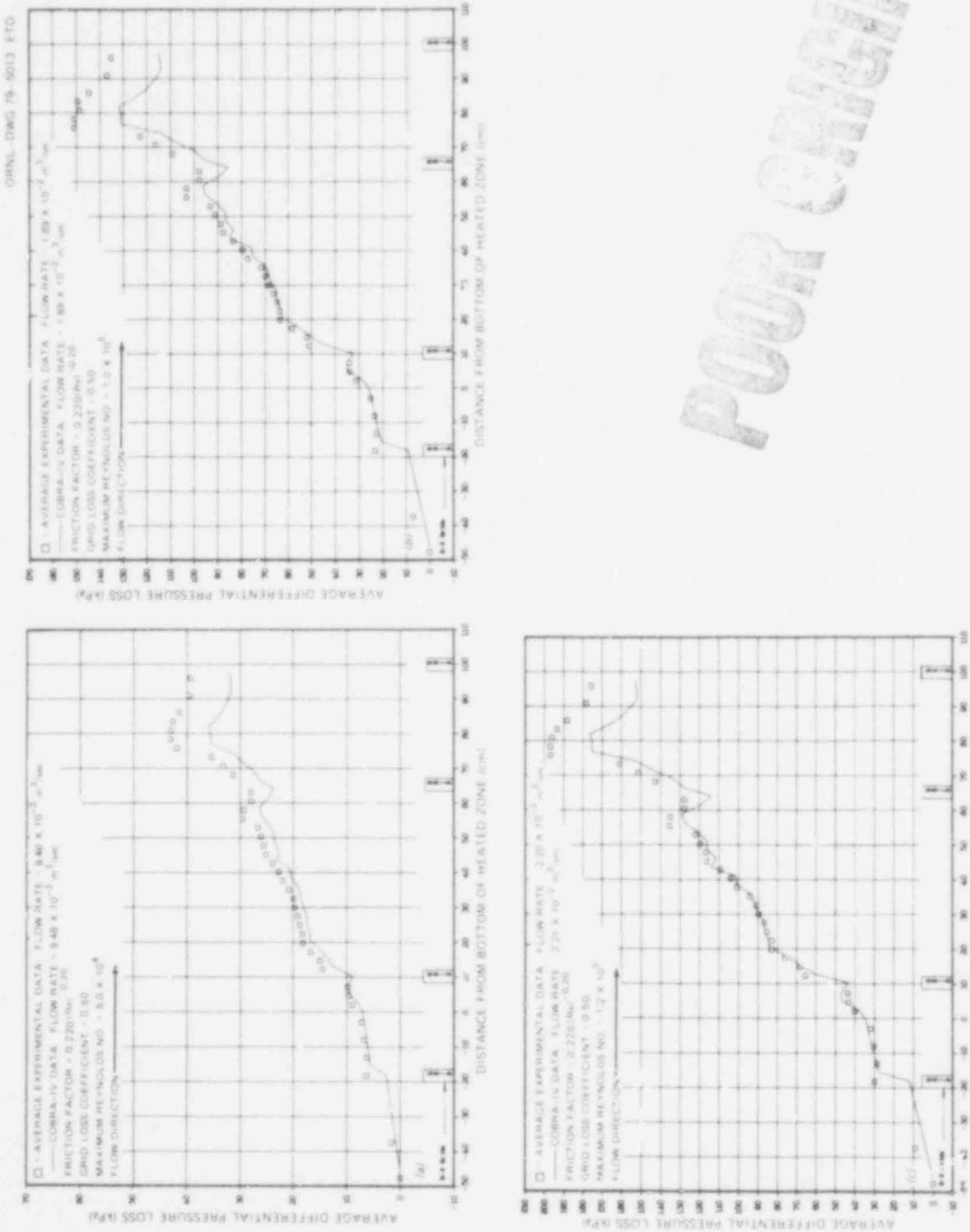

Fig. 2.125. Comparison of predicted and measured pressure loss profiles of B-2 in shroud 1 using lower-limit estimates for friction factor correlation and grid loss coefficient and maximum flow area restriction definition. (a) Re = 5.0×10^4; (b) Re = 1.0×10^5; and (c) Re = 1.2×10^5.

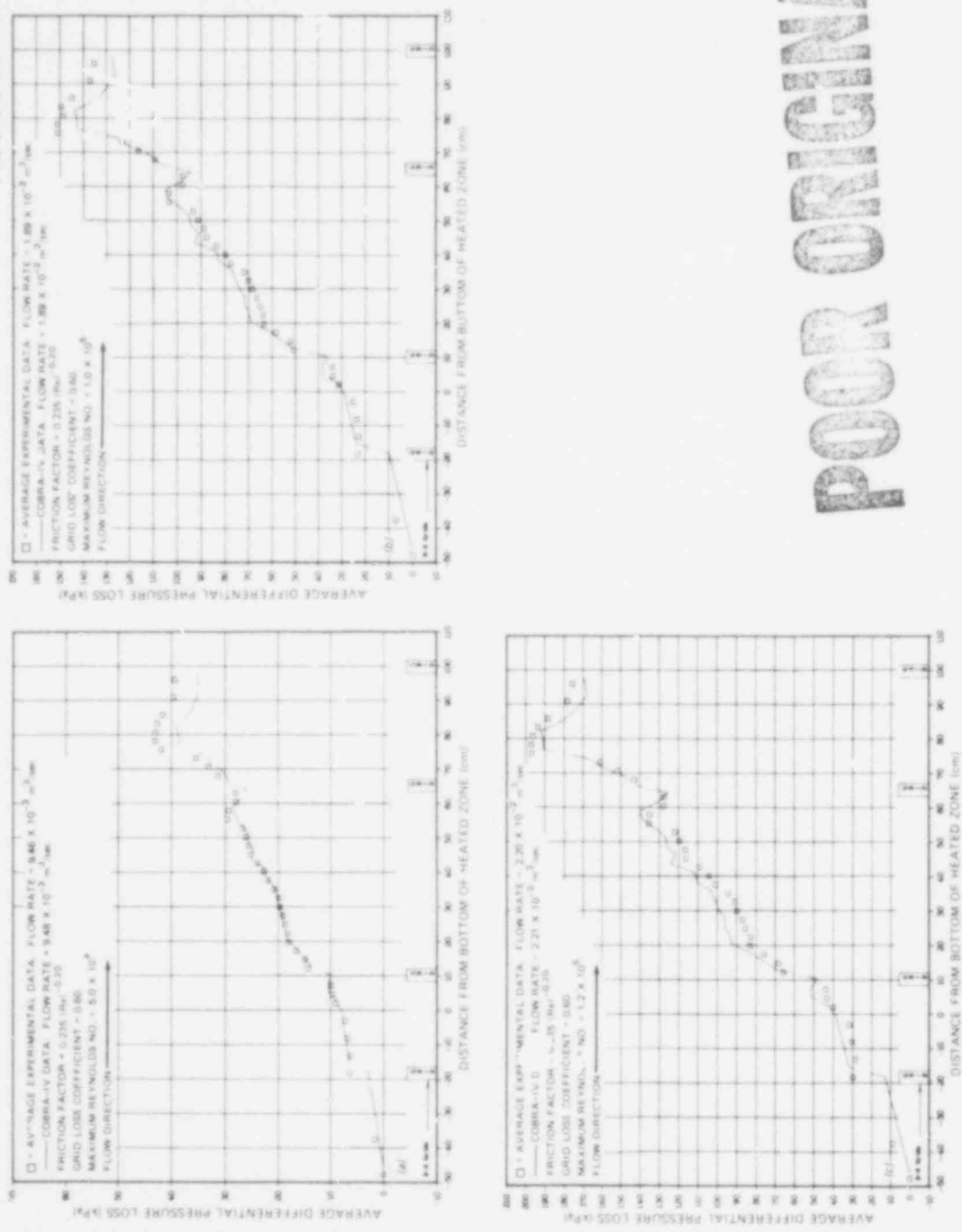

Fig. 2.126. Comparison of predicted and measured pressure loss profiles in B-2 in shroud 1 using upper-limit estimates for friction factor correlation and grid loss coefficient and maximum flow area restriction definition. (a) Re = 5.0×10^4; (b) Re = 1.0×10^5; and (c) Re = 1.2×10^5.

factor correlation and grid loss coefficient that should be used to analyze the flow tests on the deformed bundles. These parameters were determined and used to reanalyze the B-1 and B-2 flow tests, conducted in shroud 1, with the following results:

- The new friction factor correlation represents a decrease relative to the previous correlation; the new spacer loss coefficient represents an increase.
- The new friction factor correlation is much higher than that recommended by Marek et al.[9] and is more in agreement with the value suggested by Tong's summarization.[10]
- COBRA-IV best predicts B-1 pressure loss measurements with the minimum flow area restriction definition; B-2 is best represented by the maximum flow area restriction definition.
- Upper-limit estimates of the friction factor correlation and of the spacer loss coefficient produced COBRA-IV calculated pressure losses in better agreement with experiment at low flow rates; the lower-limit estimates generally gave better agreement at higher flow rates.
- Error limits on the friction factor correlation are probably traceable to flow rate measurement uncertainties. Spacer loss coefficient error limits are too large to be solely explainable by flow rate uncertainties.

2.8 Bundle B-3 Flow Tests

A. W. Longest

Flow tests using room-temperature water were conducted on the deformed B-3 bundle and on the MRBT 4 × 4 reference bundle (geometrically identical to an MRBT undeformed bundle) to characterize the flow resistance for flows in the range $10^4 \lesssim Re \lesssim 10^5$. Deformation of the B-3 array was such that a new flow shroud (identified as shroud 3) was fabricated and used for these tests. The flow shroud (Fig. 2.127) has a net coolant flow area, with the reference bundle in place, of 43.2 cm^2 compared to ~28.8 and ~34.3 cm^2 for flow shrouds 1 and 2, respectively, which were used in flow testing bundles B-1 and B-2. The flow loop configuration,

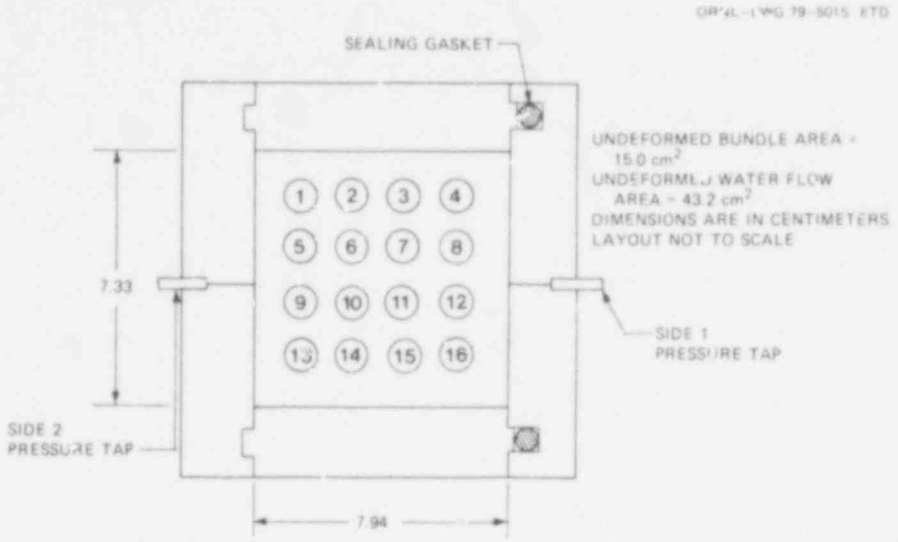

Fig. 2.127. Flow test configuration of B-3 in shroud 3.

instrumentation, bundle preparation, and test procedures were essentially the same as those used in the earlier tests.[2,3] As before, the flow was directed upward through the test assembly in all of these tests.

These tests provide experimental pressure loss data for correlation with channel restriction data (which is obtained from destructive examination of the deformed bundles after the flow tests) and for evaluation of bundle pressure loss calculational models using the COBRA-IV thermal-hydraulics code.[8] This combined experimental-computational approach should produce information useful in modeling the flow resistance of deformed bundles in other situations. Such a detailed analysis of the B-1 flow tests was given previously,[4] and the current status of the analyses is given in Section 2.7. Detailed analysis of these flow tests cannot be performed until the B-3 channel restriction data become available.

Shroud 3 was sized (rectangular cross section) to accommodate the B-3 tube deformation and burst flare-outs and yet be as close fitting as possible (see Fig. 2.128) to ensure measurable pressure losses in the existing flow loop. Even so, one burst flare-out was trimmed (see Fig. 2.129) to avoid machining a relief groove in the shroud wall. Orientation of the B-3 (and the reference bundle) tubes with respect to the pressure taps of shroud 3 is shown in Fig. 2.127.

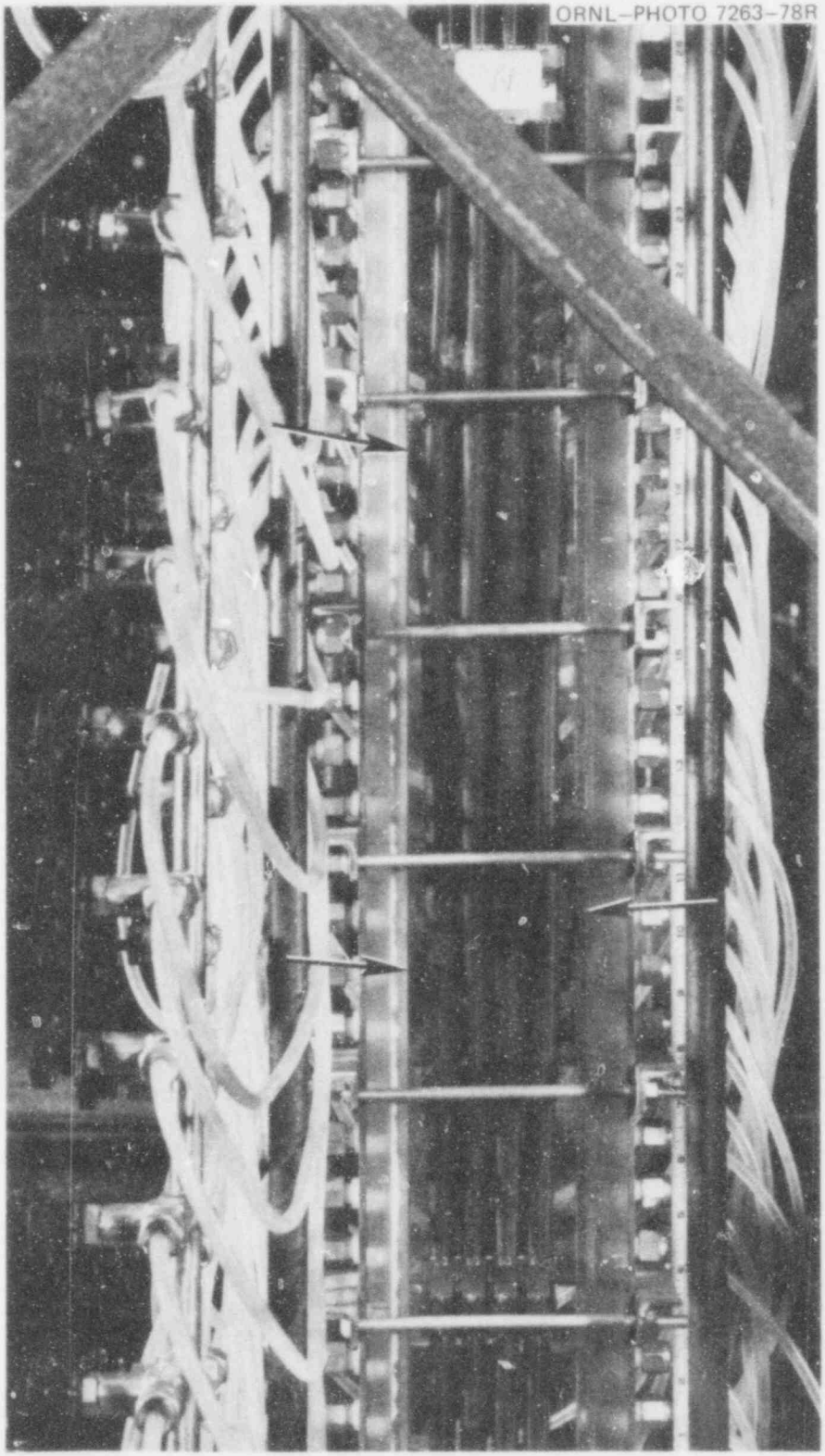

Fig. 2.128. View of bundle B- shroud 3 during flow test. Note tube burst flare-outs almost in contact with shroud walls.

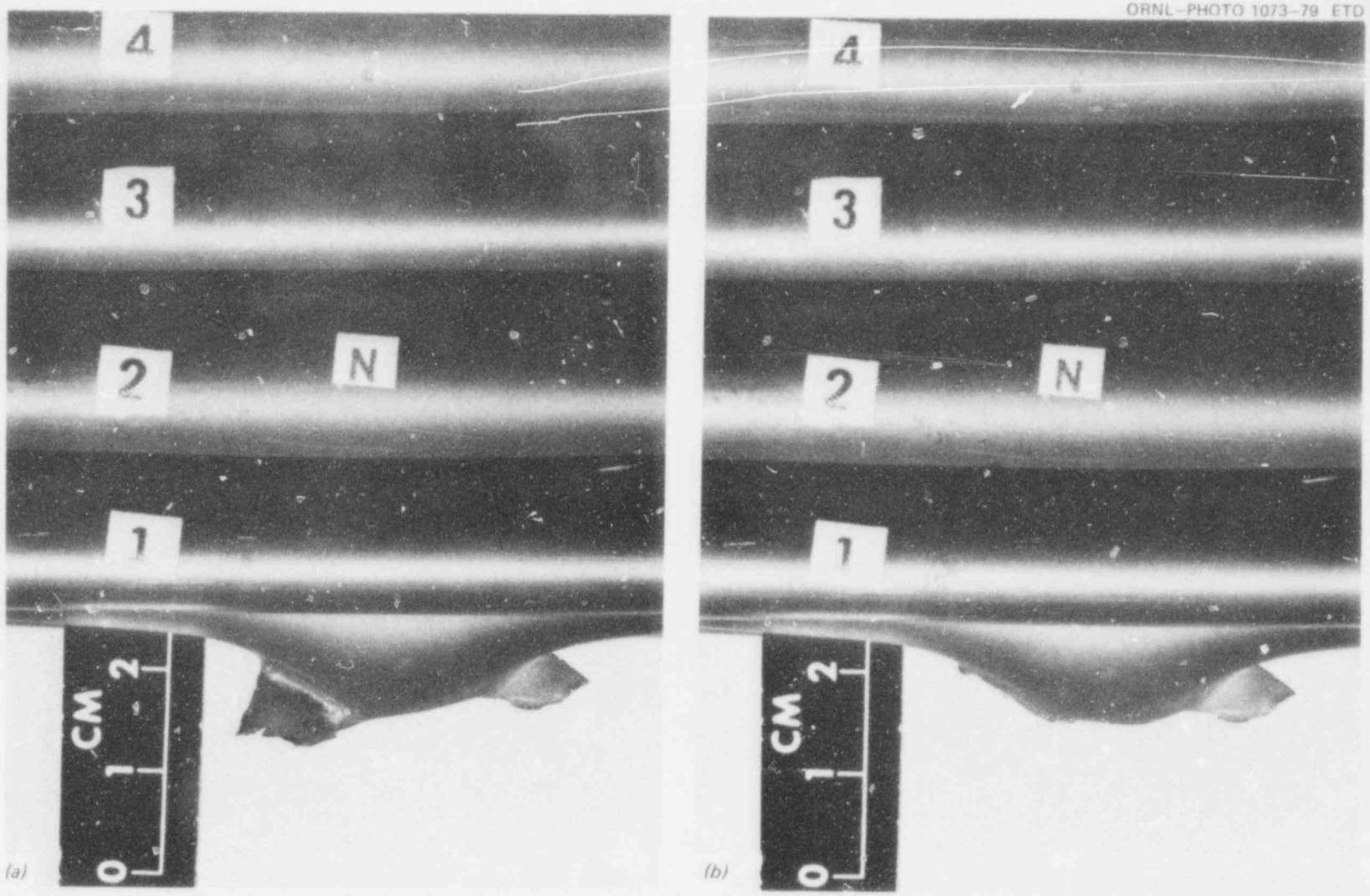

Fig. 2.129. B-3, tube 5 burst flare-out before (a) and after (b) it was trimmed to fit into shroud 3 for flow tests.

Features of flow shroud 3 different from those of flow shrouds 1 and 2 include the use of tongue-and-groove joints for added strength and ease of assembly, the use of smaller-diameter pressure tap holes (0.8 mm diam instead of 1.6 mm), and a rectangular cross section to minimize bypass flow in the annulus. The smaller pressure tap hole size was selected to ascertain if there is a dependence on hole size; the data have not yet been analyzed in this respect.

Axial pressure loss profiles were obtained with the reference bundle in shroud 3 in nine runs (at eight different flow rates) covering a Reynolds number range from $\approx 5.3 \times 10^4$ to $\approx 1.8 \times 10^5$. Representative data, presented in Fig. 2.130, show grid spacer pressure losses and linear pressure loss variation between the grids of magnitudes close to those expected from shroud design considerations. The data appear to be of reasonably good quality and probably within the previously stated error[3] of less than 15% for each pressure measurement (dependent also on the measured flow rate).

Axial pressure loss profiles were obtained with bundle B-3 in shroud 3 in seven runs (at six different flow rates) covering a range of Reynolds number (in the undeformed region) from $\approx 5.3 \times 10^4$ to 1.4×10^5. Typical data, presented in Fig. 2.131, show that the effects of the bundle deformation are consistent from one run to the next. The data appear to be reasonable when the burst locations (noted on the abscissa) and the overall bundle deformation are taken into consideration. The disturbance in the data from the pressure taps facing tubes 1, 5, 9, and 13 (side 2) at 20 to 30 cm from the bottom of the heated zone was apparently caused by the No. 5 tube burst flare-out being too close to the pressure taps (at arrow in Fig. 2.132). Thus, the data from the pressure taps facing tubes 4, 8, 12, and 16 (side 1) better represent the average bundle pressure loss profile in this region.

A comparison of the B-3 and reference bundle pressure loss profiles in shroud 3 at a Reynolds number of 1.4×10^5 is shown in Fig. 2.133. The overall axial pressure loss difference between the reference bundle and B-3 is $\sim$26 kPa. Thus, bundle deformation caused permanent pressure losses equal to $\sim$72% (26/36 × 100) of the total loss of the reference bundle in the shroud 3 test configuration.

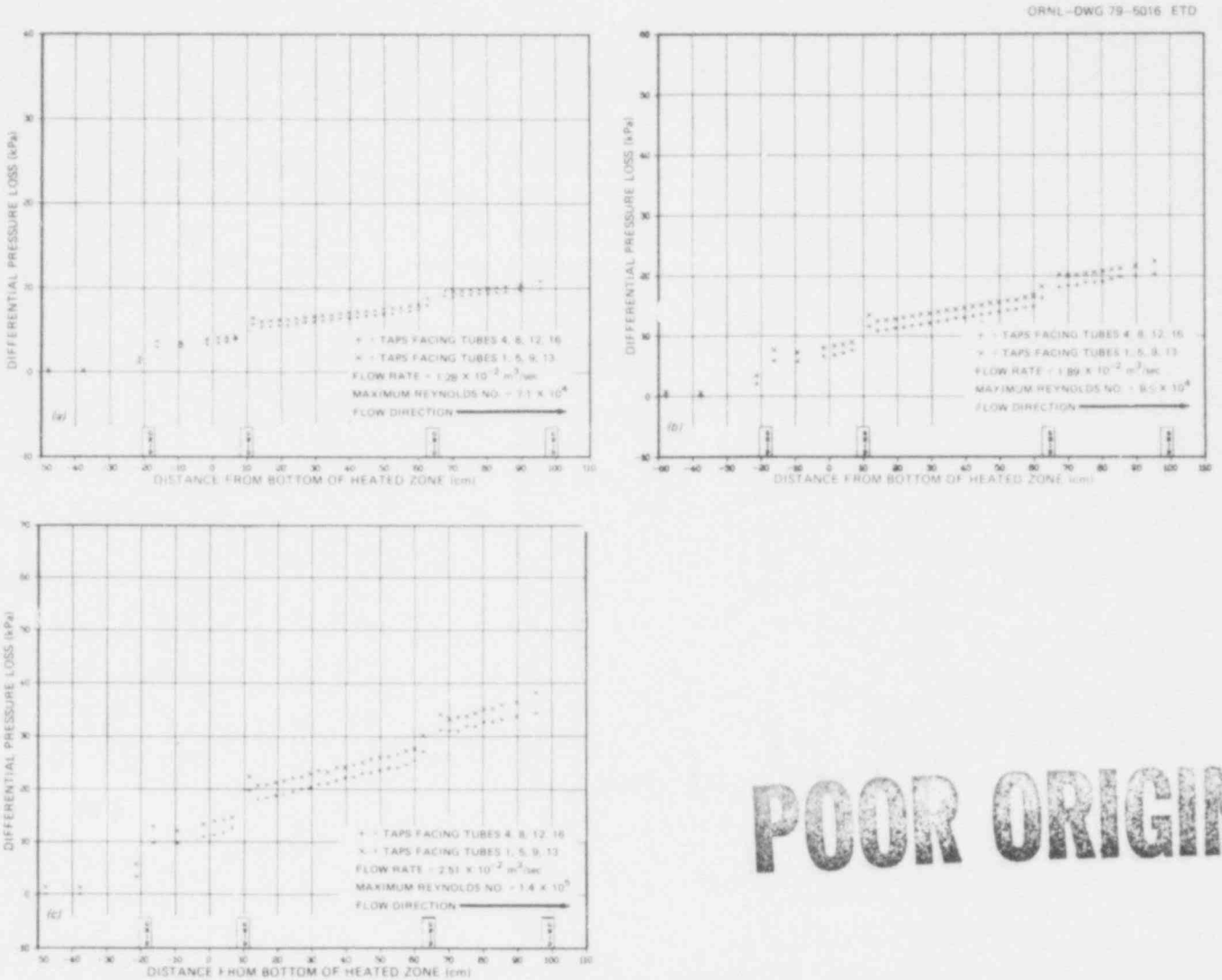

Fig. 2.130. Measured pressure loss profiles of reference bundle in shroud 3. (a) Re = 7.1×10^4; (b) Re = 9.9×10^4; and (c) Re = 1.4×10^5.

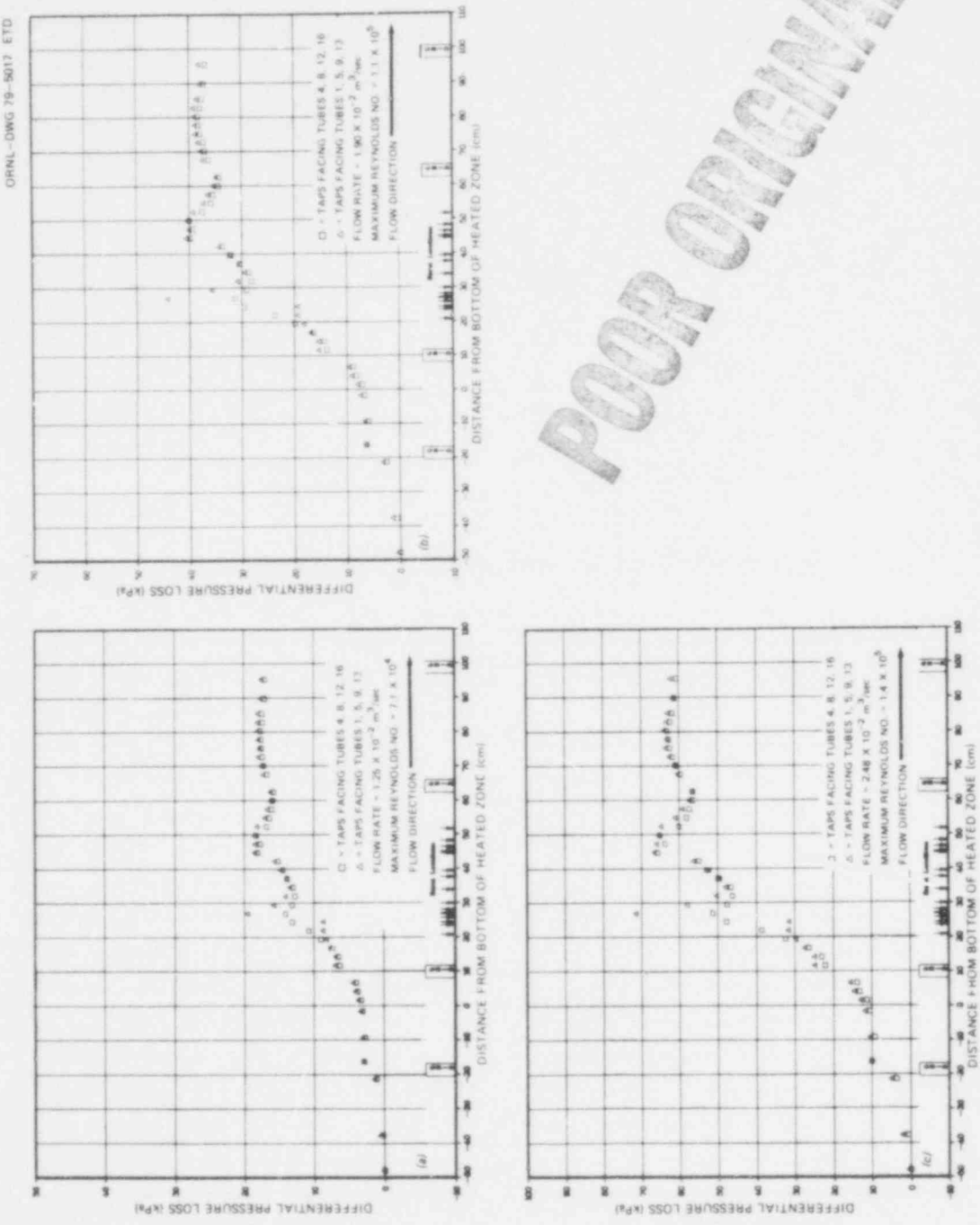

Fig. 2.131. Measured pressure loss profiles of bundle B-3 in shroud 3. (a) Re = 7.1×10^4; (b) Re = 1.1×10^5; and (c) Re = 1.4×10^5.

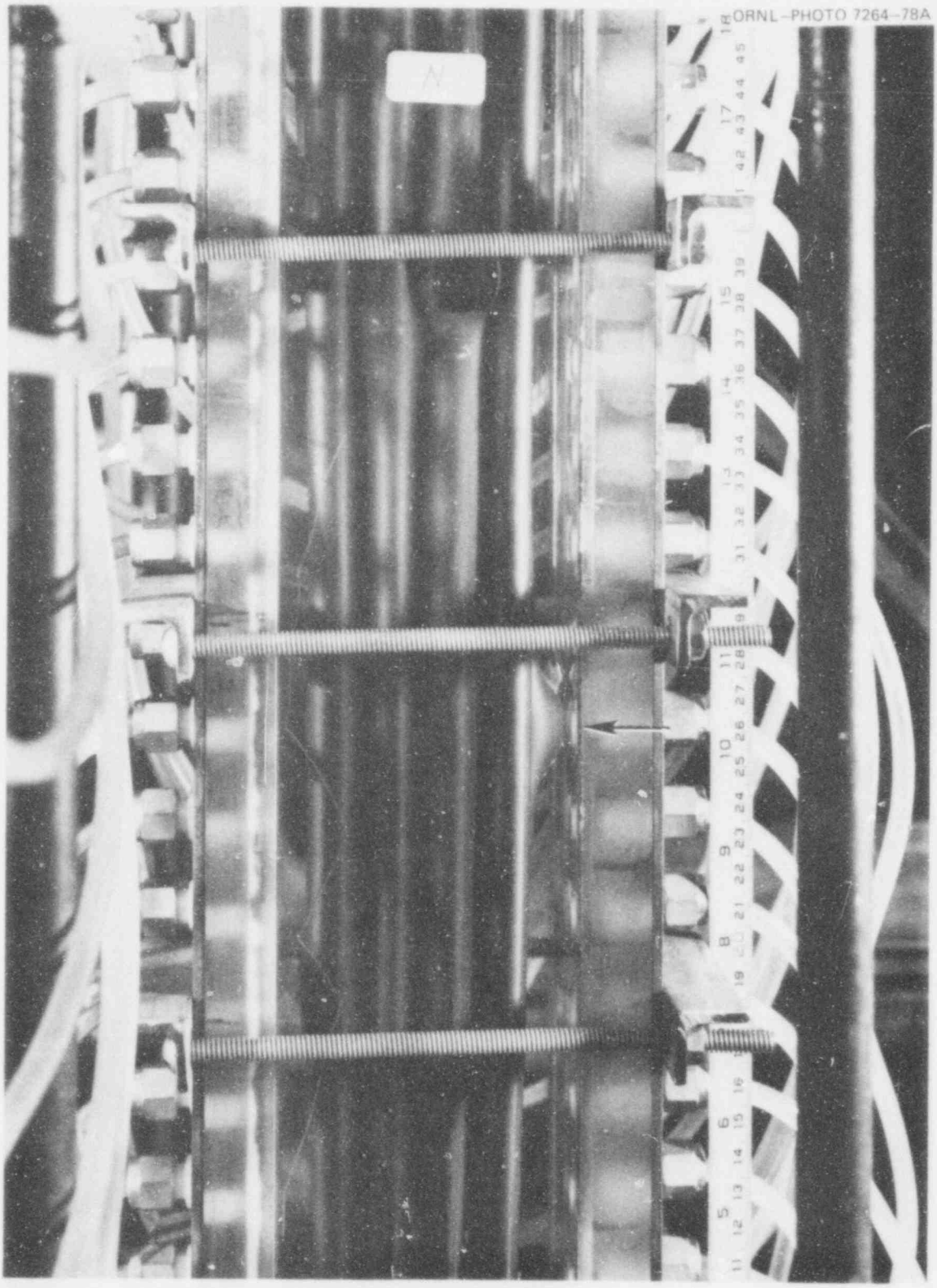

Fig. 2.132. Close-up view of B-3 in shroud 3 showing closeness of tube 5 burst flare-out to side 1 pressure taps.

ORNL-DWG 79-5018 ETD

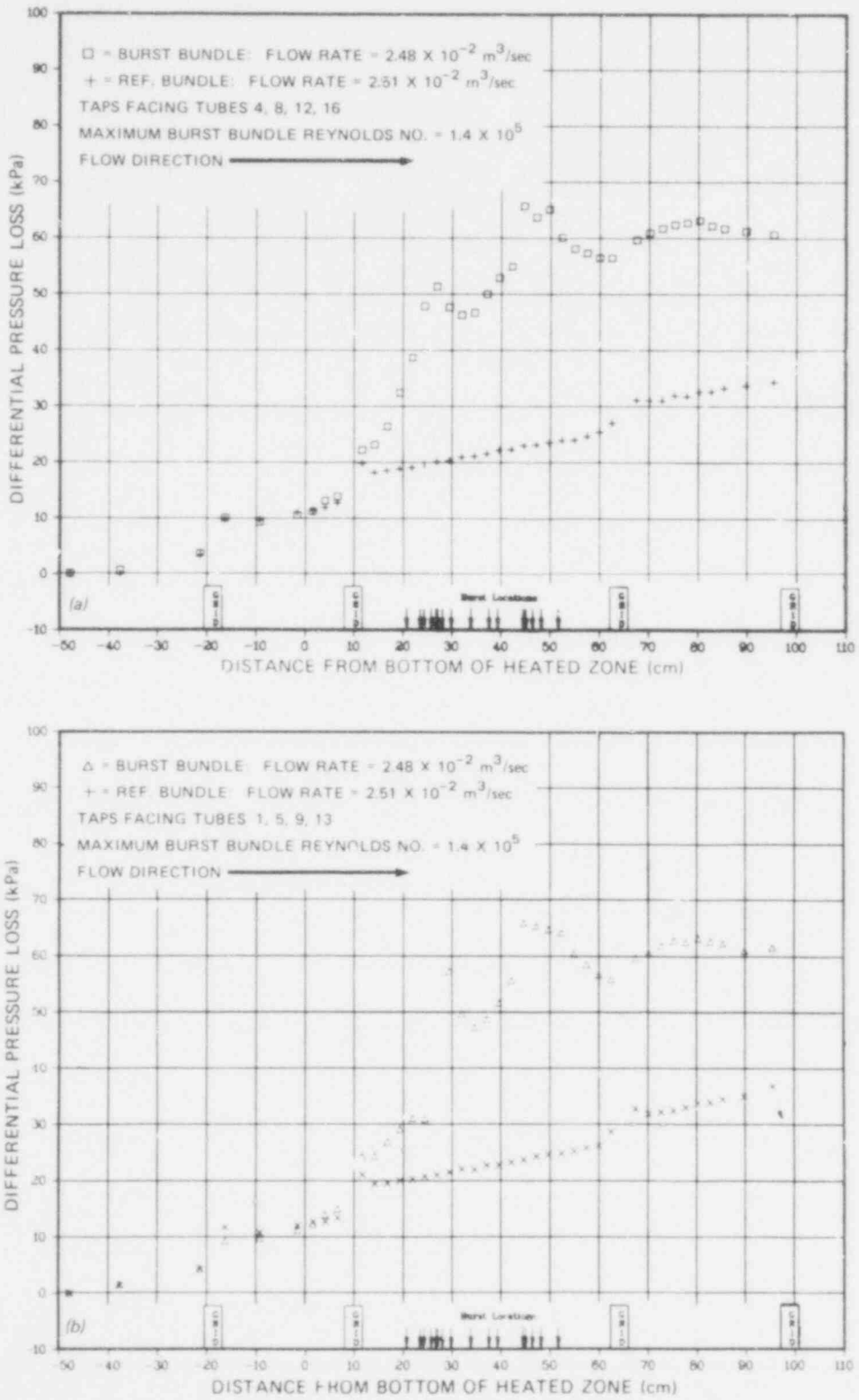

Fig. 2.133. Comparison of measured pressure loss profiles of B-3 with reference bundle in shroud 3 at Re = 1.4×10^5. (a) Side 1 pressure taps; (b) side 2 pressure taps.

The measured overall pressure losses along the B-3 and reference bundles in shroud 3 are plotted as a function of Reynolds number (in the undeformed region) in Fig. 2.134. The data were fitted to the equations given in the figure by a linear regression analysis. These correlations are in good agreement with those obtained previously for the B-1 and B-2 flow data.[3]

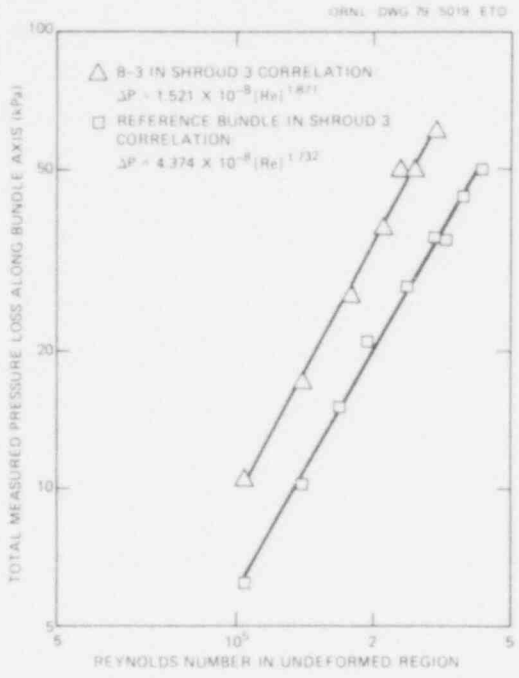

Fig. 2.134. Correlation of B-3 and reference bundle pressure losses with Reynolds number.

2.9 Digital Simulation of Bundle Tests

R. D. Dabbs M. D. White

Work has been under way to develop a transient digital simulator of the MRBT facility to assess the effect of the surrounding environment on the spatial and temporal temperature distribution in the test bundles. Preliminary investigation of experimental data has shown that both steam flow rate and bundle heating rate have an effect on the axial location of simulator bursts. In addition, the axial temperature profiles indicate that both radiation and convection heat transfer may be important during

the test. In order to establish steam conditions for the MRBT experiments, it is necessary to incorporate a detailed fuel pin simulator model in the digital simulator; this work is now complete. Work still in progress includes incorporation of combined convection and radiation heat transfer models in the simulation. The results of this simulation will be a set of parametric curves of axial temperature distribution as a function of steam flow rate and heating rate that can be used to establish operating conditions for future tests.

3. DEVELOPMENT AND PROCUREMENT

3.1 Fuel Simulators

P. T. Jacobs R. W. McCulloch

The inability to procure fuel simulators* from commercial sources on timely schedules in accordance with specifications for use in the MRBT and other ORNL test programs led to the establishment of a Fuel Rod Simulator Technology Laboratory. The mission of the laboratory is to develop components, techniques, and procedures that will assure routine fabrication of fuel rod simulators having specified characteristics. The laboratory was equipped and placed in operation during this report period with a high degree of success. A companion facility, the Infrared Inspection Facility, was also completed and placed in operation.

The laboratory developed the technology for fabricating MRBT fuel simulators by producing a number (16) of prototype units, based on the use of BN cold-pressed preforms in place of compacted BN powder for the electrical isolation material between the heating element and the outside sheath. Repeatability of the procedures was demonstrated by fabricating approximately 92 preproduction simulators that met or exceeded the specifications. These simulators will be used to assemble fuel pin simulators for the first 8 × 8 test bundle. The high degree of success obtained with these preproduction units qualifies the procedures for use in fabricating MRBT fuel simulators for future requirements.

The cold-pressed BN preforms are produced commercially from BN powder procured (from another commercial source) and supplied by ORNL. Approximately 2800 cm of inner preforms (used inside the wound ribbon heating

---

*To avoid misconceptions and confusion, we use the following terminology in MRBT reports. By "fuel simulator" we mean a long, slender, rod-type device that uses electrical energy to simulate the heating produced in a stack of nuclear fuel pellets. By "fuel pin simulator" or "fuel rod simulator," we mean a composite assembly that consists of "Zircaloy fuel cladding" and a "fuel simulator." Thus, in the MRBT, "fuel pin simulators" are distinctively different (more inclusive) from "fuel simulators," whereas in other programs they are identical. Frequent use will be made of the term "simulator" without descriptive modifiers; in these situations the context will make clear which modifier is implied.

element) were rejected due to excessive density variations. The rejected preforms were replaced without impact on the fabrication schedule. Also, excessive amounts of metallic inclusions were detected in some lots of the BN powder used to press the preforms. These metallic contaminants were introduced during powder-screening operations; a new set of stainless steel screens eliminated them. Radiographic techniques were developed and included in the inspection procedures to preclude use of contaminated preforms in the fuel simulators. Approximately 5% of the preforms were rejected for this reason.

Fabrication inspection procedures were revised after completion of ~50% of the required number of simulators to delete preswage radiographic and infrared testing. This was made possible by demonstrated confidence in the closely controlled fabrication procedure. Postswage infrared scanning includes temperature scans at 1 and 10 sec during a heating element transient and at 1 sec during a sheath heating transient.

At the end of this reporting period, all of the required number of preproduction simulators had been fabricated. Fabrication rates of 10 to 12 units per week were achieved toward the end of the production schedule with an acceptance rate of better than 90%. This is unusually good, since the 1-sec transient temperature profile uniformity requirement was increased by more than a factor of 3 (±1.5% compared to ±5% for simulators procured earlier from commercial sources). The maximum variation of the fabrication parameters is less than 1% of the mean value, and many of the simulators exhibit 10-sec transient temperature profile variations of less than 1%.

3.2 Fuel Pin Simulator Seal Development

J. L. Crowley A. W. Longest

As described in the previous report,[7] extensive testing was performed to evaluate the lower end seal leakage problem encountered in the first attempt to test bundle B-3 on April 11, 1978. It was concluded that the design of the copper gasket joint used in bundles B-1, B-2, and B-3 was marginal, due mainly to the large difference in the thermal expansion coefficients between Zircaloy and stainless steel. This difference in

thermal expansion tended to open the gasket joint during heatup even though the two materials were coupled as closely as possible. Since revision of the seal geometry was not an available option in the repair of B-3, a combination of materials consisting of a flat copper washer with Teflon backing as a sealant was used (see Section 4.1).

During this report period, testing of alternative lower end seal designs and gasket materials to determine a satisfactory solution to the leakage problem for future bundles was completed. Three possible solutions to the leakage problem were identified. In order of decreasing estimated cost, they are: (1) an all-welded construction using a commercial Zircaloy-to-stainless-steel transition section, (2) a special gasket joint design utilizing a silver-plated, Inconel X, LO-load-type seal produced by the Advanced Products Company, and (3) a modification of the original gasket joint design involving reversal of the threads on the Zircaloy adapter and on the mating stainless steel body of the Ceramaseal gland.

The second option (i.e., use of the Advanced Products Company seal) was subjected to limited testing with good success. The seal remained leaktight after several thermal cycles. Since machining requirements and careful assembly are crucial to its success and since the early results of the third option showed considerable promise, this option was not thoroughly evaluated. However, it remains a likely alternative if the selected design option proves to be unacceptable.

Conceptually, the third option — the one selected for use in subsequent tests — is not too different from the original design. By simply changing the threads on the Zircaloy adapter from female to male and vice versa on the mating stainless steel portion of the Ceramaseal gland, the joint performance was dramatically improved in our development tests. This reversal of functions tends to tighten the gasket gap during heatup due to the difference in thermal expansion. Because of its simplicity and low cost, we selected this design concept as the best solution to the problem for future MRBT fuel pin simulators.

The revised joint design, shown in Fig. 3.1, utilizes a flat copper gasket with Teflon underneath and the reversed threads mentioned above. The Teflon, applied as a tight wrapping of tape onto the Zircaloy adapter, centers the copper gasket during assembly and also serves as a backup

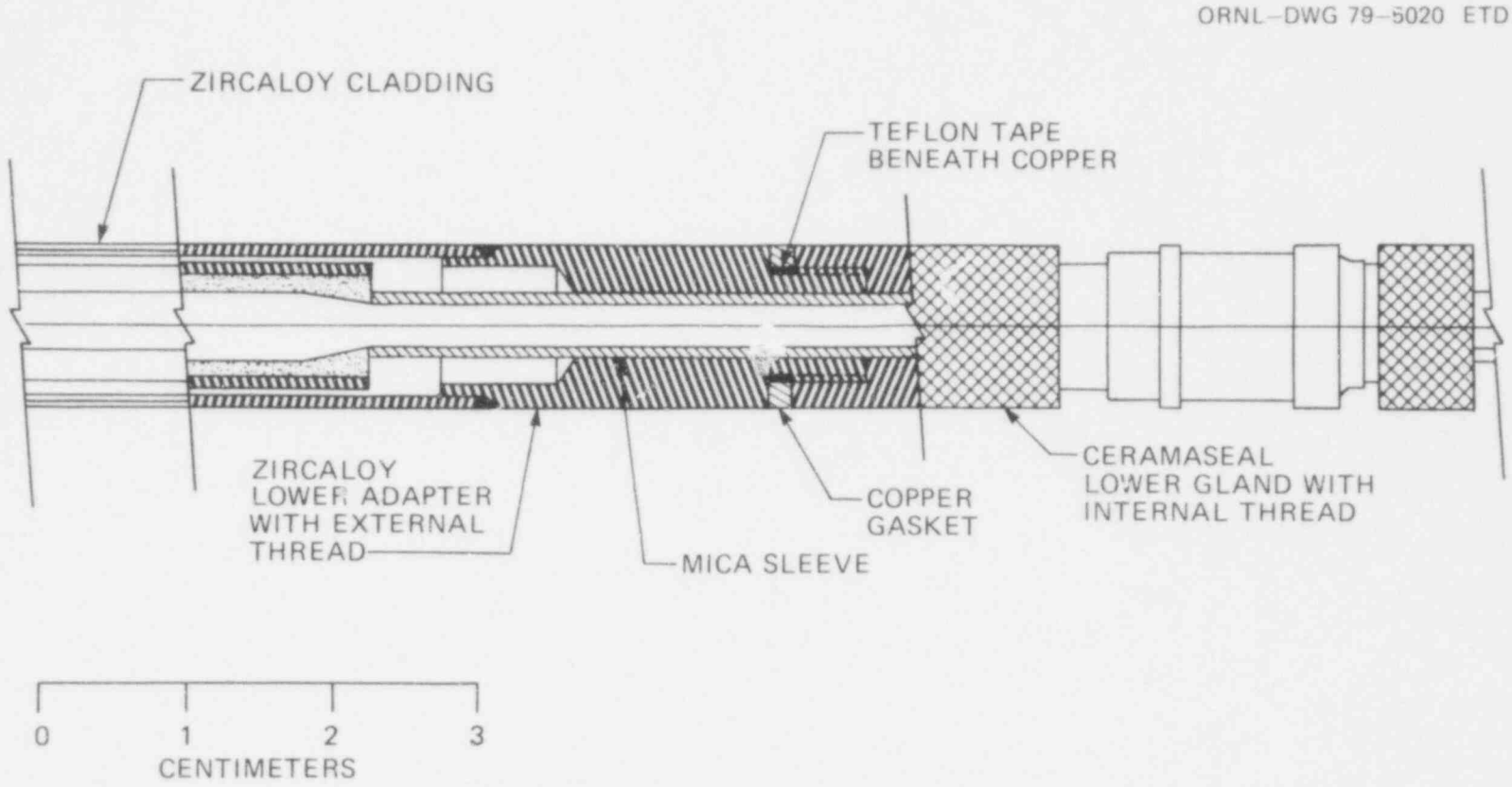

Fig. 3.1. Revised lower gasket joint design for MRBT fuel pin simulators.

sealant. This design, both with and without the Teflon being present, was demonstrated to be an adequate solution in a steam environment with single-unit tests and with two seven-unit assemblies. In these tests the assemblies were subjected to pressure and temperature cycles in excess of those encountered in the bundle tests. In addition, the assemblies were thermally cycled from 100 to 345°C about 10 times more than would be expected in a bundle test. Based on these tests, we believe the revised design, with reasonable control of sealing surface finishes and fitup, will be a satisfactory solution to the leakage problem.

3.3 Portable Power Supply

J. L. Crowley T. L. Hudson*

Delivery of a 2500-A dc portable power supply was made in September. This unit will be used to provide power for the heating of shrouds, via a programmed temperature controller, for both single-rod and multirod facilities.

An acceptance test was performed at the factory and witnessed by a representative of the MRBT Program. After delivery, the unit was installed temporarily at the single-rod test site where an additional checkout was made with a dummy load. After completion of the checkout, the unit was relocated to the Multirod Burst Test Facility where its first operational use will be for extensive shakedown tests, which will also include other new equipment being installed for use with the burst test of 4 × 4 bundle B-4.

3.4 Shroud Thermocouple End Seals

K. R. Carr**

Stainless-steel-sheathed type S thermocouples, with a portion of the sheath removed to expose the bare wires for making junctions, are used to measure shroud temperatures in the bundle tests. End seals are

---

*General Engineering Division.

**Instrumentation and Controls Division.

required at the point where the wires exit the sheath to prevent entry of moisture, resulting in loss of insulation resistance. We have encountered recurring problems with the seal during tests with a resultant loss of shroud temperature data.

We investigated both alternative end seals and an alternative method of increasing the effective resistance from the thermoelectric wires to ground to eliminate the end seal failure problem. Two types of candidate end seals, Epoxylite No. 6203 high-temperature epoxy and prefabricated hermetic end seals [Ceradyne, Inc. (Part No. A70310)], were installed on type S thermocouples and subjected to the typical MRBT test environment (time-at-temperature in steam). Insulation resistance measurements were made periodically on the thermocouples during the test. We found that the epoxy is not suitable for use in this application but that the Ceradyne end seals are acceptable. A helium leak test on the two Ceradyne end seals at the completion of the test showed that these end seals remained leaktight. Based on these limited test results, an order has been placed for eight of the Ceradyne end seals for possible use in future MRBT experiments.

In addition to tests related to the end seal problem, an alternative method of increasing the effective resistance from the thermoelectric wires to ground was investigated. Teflon TFE tubing was placed over the thermocouple sheath and subjected to typical MRBT temperature conditions, while the electrical resistance of the Teflon was monitored. The purpose of this test was to determine if the Teflon would serve as an electrical insulator (with its resistance in series with the thermal-element-to-sheath insulation resistance) to increase the thermal-element-to-ground insulation resistance and thus eliminate the ground leakage current along the thermocouple wires even if the end seal of a thermocouple were faulty. (A wire-to-wire insulation resistance of only several thousand ohms is adequate for accurate temperature measurements in this application.) The Teflon performed very well in this test. Based on these test results, we purchased heat-shrinkable Teflon TFE tubing for use on the shroud thermocouples in the forthcoming shroud heating test to provide final verification that this method will eliminate virtually all of the electrical noise on the shroud thermocouples.

Finally, as further assurance of proper operation of the shroud thermocouples when they are installed in the test vessel, we are expanding our test assembly checkout procedure to include actual current flow through the shroud while the thermocouple signals are monitored.

4. DESIGN, FABRICATION, AND CONSTRUCTION

4.1 Repair of B-3 Seals

A. W. Longest

Evaluation and testing of possible modifications to be made for the repair of the B-3 lower glands were described previously.[7] The design modification selected for the repair consisted of a flat copper washer with Teflon backing on the inside diameter. The Teflon, applied as a tape wrapping, served to hold the washer concentric during installation and also as a backup sealant.

Application of this repair concept to B-3 was complicated by two important considerations: (1) the very delicate nature of the attachment of the 64 thermocouples welded to the inside surface of the 16 fuel pin simulators and (2) the very close confines of the bundle from which it was necessary to unscrew and remove the lower gland. Rotation of the gland about the fuel simulator electrical lead would have placed the internal thermocouples in jeopardy without a technique for determining whether or not their attachment remained intact. For this reason, it was decided to sacrifice the lower glands by fracturing the ceramic insulators, which then allowed removal of the gland without imparting rotational motion to the fuel simulators.

Tools were developed to fracture the ceramic insulator, to remove the remaining portion of the gland, and to install the replacement gland with a minimum of risk to the internal thermocouples. These tools are shown in Fig. 4.1. Beginning at the left of the figure, the modified gland is shown with copper gasket, Teflon backing, and mica sleeve insulator as prepared for installation on B-3. The gland torque tool is shown with a replacement gland inserted and gripped by numerous small set screws. This tool served also to fracture the ceramic portion of the gland in the removal operation, as will be described later. The electrical lead holder was used as an extra precaution to prevent rotation of the heater rod within the fuel pin simulator during the repair operation. The internal thermocouples, lying in grooves of the heater rod sheath and

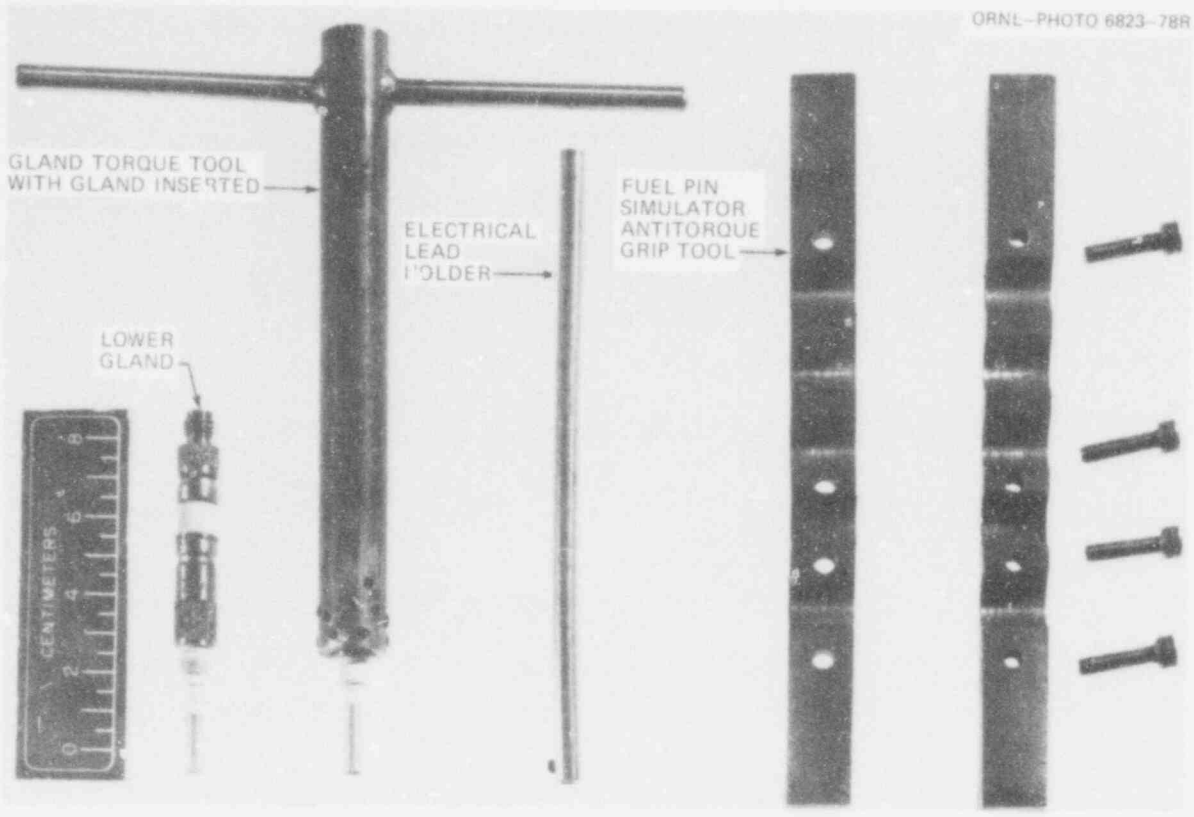

Fig. 4.1. Tools developed for the removal and replacement of B-3 lower glands. A replacement gland is shown prepared for installation.

spot-welded to the inside surface of the Zircaloy tube, are particularly vulnerable to a twisting force. The gripping tool was used to hold a specific tube during reworking operations.

Figure 4.2 shows the fracturing of a ceramic insulator by the use of a screw in the wall of the torque tool. Tightening the screw applied a force at the midsection of the insulator, resulting in a bending stress which cleanly fractured the ceramic. Protective covers are shown over most of the exposed ends; these were used during the repair operations to further reduce the possiblity of disturbing the heater rod via the exposed electrical lead. Heat was applied to melt the braze between the broken gland and the electrical lead, and the lower end of the broken gland was then removed.

Figure 4.3 shows one of the simulators being gripped by the anti-torque tool for removal of the upper portion of the broken gland. Before

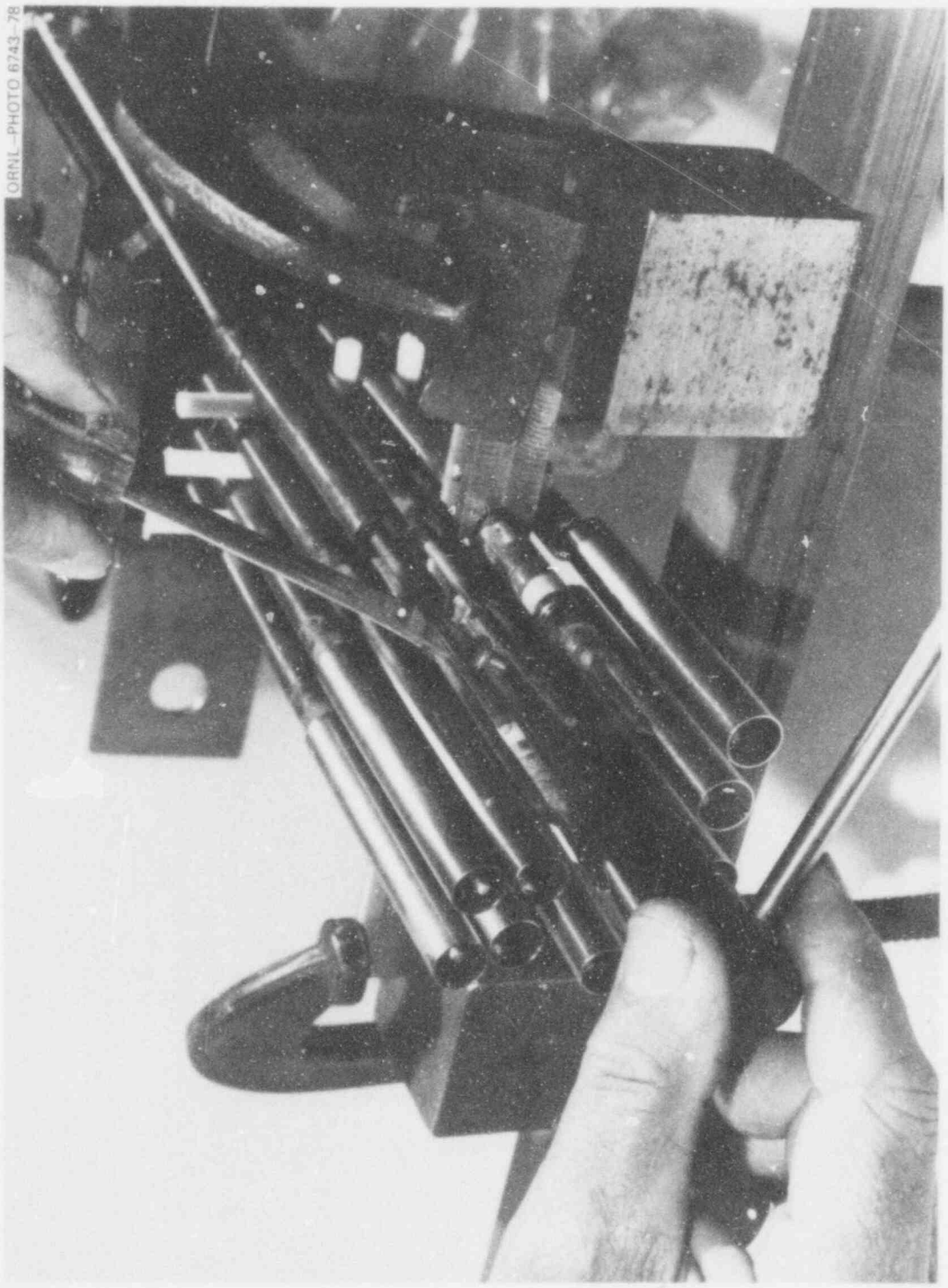

Fig. 4.2. Fracturing of ceramic insulator for removal of B-3 lower gland. Protective shields cover exposed ends to reduce possibility of thermocouple damage.

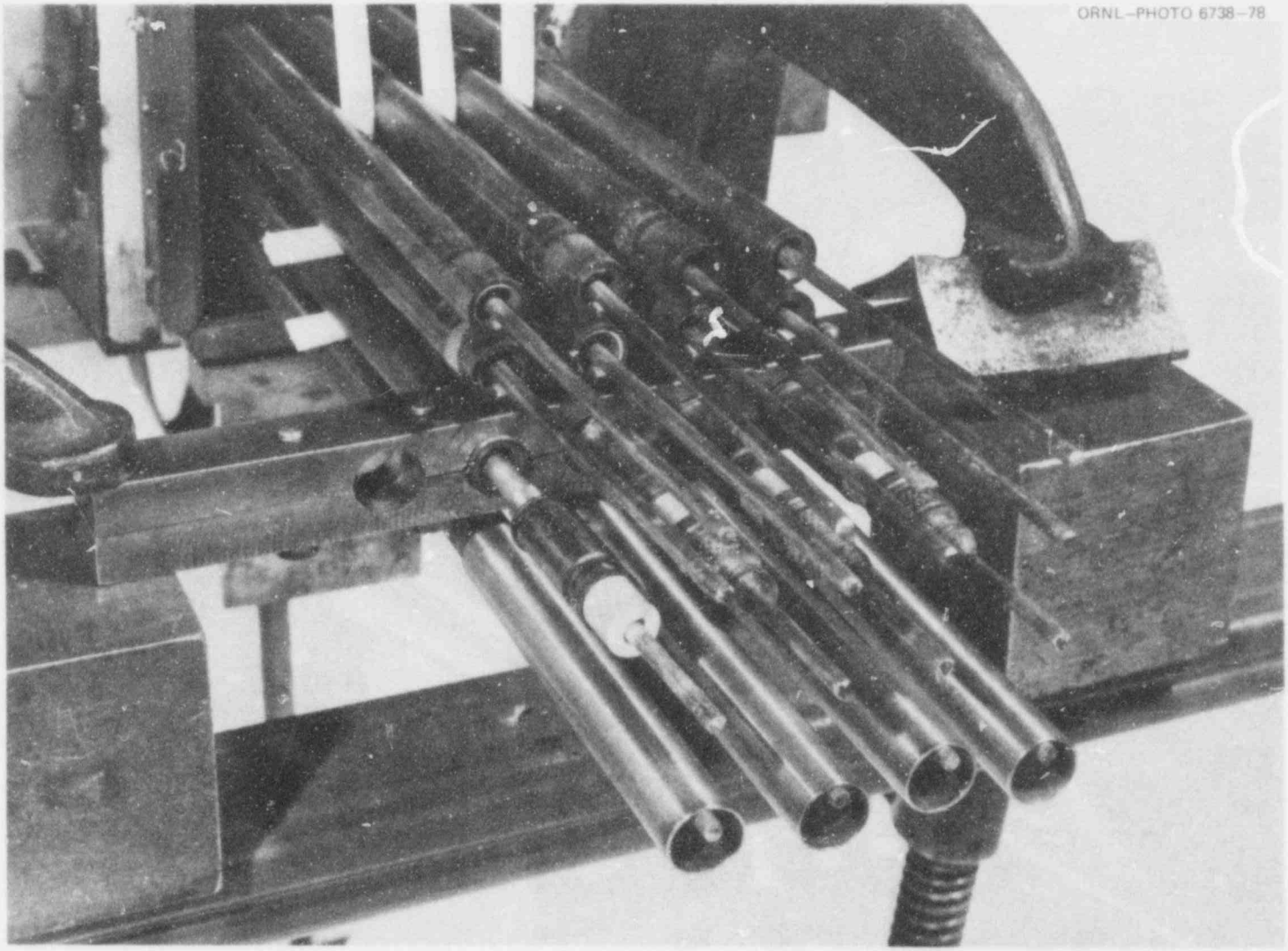

Fig. 4.3. The remaining portion of the gland is shown being removed from one of the simulators which is being held by the antitorque gripping tool.

this photograph was taken, the gland had been unscrewed by use of the torque tool while the electric lead holder was attached to prevent rotation of the fuel simulator.

Replacement glands, which had been carefully prepared with new gaskets, Teflon tape, and mica tube (see Fig. 4.1), were then installed. A temporary Teflon ferrule seal was installed at the electrical lead to make a preliminary leak test. After satisfactory leak rates were established, this temporary seal was replaced by a brazed joint. Numerous checks were made of the heaters and thermocouples to verify that their condition was acceptable. The steam outlet thermocouple was reinstalled, and the normal installation and facility checkouts were initiated in preparation for the burst test.

The B-3 bundle was installed in the test container on July 10, and the burst test operation, which is described in Section 5.2, was conducted on July 13.

4.2 B-4 Fuel Pin Simulators

A. W. Longest

It was decided that the B-4 test assembly should incorporate the B-3 fuel simulators in the same relative positions so that heater characteristics can be minimized when comparing the results of the two tests. Consequently, the B-3 fuel simulators were reconditioned, including new infrared characterization scans, and fabrication of the B-4 fuel pin simulators was initiated.

4.3 Data Acquisition and Software

K. R. Carr* F. R. Gibson*

As mentioned in previous reports, it has been necessary to revise all software to accommodate the replacement of the PDP-8-based computer-controlled data-acquisition system (CCDAS) by the new PDP-11-based CCDAS. These revisions are in progress, and many programs for data and information retrieval are nearly complete. A major part of this software was

*Instrumentation and Controls Division.

written for the Thermal Hydraulic Test Facility (THTF), and considerable modification was required in some cases to adapt it for use in the MRBT Program.

The following is a list of data-acquisition system programs (tasks), a brief description of each, and the percent of work completed:

1. Operator's Display — a program to display on the operator's console CRT the current values (temperatures, pressures, etc.) of selected instruments during pretest or posttest operations. The current readings and the rate of change, in engineering units, are displayed, and the display is updated periodically. This program is 99% complete.

2. Operator's Log — a program similar to the operator's display program, but whose output goes to the line printer. This program can be used to produce a periodic log or a printout on operator demand. This program is 90% complete.

3. Leak Check — a program to produce on demand a listing by the line printer of the rate of change in pressure (leak rate) in all fuel pin simulators. This software will be used in pretest verification of acceptable end seal performance. The leak rate is measured over an operator's selected interval of 1 to 60 min. This program is 90% complete.

4. Pressure Transducer Calibration — a program to assist in the calibration of pressure transducers. This program is essentially the same as the former PDP-8 version and is 85% complete.

5. Engineering Units Conversion — a group of subroutines that convert raw data as read from the analog multiplexer channels to engineering unit values. Calibration coefficients stored in memory are used in the conversion. This program is 50% complete.

6. Instrument Data Base Utility — a program that is used to maintain the instrument data base, containing the channel numbers, type codes, application numbers, etc., on every instrument connected to the data system. This program is 100% complete.

7. Scan Task — a program that reads data from analog channels, checks limits, and enters data onto magnetic tape or disks or into memory. This program is 99% complete.

8. Scan Profiling — a program to display on the CRT a real-time bar graph with up to 100 preselected channels of raw data. This program will be used during a burst test to permit the operator to visually monitor test conditions. It is 95% complete.

9. Real-Time Plot — a program that plots up to four curves on the Ramtek color display terminal. The first curve represents the expected test temperature vs time. The other curves are average rod temperatures, average shroud temperatures, and a selected rod pressure. The last three curves are plotted in real time during a test scan and are used to monitor temperature controller action. This program is 85% complete.

10. Quick-Look Plots — a program that plots test data read from magnetic tape on the Versatec printer/plotter. The number of plots, channels plotted, scales, etc. are selected by the operator before the test; thus, after the test, a user can start the program and all plots will be generated automatically. This program is 90% complete.

11. Power-Bump Printout — a program that will examine the results of the short (1 to 4 sec) power-bump run. The program is essentially the same as the former PDP-8 version. It is 20% complete.

12. Posttest Printout — a program to produce a summary of a test using data recorded on magnetic tape. The printout is a three-part tabulation of test results and is similar to the previous IBM-360 MRBi engineering units printout. The summary will be available within ∿30 min after completion of a test. This program is 95% complete.

4.4 Temperature Control System for Heated Shrouds

K. R. Carr*

A system of programmers and controllers was designed and is being fabricated for use with heated shrouds for both the single-rod and multi-rod test facilities. This control system, which includes the averaging

*Instrumentation and Controls Division.

of multiple temperature signals, was described briefly in the previous report.[7] The control system and the associated portable power supply (see Section 3.3) were originally intended only for use with the single-rod tests. However, in order to broaden the scope of possible test conditions and to provide the needed improvement in bundle shroud temperature characteristics, the controller was designed to function at both sites at a variety of test conditions with a minimum of modifications.

The design is now complete and the fabrication is about 60% complete. Its first operational use will be for extensive shakedown tests of the controllers, the new portable power supply, and other new equipment being installed for use with the burst test of 4 × 4 bundle B-4.

5. OPERATIONS

5.1 Single-Rod Burst Test Facility

J. L. Crowley A. W. Longest

During this report period, two fuel pin simulators were assembled and burst tested in a steam atmosphere. The primary objective of these tests, which were designated SR-45 and SR-46, was to evaluate the performance of the fuel simulators (internal heaters) produced by the Fuel Rod Simulator Development Laboratory at ORNL. A prototype fuel simulator, MR-5, was selected for the SR-45 test, and a preproduction fuel simulator, MN-L-001B4, was selected for the SR-46 test. Prior to its use in the SR-46 test, simulator MN-L-001B4 was tested several times as a bare heater to temperatures in excess of 1200°C in an inert gas atmosphere to determine its insulation resistance behavior at elevated temperatures.

Both of the fuel pin simulators were tested at a heating rate of ∿28°C/sec. Initial pressures were adjusted to cause burst at ∿995°C in the SR-45 test and at ∿1075°C in the SR-46 test. These test conditions were selected to provide tube deformation data of interest in addition to being a demanding test of the fuel simulators. Results of the SR-45 and SR-46 burst tests are presented and discussed in Section 2.2.

Both fuel simulators performed satisfactorily in the tests. Based on their performance, the fabrication procedures were judged qualified for use in fabricating fuel simulators for use in this test program.

5.2 Multirod Burst Test Facility

R. E. Bohanan J. L. Crowley
K. R. Carr* A. W. Longest

Burst test of B-3

After the B-3 bundle was repaired (as described in Section 4.1), it was installed in the test facility, and the normal installation and checkout procedures were repeated. Heating of the vessel was initiated the

*Instrumentation and Controls Division.

afternoon of July 12, and steam flow was admitted to the test vessel about 0500 on July 13. During the early heatup phase when monitoring of conditions by the CCDAS was not possible, a strip-chart recorder provided information on the internal pressure and the lower gland temperature of the fuel pin simulators. The leak rates were satisfactory during this period, and there were no unusual events.

The desired test conditions for B-3 were a burst temperature of ∿760°C and a temperature ramp rate of 10°C/sec. Due to expected differences in heat losses with the heated shroud of B-3, selecting the internal pressure and power necessary to achieve these conditions involved extrapolation of previous burst test results of both single-rod and bundle tests. For example, a ramp power of about 3 kW/rod was selected for B-3, whereas single-rod tests at this same ramp rate require ∿4 kW. Information from the power bump performed on B-3 prior to the burst test led us to reduce this ramp power even more — to about 2.7 kW/rod.

The internal pressure, which determines the burst temperature, was chosen by extrapolation of data from both single-rod and multirod tests. The ratio of initial pressures to burst pressures in previous tests had averaged about 1.1. We chose to assume a ratio of about 1.2 for B-3 with a heated shroud. Therefore, a B-3 initial pressure of ∿11,500 kPa was chosen, whereas ∿10,500 kPa gave these burst conditions in single-rod tests.

After thermal equilibration (about 335°C) of the test assembly was attained, the simulators were pressurized to ∿7700 kPa, and a short powered run (∿9.5-sec transient) was conducted to ascertain that the data-acquisition system and all the instrumentation were functioning properly and that the performance of the test components was as expected. Examination and evaluation of the quick-look data from this short transient (the temperature of the simulators increased to ∿430°C) indicated slight adjustments were needed to achieve the desired heating rate. In particular, the bundle heating rate was adjusted downward and the shroud heating rate was adjusted upward in an attempt to achieve the desired heating rate of 10°C/sec for each. The data also showed that only 2 of the 12 shroud thermocouples were functioning properly. (The shroud thermocouples are

attached directly to the current-carrying shroud and are susceptible to common-mode voltage problems, as will be discussed later.) Attempts to identify and correct the erratic behavior of the malfunctioning shroud thermocouples were unsuccessful, and it was decided to proceed with the burst test as soon as thermal equilibrium was reestablished.

During the high-temperature hold time (~6 hr) between the power-bump test and the burst test, the repaired seal in simulator 7 began to deteriorate. By the time thermal equilibrium was reestablished, the leak in the No. 7 simulator had increased to ~1850 kPa pressure loss per minute at 11,750 kPa, while the remaining simulators had not changed from the earlier values (i.e., ~15 kPa pressure loss per minute).

Since simulator 7 is one of the interior ones, it was desirable that its deformation be representative; this required that its pressure be comparable to the others during the transient. This was accomplished by admitting helium to the simulator at a rate approximately equal to the leak rate; all the other simulators were tested in the usual manner (i.e., with the isolation valves to the supply header closed to provide a closed-volume system on each). As a result of this action, simulator 7 was tested under essentially constant pressure conditions. As soon as simulator 7 burst, an operator closed the isolation valve on the supply header to stop further flow of helium into the vessel.

During the powered portion of the transient, superheated steam flowed downward through the test assembly at the same rate as used in the B-1 test — ~4.5 kg/hr. Inlet steam conditions of 320°C and 300 kPa (absolute) resulted in a Reynolds number of 263. These inlet conditions remained essentially constant until disrupted by escaping helium from the bursting tubes and from the opening of the posttest cooling steam valves. When power to the bundle was terminated, the steam flow was increased to an estimated minimum of 54.5 kg/hr (about twice that used in the B-1 and B-2 tests) to effect rapid cooldown of the bundle.

Following stabilization of the bundle temperature at 329°C, all the fuel pin simulators except No. 7 were pressurized simultaneously to ~11,600 kPa and isolated from the supply header. The supply header was vented and the leak rate of each of the 15 simulators was checked over a 2-min

period, with the pressure loss being ~10 kPa/min. The No. 7 simulator was then pressurized to 11,700 kPa and the manifold supply valve throttled to essentially maintain this pressure level (i.e., the inflow of helium was approximately equal to the seal leakage). With these initial conditions established, the test transient was initiated.

Termination of the powered portion of any burst test can be initiated by any of four actions. The primary shutdown criterion is a preset number of bursts: the number of bursts is counted by the CCDAS and shutdown is initiated at a preset number. It was decided to program the CCDAS to terminate power after 14 bursts with the expectation that all 16 tubes would probably burst. The B-3 test was terminated by this criterion, and the remaining two tubes burst as expected.

B-3 posttest investigations

Posttest investigations were made in an attempt to explain two unusual pressure traces (simulators 3 and 7) and the erratic behavior of 10 of the 12 shroud thermocouples. These investigations and results are summarized briefly below.

Pressure trace of simulator 3. The pressure trace of simulator 3 was unusual in that there were two discontinuities instead of the usual one at the time of burst. The behavior was normal for the first 43.4 sec of the transient, and the slightly decreasing pressure indicated some deformation taking place (see Fig. 2.87).

At this time the pressure decrease rate increased suddenly but not steeply enough to indicate a normal burst. The pressure continued to drop but more slowly, as indicated in the figure, until the tube finally burst ~16 sec after power was terminated.

Posttest pressure checks of the lower gland at both room and operating temperature revealed no deterioration of the seal. It was not possible to check the upper gland; however, no problems have been experienced with this seal in previous tests.

Extensive examinations of the tube by boroscope, dye penetrant, and helium mass spectrometer failed to reveal any evidence of a pinhole-type failure.

Thus far, the cause of the abnormal behavior of this simulator has not been determined. The most likely cause is believed to be a momentary slippage and/or leakage of a small amount of gas from one of the end seals. However, it may not be possible to prove or disprove this supposition.

Pressure trace of simulator 7. As discussed earlier, simulator 7 developed a significant gas leak prior to the test and modifications were made to the test procedure. To compensate for the leak, helium was admitted to the simulator at a rate approximately equal to the leakage rate by throttling a needle valve on the manifold supplying all the simulators. The other simulators were isolated from the manifold during the test as usual. As a result of this arrangement, simulator 7 was tested under essentially constant pressure conditions, as evidenced by Fig. 2.86. An operator was stationed near the isolation valve with instructions to close the valve when he observed a sudden decrease in the simulator pressure, as indicated by a pressure gage on the manifold. He observed a sudden pressure change and closed the isolation valve as quickly as possible.

It was not obvious whether the second discontinuity observed in the figure was caused by the operator's closing of the valve or perhaps by a second burst. In order to resolve this question, a mock-up of the actual test situation was made at the MBTF, using the same valves, manifold, connecting tube, etc., as were used in the burst test. A simplified sketch of the setup for this simulation is included in Fig. 5.1. In addition to the existing MBTF equipment, the simulation included a 51-ml volume to simulate the gas volume of simulator 7, a micro-needle-valve to simulate the gas leak, and a quick-opening valve to simulate the rupture. The leak was simulated by adjusting the needle valve to match the leak rate recorded on the day of the test (a pressure change rate of ~1800 kPa/min at an initial pressure of about 11,500 kPa). The quick-opening valve was then opened to simulate the burst. About 3 sec later, valve HV-7 was closed to duplicate the events on the day of the test. The B-3 simulator 7 (B3-7) test data are compared with the results of the simulation in Fig. 5.1, and the comparison provides convincing evidence that the second discontinuity was caused by operator action in closing

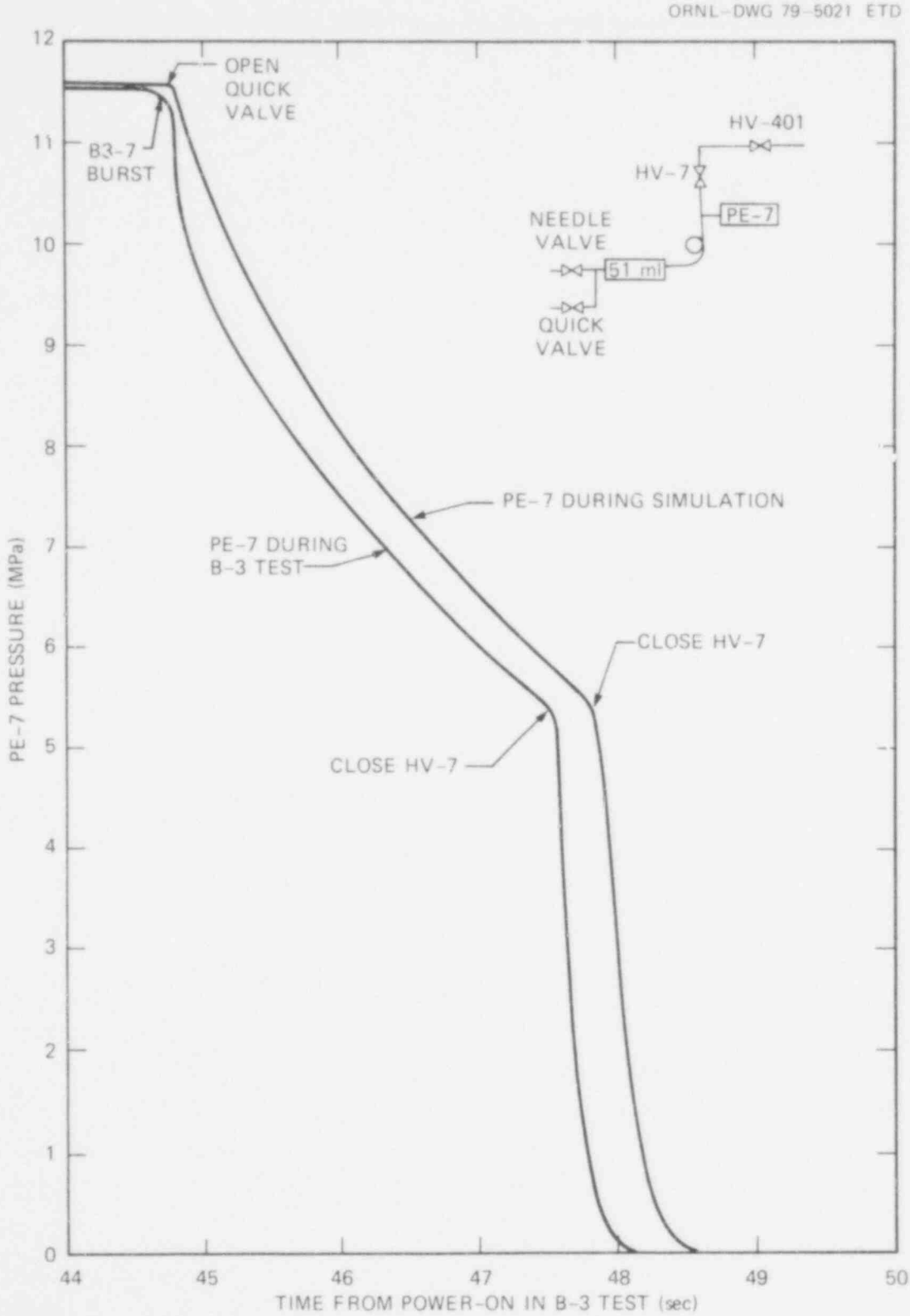

Fig. 5.1. A comparison of B3-7 burst test data with a later simulation to determine the cause of the unusual pressure trace.

the isolation valve and not by a second burst. The continued flow of helium (until HV-7 was closed) caused the pressure decay to be much slower than normally observed.

A posttest pressure check was made on the lower seal gland before disassembly to determine its condition. As suspected, a leak was found at the gland-to-Zircaloy interface when tested at operating temperature (340°C). The room-temperature leak rate was acceptably low, being ∿14 kPa/min. However, when the seal assembly was furnace heated to 340°C, the leak rate increased by a factor of 70. The gland was then disassembled, and the sealing surfaces were examined. A surface scratch was observed on the Zircaloy surface (see Fig. 5.2), and a corresponding indentation was noted on the copper seal washer. This scratch, which must have occurred during the repair operation, was the only abnormality found in the posttest investigation which might explain the leak in fuel pin simulator 7.

Investigation of shroud thermocouple erratic behavior. The Multirod Burst Test Facility now has instrumentation to provide temperature measurements at 12 locations on the shroud, using type S thermocouples with the sensing junctions spot-welded directly to the shroud. The susceptibility of these temperature measurements to noise and signal error is intensified by the potential placed on the thermocouples by the shroud. There was noise on the signals from 10 of the 12 thermocouples in the B-3 burst test for two reasons: (1) seal failure at the sensing-junction end resulted in low insulation resistance to ground and subsequent leakage currents to ground, and (2) six of the channels (which had been installed just prior to the B-3 test) had an improperly wired shield connection in a thermocouple plug which introduced a current leakage path to ground. Methods of alleviating the end seal problem are discussed in Section 3.4. The latter problem was particularly elusive to find and correct, since a systematic error had occurred in the wiring checkout of these six channels. Several B-3 posttest checks were made before the wiring error was detected. These checks, in which all results were normal, included channel-to-channel isolation, input-to-output isolation, and data system overload recovery. These actions should improve the quality of the shroud temperature measurements appreciably in future tests.

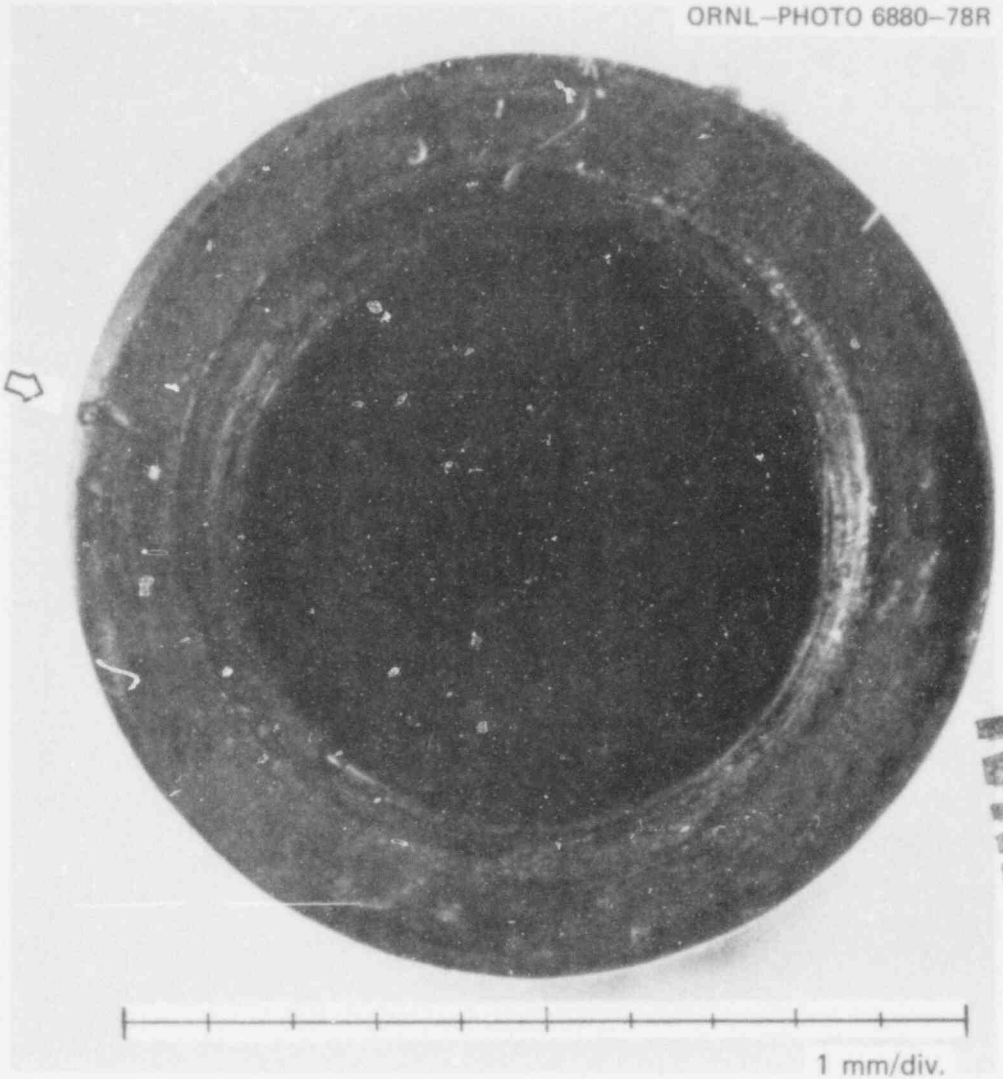

Fig. 5.2. The Zircaloy half of the lower gland showing the surface scratch which is thought to be the cause of the leak in fuel pin simulator 7 in B-3 test.

5.3 B-3 and Reference Bundle Flow Tests

A. W. Longest

During this report period, water flow tests were conducted on the 4 × 4 reference bundle in flow shroud 1 to obtain detailed measurements of the pressure losses occurring with a single grid spacer on the tube bundle and those occurring in the tube bundle in the absence of grid spacers. The results of these tests are presented in Section 2.7.

Flow tests were also performed on the deformed B-3 bundle and the reference bundle in a new flow shroud (identified as shroud 3) to determine the effect of the B-3 deformation on the pressure loss profile. Fabrication of the new flow shroud was necessary, since the B-3 array could not be fitted into either of the smaller flow shrouds (1 and 2) used in flow testing bundles B-1 and B-2. Results of the B-3 bundle and the reference bundle tests in shroud 3 are presented and discussed in Section 2.8.

REFERENCES

1. R. H. Chapman, *Multirod Burst Test Program Quarterly Progress Report for January–March 1976*, ORNL/NUREG/TM-36.

2. R. H. Chapman, *Multirod Burst Test Program Quarterly Progress Report for April–June 1977*, ORNL/NUREG/TM-135.

3. R. H. Chapman, *Multirod Burst Test Program Progress Report for July–December 1977*, NUREG/CR-0103 (ORNL/NUREG/TM-200).

4. R. H. Chapman, *Multirod Burst Test Program Progress Report for January–March 1978*, NUREG/CR-0225 (ORNL/NUREG/TM-217).

5. R. H. Chapman et al., *Effect of Creep Time and Heating Rate on Deformation of Zircaloy-4 Tubes Tested in Steam with Internal Heaters*, NUREG/CR-0343 (ORNL/NUREG/TM-245).

6. R. H. Chapman, *Quick-look Report on MRBT No. 3 4 × 4 Bundle Burst Test*, Internal Report ORNL/MRBT-4 (August 1978).

7. J. L. Crowley, *Multirod Burst Test Program Progress Report for April–June 1978*, NUREG/CR-0398 (ORNL/NUREG/TM-243).

8. C. L. Wheeler et al., *COBRA-IV-1: An Interim Version of COBRA for Thermal-Hydraulic Analysis of Rod Bundle Nuclear Fuel Elements and Cores*, BNWL-1962 (March 1976).

9. J. Marek, K. Maubach, and K. Rehme, "Heat Transfer and Pressure Drop Performance of Rod Bundles Arranged in Square Arrays," *Int. J. Heat Mass Transfer* 16(12), 2215–27 (December 1973).

10. L. S. Tong, "Pressure Drop Performance of a Rod Bundle," p. 65 in *Heat Transfer in Rod Bundles*, papers presented at Winter Annual Meeting of the ASME in New York, Dec. 3, 1968, American Society of Mechanical Engineers, New York, 1968.

NUREG/CR-0655
ORNL/NUREG/TM-297
Dist. Category R3

Internal Distribution

1. M. Bender
2. K. R. Carr
3-17. R. H. Chapman
18. W. G. Craddick
19. J. L. Crowley
20. H. L. Falkenberry
21. D. O. Hobson
22. P. T. Jacobs
23. Milton Levenson
24. D. B. Lloyd
25. A. W. Longest
26. A. P. Malinauskas
27. R. W. McCulloch
28. C. A. Mills
29. J. F. Mincey
30. R. L. Moore
31. F. R. Mynatt
32. F. H. Neill
33. H. R. Payne
34-35. J. L. Rich
36. R. D. Stulting
37. H. E. Trammell
38. J. D. White
39. Patent Office
40. Nuclear Safety Information Center
41-42. Central Research Library
43. Document Reference Section
44-46. Laboratory Records Department
47. Laboratory Records (RC)

External Distribution

48. Office of Assistant Manager, Energy Research and Development, DOE, ORO
49. M. L. Picklesimer, Division of Reactor Safety Research, Office of Nuclear Regulatory Research, NRC, Washington, D.C. 20555
50. M. Fischer, PNS-Leitung, Gesellschaft für Kernforschung, Postfach 3640, 75 Karlsruhe, FRG
51-56. Special distribution by NRC
57-58. Technical Information Center, DOE
59-368. Given distribution as shown for NRC category R3 (10-NTIS)

☆U.S. GOVERNMENT PRINTING OFFICE: 1979-640-079/60